



U.S. Department of Transportation  
Federal Aviation Administration

# NASA/FAA Tailplane Icing Program: Flight Test Report

Thomas P. Ratvasky  
Glenn Research Center, Cleveland, Ohio

Judith Foss Van Zante  
Dynacs Engineering Company, Inc., Brook Park, Ohio

Alex Sim  
Dryden Flight Research Center  
Edwards Air Force Base, California

20000515 068

## The NASA STI Program Office . . . in Profile

Since its founding, NASA has been dedicated to the advancement of aeronautics and space science. The NASA Scientific and Technical Information (STI) Program Office plays a key part in helping NASA maintain this important role.

The NASA STI Program Office is operated by Langley Research Center, the Lead Center for NASA's scientific and technical information. The NASA STI Program Office provides access to the NASA STI Database, the largest collection of aeronautical and space science STI in the world. The Program Office is also NASA's institutional mechanism for disseminating the results of its research and development activities. These results are published by NASA in the NASA STI Report Series, which includes the following report types:

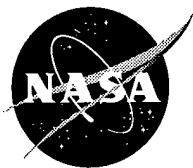
- **TECHNICAL PUBLICATION.** Reports of completed research or a major significant phase of research that present the results of NASA programs and include extensive data or theoretical analysis. Includes compilations of significant scientific and technical data and information deemed to be of continuing reference value. NASA's counterpart of peer-reviewed formal professional papers but has less stringent limitations on manuscript length and extent of graphic presentations.
- **TECHNICAL MEMORANDUM.** Scientific and technical findings that are preliminary or of specialized interest, e.g., quick release reports, working papers, and bibliographies that contain minimal annotation. Does not contain extensive analysis.
- **CONTRACTOR REPORT.** Scientific and technical findings by NASA-sponsored contractors and grantees.

- **CONFERENCE PUBLICATION.** Collected papers from scientific and technical conferences, symposia, seminars, or other meetings sponsored or cosponsored by NASA.
- **SPECIAL PUBLICATION.** Scientific, technical, or historical information from NASA programs, projects, and missions, often concerned with subjects having substantial public interest.
- **TECHNICAL TRANSLATION.** English-language translations of foreign scientific and technical material pertinent to NASA's mission.

Specialized services that complement the STI Program Office's diverse offerings include creating custom thesauri, building customized data bases, organizing and publishing research results . . . even providing videos.

For more information about the NASA STI Program Office, see the following:

- Access the NASA STI Program Home Page at <http://www.sti.nasa.gov>
- E-mail your question via the Internet to [help@sti.nasa.gov](mailto:help@sti.nasa.gov)
- Fax your question to the NASA Access Help Desk at (301) 621-0134
- Telephone the NASA Access Help Desk at (301) 621-0390
- Write to:  
NASA Access Help Desk  
NASA Center for AeroSpace Information  
7121 Standard Drive  
Hanover, MD 21076



U.S. Department of Transportation  
Federal Aviation Administration

# NASA/FAA Tailplane Icing Program: Flight Test Report

Thomas P. Ratvasky  
Glenn Research Center, Cleveland, Ohio

Judith Foss Van Zante  
Dynacs Engineering Company, Inc., Brook Park, Ohio

Alex Sim  
Dryden Flight Research Center  
Edwards Air Force Base, California

National Aeronautics and  
Space Administration

Glenn Research Center

## Acknowledgments

The NASA/FAA Tailplane Icing Program flight testing phases were accomplished only through the dedicated effort of the outstanding flight operations and technical staff at the NASA Glenn Research Center. Special recognition is made to Richard Ranaudo, who served as chief pilot and lead pilot for the Tailplane Icing Program flight tests. His unparalleled knowledge of icing effects on aircraft performance and stability and control provided an increased safety margin in this risky flight test activity. The contributions of pilots Bill Rieke, Bob McKnight and Dennis O'Donoghue, and operations engineers Ed Emery, Chris Hegedus, Mike Ernst and Jon Yenko were key to the productivity of the flight tests. Special acknowledgment to crew chief Dan Gorman and fabrication specialist Steve Hayes for their accomplishments of preparing the aircraft for this unprecedented type of flight testing. Regarding the dynamic data analysis, the authors would like to thank Tom Nettleton of DeHavilland for suggesting the cross-plot method, and also Mike Hinson of Learjet and Dana Herring of Raytheon for their analysis suggestions. The authors would also like to recognize Jim Riley of the FAA William J. Hughes Technical Center for his continuous encouragement throughout this four-year program and careful review of this document. He provided much guidance and motivation throughout the entire program. Finally, we would like to express our appreciation to the sponsors of this research effort: the NASA Aerospace Operations Systems Program and the FAA William J. Hughes Technical Center.

Trade names or manufacturers' names are used in this report for identification only. This usage does not constitute an official endorsement, either expressed or implied, by the National Aeronautics and Space Administration.

Available from

NASA Center for Aerospace Information  
7121 Standard Drive  
Hanover, MD 21076  
Price Code: A08

National Technical Information Service  
5285 Port Royal Road  
Springfield, VA 22100  
Price Code: A08

## Table of Contents

Executive Summary .....	viii
List of Symbols and Abbreviations .....	ix
1.0 Introduction .....	1
2.0 Research Aircraft and Ice Shapes .....	3
3.0 Instrumentation System .....	5
3.1 Aircraft Dynamics System .....	5
3.2 Tail Aeroperformance System .....	5
3.3 Video Systems .....	6
3.4 Calibration Procedures .....	6
4.0 Data Handling Process .....	7
5.0 Steady State Analysis .....	9
5.1 Flight Test Procedures .....	9
5.1.1 Steady-Wings-Level (SWL): .....	9
5.1.2 Steady-Heading Sideslips (SHSS): .....	9
5.2 Method of Analysis for Steady State Data .....	9
5.2.1 General .....	9
5.2.2 Data Consistency Check .....	9
5.3 Results .....	10
5.3.1 Basic Aircraft Performance Description .....	10
5.3.2 Tailplane Angle of Attack Description .....	12
5.3.3 Tailplane Lift Description .....	14
5.3.4 Elevator Hinge Moment Description .....	17
5.3.5 Icing Effects on Tailplane Lift .....	19
5.3.6 Icing Effects on Elevator Hinge Moment .....	24
5.3.7 Center of Gravity Effects on Tailplane Lift .....	27
5.3.8 Thrust Effects on Tailplane Flow Field and Performance .....	29
5.3.9 Spanwise Variation of Flow at the Horizontal Tail .....	31
5.3.10 Effect of Steady Heading Sideslips on Tailplane Flow Field and Performance .....	33
6.0 Dynamic Maneuver Analyses .....	37
6.1 Maneuver Description and Analysis .....	38
6.1.1 Data Compatibility .....	38
6.1.2 Flap Transition .....	39
6.1.3 Speed Transition .....	42
6.1.4 Thrust Transition .....	45
Propwash Effect .....	47
6.1.5 Pushover .....	49
Shaped Maneuver .....	53
Trailing Edge Stall .....	53
Advanced Analysis Methods .....	54
6.1.6 Elevator Doublet .....	58
6.1.7 Balked Landing .....	63

6.1.8 A Case of Turbulence .....	64
6.2 Comparison Between the Pushover and Elevator Doublet .....	65
6.3 Repeatability Analysis for the Pushover .....	68
6.3.1 Description of the Analysis .....	68
6.3.2 Description of the Results .....	69
6.4 Dynamic Maneuvering Conclusions .....	72
6.4.1 Transition Maneuvers .....	72
6.4.2 Dynamic Maneuvers .....	72
7.0 Parameter Estimation Analysis .....	75
7.1 Flight Test Procedures .....	75
7.2 Method of Analysis for Parameter Estimation .....	76
7.3 Results .....	76
7.4 Parameter Estimation Conclusions .....	84
8. Guest Pilot Workshop .....	85
8.1 Attendees .....	85
8.2 Guest Pilot Workshop Flight Test Procedures and Maneuvers .....	85
8.3 Handling Qualities Assessment .....	86
9. Concluding Remarks .....	89
9.1 Data Analysis Techniques .....	89
9.2 Maneuvers .....	90
9.3 Aircraft Configuration .....	90
9.4 Closing Commentary .....	91
10. References .....	93
Appendix A. Flight Test Summaries, Research Aircraft, Ice Shapes and Instrumentation .....	95
Appendix B. Select Steady State Data Plots .....	101
Appendix C. Time Histories of Select Dynamic Maneuvers .....	105
Appendix D. Pressure Coefficient Distributions of the Full Tail Stall .....	147
Appendix E. Recommendations to the Pilot .....	153

## List of Figures

Figure 1. Total lift coefficient vs. aircraft angle of attack for various flap settings. ....	10
Figure 2. Typical lift curve during landing transition .....	10
Figure 3. Force and moment diagram. ....	11
Figure 4. Tailplane angle of attack vs. aircraft angle of attack. ....	12
Figure 5. Tailplane angle of attack vs. airspeed. ....	13
Figure 6. Typical tail AOA during landing transition. ....	13
Figure 7. Horizontal tail diagram.....	14
Figure 8. Tail lift coefficient from wind tunnel data. ....	14
Figure 9. $C_p$ distribution for Baseline tail. ....	15
Figure 10. $C_{L\_Tail}$ vs. $\alpha_{tail}$ from flight data. ....	15
Figure 11. $C_{L\_Tail}$ vs. VTAS from flight data. ....	15
Figure 12. Tail lift coefficient from wind tunnel data and flight data. ....	16
Figure 13. Horizontal stabilizer, elevator and trim tab. ....	17
Figure 14. Elevator hinge moment coefficient vs. tail angle of attack. ....	18
Figure 15. Elevator hinge moment coefficient vs. airspeed. ....	18
Figure 16. Tail lift coefficients for $\delta F = 0^\circ$ . ....	19
Figure 17. Tail lift coefficients for $\delta F = 10^\circ$ . ....	19
Figure 18. Tail lift coefficients for $\delta F = 20^\circ$ . ....	20
Figure 19. Tail lift coefficients for $\delta F = 30^\circ$ . ....	20
Figure 20. Tail lift coefficients for $\delta F = 40^\circ$ . ....	20
Figure 21. Elevator deflection for $\delta F = 0^\circ$ . ....	21
Figure 22. Elevator deflection for $\delta F = 10^\circ$ . ....	21
Figure 23. Elevator deflection for $\delta F = 20^\circ$ . ....	22
Figure 24. Elevator deflection for $\delta F = 30^\circ$ . ....	22
Figure 25. Elevator deflection for $\delta F = 40^\circ$ . ....	22
Figure 26. Elevator hinge moment coefficient for $\delta F = 0^\circ$ . ....	24
Figure 27. Elevator hinge moment coefficient for $\delta F = 10^\circ$ . ....	24
Figure 28. Elevator hinge moment coefficient for $\delta F = 20^\circ$ . ....	25
Figure 29. Elevator hinge moment coefficient for $\delta F = 30^\circ$ . ....	25
Figure 30. Elevator hinge moment coefficient for $\delta F = 40^\circ$ . ....	25
Figure 31. CG effect: $C_{L\_Tail}$ vs. $\alpha_{tail}$ . ....	27
Figure 32. CG effect: $C_{L\_Tail}$ vs. VTAS. ....	27
Figure 33. CG effects on $C_{L\_Tail}$ with respect to $C_{L\_a/c}$ . ....	28
Figure 34. Thrust effect on $\alpha_{tail}$ . ....	29
Figure 35. Thrust effect on $V_{tail}$ . ....	30
Figure 36. Thrust effect on $C_{L\_Tail}$ . ....	30
Figure 37. Span variation of $\alpha_{tail}$ . ....	31
Figure 38. Span variation of $\beta_{tail}$ . ....	32
Figure 39. Span variation of $V_{tail}$ . ....	32
Figure 40. Sideslip effect on $\alpha_{tail}$ . ....	33
Figure 41. Sideslip effect on $\alpha_{a/c}$ . ....	34
Figure 42. Sideslip effect on $C_{L\_Tail}$ . ....	35
Figure 43. Data compatibility time traces. ....	38
Figure 44. Flap transition; clean tail, VIAS = 85kts. ....	40
Figure 45. Flap transition; Failed Boot, VIAS = 80kts (VTAS = 91kts). ....	41
Figure 46. Speed transition time histories; Failed Boot at $\delta F = 20^\circ$ and $C_T = 0.1$ . ....	43
Figure 47. Detail of speed transition: (a) $\alpha_t$ time history with two highlighted data points, and (b) $C_{L\_Tail}$ vs. $\alpha_t$ . ....	44
Figure 48. Thrust transition time histories; Failed Boot at $\delta F = 40^\circ$ and $V = 1.5V_s$ . ....	46
Figure 49. Propwash effect for a clean tail at different flap settings and constant speed, $V = 1.25V_s$ . ....	48
Figure 50. Non-critical pushover time histories: clean tail, $\delta F = 0^\circ$ and $V = 1.5V_s = 100kts$ . ....	51
Figure 51. Critical pushover time histories: Failed Boot ice shape, $\delta F = 20^\circ$ and $V = 1.06V_s = 55kts$ . ....	52

Figure 52. Example of elevator shaping during pushover maneuver.	53
Figure 53. Example of a trailing edge tail stall. Baseline, $\delta F = 40^\circ$ , $V = 0.94V_s = 50\text{kts}$ , $C_T = 0.23$ .	54
Figure 54. Co-plots of $\delta E$ and $FYE$ for pushover. Failed Boot, $VTAS = 80\text{kts}$ , increasing flap deflection.	55
Figure 55. Co-plots of $\delta E$ and $q$ for pushover. Same data base as in Figure 54.	55
Figure 56. Cross-plots for Baseline case at $\delta F = 0^\circ$ and $V = 1.5V_s$ .	56
Figure 57. Cross-plots for same database as Figure 54. Top row is $\delta F = 0^\circ$ , middle $10^\circ$ and bottom $20^\circ$ .	57
Figure 58. Cross-plots corresponding to data in Figure 53, the trailing edge stall pushover case.	57
Figure 59. Elevator doublet for a clean tail, $\delta F = 0^\circ$ , $V = 1.5V_s = 100\text{kts}$ .	59
Figure 60. Elevator doublet for the Failed Boot, $\delta F = 20^\circ$ , $V = 1.1V_s = 55\text{kts}$ .	60
Figure 61. Pitch response and damping characteristics for extreme elevator doublet cases.	61
Figure 62. Cross-plots of $q$ vs. $\delta E$ for elevator doublet data from Figure 61.	62
Figure 63. Cross-plots of $N_z$ vs. $FYE$ for elevator doublet data from Figure 61.	62
Figure 64. Balked landing tracking task.	63
Figure 65. Comparison between quiescent and turbulent environment. Failed Boot, $\delta F = 0^\circ$ flaps.	64
Figure 66. Three maneuvers (thin lines) and their average (thick line) vs. scaled time for an Inter-Cycle ice, $\delta F = 0^\circ$ , $V = 1.5V_s = 100\text{kts}$ test point. Error bars are indicated on select traces.	70
Figure 67. Additional elevator required to trim.	77
Figure 68. Icing effects on pitching moment derivatives, $\delta F = 0^\circ$ .	79
Figure 69. Icing effects on pitching moment derivatives, $\delta F = 10^\circ$ .	80
Figure 70. Icing effects on pitching moment derivatives, $\delta F = 20^\circ$ .	81
Figure 71. Icing effects on pitching moment derivatives, $\delta F = 30^\circ$ .	82
Figure 72. Icing effects on pitching moment derivatives, $\delta F = 40^\circ$ .	83
Figure 73. Cooper-Harper handling qualities rating flow chart.	86
Figure 74. Cooper-Harper ratings for approach and go-around MTE.	87
Figure A-1. NASA Glenn Research Center Icing Research Aircraft.	97
Figure A-2. Inter-Cycle Ice on tailplane.	98
Figure A-3. Failed Boot Ice on tailplane.	98
Figure A-4. S&C Ice on tailplane.	99
Figure A-5. Tail flow probes and pressure belt.	99
Figure A-6. 5-hole tail flow probe head.	100
Figure A-7. Tail camera position.	100
Figure B-1. 1995 data consistency results.	101
Figure B-2. 1997 data consistency results.	102
Figure B-3. Tail flow field during SHSS maneuvers.	103
Figure C-1. Pushover, Baseline, $\delta F = 0^\circ$ , $VIAS = 1.50V_s = 100\text{kts}$ .	106
Figure C-2. Pushover, Baseline, $\delta F = 40^\circ$ , $VIAS = 1.06V_s = 55\text{kts}$ .	108
Figure C-3. Pushover, Inter-Cycle Ice, $\delta F = 0^\circ$ , $VIAS = 1.50V_s = 100\text{kts}$ .	110
Figure C-4. Pushover, Inter-Cycle Ice, $\delta F = 40^\circ$ , $VIAS = 1.06V_s = 55\text{kts}$ .	112
Figure C-5. Pushover, Failed Boot, $\delta F = 20^\circ$ , $VIAS = 1.33V_s = 75\text{kts}$ .	114
Figure C-6. Pushover, Failed Boot, $\delta F = 20^\circ$ , $VIAS = 0.97V_s = 55\text{kts}$ .	116
Figure C-7. Pushover, S&C, $\delta F = 0^\circ$ , $VIAS = 1.50V_s = 100\text{kts}$ .	118
Figure C-8. Pushover, S&C, $\delta F = 20^\circ$ , $VIAS = 0.97V_s = 55\text{kts}$ .	120
Figure C-9. Elevator doublet, Baseline, $\delta F = 0^\circ$ , $VIAS = 1.50V_s = 100\text{kts}$ .	122
Figure C-10. Elevator doublet, Baseline, $\delta F = 40^\circ$ , $VIAS = 1.06V_s = 55\text{kts}$ .	124
Figure C-11. Elevator doublet, Inter-Cycle Ice, $\delta F = 30^\circ$ , $VIAS = 1.59V_s = 85\text{kts}$ .	126
Figure C-12. Elevator doublet, Inter-Cycle Ice, $\delta F = 40^\circ$ , $VIAS = 1.63V_s = 85\text{kts}$ .	128
Figure C-13. Elevator doublet, Failed Boot, $\delta F = 30^\circ$ , $VIAS = 1.59V_s = 85\text{kts}$ .	130
Figure C-14. Elevator doublet, Failed Boot, $\delta F = 30^\circ$ , $VIAS = 1.03V_s = 55\text{kts}$ .	132
Figure C-15. Elevator doublet, S&C, $\delta F = 20^\circ$ , $VIAS = 0.97V_s = 55\text{kts}$ .	134
Figure C-16. Elevator doublet, S&C, $\delta F = 30^\circ$ , $VIAS = 1.40V_s = 75\text{kts}$ .	136



Figure C-17. Thrust transition, Baseline, $\delta F = 0^\circ$ , VIAS = 1.20Vs = 80kts. ....	138
Figure C-18. Thrust transition, Baseline, $\delta F = 40^\circ$ , VIAS = 1.63Vs = 85kts. ....	140
Figure C-19. Thrust transition, Failed Boot, $\delta F = 0^\circ$ , VIAS = 1.20Vs = 80kts. ....	142
Figure C-20. Thrust transition, Failed Boot, $\delta F = 40^\circ$ , VIAS = 1.63Vs = 85kts. ....	144
Figure D-1. Select time histories of the stall event. Circles indicate times presented in Figure D-3. ....	147
Figure D-2. Location of pressure taps on clean airfoil. ....	148
Figure D-3. Plots of $C_p$ for full tail stall event at various times. Solid, blue line for lower surface. ....	149

## List of Tables

Table 1. Dynamic maneuvers flown and number of test points for each. ....	37
Table 2. Pushover – elevator doublet comparison. ....	65
Table 3. Pass/Fail maps for both the control force and pitch response ratings during a pushover maneuver ....	67
Table 4. Repeatability analysis – precision levels for several flight conditions to minimum $N_z$ . ....	71
Table 5. Repeatability analysis – accuracy of achieving the target values for non-critical and critical cases. ....	71
Table 6. Comparison of the advantages and disadvantages for both the pushover and elevator doublet. ....	74
Table 7. Conditions for the parameter estimation maneuvers. ....	75
Table 8. Guest pilot attendees. ....	85
Table 9. Critical and non-critical aircraft configurations for tailplane stall. ....	90
Table A-1. 1995 flight test summary. ....	95
Table A-2. 1997 flight test summary. ....	95
Table A-3. Physical characteristics of research aircraft. ....	96
Table A-4. Instrumentation specifications. ....	96

## Executive Summary

The purpose of this report is to present the results from research flights that explored the characteristics of an ice-contaminated tailplane. Using the NASA Twin Otter Icing Research Aircraft, fifty-one test flights were conducted with various simulated ice shapes attached to the leading edge of the horizontal tailplane. A clean leading edge provided the baseline case, then three ice shapes were flown in order of increasing severity. Flight tests with each ice shape included both steady state and dynamic maneuvers. The steady state points were 1G wings level and steady heading sideslips. The primary dynamic maneuvers were pushovers to approximately 0.5G, 0.25G, and 0G; elevator doublets; thrust transitions and simulated balked landings. These maneuvers were conducted for a full range of flap positions and aircraft angle of attack where possible. In some iced cases, full flaps could not be deployed without leading to a full tail stall.

The analysis of this data set has clearly demonstrated the detrimental effects of ice contamination on aircraft stability and controllability. Paths to tailplane stall were revealed through parameter isolation and transition studies. These paths are (1) increasing ice shape severity, (2) increasing flap deflection, (3) high or low speeds, depending on whether the aircraft is in a steady state (high speed) or pushover maneuver (low speed), and (4) increasing thrust. It is suspected that the adverse response to thrust is configuration specific, *i.e.*, it occurs when the thrust line is positioned above the aircraft's center of gravity.

The two dynamic maneuvers, the pushover and elevator doublet, were studied in depth. Analysis of the pushover provided an understanding of its effect on tailplane angle of attack and the imminent tail stall characteristics. A possible alternate maneuver, the elevator doublet, was compared to the pushover. From this comparison, it became apparent that the extreme tailplane angles of attack attained by the pushover are not a necessary precursor to tail stall. Rather, it is the combination of tail angle of attack and elevator deflection; *i.e.*, the more extreme the elevator deflection trailing edge up, the lower the stall margin. Finally, the elevator doublet was also used for a stability and control parameter estimation process. These results indicated that the elevator control effectiveness derivative,  $C_{m\delta E}$ , was severely degraded by the ice contamination.

Although it was not the intention of this research program, a full tail stall was experienced during one of the thrust transition test points. The data acquired during this event provided great insight into the recovery procedure. It is interesting to note from this one experience that even though corrective actions – yoke back, power to idle and flaps up – were applied within 0.4 seconds, the aircraft continued to lose 300 ft of altitude over 8 seconds before the aircraft recovered.

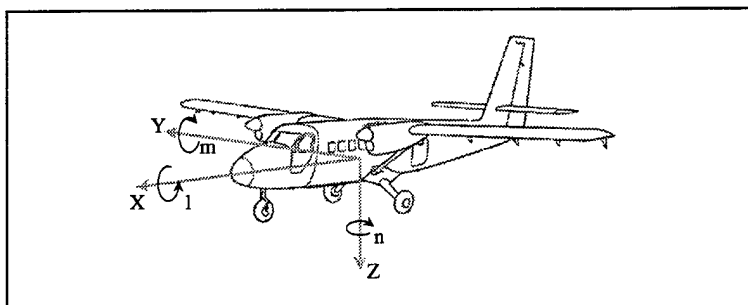
The concluding phase of the Tailplane Icing Program was a Guest Pilot Workshop. It was conducted to quickly transfer “lessons learned” on ice-contaminated tailplane stall to the FAA and Transport Canada, airframe manufacturers, and the general public through the aviation media. The Guest Pilot Workshop served as an excellent forum to transfer this information and to obtain handling quality ratings of the test aircraft from the guest pilots. The handling quality results unanimously demonstrate the degradation of the aircraft with increased flap angle. In addition, an educational video for pilots entitled *Tailplane Icing* was produced and disseminated internationally. Of crucial importance to the pilot is the point that although the difference in tactile cues between an impending wing and tail stall are subtle, the recovery procedures are diametric.

The flight research effort was very comprehensive, but limited to one aircraft, and therefore did not examine effects of tailplane design and location, or other aircraft geometry configuration effects. However, this effort provided the role of some of the parameters in promoting tailplane stall. The lessons learned from this effort will provide guidance to regulatory agencies, aircraft manufacturers, and operators on ice-contaminated tailplane stall in the effort to increase aviation safety and reduce the fatal accident rate.

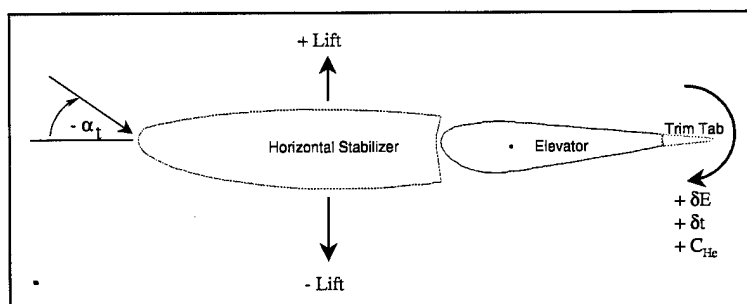
## List of Symbols and Abbreviations

$A$	Aspect Ratio, wing	$VIAS$	Indicated airspeed, kts
AOA	angle of attack, deg	$V_{FE}$	flap extension speed
$alt$	altitude, ft	$V_S$	stall speed
$C_{He}$	elevator hinge moment coefficient	$V_b, V_{probe}$	tailplane velocity, kts
$C_{L_{Tail}}$	tail section coefficient of lift		
$C_m$	A/C pitching moment coefficient	<b>Greek:</b>	
$C_P$	pressure coefficient	$\alpha, \alpha_{alpha}$	angle of attack, deg
$C_T$	thrust coefficient	$\beta, \beta_{beta}$	angle of sideslip, deg
CG	aircraft center of gravity	$\delta E, \delta E_{delE}$	elevator deflection angle, deg
FAA	Federal Aviation Administration	$\delta A, \delta A_{delA}$	aileron deflection angle, deg
$F_{YE}$	yoke force, lbs	$\delta R, \delta R_{delR}$	rudder deflection angle, deg
$G$	acceleration due to gravity	$\delta F, \delta F_{delF}$	flap deflection angle, deg
IRT	NASA Icing Research Tunnel	$\delta T, \delta T_{delT}$	trim tab deflection angle, deg
MAC	mean aerodynamic chord	$\epsilon$	downwash, deg
MTE	mission task element	$\theta, \theta_{theta}$	pitch angle, deg
NASA	National Aeronautics and Space Administration		
$N_z$	normal acceleration	<b>Subscripts:</b>	
OSU	Ohio State University	$a/c$	aircraft
$P_{beta}$	tailplane sideslip angle	$L, l$	total lift, section lift
$q$	pitch rate, deg/s	$tail, t$	horizontal tailplane
ROD	rate of descent, ft/s	$i$	refers to one of three tailplane
S&C	stability and control		5-hole probes: 1 = outboard,
SHSS	steady heading sideslip		2 = midspan, 3 = inboard
TAOA	tailplane angle of attack, deg		
TED	trailing edge down		
TEU	trailing edge up		

### Aircraft Axis System and Sign Convention:



### Stabilizer and Elevator Sign Convention:



## 1.0 Introduction

Aircraft accident analyses have revealed ice contamination on horizontal tailplanes as the primary cause of 16 accidents resulting in 139 fatalities. Ice can lead to a premature tail stall that causes the aircraft to pitch nose-down, which at low altitude, may not be recoverable prior to impact with the ground. Three International Tailplane Icing Workshops were convened to appraise the collective experience on ice-contaminated tailplane stall (ICTS) from airframe manufacturers, operators, aviation regulators, and other interested parties. Workshop attendees provided recommendations to reduce the number of accidents attributed to ICTS. In response to some of these recommendations, the Federal Aviation Administration (FAA) requested the National Aeronautics and Space Administration (NASA) to conduct research into the characteristics of ice-contaminated tailplane stall and to develop techniques and methodologies to minimize the hazard.

NASA responded to the FAA request by developing the NASA/FAA Tailplane Icing Program (TIP).<sup>1</sup> The TIP was a four-year research program that utilized a combination of icing experts and test facilities that included the NASA Glenn (formerly NASA Lewis) Icing Research Tunnel (IRT), The Ohio State University (OSU) Low Speed Wind Tunnel, and the NASA Glenn DeHavilland DHC-6 Twin Otter Icing Research Aircraft. These resources were used to accomplish the following program goals: 1) improve understanding of iced tailplane aeroperformance and aircraft aerodynamics, 2) develop analytical tools to help discriminate tailplane sensitivity to icing, and 3) develop training aids to expand the awareness of the ICTS aviation hazard.

The purpose of this report is to document the flight data results acquired during this four-year program. Subsequent reports will document results from the wind tunnel tests and analytical code development.

NASA conducted extensive flight tests using its Twin Otter Icing Research Aircraft with three simulated ice shapes attached to the leading edge of the horizontal tail, and a clean tail baseline. Testing the Twin Otter was advantageous because of low operating costs, adaptability for the intended experiment, and known flight characteristics from previous iced stability and control experiments.<sup>2, 3</sup> The Twin Otter also has a known ice-contaminated tail stall susceptibility. Fifty-one research flights were conducted in the two-phase flight test program (Table A-1 and Table A-2). Flight test maneuvers with each ice shape included 1G wings level points; steady-heading sideslips; pushovers to 0.5G, 0.25G, and 0G; elevator doublets; and thrust transitions. These maneuvers were conducted for a full range of flap positions and aircraft angles of attack until tail stall was imminent. Over 2000 test points were collected. Specific test points were selected for an in-depth analysis and are reported in this document.

This report is organized in the following sections: description of the research aircraft, instrumentation systems, and three data analysis sections: steady state, dynamic maneuvers, and parameter estimation. Within each of these sections, the flight test procedures, data analysis methods, results, and conclusions are presented. Concluding remarks on the analysis methods and maneuvers are offered.

## 2.0 Research Aircraft and Ice Shapes

The NASA Icing Research Aircraft is a modified DeHavilland DHC-6 Twin Otter (Appendix A, Figure A-1). The horizontal tailplane has a fixed stabilizer with an elevator and trim tab. It is powered by two 550 SHP Pratt and Whitney PT6A-20A turbine engines driving three-bladed Hartzell constant speed propellers. The flight controls are mechanically operated through a system of cables and pulleys. Control surfaces consist of elevator, ailerons, rudder, and wing flaps. Physical characteristics of the aircraft are listed in Table A-3.

The Twin Otter was tested in a Baseline configuration (clean tail) and with three simulated ice shapes. One ice shape represented an Inter-Cycle ice accretion (Figure A-2), the second represented a Failed Boot ice accretion (Figure A-3), and the third represented a double-horn, glaze ice shape (Figure A-4). The Inter-Cycle and Failed Boot shapes resulted from an Icing Research Tunnel (IRT) test on a full scale Twin Otter tailplane model. These ice shapes were urethane casts made from molds of the ice accreted during the IRT test and retained the overall shape and rough texture of the actual ice shape. The third shape was used extensively in NASA's previous stability and control tests and was named the S&C ice shape. The S&C ice shape was cut from Styrofoam blocks and did not incorporate surface roughness or 3D effects. Each of the simulated ice shapes was attached to the leading edge of the horizontal stabilizers only. No other surfaces were contaminated.

### 3.0 Instrumentation System

To gain a complete understanding of the parameters that lead to ice-contaminated tailplane stall, the aircraft was instrumented to acquire three distinct types of data: 1) aircraft dynamics, 2) tail aeroperformance and 3) tailplane flow visualization and pilot visual and tactile cues. Each type of data and instrumentation used to acquire it is discussed in detail below.

#### 3.1 Aircraft Dynamics System

The aircraft dynamics data set included: inertial data, air data, control surface deflection data, pilot forces, and engine parameter data. The inertial data consisted of three orthogonally-mounted linear accelerometers, three orthogonally-mounted rate gyros, and a vertical gyro to provide pitch and roll angle data. All sensors were aligned with the body-axes of the aircraft, and contained in a single box near the aircraft center of gravity (CG). Yaw angle was provided by the aircraft directional gyro. Instrumentation specifics are listed in Table A-4.

Air data consisted of airspeed, angle of attack, angle of sideslip, pressure altitude, and outside air temperature (OAT). All air data parameters (except OAT) were sensed by a Rosemount 858 probe head extended from the aircraft on a 9-foot noseboom.

The control surface deflections,  $\delta E$ ,  $\delta A$ ,  $\delta R$ ,  $\delta F$ , were measured using linear control position transducers (CPTs) located near the control horns, which eliminated cable stretching errors. Pilot forces were measured using a custom-designed yoke wheel and rudder pedals that incorporated load cells to measure forces required to deflect the ailerons, elevator and rudder.<sup>4</sup>

Engine data consisted of torque pressure, propeller RPM, and fuel flow from both engines. By recording fuel flow, the aircraft mass and CG were adjusted for fuel burn during the test flights. All aircraft dynamic sensor data signals (except engine torque pressure and RPM) were passed through a Precision 6000 Filters System unit for conditioning, digitized and recorded using a Science Engineering and Associates (S.E.A) data acquisition system. The engine torque pressure and RPM data were digitized and recorded directly to the S.E.A. system without the signal conditioning of the Precision 6000 system.

#### 3.2 Tail Aeroperformance System

Tail aeroperformance data consisted of tail inflow angles and velocities as well as surface pressures. To measure the former, three 5-hole probes were mounted to the leading edge of the left-side horizontal tail (Figure A-5). One probe was mounted near the tail tip, the second was mounted mid-span, and the third was mounted near the tail root. To measure the latter, a pressure belt wrapped chordwise around the stabilizer and elevator.

Each 5-hole probe measured the local angle of attack, angle of sideslip, and airspeed at the designated spanwise location. The probes were a variation on a design used by Raytheon for the Beech Starship<sup>5</sup> but modified by increasing the probe size to reduce vibration errors (Figure A-6). Each 5-hole probe was extensively calibrated at NASA and OSU to determine angle of attack, sideslip, and dynamic pressure over the anticipated ranges encountered in flight. These 5-hole probes related pressure sensed at holes on the probe tip to the relative incoming velocity and flow angle.

On the aircraft, the pressure on each hole (18 total) was transmitted through tubing to two Scannivalve electronic scanning differential pressure transducers. From the Scannivalve transducers, analog signals were transmitted to an S.E.A. pressure multiplexer interface unit, where the flow probe signals were digitized and recorded with the aircraft dynamic parameters.

The other aeroperformance data consisted of chordwise distributed surface pressures around the horizontal tail. These data were obtained using a pressure belt made from a series of strip-a-tube tygon tubing wrapped completely around the horizontal tail in a mid-span location (Figure A-5). The end of each tube on the tail was plugged. Each tube in the belt had a single hole cut at a specific chordwise location where the surface pressure was sensed. The other end of each tube was routed to Scannivalve electronic scanning pressure transducers. In this way, the surface pressures about the tail were sensed at 50 holes on the pressure belt and measured by the Scannivalve unit inside the aft section of the aircraft. Like the flow probe data, the Scannivalve transmitted the pressure belt data to the S.E.A. pressure multiplexer interface unit, where the signals were digitized and recorded with the other parameters. A theoretical analysis of the pressure belt and flow probe system dynamic response characteristics indicated an approximate lag of 0.2 sec for step input changes.

### **3.3 Video Systems**

Flow visualization on the tailplane was accomplished by attaching yarn tufts to the lower surface of the horizontal tail and mounting a video camera to the bottom aft section of the fuselage (Figure A-7). The camera field-of-view could be adjusted by research personnel through a tilt/roll mounting mechanism during the flight. The video lens also incorporated a zoom capability to provide a close-up or far-field perspective. The video signal was annotated with real-time engineering unit values of specific parameters. This annotation improved the information content of the video by informing the viewer of information such as airspeed, thrust coefficient, elevator deflection and pilot forces. Lastly, the video signal with annotation was recorded in SVHS format.

Another unique video system was installed to record the pilot actions during the maneuvers and also record the view through the windscreen to obtain the pilots perspective. These two views were merged onto a single screen format by using a screen splitter so that the upper part of the screen showed the view through the windscreen, while the lower part of the screen presented an over-the-shoulder look at the pilot controlling the aircraft. This single screen presentation was annotated with engineering unit data to indicate the aircraft pitch and roll angles, pilot forces, thrust coefficient and elevator angle, and then recorded in SVHS format.

### **3.4 Calibration Procedures**

Extensive calibrations were conducted on all components of the data systems. Prior to the flight seasons, individual calibrations were conducted for all sensors, and through-put calibrations (sensor-filter-data acquisition-recording) were performed prior to each flight. Specifically, the Scannivalve pressure transducers and all 32 analog channels underwent a three-point check prior to each flight. The transducer coefficients obtained from these checks were used in the post-flight data reduction process.

#### **4.0 Data Handling Process**

All together, the data from the flight program consisted of the three video signals and 95 data signals. The data signals were recorded at 100 Hz sampling frequency and had 16-bit resolution. These data were recorded onto 8-mm tape using a ruggedized PC compatible data acquisition system. The data on the 8-mm tapes were converted to ASCII files post-flight for further processing on ground-based computer systems. The initial ASCII files consisted of row and column data for each sensor voltage. A FORTRAN program was written to read these files, apply the calibration conversion equations for each sensor, and perform correction algorithms for sensor position errors and other relevant calculations for data analysis. The resultant files were uploaded into Excel for plotting and other data analysis to be described in the subsequent sections.



## 5.0 Steady State Analysis

Steady flight test points enabled an in-depth examination of the effects of tailplane icing on tailplane lift and hinge moments, and elevator deflections required to trim the aircraft. The parameter space examined in this study varied the tailplane configuration [clean, Inter-Cycle ice, Failed Boot ice, S&C ice], the flap deflection –  $\delta F$ , the thrust setting –  $C_T$ , the aircraft airspeed –  $VIAS$  (hence angle of attack –  $\alpha_{a/c}$ ), and the aircraft sideslip angle –  $\beta$ . A comprehensive matrix of test points were conducted with a forward center of gravity (CG) location. In addition, a limited number of test points were conducted with an aft CG location. The following section details the flight test procedures, method of analysis, shows results and provides conclusions.

### 5.1 Flight Test Procedures

#### 5.1.1 Steady-Wings-Level (SWL):

The aircraft was configured to a specific tail condition (clean or iced) and flap deflection angle ( $\delta F$ ), and then the thrust setting ( $C_T$ ) was set at the appropriate test speed. The aircraft was trimmed at this initial test speed, so that the elevator hinge moment was nulled. With the aircraft in a steady condition, data records were taken for approximately 15 seconds. Due to the fixed thrust setting, the aircraft was sometimes in a steady climb, level flight, or in a steady descent. After the initial test point, the next test speed was reached by adjusting the yoke position and resetting the throttles to obtain the consistent  $C_T$ . The elevator was not retrimmed, so that the yoke force required to hold the elevator in that position could be translated into an elevator hinge moment ( $C_{He}$ ). This procedure was repeated for six airspeeds at each thrust setting, flap deflection and tail ice configuration. All of these test points were done with minimal sideslip ( $\beta \approx 0$ ) on the aircraft.

#### 5.1.2 Steady-Heading Sideslips (SHSS):

A limited number of steady-heading sideslips (SHSS) test points were obtained. The procedure was similar to the steady-wing-level points, except that the aircraft was put into approximately a  $17^\circ$  sideslip to the right and to the left, while maintaining a specified airspeed, flap angle and thrust coefficient. The sideslip was accomplished by the pilot applying either right or left rudder and cross-controlling with left or right aileron to yaw and roll the aircraft into a steady-heading sideslip.

### 5.2 Method of Analysis for Steady State Data

#### 5.2.1 General

Each 15 second data file was converted and corrected as stated in the data handling process section. For each measured and calculated parameter, the average and standard deviation were calculated. These averaged values were then input to a spreadsheet program for plotting and analysis.

#### 5.2.2 Data Consistency Check

Data consistency check points were added to the test matrix after the fifth flight in 1995 (FLT 95-17). These steady state points were performed with a consistent aircraft configuration and flight condition, *i.e.*,  $\delta F = 10^\circ$ ,  $VIAS = 100$ knots, and  $C_T = 0.10$  or  $0.05$ . These check points were analyzed using the steady state processing techniques described above to determine flight-date-dependent, systematic errors in various instruments. These in-flight check points enabled the discovery of problems in the pressure instrumentation for the tail flow probes and pressure belt. Selected parameters from the data consistency results are shown in Figure B-1 and Figure B-2 in Appendix B.

## 5.3 Results

### 5.3.1 Basic Aircraft Performance Description

The total lift coefficient of the test aircraft was measured for flap deflections [0, 5, 10, 15, 20, 25, 30, 35 and 40°], and is displayed in Figure 1. Clearly, the effect of increasing angle of attack within a specific flap deflection increases total lift coefficient, and the effect of increasing flap deflection shifts the lift curve up and to the left. This is well known and understood.

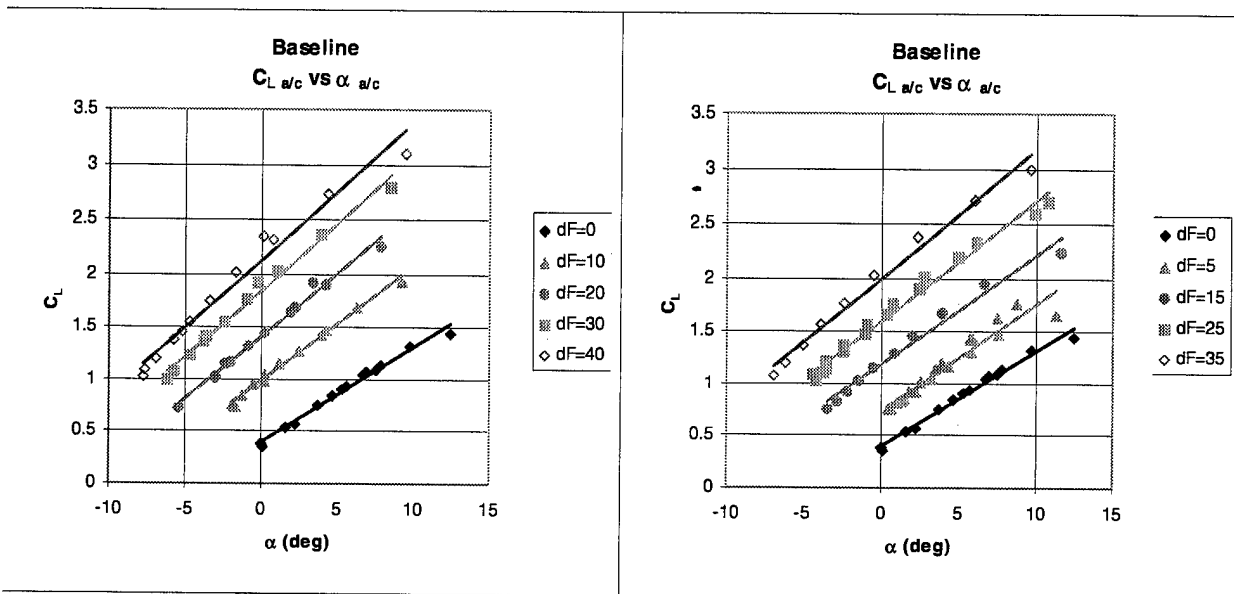


Figure 1. Total lift coefficient vs. aircraft angle of attack for various flap settings.

As a typical aircraft transitions from cruise to landing configurations, the path along the  $C_L$  vs. angle of attack curve looks similar to Figure 2.

Beginning at point 1, the cruise speed is reduced to flap extension speed ( $V_{FE}$ ) or slower by reducing thrust and increasing angle of attack (point 2). To maintain altitude, the aircraft  $C_L$  also increased. Flap deflection drives the situation from point 2 to point 3 causing a significant reduction in aircraft angle of attack. Next, the speed is again decreased by reducing thrust and increasing angle of attack (point 3 to 4). When full flaps are selected (point 4 to 5), the minimum angle of attack is attained assuming the transition took place at  $V_{FE}$ . As the aircraft airspeed is further reduced for landing, the lift condition and angle of attack increases as shown in point 5 to 6.

This scenario depicts some of the benefits of wing flaps. Flaps allow an aircraft to land at reduced airspeeds, which in turn reduces the runway length required for landing. Flaps also reduce the angle of attack required for high lift situations, which provides better forward visibility to the pilot during landing.

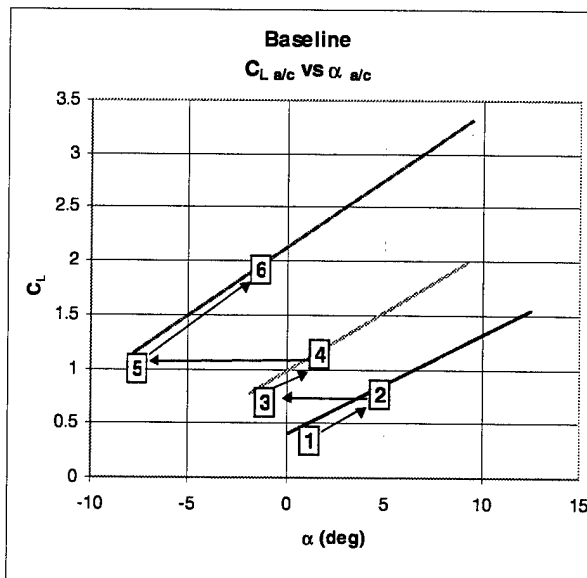
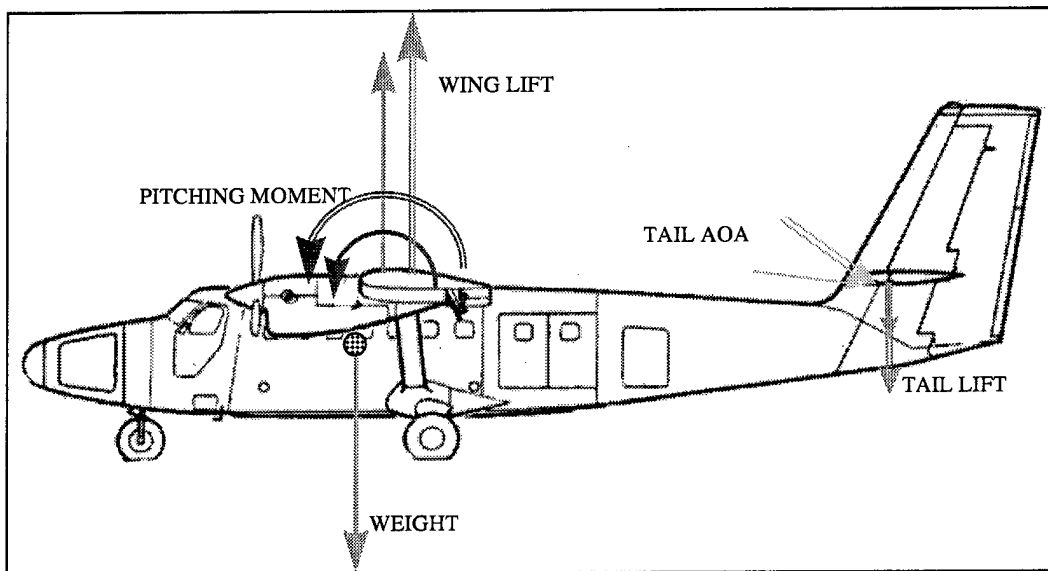


Figure 2. Typical lift curve during landing transition

However, with the benefits of flaps, there are drawbacks as well. Since flaps increase the wing lift by increasing the circulation, there is an increase in the downwash angle into the horizontal tail. Flap extension also increases the nose-down pitching moment because of both the increased wing lift vector and the increased moment arm due to increased chord length. Figure 3 indicates how the pitching moment increases with flap deflection, and how the tail down lift must be increased to balance this moment. The double lines indicate vectors after flap deflection. Note the magnitudes of the vectors in Figure 3 are for illustration purposes only.



**Figure 3. Force and moment diagram.**

The function of the horizontal tail is to stabilize the aircraft in pitch. Therefore, when flaps are deployed, the nose-down pitching moment due to increased wing lift and aft movement of the wing center of lift requires the tail to provide an increased down lift to balance the pitching moment. The increased downwash angle from the wing assists the horizontal tail in performing its function by increasing the tail angle of attack. This increase in tail angle of attack may be too much or too little for the particular trim airspeed, in which case the elevator angle is adjusted by the pilot to either decrease or increase the tail down lift.

### 5.3.2 Tailplane Angle of Attack Description

The test aircraft was used to measure the effects of wing flap and aircraft angle of attack on the tail angle of attack. The effects of aircraft angle of attack and downwash can be seen in Figure 4 for the clean tail configuration. Note that the lines in the figures are drawn to highlight trends; they are not meant for quantitative analysis.

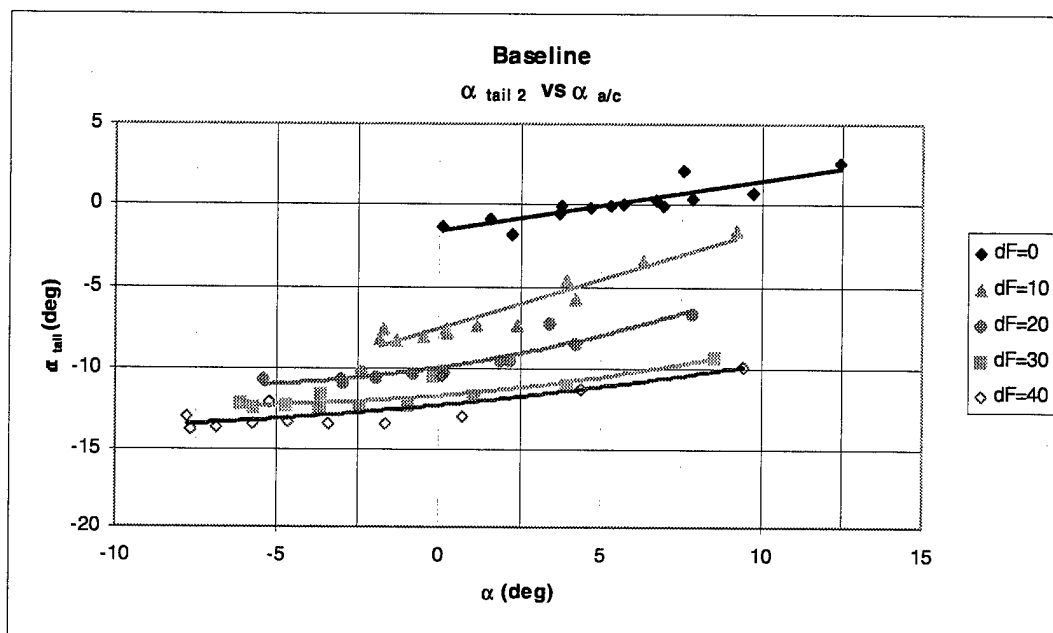


Figure 4. Tailplane angle of attack vs. aircraft angle of attack.

For a given flap deflection, it is clearly seen that as the aircraft angle of attack was decreased, the tailplane angle of attack also decreased. For the test aircraft in a given flap setting, this change in aircraft angle of attack was greater than the change in tailplane angle of attack such that the slope  $\Delta\alpha_{tail} / \Delta\alpha_{a/c} < 0.6$  for  $\delta F = 10^\circ$ , and much less than 0.6 for the other flap settings. Likewise, as the flap deflection was increased, there was a bias shift in the tailplane angle of attack in the negative direction. This bias shift was due to the increase in wing downwash. The largest incremental downwash contribution due to flap deflection was observed when flaps were extended from 0–10°. This caused approximately a  $-5^\circ$  shift in tailplane angle of attack. As flaps were further deflected, the incremental change in tailplane angle of attack decreased such that when flaps deflected from 30–40°, the shift in tailplane angle of attack was less than  $-1^\circ$ .

The relationship between tailplane angle of attack, aircraft angle of attack and downwash is described in Ref. 6 as the following equation:

$$\alpha_t = \alpha_{a/c} - \epsilon - i_t$$

where  $\alpha_t$  = tailplane angle of attack

$\alpha_{a/c}$  = aircraft angle of attack

$\epsilon$  = downwash angle

$i_t$  = tail incidence angle (fixed at  $0^\circ$  for test aircraft)

We also know from Ref. 7 that wing downwash is a function of lift coefficient ( $C_L$ ). In theory, the downwash at the tail is approximated by ( $A$  is the wing aspect ratio)  $\epsilon^\circ = \frac{114.6C_L}{\pi A}$ .

As the aircraft angle of attack ( $\alpha_{a/c}$ ) decreases, there is also a decrease in downwash angle ( $\epsilon$ ), such that if the changes in these two parameters were the same, there would be no net change in the tail alpha. But we see in this data that as the aircraft alpha and corresponding downwash decrease within a given flap setting, that the tail alpha also decreases. Thus within a given flap setting, the aircraft alpha dominates the tail alpha equation.

An alternative way of looking at the variation in tail alpha with the flap configuration is with respect to aircraft airspeed (Figure 5). For all flap settings, an increase in airspeed results in a more negative tail angle of attack.

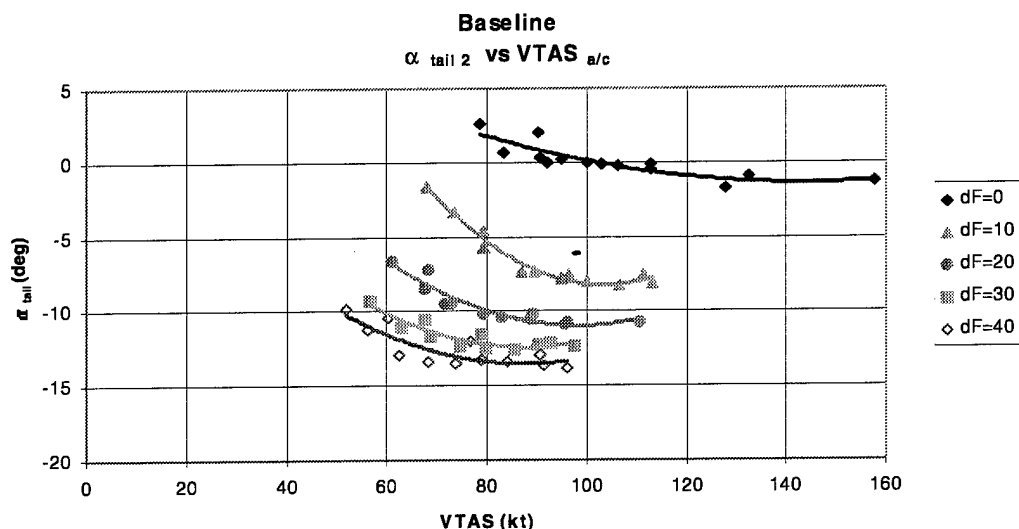


Figure 5. Tailplane angle of attack vs. airspeed.

Tying this information together with the typical transition from cruise to landing scenario developed above (see Figure 2), we see in Figure 6 that the tail angle of attack is greatly affected by both the flap transition and aircraft angle of attack changes. In the same way as before, the cruise aircraft (point 1) is slowed to  $V_{FE}$  (point 2). Then by selecting the first flap setting of  $10^\circ$ , the tail AOA is reduced from  $0^\circ$  to  $-8^\circ$  (point 3). The tail AOA increases as the aircraft is slowed further to the next flap  $V_{FE}$  (point 4), and then reduced from  $-6^\circ$  to  $-13^\circ$  as the flaps are fully deflected (point 5). As the aircraft flares for landing, the tail AOA again increases for landing (point 6).

The relevance of this information is not in the exact values of tailplane AOA, as that will vary from aircraft to aircraft. The relevance is in the relationship between the aircraft angle of attack, flap setting and tailplane angle of attack. This information is positive evidence that as the aircraft angle of attack is reduced, or as the aircraft is at or near  $V_{FE}$ , the tailplane AOA is at the most negative value for that flap setting. Therefore in non-maneuvering flight, maximum flap deflection and lowest aircraft AOA or  $V_{FE}$  (point 5) clearly subjects the tailplane to the most negative angle of attack. This condition is where the tailplane stall margin is a minimum. This is exactly opposite of the wing stall scenario where slow speeds and high aircraft angle of attack put the wing near its stalling

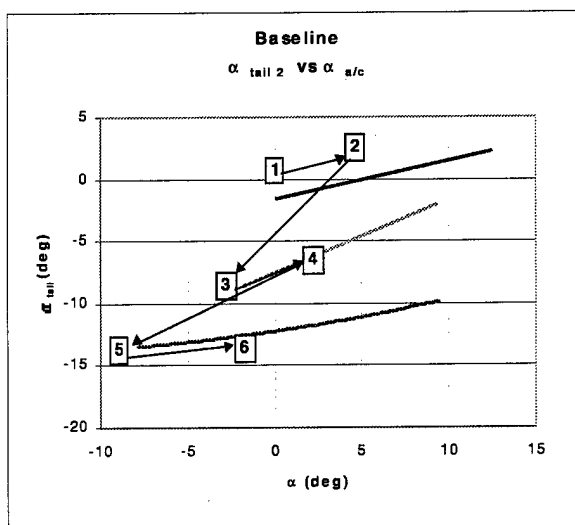


Figure 6. Typical tail AOA during landing transition.

angle. Therefore, in steady-state (non-maneuvering) flight, the pilot has two stalling limits. A low speed limit for the wing, and a high speed limit for the tail.

### 5.3.3 Tailplane Lift Description

As stated in Section 5.3.1, the function of the horizontal tailplane is to provide stability and control in the pitch axis. Conventional horizontal tails incorporate a fixed stabilizer and hinged elevator with trim tab on the elevator (Figure 7). Pitch stability and control is accomplished by modifying the amount of lift generated at horizontal tail by moving the elevator. The elevator cambers the tail to modify the amount and direction of the lift. Conventionally, a positive elevator deflection moves the trailing edge down (TED) and reduces the down lift. A negative elevator deflection moves the trailing edge up (TEU) and increases the down lift. Previous wind tunnel tests documented in Refs. 8 and 9 show how the elevator effects the magnitude of lift and stalling angle of attack. Data from Ref. 9 are shown in Figure 8 where the lift coefficient becomes more negative and the stall angle of attack becomes less negative (moves to the right) as  $\delta E$  decreases. Also, for a given elevator deflection ( $\delta E$ ), the tail lift becomes more negative as the tail AOA becomes more negative. This behavior is similar to a wing, but inverted.

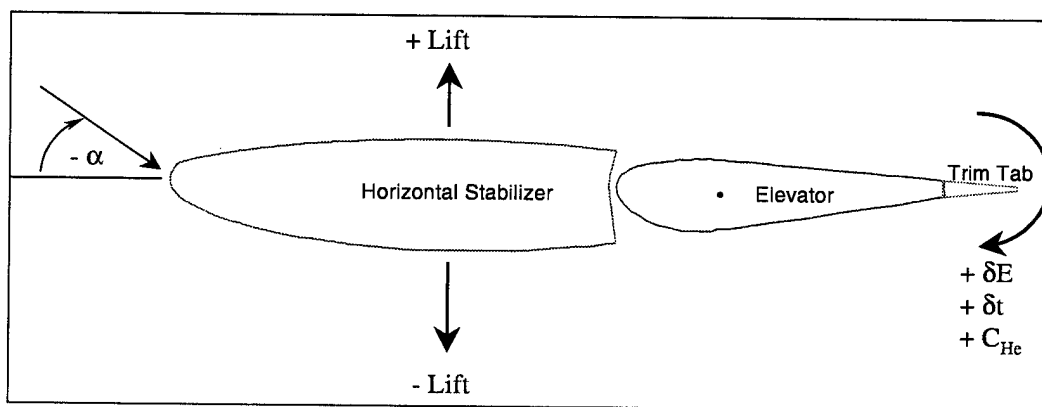


Figure 7. Horizontal tail diagram.

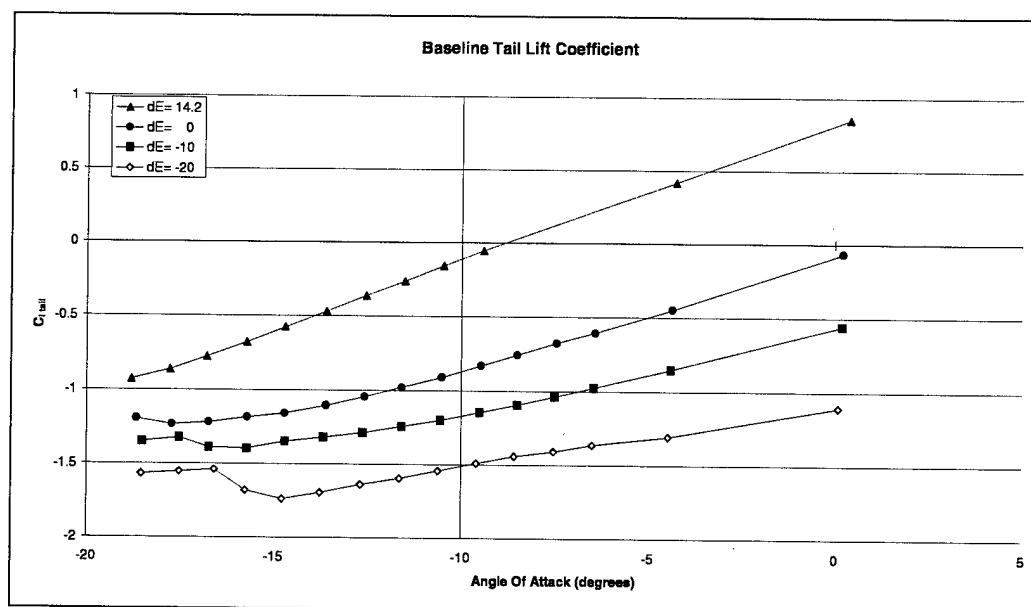


Figure 8. Tail lift coefficient from wind tunnel data.

Similar to the wind tunnel testing in Ref. 9, the test aircraft was equipped with a pressure belt on the left side of the horizontal tail as described in Section 3.2. The pressure belt enabled the researchers to observe and measure the surface pressures (Figure 9) and calculate the section lift coefficient by integrating the  $C_p$  distribution.

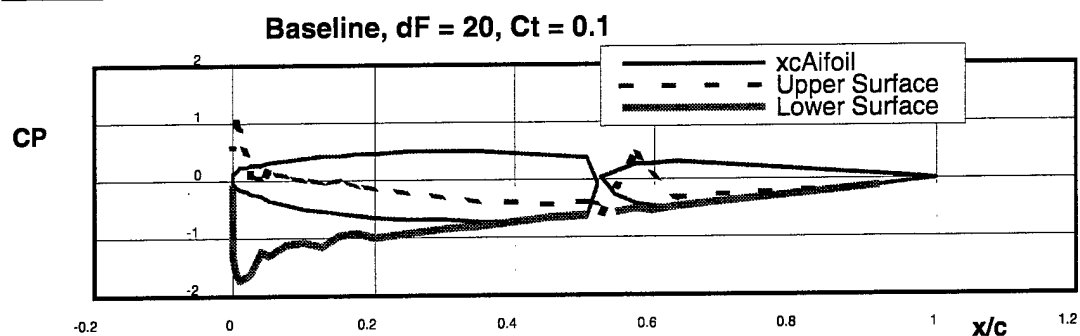
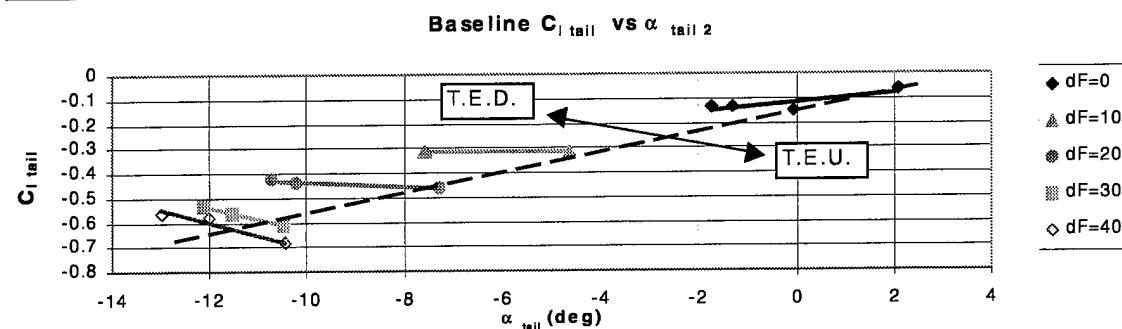
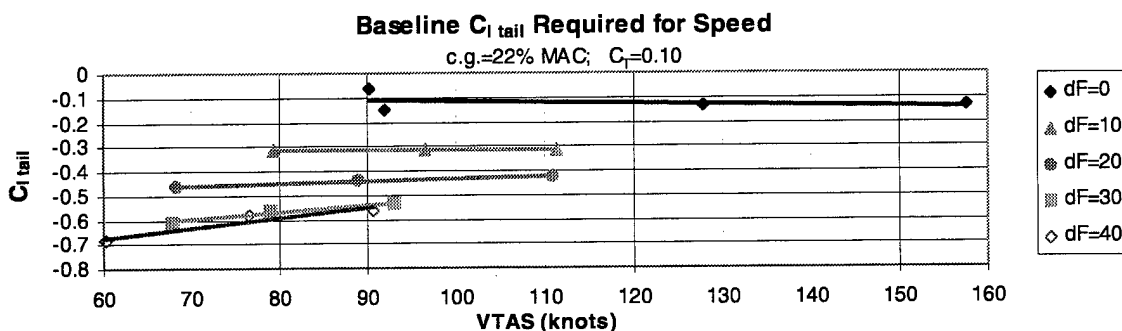


Figure 10 shows the tail lift coefficients from the flight data plotted versus tailplane angle of attack measured at the mid-span (probe 2). All test points in Figure 10 were with a forward CG location (22% MAC) and moderate thrust setting ( $C_T \approx 0.10$ ).



Another way of representing these data are with respect to aircraft airspeed. Figure 11 shows the variation in tail download required to maintain specific airspeeds at various flap settings.



One of the key observations from these data presented in Figure 10 and Figure 11 is the increased download required for steady flight as the flaps were extended. For the test aircraft, there was a substantial increase in the magnitude of tail section lift coefficient from the no flap to full flap extension. Within a given flap setting, the tail lift coefficient varied with the flight condition. Especially for the larger flap deflections, the  $C_{L\_Tail}$  required to stabilize the aircraft was most negative at the higher angle of attack or slow speed flight.

Another key observation was that at the larger flap deflection cases, the  $C_{L\_Tail}$  magnitude decreased as tail AOA became more negative. This seems counterintuitive to the wind tunnel results in Ref. 9, but the difference is because the wind tunnel data were with constant elevator deflection angles ( $\delta E$ ), whereas the flight  $C_{L\_Tail}$  data presented in Figure 10 had various elevator deflections based on the tail download requirement. Since the aircraft was held in a steady wings level condition, the elevator was adjusted to hold the aircraft at the specified airspeed. In the higher speed conditions, the elevator was held in a TED position, thereby unloading the horizontal tail. In order to hold the low speed points, a greater down load is required from the tail. For that condition, the elevator was held in the TEU position to create a higher down load and slow the aircraft. The dashed line in Figure 10 indicates the approximate location of  $\delta E = 0^\circ$ . The arrow pointing to the upper left indicates the elevator position with the trailing edge down, and the opposing arrow indicates the elevator in a trailing edge up position.

Figure 12 compares the wind tunnel to the flight test results. Flight data from the  $\delta F = 40^\circ$  case are superimposed on the wind tunnel data with the elevator deflection angle noted. Also, a dashed line has been added to the plot to indicate the stalling angles of attack for each elevator angle. Note that the wind tunnel data are from a 2-D test and have not been corrected for 3-D effects of flight. For these reasons, the actual flight and wind tunnel  $C_L$  values for a given elevator deflection do not agree well.

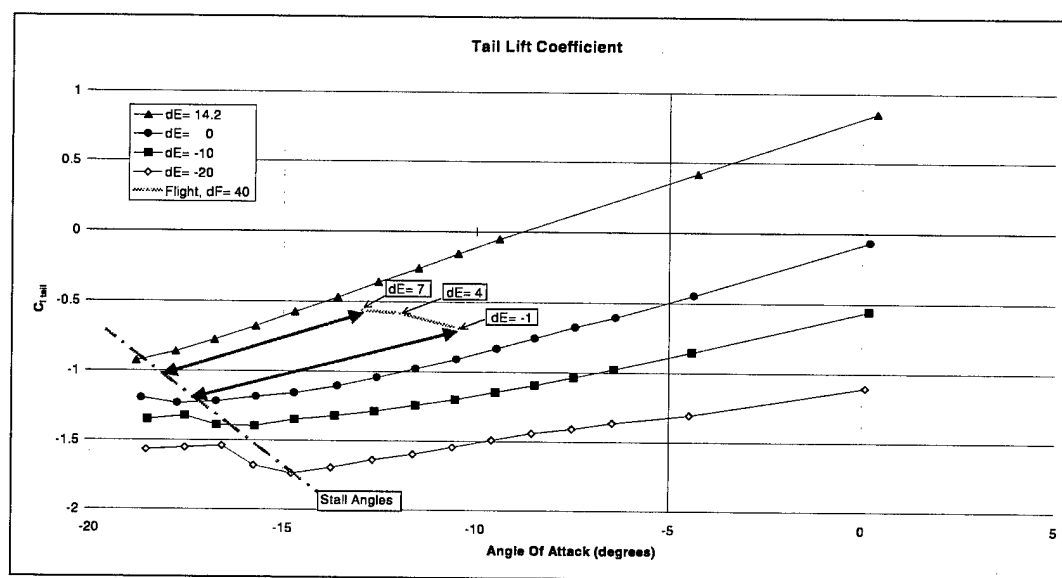


Figure 12. Tail lift coefficient from wind tunnel data and flight data.

Figure 12 does illustrate, however, relative stall margins. Even though slow speed flight test points required a greater tail down load ( $C_{L\_Tail} \approx -0.7$ ), the tail AOA was well within the linear range of  $C_{L\_Tail}$  for that particular elevator deflection ( $\delta E \approx -1^\circ$ ). On the other hand, the high speed test point required less tail down load ( $C_{L\_Tail} \approx -0.55$ ), but subjected the tailplane to an angle of attack closer to the stalling angle for the respective elevator deflection ( $\delta E \approx 7^\circ$ ). One can see that the high speed point is closer to the stall angle line than the low speed point.

Although this comparison of wind tunnel data to flight data is not fully developed, it is used to illustrate the decrease in tail stall margin as flaps are deployed and the aircraft is flown at speeds near the flap extension speed.



### 5.3.4 Elevator Hinge Moment Description

Recall from Section 5.1.1 that the steady state points were initiated with the elevator trimmed using the pilot-controlled elevator trim tab for the specified speed (Figure 13). This initial test speed was typically near  $1.1V_S$ , so the elevator was positioned TEU. In order to hold the elevator in that position, the trim tab was adjusted TED. The aerodynamic forces over the trim tab provided a hinge moment to counteract the hinge moment of the whole elevator. In this way, the elevator force felt by the pilot was zeroed for the initial test point.

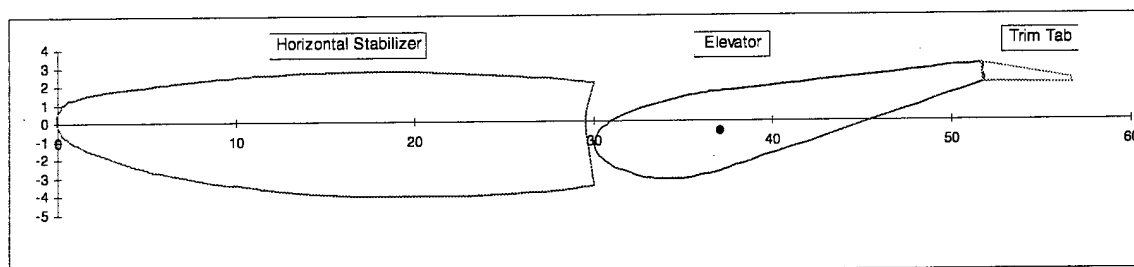


Figure 13. Horizontal stabilizer, elevator and trim tab.

Test points following the initial test point were obtained by the pilot positioning the yoke more forward to reach and maintain the next higher test speed. The force applied by the pilot was measured and transformed into the elevator hinge moment coefficient through the relation below:

$$C_{H_e} = \frac{\frac{1}{g} F_e}{q_{tail} S_e c_e}$$

where:  $g$  = elevator gearing ratio = 0.073 lb/in-lb for test aircraft (obtained experimentally)  
 $F_e$  = pilot stick force to move elevator  
 $q_{tail}$  = dynamic pressure at the tailplane  
 $S_e$  = area of elevator aft of hinge line  
 $c_e$  = elevator chord aft of hinge line

As the pilot set the yoke more forward, the elevator moved to a more TED position. Typically, the pilot provided a push force to move the yoke forward which resulted in a negative elevator hinge moment. The negative hinge moment on an elevator that is being moved TED is a restoring moment. The restoring moment would return the elevator to the trimmed position and the aircraft would return to the trim speed if the pilot were to release the controls.

The useful way of expressing elevator hinge moment from Ref 11 is below. The terms in this model will be used to help describe the icing effects on tailplane performance in later sections.

$$C_{He} = b_0 + b_1 \alpha_t + b_2 \delta_E + b_3 \delta_T$$

where:  $\alpha_t$  is the change in tail angle of attack  
 $\delta_E$  is the change in elevator deflection angle  
 $\delta_T$  is the change in trim tab angle  
 $b_0$  is the value of the hinge moment when  $\alpha_t = \delta_E = \delta_T = 0$   
 $b_1$  is referred to as the elevator "floating" parameter and is usually negative, but can be positive by design. If negative, the elevator floats with the wind when the angle of attack is changed.  
 $b_2$  is referred to as the elevator "heaviness" parameter since it relates the amount of pilot force required to deflect the elevator. A preferred control characteristic is to have the hinge moment acting to oppose the motion of the control surface, so the term  $b_2$  should always be negative. If  $b_2$  is positive, the control surface would be considered "overbalanced."  
 $b_3$  is the trim tab effectiveness parameter and is typically positive so that the  $b_3 \delta_T$  will oppose the  $b_2 \delta_E$  term.

Figure 14 and Figure 15 show the total elevator hinge moment  $C_{He}$  for the Baseline aircraft with respect to tail AOA and aircraft airspeed.

The test aircraft in the baseline configuration experienced the restoring moment for all flap settings. Note that in the  $\delta F = 40^\circ$  case, the aircraft was not able to be trimmed at the slow speed test point and the pilot had to pull slightly (3 lb.) to maintain the 55 knot indicated airspeed. This suggests that the pilot-controlled elevator trim tab was unable to produce enough hinge moment (magnitude of  $b_3\delta_T$  was too small) to counter the effective elevator hinge moment caused by the elevator deflection angle ( $b_2\delta_E$  term).

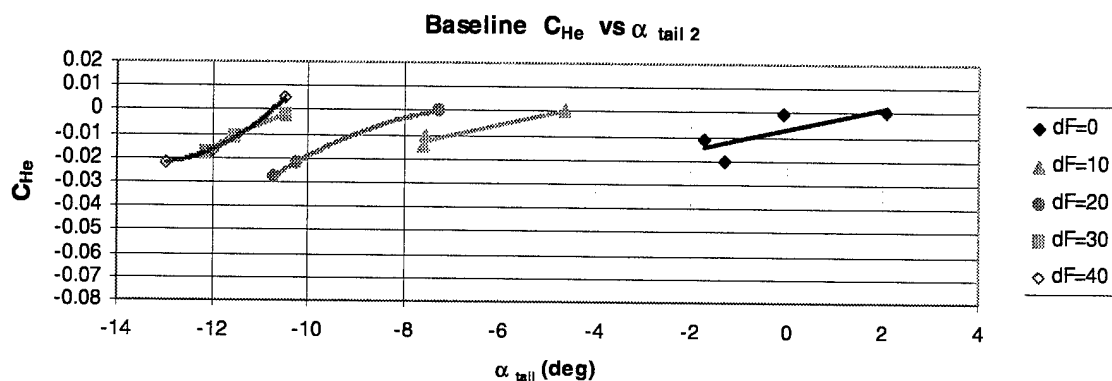


Figure 14. Elevator hinge moment coefficient vs. tail angle of attack.

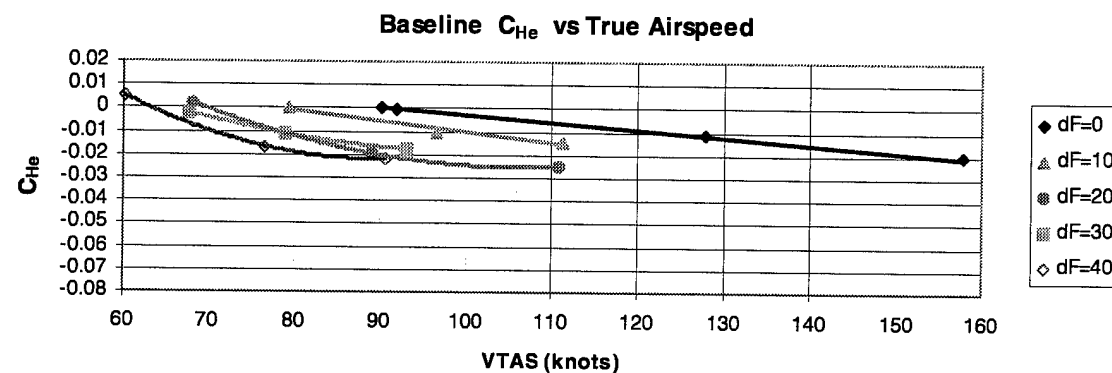


Figure 15. Elevator hinge moment coefficient vs. airspeed.

### 5.3.5 Icing Effects on Tailplane Lift

Using one of the techniques in Section 5.3.3, the effects of various levels of icing on tailplane lift are examined in this section. Since the effects of the various levels of icing are of interest, the data series on each plot consists of the clean baseline, Inter-Cycle Ice, Failed Boot Ice, and the S&C Ice. The tailplane section lift coefficient versus aircraft true airspeed data are presented in Figure 16 through Figure 20. Each figure is for a specified flap deflection.

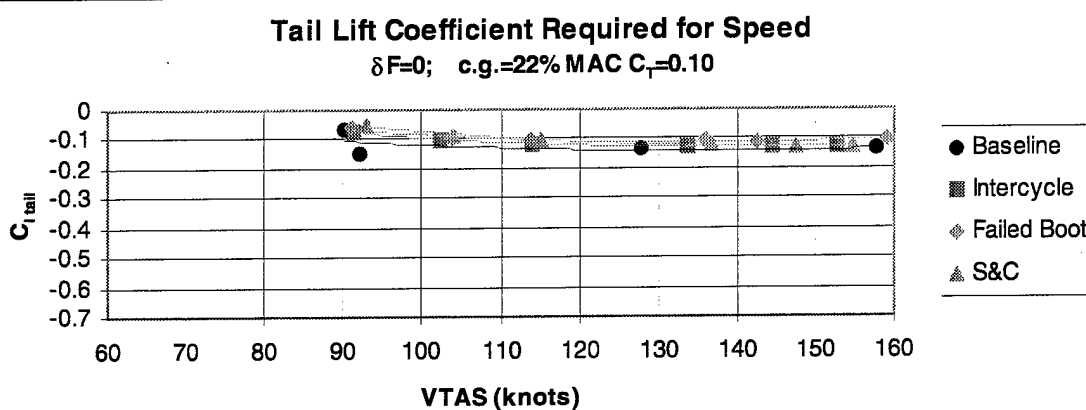


Figure 16. Tail lift coefficients for  $\delta F = 0^\circ$ .

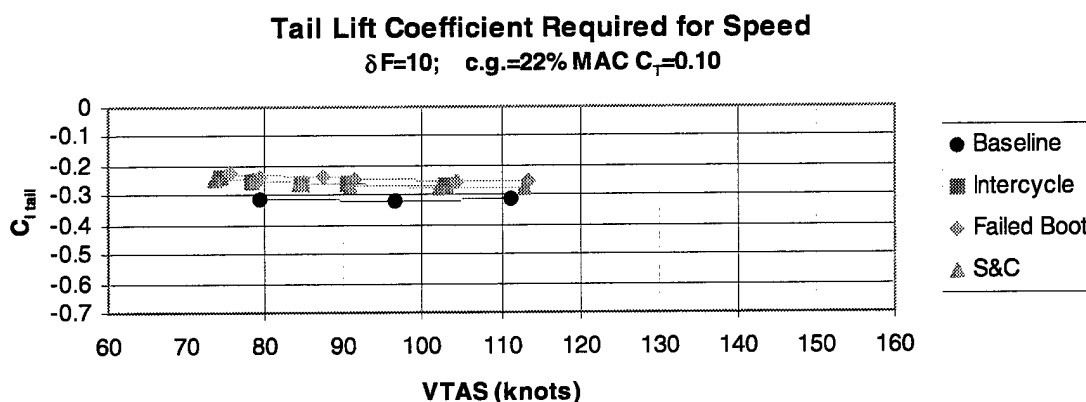


Figure 17. Tail lift coefficients for  $\delta F = 10^\circ$ .

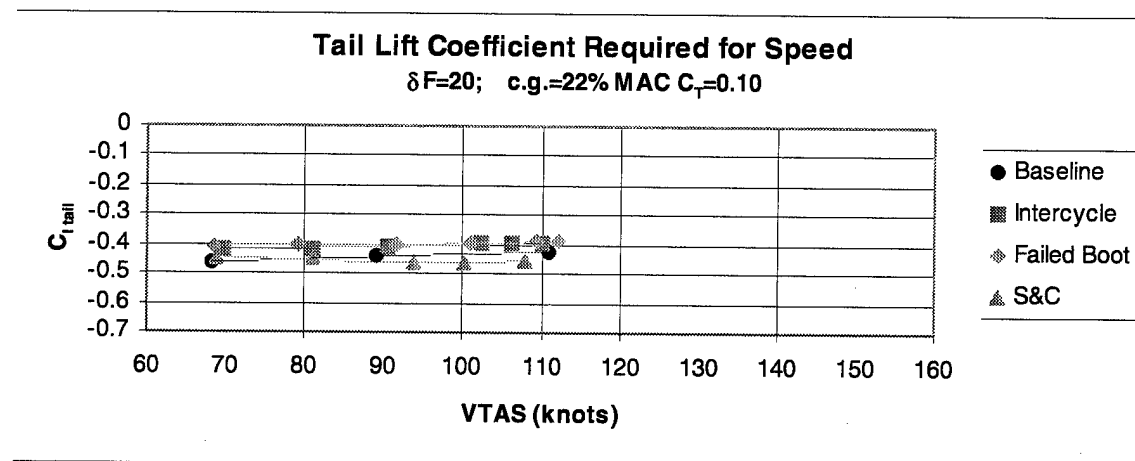


Figure 18. Tail lift coefficients for  $\delta F = 20^\circ$ .

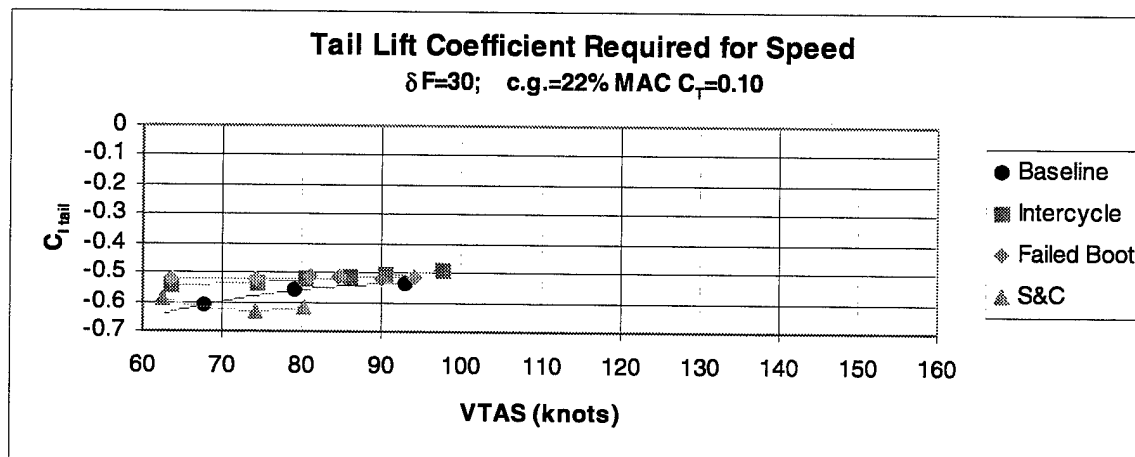


Figure 19. Tail lift coefficients for  $\delta F = 30^\circ$ .

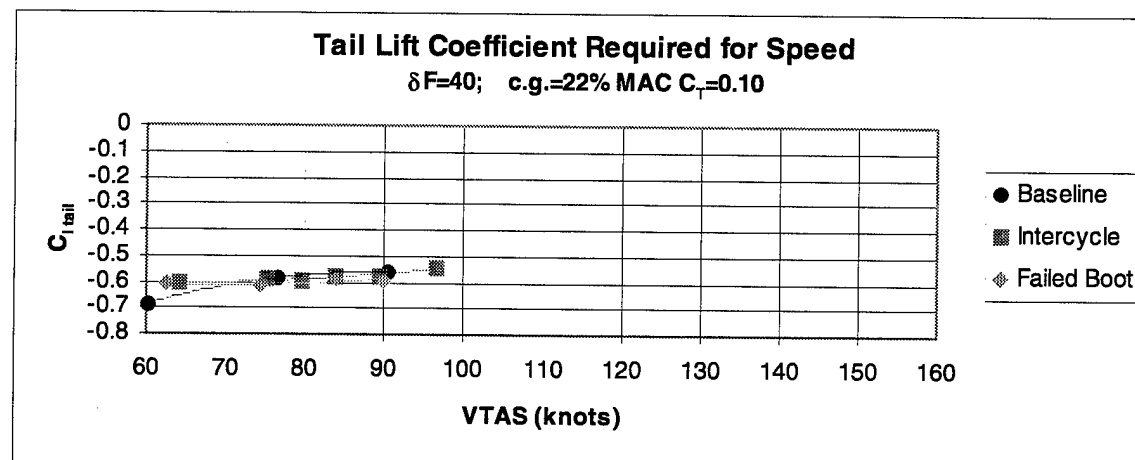


Figure 20. Tail lift coefficients for  $\delta F = 40^\circ$ .

Although there were some variations in the lift coefficients developed with the ice contamination, the general amount of down load generated for the given flap deflection are similar. This is not surprising since the aircraft requires a specific amount of down load from the tail for the flight condition and aircraft configuration. Note that the S&C ice shape was not tested in the  $\delta F = 40^\circ$  configuration because the tailplane could not stabilize or control the aircraft adequately.

Having similar tail down loads did not mean the tailplane was not affected by the ice contamination. The lift loss due to the ice was accounted for by deflecting the elevator and cambering the tail more than in the clean baseline cases. Figure 21 through Figure 25 illustrate how much elevator deflection was required for the iced cases and various flap configurations. In the  $\delta F = 0^\circ$  case, there is virtually no difference between the iced cases. As the flaps extend to  $10^\circ$ , the effects of the ice can be seen in the 1-2° decrease in  $\delta E$  from the baseline case.

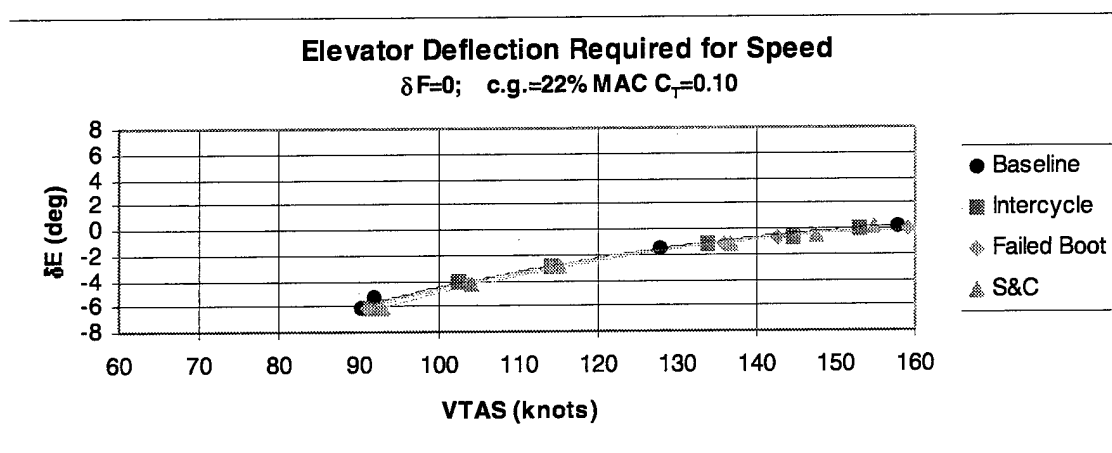


Figure 21. Elevator deflection for  $\delta F = 0^\circ$ .

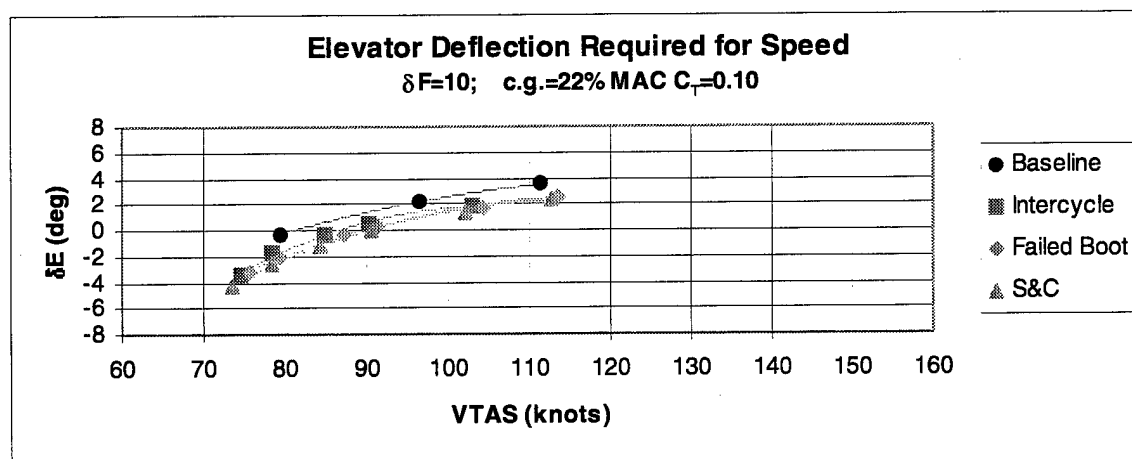


Figure 22. Elevator deflection for  $\delta F = 10^\circ$ .

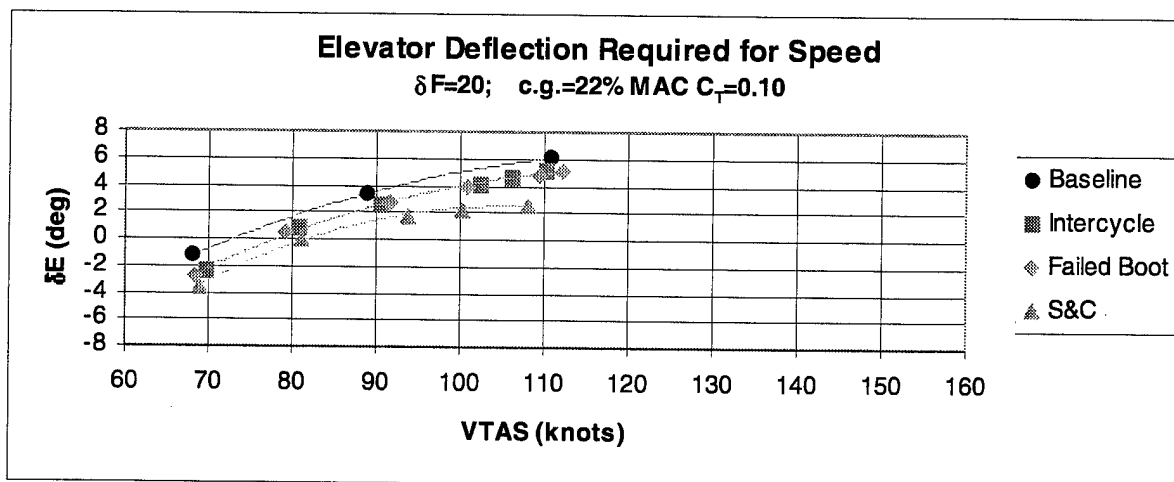


Figure 23. Elevator deflection for  $\delta F = 20^\circ$ .

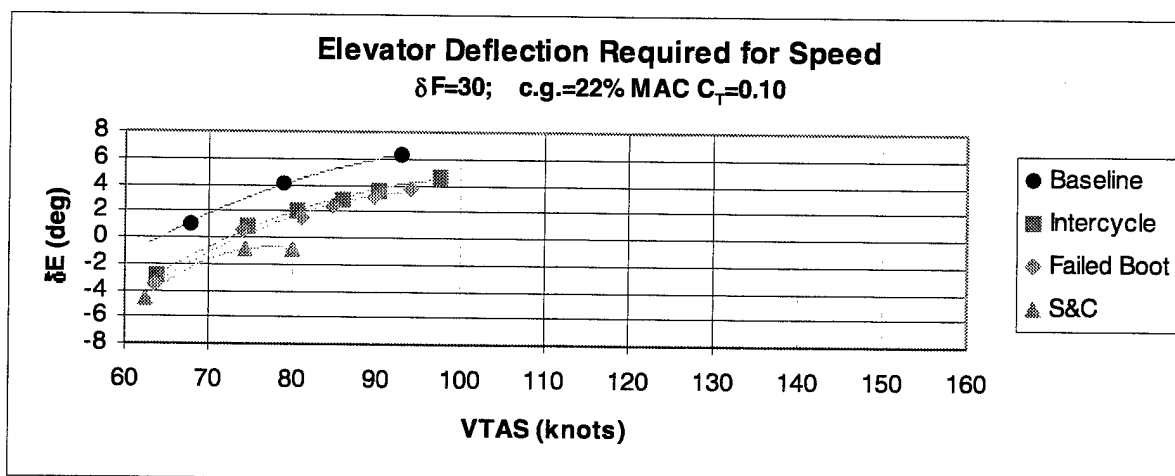


Figure 24. Elevator deflection for  $\delta F = 30^\circ$ .

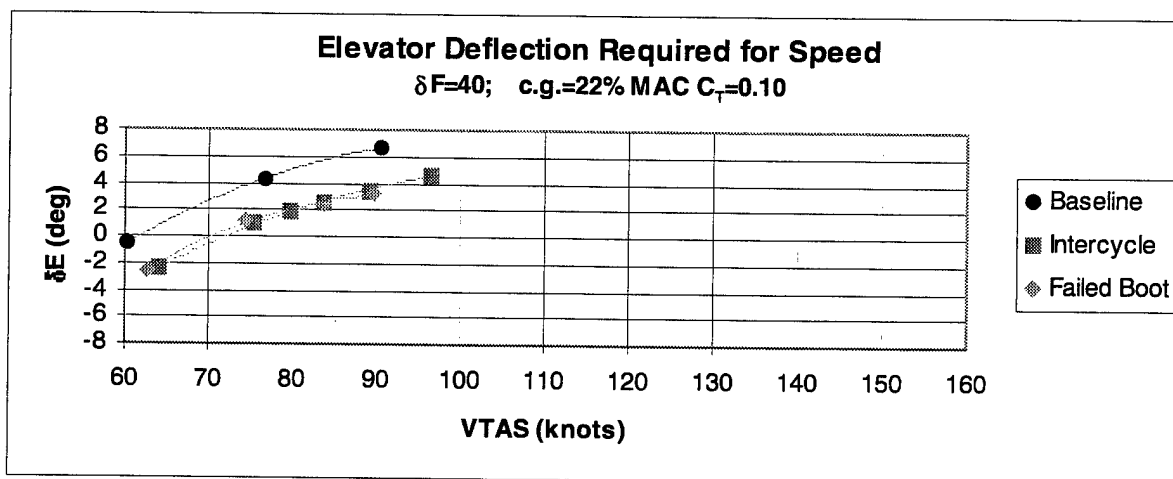


Figure 25. Elevator deflection for  $\delta F = 40^\circ$ .

The trend continues as flaps are further extended. With  $\delta F = 30^\circ$ , the S&C iced tail required about  $5^\circ$  more TEU elevator to stabilize the airplane at 80 knots. Due to the large amount of flow separation and control force reversal, the test points with the S&C ice were discontinued before completing the  $\delta F = 30^\circ$  speed points. Note that for the S&C ice case in both the  $\delta F = 20^\circ$  and  $30^\circ$ , the difference in  $\delta E$  requirement from the baseline increased as the speed increased. This again signifies that as the tailplane angle of attack became more negative, the flow separation and lift loss increased, and reduced the elevator effectiveness.

Another interesting observation was the similarity in the Inter-Cycle and Failed Boot cases in these plots. This suggests that the level of lift loss in both of these iced cases was accounted for by the same amount of elevator deflection.

### 5.3.6 Icing Effects on Elevator Hinge Moment

Similar to the last section, the techniques of Section 5.3.4 will be used to demonstrate the effects of various levels of icing on elevator hinge moment. The elevator hinge moment coefficient is plotted with respect to the aircraft true airspeed for each ice shape case. Figure 26 represents the  $\delta F = 0^\circ$  case; one can see that there is little difference between the ice cases. The Inter-Cycle is slightly offset, but that is due to the test run starting without fully trimming the elevator. Likewise, Figure 27 shows the data from the  $\delta F = 10^\circ$  case. Again an offset is seen but in the baseline case instead of the Inter-Cycle ice. The offset in hinge moment resulted from trimming the baseline case at a higher airspeed. For these flap settings, the ice did not have a strong effect on the hinge moment sensed by the pilot.

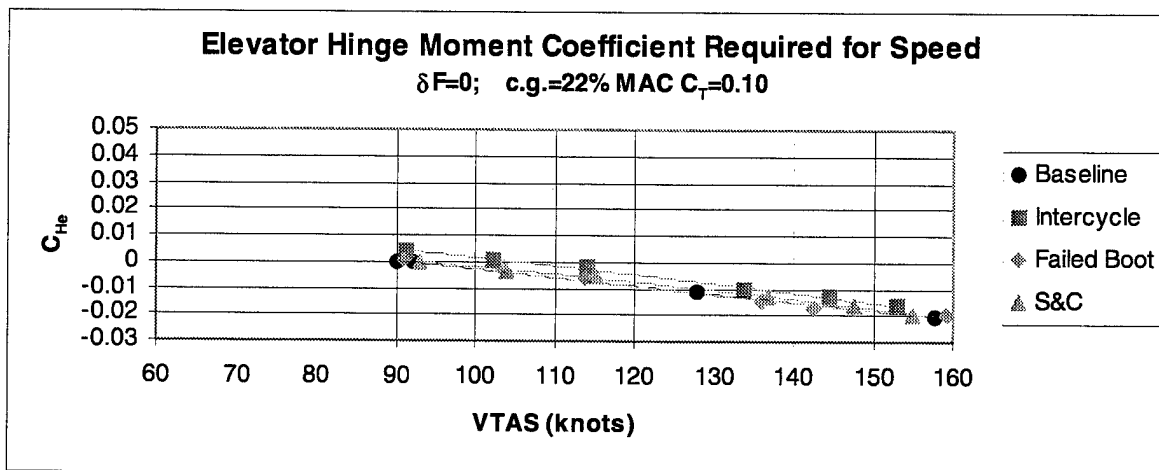


Figure 26. Elevator hinge moment coefficient for  $\delta F = 0^\circ$ .

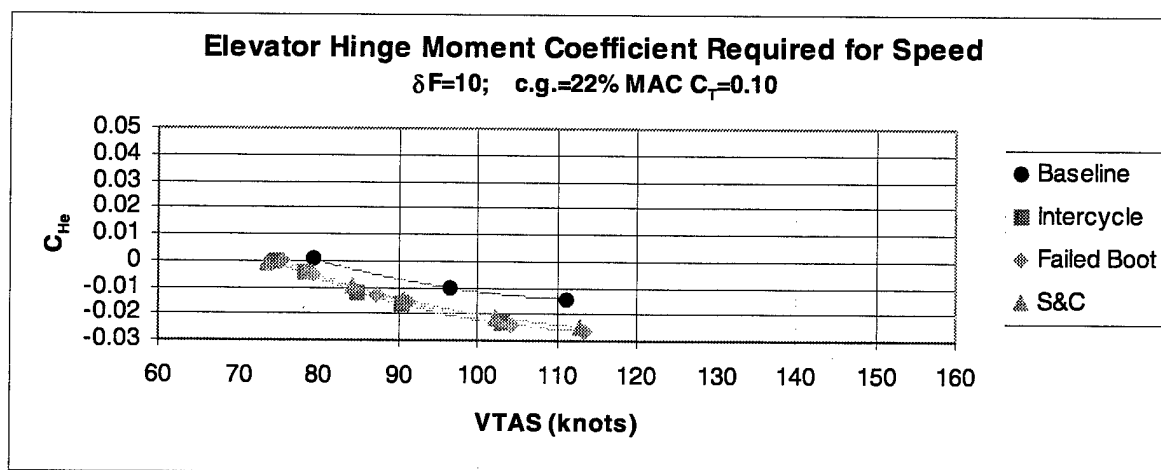


Figure 27. Elevator hinge moment coefficient for  $\delta F = 10^\circ$ .



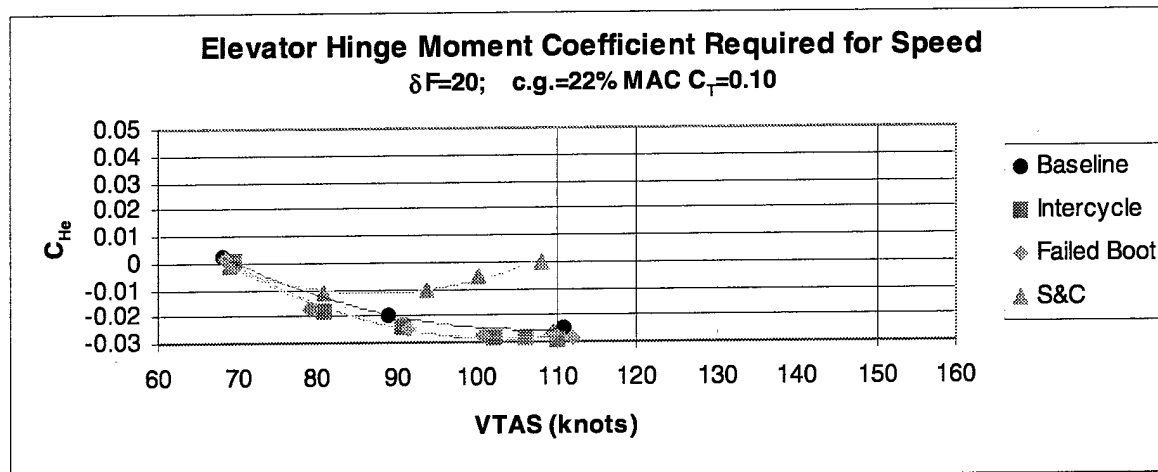


Figure 28. Elevator hinge moment coefficient for  $\delta F = 20^\circ$ .

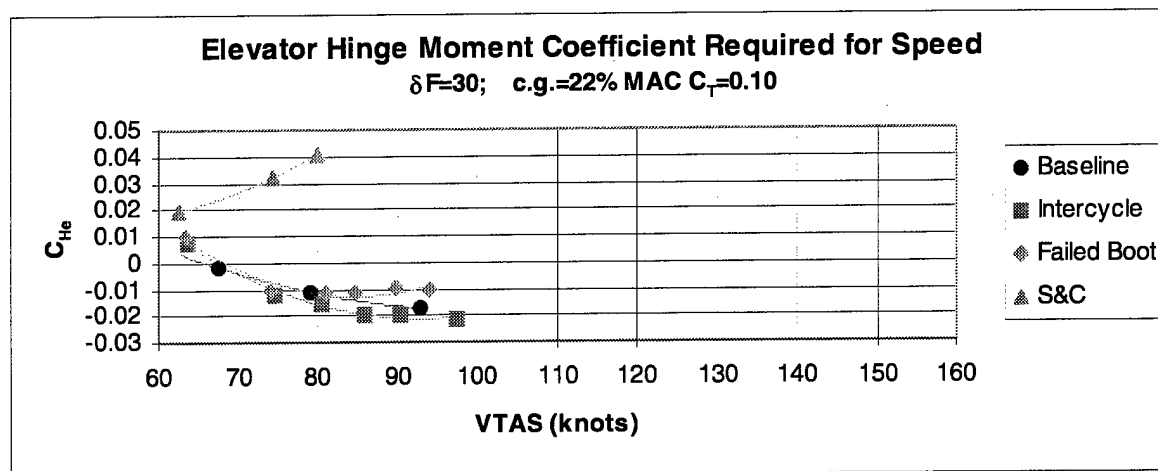


Figure 29. Elevator hinge moment coefficient for  $\delta F = 30^\circ$ .

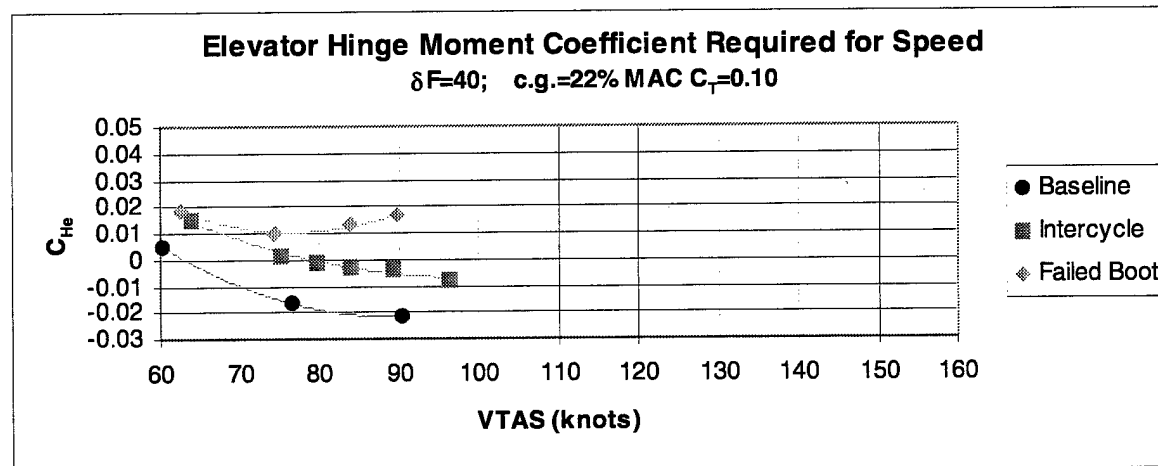


Figure 30. Elevator hinge moment coefficient for  $\delta F = 40^\circ$ .

In Figure 28 with  $\delta F = 20^\circ$ , the effects of the S&C ice became significant. The slope of  $C_{He}$  to VTAS reversed signs causing the final  $C_{He}$  value to be nearly zero. This switch in slope is indicative of a control force lightening. Note this is only lightening instead of a CFR because the  $C_{He}$  did not cross the zero line (initial trim point).

When the flaps were deflected to  $30^\circ$  (Figure 29), three observations can be made. One observation is that the yoke forces could not be trimmed in all iced configurations. The pilot had to pull the yoke to establish the low speed test point. This indicates that the pilot-actuated trim tab could not produce enough of a moment to counter the hinge moment required to hold the elevator in position for that airspeed. The trim tab creates a counter-moment through the aerodynamic force created over its surface. When the airflow upstream of the trim tab is perturbed, the trim tab is not as effective (the term  $b_3$  from Section 5.3.4 is reduced). The second observation concerns the control force reversal caused by the S&C ice. The slope of  $C_{He}$  to VTAS is positive and increases to a more positive value than the initial test point. In other words, as the pilot moved the yoke forward to increase airspeed, he had to pull back with an increasing amount of force to hold the yoke in that forward position. The reason for this is because the yoke was transmitting the force caused by the separation over the lower surface of the elevator. In terms of the math model in section 5.3.4, the  $b_1$  and  $b_2$  terms became positive so that the total hinge moment,  $C_{He}$  became positive. The pressure distribution about the tailplane caused the elevator to float against the wind ( $b_1 > 0$ ) and to behave as if overbalanced ( $b_2 > 0$ ). The third observation is to note the beginning of control force lightening in the Failed Boot ice case.

The  $\delta F = 40^\circ$  configuration is depicted in Figure 30. As in the previous configuration, neither ice nor the baseline cases were trimmable. The Failed Boot ice shape clearly causes a control force lightening and nearly a reversal because the final  $C_{He}$  was very close to the initial  $C_{He}$ .

Comparing the data sets in this way indicates the seriousness of the control issues caused by tailplane icing. In the worst case, the control forces recorded to hold the aircraft steady were on the order of 35 lbs. This was not excessive, but the forces were in the opposite direction from the norm and represent poor control "float" and "heaviness" parameters. Also, the degradation caused by the various ice shapes was clearly observed such that the S&C ice shape was by far the worst, followed by the Failed Boot. As expected, the Inter-Cycle ice had the least aerodynamic effect on hinge moment, but still caused a reduction in trim tab effectiveness.

### 5.3.7 Center of Gravity Effects on Tailplane Lift

The effect of aircraft center of gravity (CG) on  $C_{L_{Tail}}$  was also examined and the results are shown below. The forward CG test points have a solid trend line associated with them, and all the symbols are filled in except  $\delta F = 40^\circ$  case. The aft CG test points have similar symbols to designate flap settings, but the symbols are not filled except the  $\delta F = 40^\circ$  case. The forward CG locations were approximately 22% MAC whereas the aft CG locations were about 33% MAC.

The key observation from Figure 31 is the decreased magnitude of  $C_{L_{Tail}}$  required with an aft center of gravity. This result was expected; as the moment arm from the wing center of lift to the CG location was reduced, so was the tail

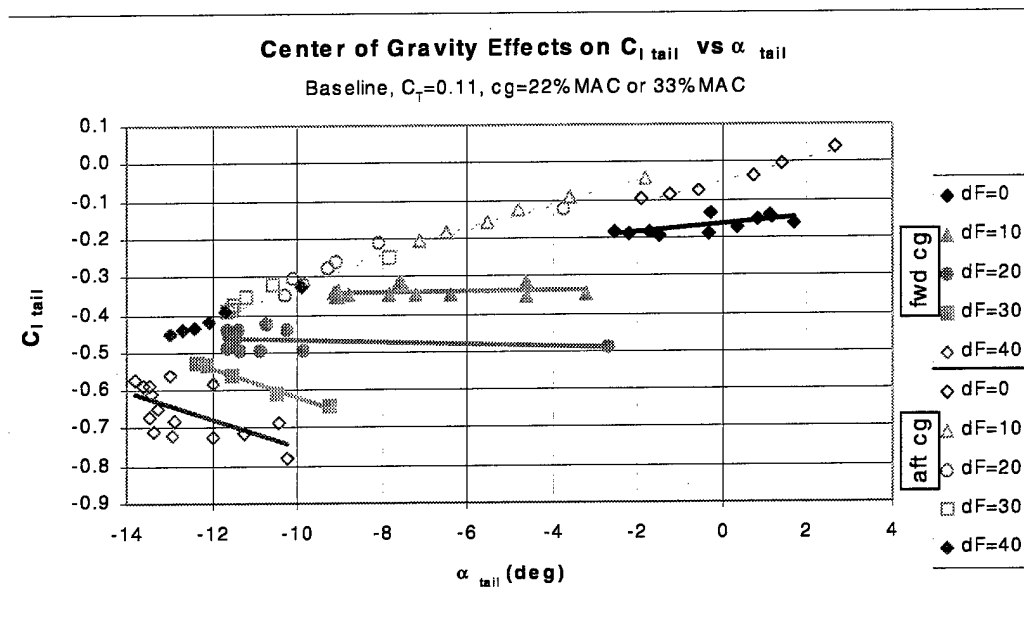


Figure 31. CG effect:  $C_{L_{Tail}}$  vs.  $\alpha_{tail}$ .

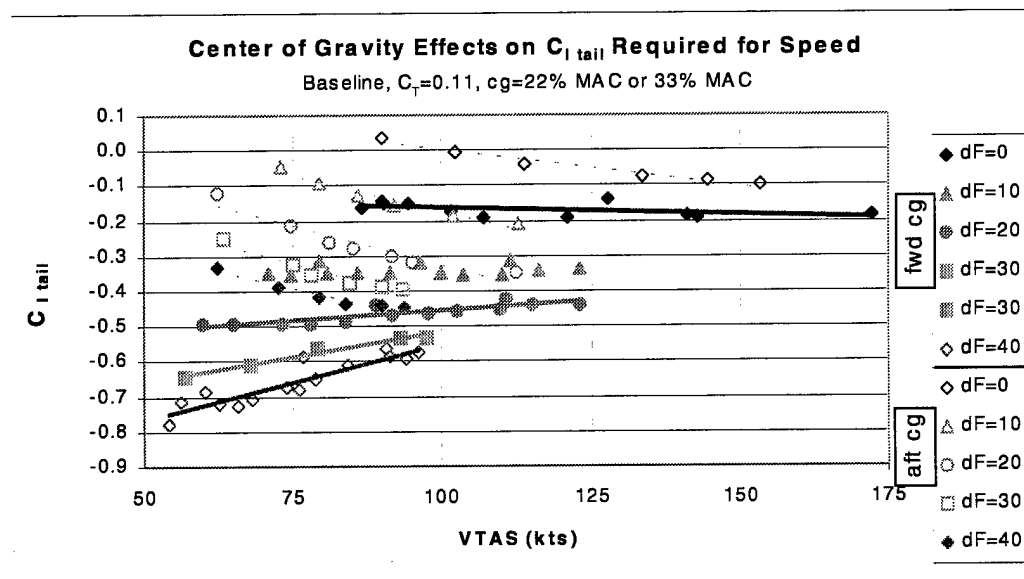


Figure 32. CG effect:  $C_{L_{Tail}}$  vs. VTAS.

download required to hold the aircraft steady. However, for the aft CG case and within a given flap position, the tail down load increased as  $\alpha_{tail}$  became more negative. This trend is opposite the one with the forward CG, so further investigation was warranted. The  $C_{l\_Tail}$  data were also plotted versus aircraft speed to gain further insight (Figure 32).

Again the decreased  $C_{l\_Tail}$  is observed with the aft CG, and again the divergence in tail lift requirement is observed. Examination of the tail surface pressures verified the trends. These data were consistent with the results shown in Ref. 12. Since the CG is aft of the wing aerodynamic center, the tail down lift needed to be reduced as the wing lift increased to balance the pitching moment. This effect is further demonstrated in Figure 33. For the forward CG test points, all the trend lines (except  $\delta F = 0^\circ$ ), have a negative slope, which indicates more tail down load required as the aircraft lift increases. In the aft CG cases, the trend lines have a positive slope, indicating less tail down load as the aircraft lift increases. The aircraft is still statically stable since the CG is forward of the neutral point; however, there were some flight conditions ( $\delta F = 0^\circ$ ,  $C_{L\_a/c} > 1.0$ ) where the tail was required to have a positive lift.

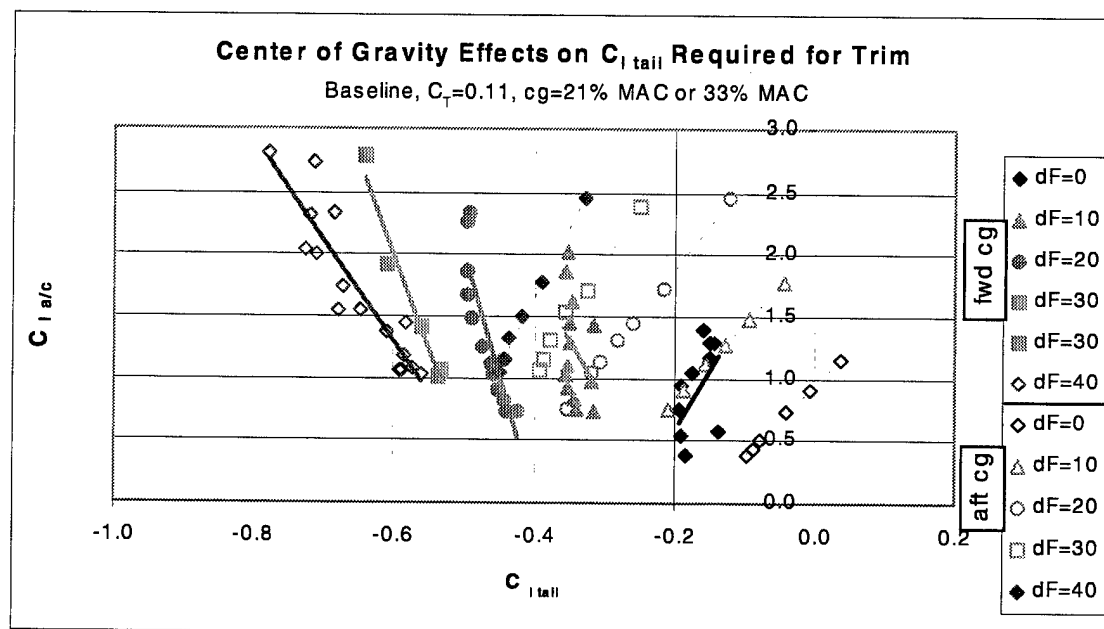


Figure 33. CG effects on  $C_{l\_Tail}$  with respect to  $C_{L\_a/c}$ .

The effect of CG on tailplane lift was demonstrated above. Greater down loads were required for the forward CG position than the aft CG position. As the aircraft lift was increased, the tail lift was increased for the forward position and decreased for the aft position. The greatest tail down load required for steady wings level flight was with flaps fully deflected, a forward CG position, and the aircraft in a high lift flight condition (near  $V_s$ ).

### 5.3.8 Thrust Effects on Tailplane Flow Field and Performance

The steady-state effect of propeller thrust ( $C_T$ ) on the flow field at the tail and on the  $C_{l\_Tail}$  were examined and the results are shown in Figure 34 through Figure 36.

As the thrust was increased, and the aircraft velocity held constant ( $V \cong 1.3V_S$ ), the tail AOA at the midspan nominally remained constant for a given flap setting (Figure 34). With  $\delta F = 0^\circ$ , the trend indicates a small increase in negative  $\alpha_{tail}$  as thrust increased, but considering the scatter in the data, this was not a significant result. Other constant velocity cases were examined and similar results were observed for the midspan flow probe. From the spanwise analysis (next section), there may have been a more substantial thrust effect on  $\alpha_{tail}$  observed at the tail tip. This analysis was not performed on the flow probe near the tail tip (Probe 1) due to initial problems caused by a blocked pressure port.

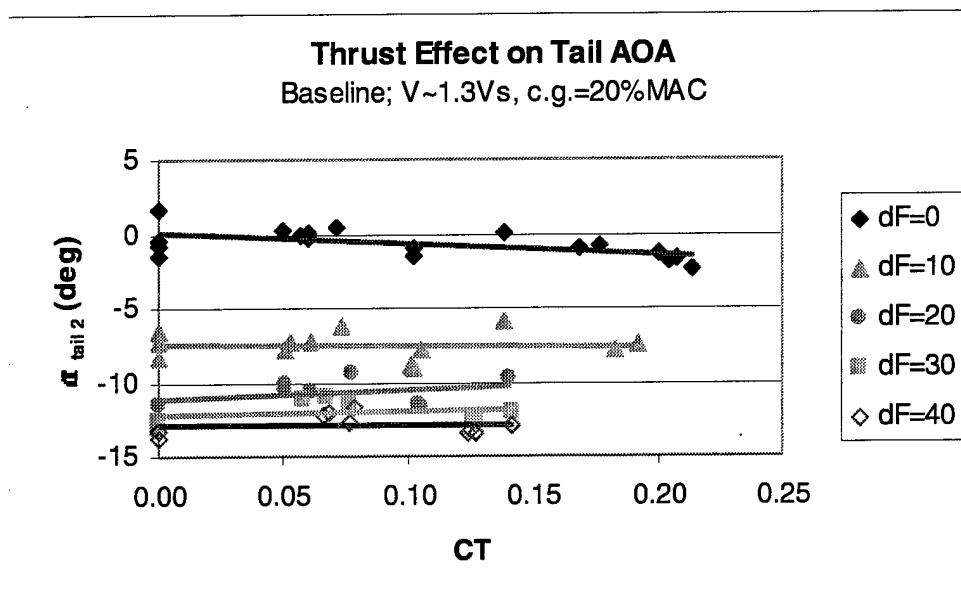


Figure 34. Thrust effect on  $\alpha_{tail}$ .

Another observation of the thrust effects on the flow field is the impingement of propeller slipstream on areas of the horizontal tail. With  $\delta F = 0^\circ$  and  $10^\circ$ , there is a clear increase in flow velocity at the midspan probe position (Figure 35). This increase in velocity was attributed to the propeller slipstream. As the flaps were extended greater than  $10^\circ$ , there were only minor velocity increases observed at the midspan location. This indicated that the propeller slipstream moved below the horizontal tail for flap positions greater than  $10^\circ$ .

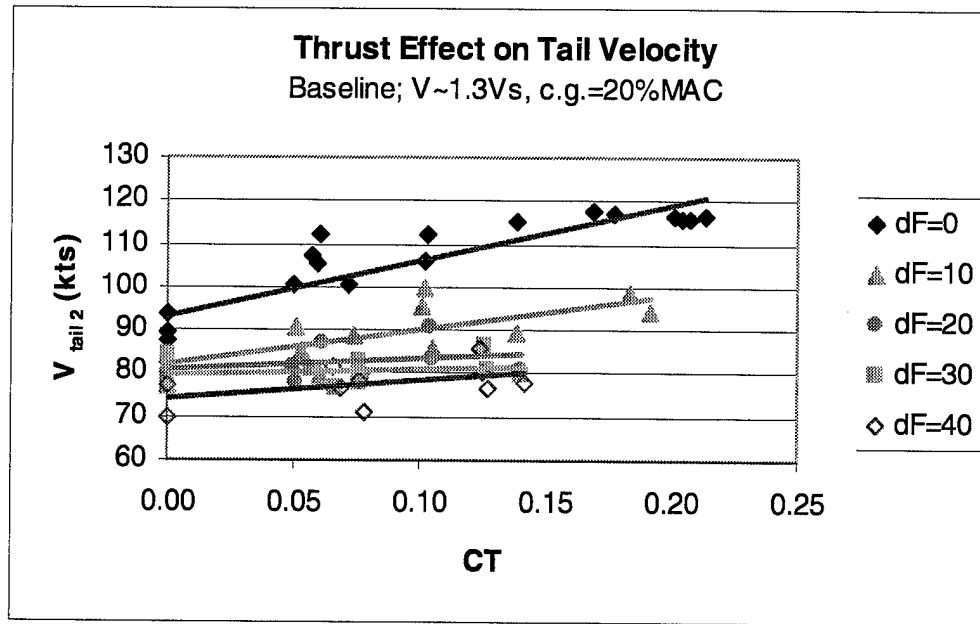


Figure 35. Thrust effect on  $V_{tail}$ .

The effect of thrust on the tailplane section lift coefficient was of greater interest. For all the forward CG cases examined, the tail lift coefficient increased as the thrust was increased (Figure 36). In the  $\delta F = 0^\circ$  and  $10^\circ$  cases, there were only small increases in the negative  $C_{l\_Tail}$  required as the thrust increased. However, for the  $\delta F = 30^\circ$  and  $40^\circ$  cases, there was a substantial increase in the  $C_{l\_Tail}$  required as the thrust increased. This behavior was consistent with the requirement for greater tail down load to balance the nose-down pitching moment caused by the vertical displacement of the thrust vector to the CG position. Since the thrust line on the Twin Otter is above the CG, the increased thrust caused a nose-down pitching moment. With flaps deflected, the thrust was also deflected downwards, causing an even greater nose-down moment that required counter-balancing by the tail down load.

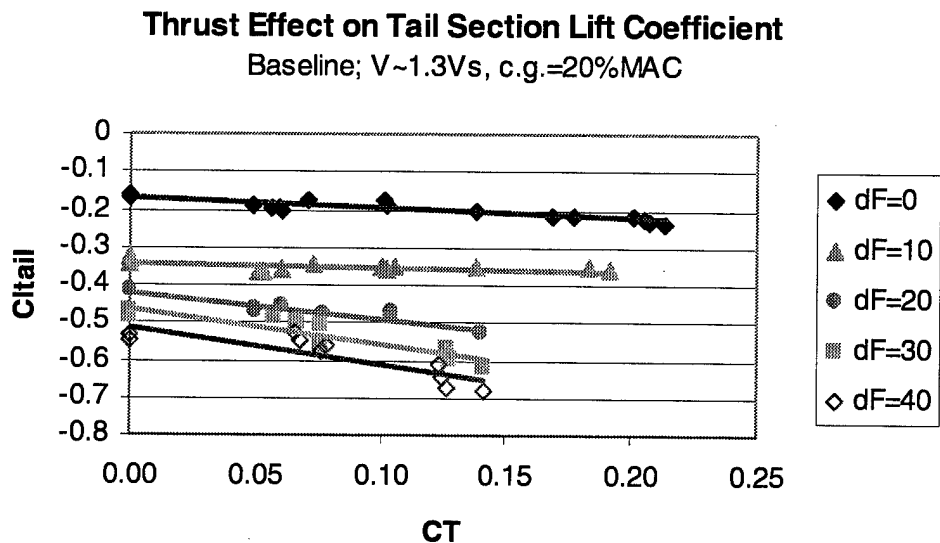


Figure 36. Thrust effect on  $C_{l\_Tail}$ .

### 5.3.9 Spanwise Variation of Flow at the Horizontal Tail

The variation of the flow field across the semi-span of the tailplane was examined through use of the three 5-hole probes. For each probe, the  $\alpha_{tail}$ ,  $\beta_{tail}$  and  $V_{tail}$  are plotted (Figure 37 through Figure 39) for  $\delta F = [0^\circ, 10^\circ, 20^\circ, 30^\circ, 40^\circ]$  to display the complex flow field at the tailplane. The primary cause of the spanwise variation is likely the combination of the propeller slipstream and flap deflection. Secondary contributors to the variation are the fuselage and vertical tail, and other aircraft features like engine nacelles and wing struts may also play a role in the complex nature of the tailplane flow field. It should also be noted that the data presented here are for one set of conditions, and if those conditions are varied, the flow field can be altered significantly.

For a given flap setting, the  $\alpha_{tail}$  typically varied  $1^\circ$ - $2^\circ$  across the semi-span (Figure 37). For all flap settings except  $\delta F = 0^\circ$ , the outboard position measured the most negative  $\alpha_{tail}$ . With  $\delta F = 0^\circ$ , the outboard position measured the most positive angle, indicating the presence of some flow disturbance ahead of this probe location for that flap position. Such a flow disturbance may be caused by the propeller wash, engine exhaust, nacelle, or wing strut. With the low level of variation in  $\alpha_{tail}$ , particularly with the larger flaps settings, the leading edge flow separation caused by ice should be fairly uniform across the span. From observation of yarn tufts during the flight, this was commonly found to be true during  $\beta = 0^\circ$  test points.

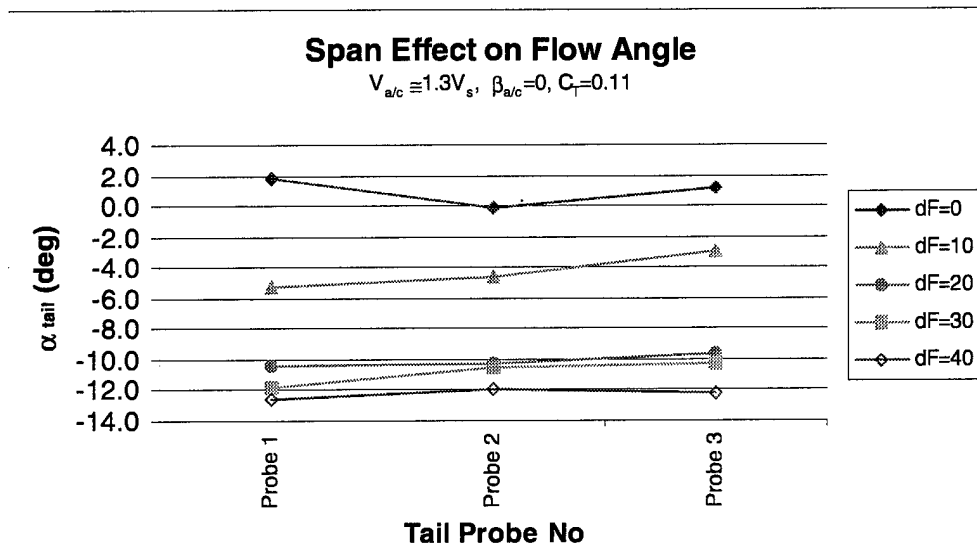


Figure 37. Span variation of  $\alpha_{tail}$ .

Looking at the  $\beta_{tail}$  (Figure 38), the typical variation for a given flap setting was  $5^\circ$  across the semi-span, with  $\Delta\beta_{tail} = 7^\circ$  for the  $\delta F = 10^\circ$  case. Typically the trend was an outboard side-wash near the tail root, a small *inboard* side-wash at the midspan, and a larger *inboard* side-wash near the tail tip. The one exception to this trend was again the  $\delta F = 0^\circ$  case, where the largest *inboard* side-wash was measured at the midspan position. The outboard side-wash near the root was most likely due to the flow around the vertical tail. With the flow probe on the left side of the tail, the flow circulating around the vertical tail caused a positive  $\beta$  measurement on the tail probe. The *inboard* side-wash near the tip was most likely caused by the propeller wash or tip vortex flow. The change in side-wash direction near the midspan location indicates that there was a spanwise location of confluence between the outboard wash caused by the vertical tail and the *inboard* wash caused by the propeller wash. At that location, there would be a small acceleration in the flow speed. The values of these  $\beta_{tail}$  angles were fairly small as expected since the horizontal tail had a  $0^\circ$  sweep angle, and would not play a significant factor in the ice-contaminated tail stall event.

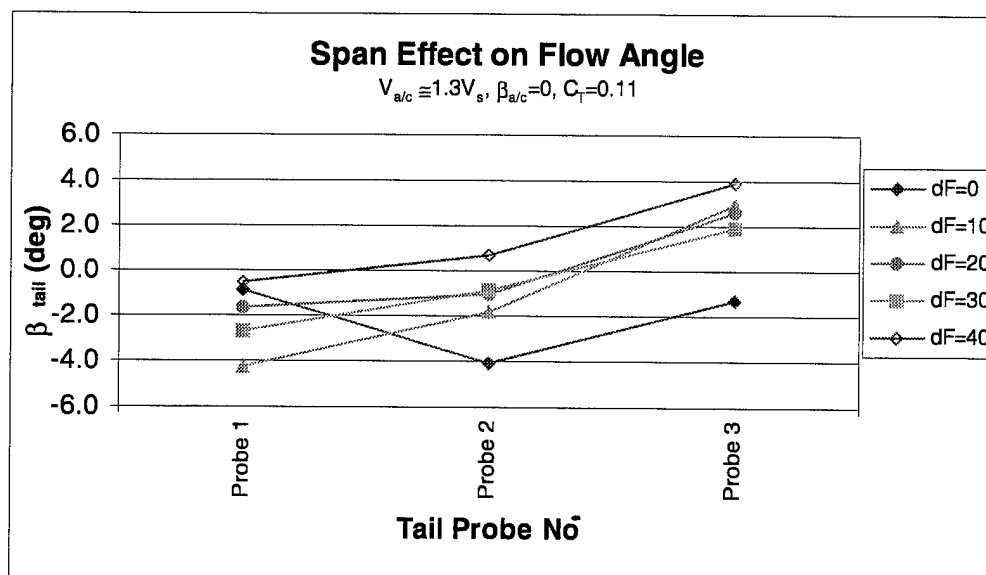


Figure 38. Span variation of  $\beta_{tail}$ .

The most significant variation in the flow field was in the velocities. The propeller wash effects are clearly observed in the  $V_{tail}$  plots (Figure 39). With  $\delta F = 0$ , the mid-span probe measured a significant increase (20 knots) in the flow velocity ( $V_{a/c} = 92$  knots). As the flap angle increased to  $10^\circ$ , the propeller wash was more concentrated at the out-board position (probe 1), where a 20 knot increase was observed above the aircraft airspeed. As flaps were extended between  $20^\circ$  to  $40^\circ$ , there was a small velocity increase above the aircraft airspeed observed at the midspan probe, but the effect was much smaller. These observations further support the idea that the propeller slipstream moves below the tailplane as flaps extend beyond  $10^\circ$ . Also, the atypical behavior in  $\alpha_{tail}$  and  $\beta_{tail}$  for  $\delta F = 0^\circ$  and  $10^\circ$  is better established as a propeller wash effect. Finally, it should be noted that for the  $\delta F = 0^\circ$  and  $10^\circ$  cases, the dynamic pressure at the tail ( $q_{tail}$ ) can be higher than the dynamic pressure of the aircraft ( $q_{a/c}$ ).

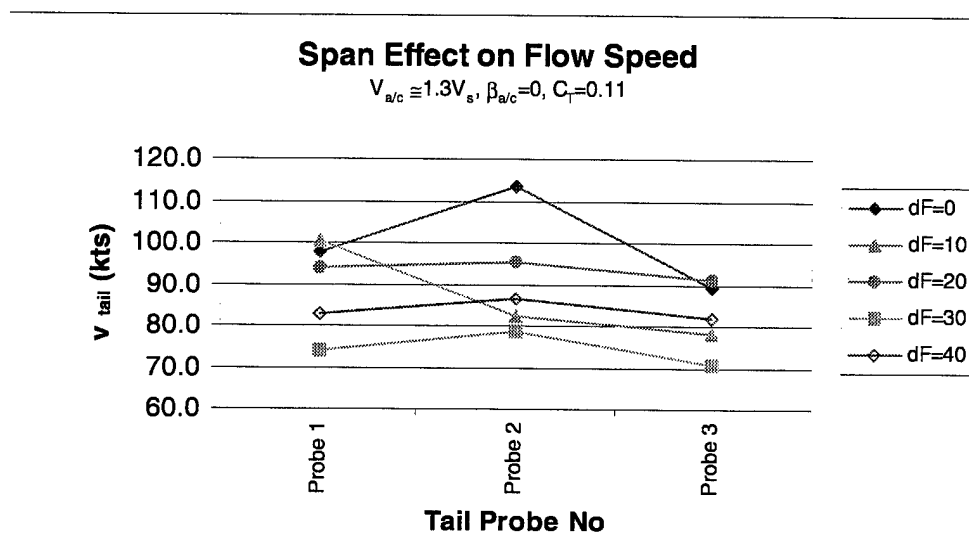


Figure 39. Span variation of  $V_{tail}$ .

As stated above, the flow field at the tail can be very complex with multiple cause and effect relationships. The variation across the tail span was demonstrated in this section and possible explanations were provided. For the cases examined, the variation does not appear to be significant enough to cause a spanwise variation of ice-induced separation.



### 5.3.10 Effect of Steady Heading Sideslips on Tailplane Flow Field and Performance

Steady heading sideslip (SHSS) maneuvers were included as part of the test matrix since an SHSS may help to determine susceptibility to ice-contaminated tailplane stall for some aircraft<sup>13</sup>. The SHSS maneuvers conducted as part of this investigation revealed more about the complex flow field presented to the horizontal tailplane. Figure 40 shows the effects of aircraft sideslip on tailplane angle of attack measured by the mid-span flow probe. Note that these data are for the no-ice baseline and all iced tail configurations with the test point velocity approximately at  $1.3V_s$  speed. As noted in the previous section, there is a strong influence of the propeller wash for the  $\delta F = 0^\circ$  case at the mid-span probe. However, as the flaps deflected beyond  $10^\circ$ , the trends due to aircraft sideslip were evident. The positive SHSS caused the tail angle of attack to become more positive (approximately  $+4^\circ$ ). In comparison, the negative SHSS caused only a small positive increase in the tail angle of attack. Similar trends were observed for the probe near the tail root (probe 3). The outboard probe (probe 1) generally had similar trends, but the positive increase with negative SHSS was comparable with the increase due to positive SHSS (approximately  $+4^\circ$ ).

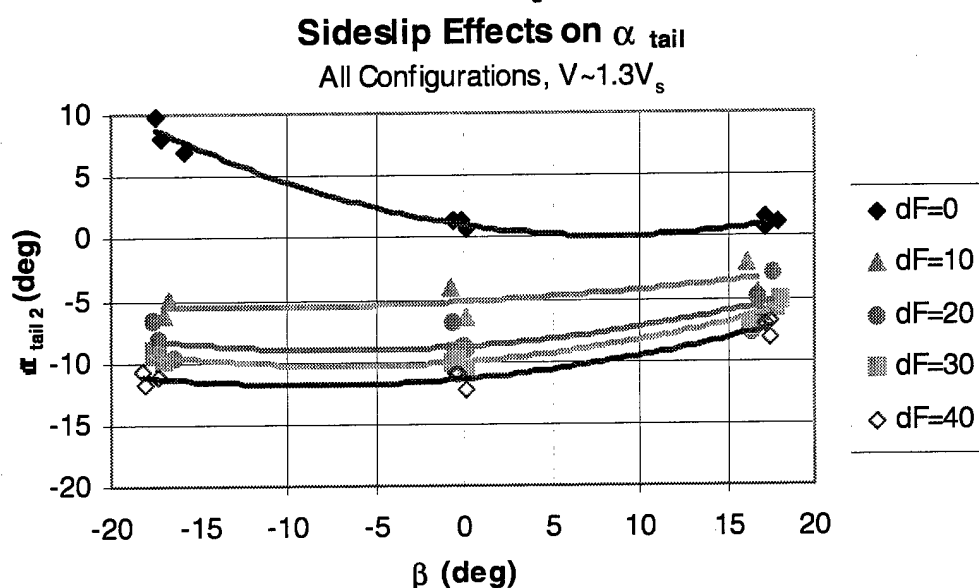


Figure 40. Sideslip effect on  $\alpha_{tail}$ .

The significance of the positive increase in tail angle of attack with sideslip is that the tail stall margin is reduced with the SHSS maneuver. The cause of this positive increase in  $\alpha_{tail}$  was most likely due to the increase in aircraft angle of attack (Figure 41) to maintain constant lift for holding altitude or vertical speed. In performing the SHSS maneuver, a bank angle and a crab angle were held relatively constant. With the wings banked (up to  $14^\circ$  bank angle), the lift component normal to the aircraft was increased by the increase in angle of attack to maintain a relatively constant vertical lift component. This increase in aircraft angle of attack effectively made the tail angle of attack less negative and reduced the tail stall margin.

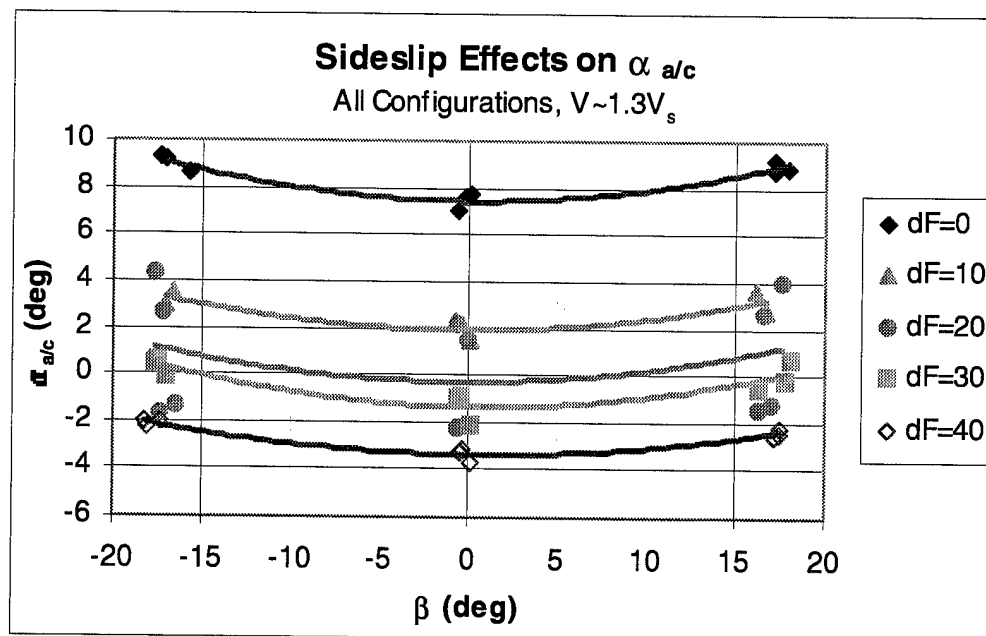


Figure 41. Sideslip effect on  $\alpha_{a/c}$ .

Observations of the yarn tufts during the SHSS maneuvers confirmed this finding. At the larger flap settings with the Failed Boot or S&C ice shapes, a significant chordwise separation bubble existed across the entire span of the tailplane with the aircraft at  $\beta = 0^\circ$ . As the aircraft was sideslipped in either direction, the size of the separation bubble was reduced and moved away from the direction of the sideslip. Also, there was significant pulsing in the elevator caused by flow separation and reattachment for the  $\beta = 0^\circ$  cases described. This pulsing was effectively eliminated when the aircraft was placed in a sideslip angle greater than approximately  $12^\circ$ .

The results from the pressure belt data for the SHSS maneuvers are shown in Figure 42. The trends suggest that less down lift is needed with the positive sideslip and more down lift with the negative sideslip. However, this is an artifact of the test setup and the flow field presented to the pressure belt. The primary cause of these trends was the flow around the vertical stabilizer and rudder. The positive sideslips were accomplished with a rudder deflection to the left side horizontal tail – where the pressure belt was located. The leading edge of the left side of the vertical tail had a large suction peak with a pressure rise over the left side of the rudder. The flow field around the vertical stabilizer and rudder affected the pressures near the pressure belt such that the integrated values showed a more positive lift. On the other hand, when the rudder was moved to the right side for the negative sideslips, the flow field around the vertical/rudder combination caused the integrated pressures about the horizontal tail to become more negative than the zero sideslip case. Since this behavior is symmetrical about the zero sideslip case, it is reasonable to assume that the increased section lift coefficient on one side is equally decreased on the other side during the sideslip maneuver to accomplish a constant tail lift during the SHSS.

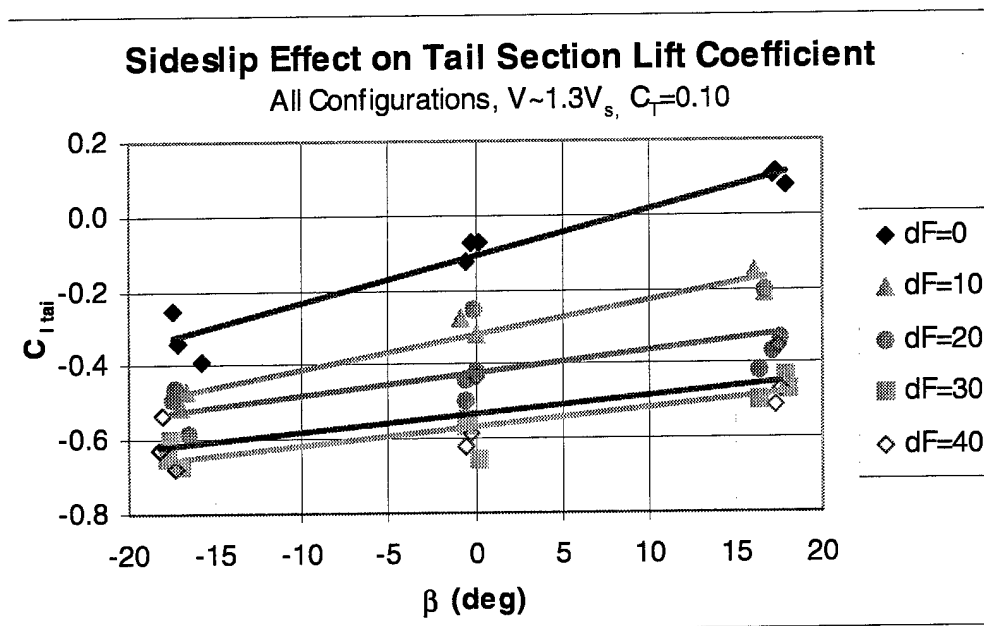


Figure 42. Sideslip effect on  $C_{L_{Tail}}$ .

The SHSS maneuver was performed for wide range of test conditions and ice configurations on the NASA Twin Otter. None of the SHSS maneuvers led to a stalled condition. To the contrary, the SHSS maneuvers significantly reduced flow separation caused by leading edge contamination. It should be noted no ice contamination was tested on the vertical stabilizer during these tests. If ice contamination had been present on the vertical stabilizer, it would have affected the pressure field about the vertical and horizontal tail junction. It is unknown whether such a disturbance would have led to a greater sensitivity to sideslip. In addition, since there were some aircraft known to have a sensitivity to tail stall preceded by sideslip, the results shown above should not be considered universal. The reduction of flow separation experienced in these tests may have been a configuration specific phenomenon, and as such, the SHSS is not a recommended procedure for recovering from an impending tail stall.

## 5.4 Steady-State Analysis Conclusions

Steady state data points with the test aircraft's tail configured with various levels of ice contamination were acquired and analyzed as described in the previous sections. For steady state flight, the following conclusions were made:

1. For any ice configuration, the most negative tailplane AOA and smallest tailplane stall margin occur at full flap deflection while flying at flap extension speed,  $V_{FE}$ .
2. The difference in elevator deflection angle between a clean and iced tail is a good indicator of reduced tailplane performance. The larger the difference, the greater the performance degradation. This assumes that aircraft configuration (flaps, landing gear, CG, etc) and flight condition (airspeed, thrust setting) are held constant for the clean and iced cases considered. This method clearly discriminated between the iced and clean cases, but it did not discriminate between the Failed Boot ice and the Inter-Cycle ice.
3. The difference in elevator hinge moment is also a good indicator of reduced tailplane performance. It may be better than the elevator deflection method since it can discriminate between smaller levels of degradation as in the Failed Boot and Inter-Cycle ice cases. The elevator hinge moment method requires consistency in aircraft configuration and flight condition between the baseline and iced cases, and requires the pilot to fly the aircraft in an untrimmed condition to acquire the appropriate forces. This method also provided data on the progressive hinge moment lightening and reversal as the tailplane stall margin was reduced.
4. As the tailplane approached stall, the trim tab effectiveness was reduced such that the tab could not effectively balance the elevator hinge moment. This provides another good indicator of approaching ice-contaminated tailplane stall. In other words, the inability or difficulty to trim the iced aircraft with flaps deflected could indicate an imminent tail stall.
5. A forward CG location demanded a higher performance from the horizontal tail to provide stability. It was shown that the most negative tail section lift coefficient was required with a forward CG, the flaps fully deflected, and at a speed near stall speed,  $V = 1.0V_S$ .
6. As thrust increased, a more negative tail section lift coefficient was required of the horizontal tail to maintain stability. This was most likely due to the vertical displacement between the CG and the high thrust line of the test aircraft causing a nose-down pitching moment due to thrust increase. It is reasonable to assume that high thrust line aircraft would have similar results. Thrust did not have a substantial effect on  $\alpha_{tail}$  or  $V_{tail}$  when flaps were deflected beyond  $\delta F = 10^\circ$ .
7. The flow field presented to the tail was quite complex especially with the flaps retracted or at  $\delta F = 10^\circ$ . The complex nature at these flap settings was most likely due to the propeller wash impinging on the horizontal tail. However, at these flap settings, the tail stall margin was large, so the complexity in flow field did not provide insight into the tail stall phenomenon for the test aircraft.
8. For flaps greater than  $\delta F = 10^\circ$ , there was relatively little spanwise variation in  $\alpha_{tail}$ ,  $\beta_{tail}$  or  $V_{tail}$  so that this tail would stall relatively symmetrically across the span. This result was verified through use of the yarn tuft visualizing the separation bubble on the lower surface of the tail.
9. Steady heading sideslips did not precipitate an ICTS condition for the test aircraft. To the contrary, SHSS alleviated flow separation caused by leading edge ice contamination and eliminated control pulsing when the sideslip angle reached approximately  $\beta = \pm 12^\circ$ . The reduction in flow separation is likely due to an increase in aircraft AOA and subsequent positive increase in tail AOA, causing an increase in tail stall margin. However, since no ice contamination was present on the vertical tail, and the interaction of flow separation on the vertical may play a role in flow separation on the horizontal tail, this conclusion is limited to the clean vertical tail cases.

## 6.0 Dynamic Maneuver Analyses

The primary purpose of the dynamic maneuvers was to measure the aerodynamic behavior of the horizontal tailplane while driving it toward stall. This was achieved by either intentionally manipulating the elevator or changing one of several parameters. For convenience, the parameter space is reiterated below:

- ice shape severity
- flap deflection,  $\delta F$
- speed,  $V_{IAS}$  (aircraft angle of attack,  $\alpha_{wc}$ )
- thrust,  $C_T$

Increasing any one of these parameters will put the aircraft on a path toward tail stall. The “paths to stall” maneuvers flown include the flap transition, speed transition and thrust transition. Another category of maneuver involves the controlled manipulation of the elevator. These include the elevator doublet and pushover maneuvers. Finally, a closed-loop tracking task was performed: the balked landing maneuver, which simulated an ILS approach and go-around. In contrast to the other maneuvers, the closed-loop task offered a clear criterion for whether or not the pilot met the performance objective. Table 1 lists these dynamic maneuvers, along with the number of test points flown and the parameter space. It should be noted that the location of the aircraft’s center of gravity was also briefly studied. As expected, the more forward the CG, the greater the loading on the tailplane. This is discussed in Section 5.3.7. The other parameter mentioned in the steady state section, the sideslip angle, was not an element of the dynamic maneuvers.

Maneuver	Test Points	Comments
Data Compatibility	22	All Shapes, $\delta F = 0^\circ$ , $V = 1.8V_s$ , Thrust for level flight
Flap Transition	6	Clean Tail and Failed Boot, Moderate Thrust
Speed Transition	2	Failed Boot, Full Flaps, Moderate Thrust
Thrust Transition	98	All Shapes, Flaps & Speeds, Mod Thrust
Elevator Doublet	103	All Shapes, Flaps & Speeds, Mod & Hi Thrust
Pushover	133	All Shapes, Flaps & Speeds, Mod & Hi Thrust
Balked Landing	9	Failed Boot, Flaps, $V = 1.3V_s$ , Thrust as Required

Table 1. Dynamic maneuvers flown and number of test points for each.

Airfoils stall due to either a leading or trailing edge separation. For this series of flight tests, evidence of stall was documented by both the tailplane tuft video and the pressure distributions from the static pressure belt around the tailplane. Preliminary observations suggest agreement with the Ohio State University wind tunnel tests<sup>9</sup>. That is, the clean leading edge was found to undergo only trailing edge separation at sufficiently negative tail angles of attack and elevator deflections (more cambered). For the ice shapes tested, on the other hand, separation occurred from the leading edge. From the tuft video, three distinct zones of activity along the underside of the tail could be identified. There were several cases where both the leading and trailing edge zones exhibited flow unsteadiness while the tufts in the middle zone were less active.

The dynamic maneuvers are introduced in Section 6.1. Herein, the pushover is also examined with some advanced analysis techniques. In Section 6.2, a direct comparison between the pushover and elevator doublet is presented. This section also contains a comparison between two relevant metrics regarding the pass/fail criteria: the control force reversal versus the undamped pitch response. In Section 6.3, the precision and accuracy with which one pilot flew the pushovers is investigated. The main findings are summarized in Section 6.4. Appendix C contains time histories of 21 quantities from select test points within the parameter space. Finally, Appendix D presents a time history of  $C_P$  distributions around the tailplane for one of the thrust transition test points.

## 6.1 Maneuver Description and Analysis

### 6.1.1 Data Compatibility

This maneuver was the first test point of each flight. The purpose was to check for instrument errors by performing this data consistency check. Beyond noting that the data are within range, further analysis had not been done.

**Description:** As seen from the time histories in Figure 43, the maneuver began with a sharp, stick back input (about 1" column movement) so that the short period was excited. The column was held there for a short time (3 sec). Then, a sharp, forward stick movement (about 2") was applied and the column frozen there for a slightly longer time (5 sec). Next, the column was sharply returned to trim and frozen. As soon as the elevator reached trim, sharp rudder step inputs on the order of 1-2" pedal deflection were applied and timed with the lateral response of the aircraft. The control column was kept frozen and the ailerons in the neutral position. Six alternating rudder kicks were applied in all. After the last kick, the pedals were returned to neutral and all controls were held frozen for a few more seconds. The elevator step inputs mark the pitch response and damping characteristics ( $q$ ) of the Twin Otter, while the rudder kicks highlight the dutch-roll and damping characteristics ( $r$ ).

**Configuration:** This maneuver was flown with all ice shapes at  $\delta F = 0^\circ$ ,  $V = 1.8V_s = 120\text{kts}$ ,  $C_T$  as required for level flight, and propeller RPM = 90%.

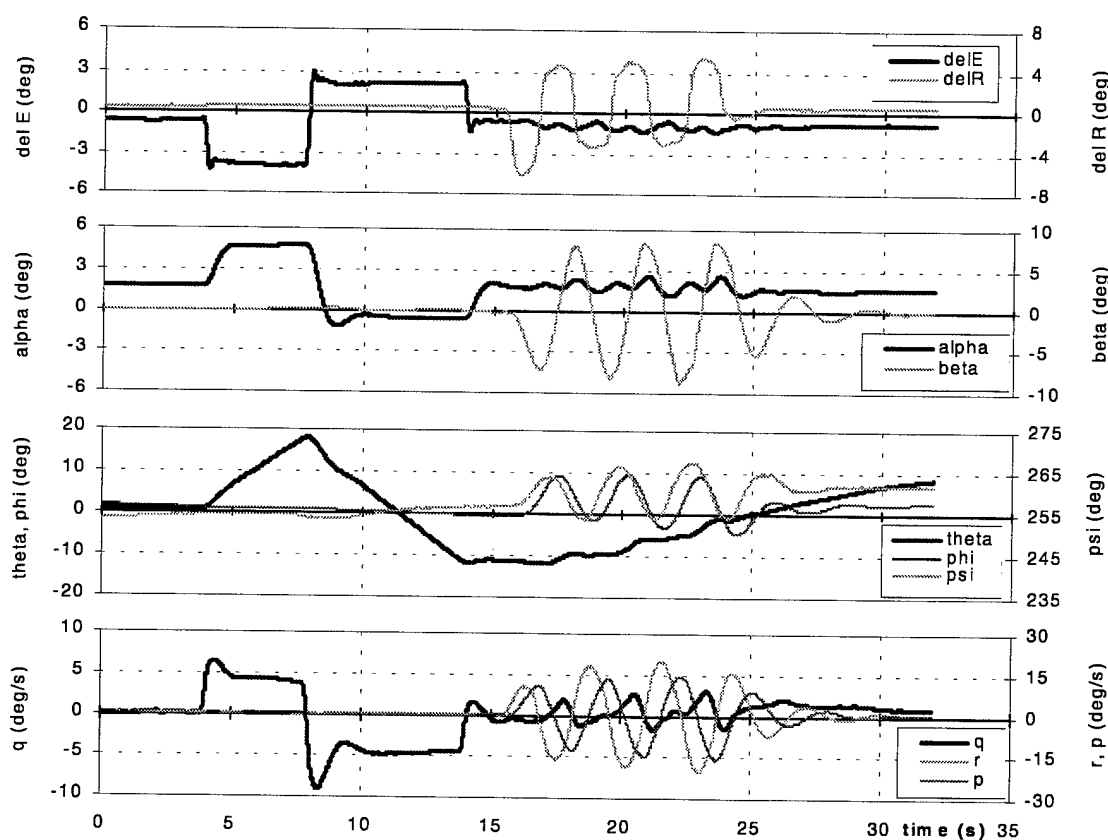


Figure 43. Data compatibility time traces.

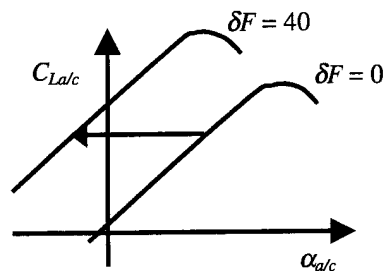
### 6.1.2 Flap Transition

One of the key parameters, of course, was the flap deflection angle. All of the test points flown included this setting as a factor. To more efficiently isolate the effect of the flap deflection, the flap transition was constructed and flown six times.

**Description:** The flaps were deployed from zero to full deflection,  $0^\circ$ – $37.5^\circ$  (hereinafter rounded to  $40^\circ$ ) while the remainder of the parameter space remained unchanged.

**Configuration:** This maneuver was flown for only the Baseline and Failed Boot cases at a moderate thrust setting,  $C_T = 0.10$ , and a constant airspeed, 85 KIAS, which corresponded to  $1.3$ – $1.6V_s$  as  $\delta F$  increased steadily from  $0^\circ$  to  $40^\circ$ .

**Analysis:** The flap transition profile for the aircraft is depicted in the sketch to the right. Selected time histories are shown in Figure 44 for the Baseline case. As the flap angle increased, the aircraft angle of attack was decreased to maintain velocity. Since neither the speed nor the aircraft lift ( $=$  weight) changed,  $C_{L_{a/c}}$  was also constant. Furthermore, a constant  $C_{L_{a/c}}$  also implies that the downwash is constant (see Section 5.3.2). The decrease in  $\alpha_{a/c}$  drove  $\alpha_i$  more negative. The more negative  $\alpha_i$  caused the  $C_{L_{Tail}}$  to be more negative than required; thus the  $\delta E$  was increased (deflected TED) to maintain the speed condition. Had  $\delta E$  been maintained, the aircraft would have pitched up and slowed down.



The nominally same flight conditions with the Failed Boot ice shape are presented in Figure 45. Also plotted on Figure 45 are the equivalent trim cases (o, \*). These points were added because the speed was not as tightly controlled during this test point (the flight was for demonstration purposes). In general, the trends are very similar to those of the Baseline. Some key differences between the clean and iced tail, however, appear in the traces of elevator deflection ( $\delta E$ ) and control force ( $F_{YE}$ ). For the Baseline case, a push force was required throughout the entire maneuver, and the elevator deflection changed only slightly for  $\delta F > 20^\circ$ . For the Failed Boot case, on the other hand, the required force transitioned from a push to a pull force at  $\delta F \approx 20^\circ$ . Beyond  $\delta F > 35^\circ$ , oscillations in the elevator appeared both in the data and are dramatically apparent from a video shot by a chase plane. The video also captured that the tufts across the whole underside of the tailplane had lifted off the surface and were moving fore to aft.

While maintaining a high airspeed, increasing the flap deflection with an ice contamination drove the tailplane toward stall by driving  $\alpha_i$  more negative.

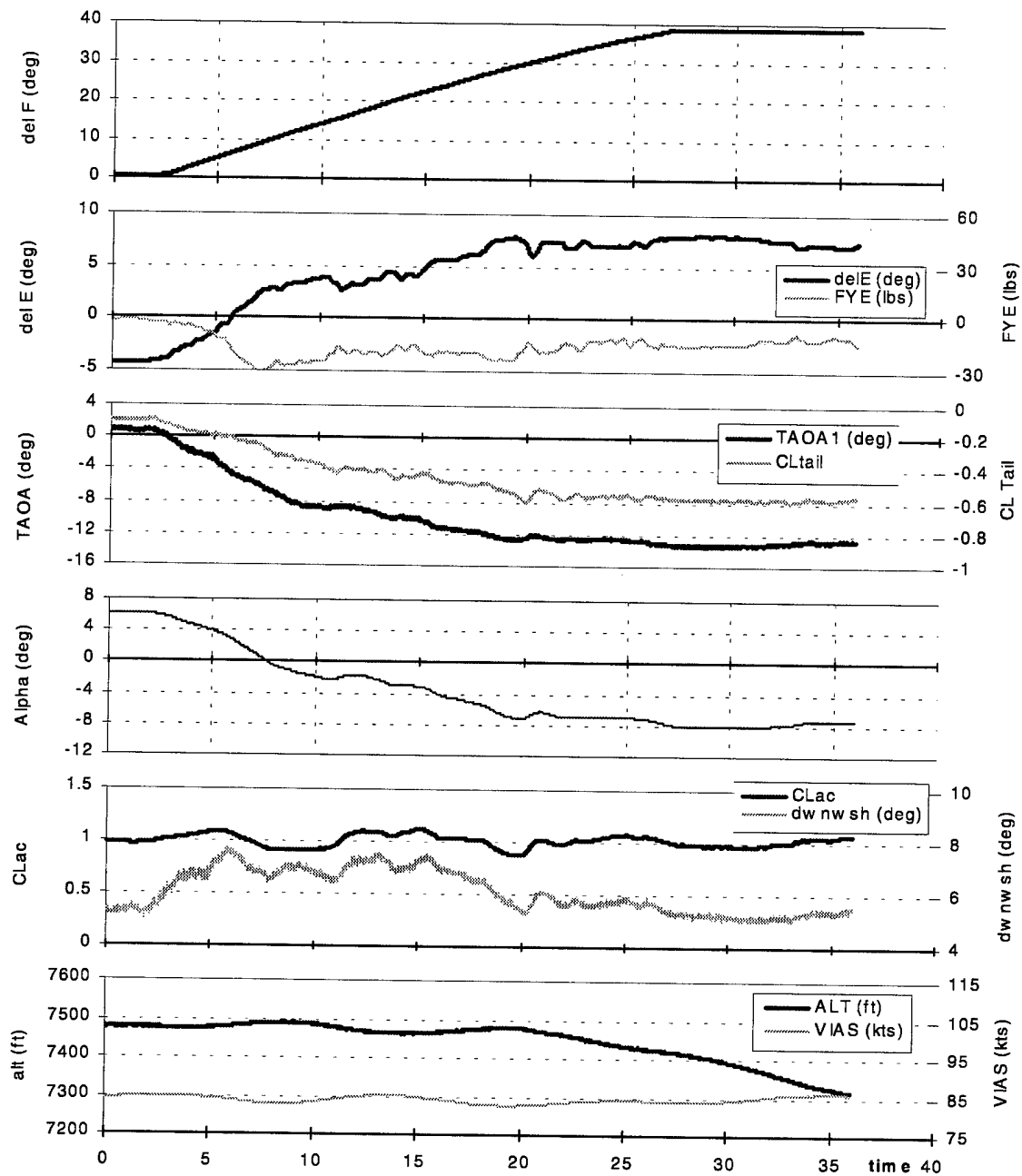


Figure 44. Flap transition; clean tail, VIAS = 85kts.



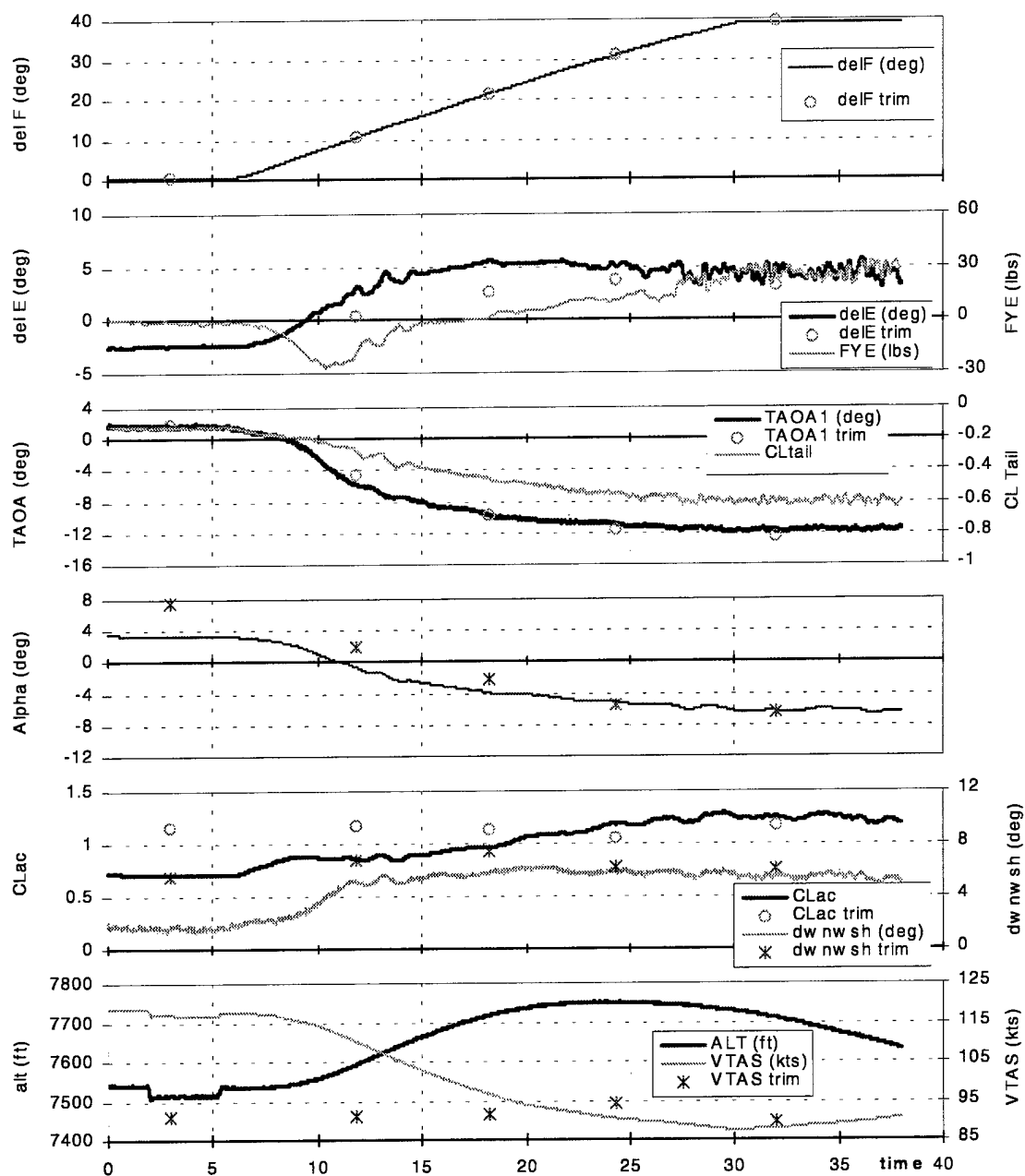
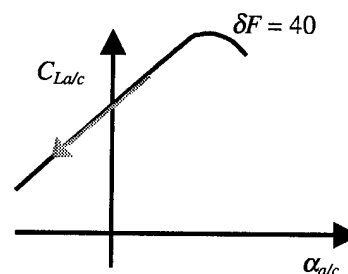


Figure 45. Flap transition; Failed Boot, VIAS = 80kts (VTAS = 91kts).

### 6.1.3 Speed Transition

The speed transition was a singular test point until the Guest Pilot Workshop. The original intent for this test point was to fly steady wings level with the Failed Boot ice shape at full flaps, moderate thrust  $C_T = 0.10$ , and  $V = 85\text{kts} = 1.5V_s$ , the highest target speed. The experience from the previous test point at  $V = 75\text{kts}$  had indicated this might be difficult. The pilot started from a lower speed ( $65\text{kts} = 1.2V_s$ ) and gradually brought the nose down to increase to the target speed. The graph to the right depicts the transition of aircraft lift coefficient during for this maneuver.



The data record was initiated at  $73\text{kts} = 1.4V_s$  because the tufts were indicating highly unsteady flow, see Figure 46. As the aircraft angle of attack decreased from  $-5.5^\circ$  to  $-7.5^\circ$  and the elevator deflected TED (gross trend from  $2^\circ$  to  $4^\circ$ ), the control yoke started to oscillate back and forth. As noted from the tuft video, this was associated with flow separation and reattachment beyond the hinge point. With increasing speed, the oscillation of the control forces grew rapidly. By the target speed, the force cycled between 0–50 lbf at a nominally 0.3 Hz cycle; the traces also show smaller oscillations on the order of 2 Hz. Note that the mean  $\alpha_i$  line remained unchanged throughout the entire maneuver. It is interesting to note that the  $\alpha_i$  features lead the  $\alpha_{a/c}$  features by about 1.4 sec. This suggests that the events at the tailplane are dominating the flight mechanics.

The events at the tailplane presented in Figure 47 demonstrate that indeed, the tailplane was going in and out of stall. Following the discussion outlined Section 5.3.3, two data points representing the extrema of one of these cycles were selected. These are depicted as circles in Figure 47(a); they are the local maximum at  $t = 26.07\text{s}$ , ( $\alpha_i = -11.4^\circ$ ,  $\delta E = 0.5^\circ$ ) and the local minimum at  $t = 28.41\text{s}$  ( $\alpha_i = -13.3^\circ$ ,  $\delta E = 6.3^\circ$ ). In Figure 47(b), these two points from the speed transition are graphed against the  $C_{l\_tail}$  vs.  $\alpha_i$  plot from the wind tunnel. The correction to the wind tunnel data refers to the standard 3-D correction.

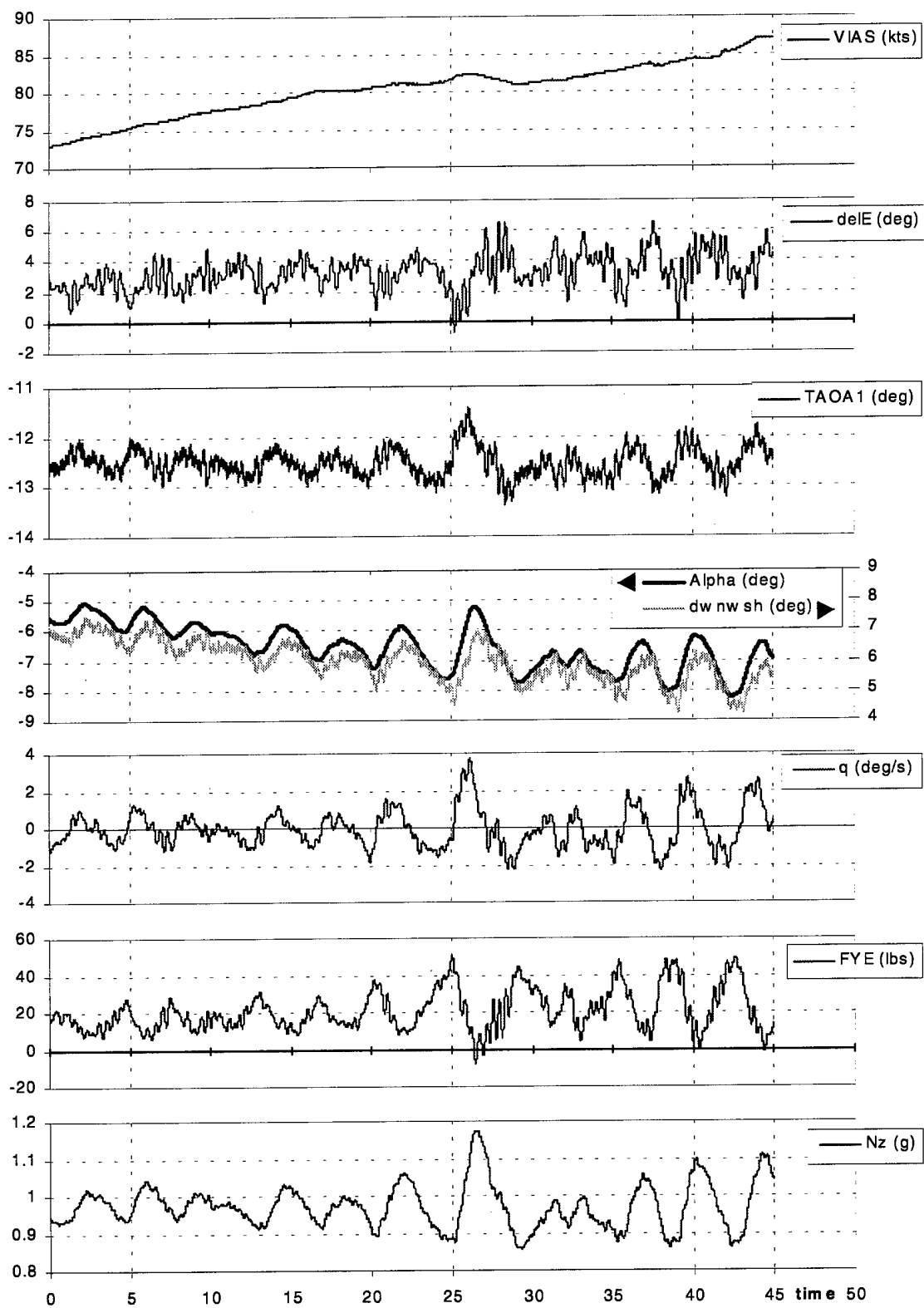


Figure 46. Speed transition time histories; Failed Boot at  $\delta F = 20^\circ$  and  $C_T = 0.1$ .

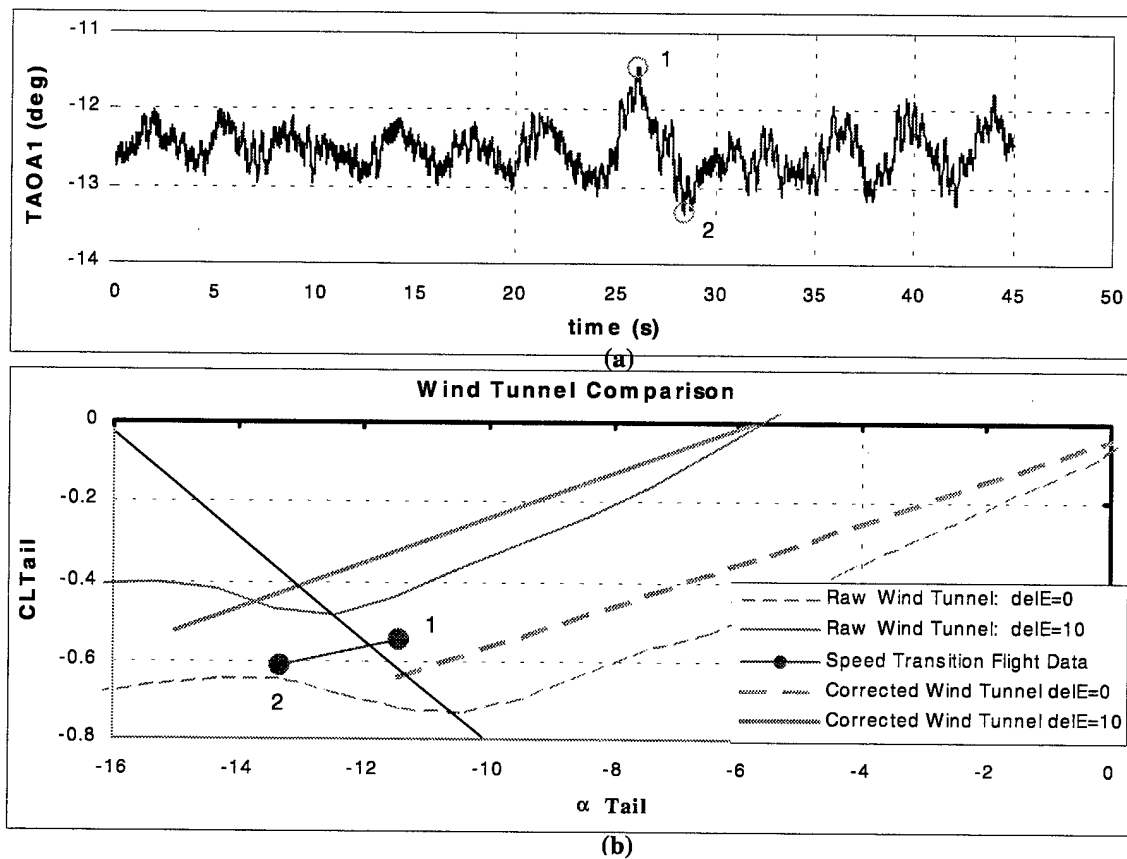


Figure 47. Detail of speed transition: (a)  $\alpha_t$  time history with two highlighted data points, and (b)  $CL_{Tail}$  vs.  $\alpha_t$ .

#### 6.1.4 Thrust Transition

The thrust transition was added in mid-program after the Twin Otter's sensitivity to thrust effects became apparent.

Description: The thrust was increased from idle to maximum continuous while the remainder of the parameter space was maintained. To maintain airspeed while increasing thrust, the pilot had to pitch the nose up. The thrust line for the Twin Otter is above the CG.

Configuration: This maneuver was flown with all ice shapes, flap deflections and speeds; except that the S&C shape was not flown beyond  $\delta F = 30^\circ$ .

Analysis: Because the thrust line is positioned above the CG, this maneuver challenged the horizontal stabilizer by increasing the download requirement at the tail. This maneuver also drives the elevator toward the common landing position – TEU. While the intent of the program was only to fly toward the stall angle, a full tail stall did occur during one execution of this maneuver. This stall event occurred for the Failed Boot ice shape at full flap deflection and maximum speed, 85kts = 1.5Vs. Figure 48 presents selected time histories as well as the probable stall point and the time at which thrust was reduced. Corrective actions – thrust to idle, yoke back and flaps up – were applied within 0.4 sec of stall, yet the aircraft lost a total of 300 ft in 8 sec and reached a (nose down) pitch angle of  $-37^\circ$ . The “kink” in both the  $\alpha$  and  $\alpha_i$  curves at 32.09 sec was identified to be the probable stall point. From the tuft video, there was a point where the last row of tufts ( $x/c = 0.95$ ) all pointed upstream. Prior to stall, the  $\alpha_i$  signal led the  $\alpha_{w/c}$  signal by about 0.7 sec.

During the recovery effort, note that even with considerable and increasing pull force, 75–100 lbs, the elevator continued to move TED. With the thrust reduced to idle and the flaps rising, the pilot was able to continue to pull, 100–172 lbs, to bring the elevator TEU. Eventually, according to the video, the flow reattached around 35 sec and the pitch over ended. Note that even though the pilot had regained control of the aircraft, the greatest altitude loss (200 ft) occurred between  $t = 35$ –37 sec because of the increased airspeed.

Select static pressure distributions are shown in Appendix D for various times. From these figures, the pressure distribution on the lower surface flat lined – indicating full separation – after 32.34 sec. Recall from Section 3.2 that the system response lag was estimated to be about 0.2 sec; this corresponds well with the stall point as identified by the kink in the  $\alpha$  and  $\alpha_i$  traces. The distribution remained flat until after 34.86 sec.

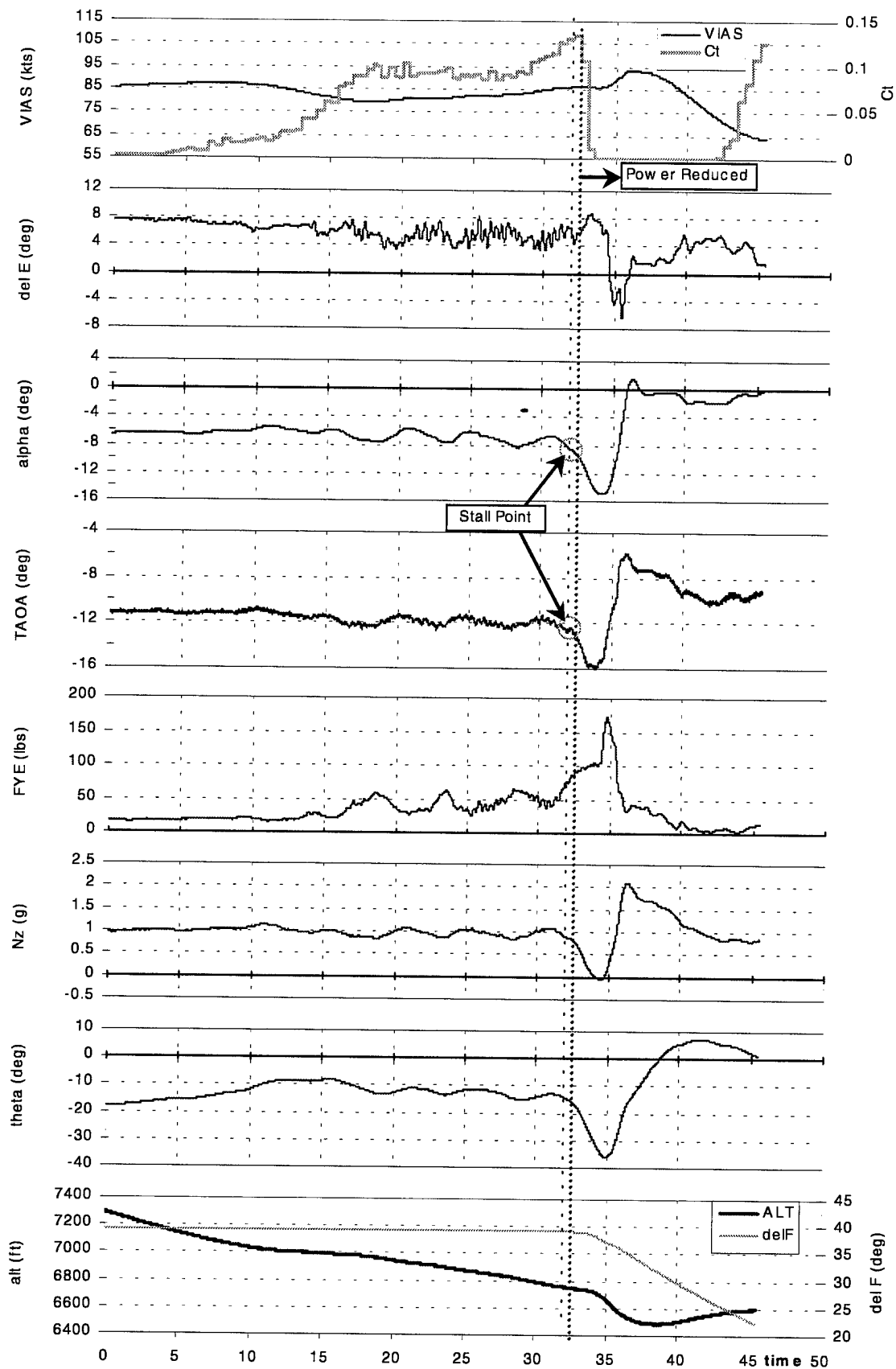


Figure 48. Thrust transition time histories; Failed Boot at  $\delta F = 40^\circ$  and  $V = 1.5V_s$ .

### Propwash Effect

The thrust transition maneuver is also an ideal method to investigate the effect of propwash on the horizontal stabilizer. The assumption is that if or when the flow from the propeller impacts the tailplane, increasing the thrust will identify the propwash impact. The output of the three 5-hole probes on the tailplane was compared to the output of the noseboom and the coefficient of thrust profile.

These comparisons were made primarily for the clean tail; an ice shape on the leading edge of the tailplane should have minimal effect on the propwash effect. However, a few of the observed trends were also checked against some of the ice shape results. The results show the same trend.

Figure A-1 details the aircraft probe locations with respect to the propeller. The outboard probe, probe #1, is aligned directly behind the hub of the propeller. The midspan probe, probe #2, is aligned behind the propeller tip, and the inboard probe, probe #3 is located upstream of the vortex generators on the horizontal stabilizer. The relative location between the horizontal stabilizer and wing is also identified.

There is a propwash effect in the span; it is a function of flap setting and airspeed. This effect was determined by plotting the three tail probe velocities in time along with the aircraft velocity and also noting the thrust increase. For the Twin Otter, the greatest effect occurred for  $\delta F = 10^\circ$ . Figure 49 presents a limited set of these results: the clean tail at different flap settings for nominally 1.2Vs. This set is representative of all the speeds flown with clean tail. This figure demonstrates that for  $\delta F = 10^\circ$ , the true airspeeds from the noseboom ( $VTAS \equiv Va/c$ ) and two inner probes ( $V_{probe2}$  & 3) are flat and parallel to each other. The outboard true airspeed ( $V_{probe1}$ ), however, climbs like the thrust ( $C_T$ ) profile. The calculations indicate a 30 knot increase in the outboard velocity over that of the noseboom:  $V_{probe1} = 120\text{kts}$ ,  $Va/c = 90\text{kts}$ . Note that the probes were calibrated to 120kts, and values were extrapolated above 100kts. Even though the numerical values should not be accepted with certainty, the trend is indisputable. Also, there is an acknowledged difference between  $VTAS$  and  $V_{probe}$  values beyond  $\delta F = 20^\circ$ . The  $V_{probe}$  values are believed to be nominally 10% greater than actual. This was found to be a result of calibration methodology.

Now the issue concerning the mechanism that drove the Twin Otter tailplane toward stall (see Figure 48) at large flap deflections and moderately high thrust settings can be resolved. The two competing hypotheses were these:

- (1) turbulence from the propeller impacted the horizontal tail, destabilized the boundary layer and caused separation, or
- (2) because the thrust line is above the CG, thrust addition increases the nose down pitching moment. To maintain airspeed, the tailplane had to provide more downward lift, *i.e.*, increase its camber by deflecting the elevator TEU.

Knowing that the propwash at  $\delta F = 40^\circ$  slips well below the tail eliminates the first explanation. The leading hypothesis, therefore, is the high thrust line. Ultimately, this should be verified with other aircraft. Until this issue is resolved fully, pilots of aircraft with thrust lines above the CG should be aware that adding thrust in a potential tail stall situation might only exacerbate the situation.

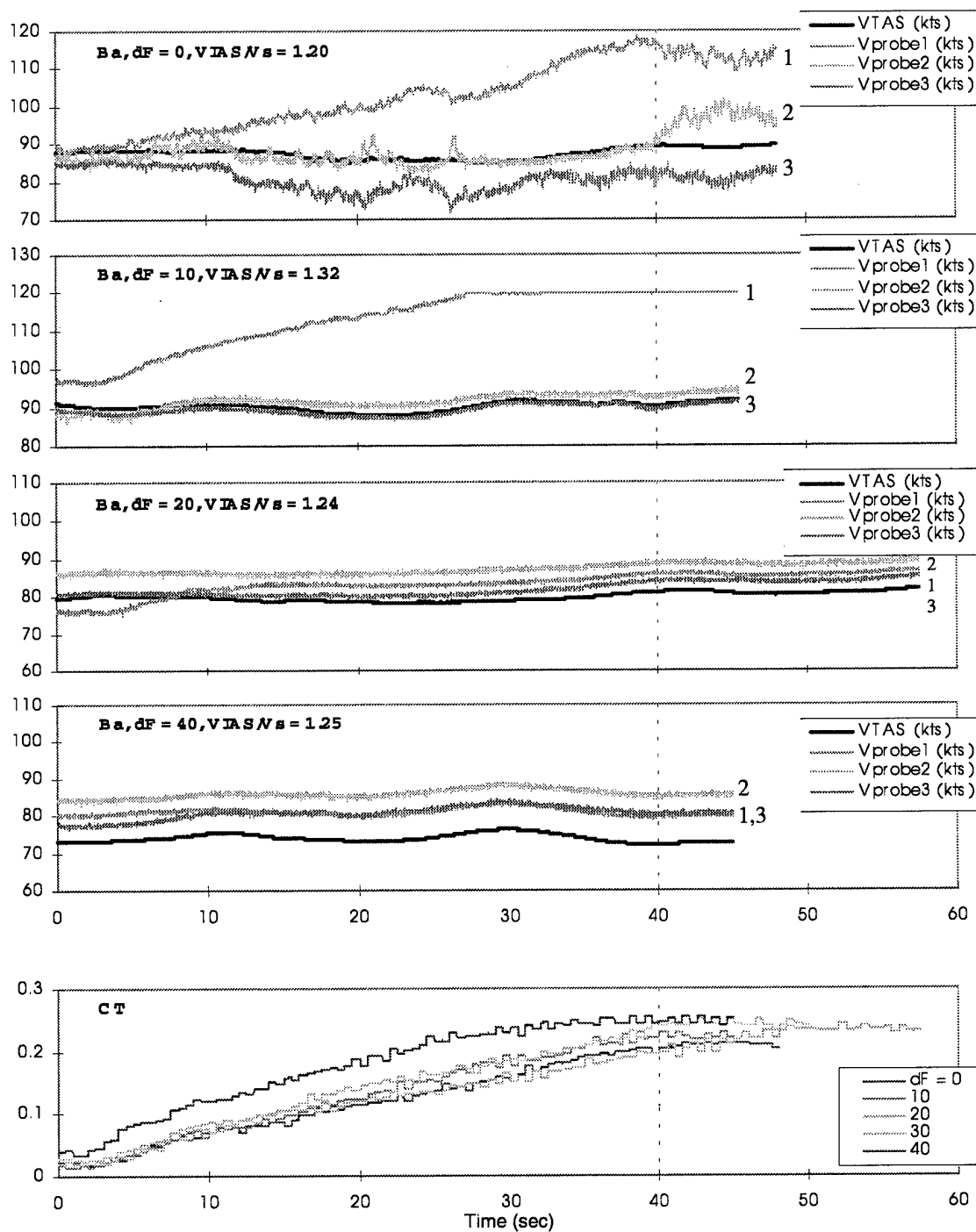


Figure 49. Propwash effect for a clean tail at different flap settings and constant speed,  $V = 1.25V_s$ .



### 6.1.5 Pushover

**Description:** The pushover was flown in a manner similar to that described in current aircraft certification programs. The aircraft was configured at the proper thrust and flap deflection, then trimmed at the target airspeed,  $V_{target}$ . The pitch angle,  $\theta_{target}$ , was noted. The task was to hit a specified pitch rate,  $q_{target}$ , (or G) at  $V_{target}$  and as the nose of the aircraft tracked through the horizon,  $\theta_{target}$ . (The pitch rate and vertical acceleration are coupled.) In order to achieve this from trim, the pilot first pushed forward on the column to gain speed, then pulled back on the column to raise the pitch angle prior to the pushover at  $V_{target}$ . Just prior to  $V_{target}$ , the control column was pushed forward to hit  $q_{target}$  at  $\theta_{target}$ . One such maneuver is called a parabola. For the Twin Otter, the parabolas typically lasted up to 20 sec with a maximum of five seconds at the minimum gravity. For this flight program, three parabolas were flown in a row during one test point.

**Configuration:** This maneuver was flown for all ice shapes and the full range of flap deflections and speeds with  $C_T = 0.10$ . However, because a control force reversal (CFR) was experienced at  $\delta F = 20^\circ$  for both the Failed Boot and S&C ice shapes, no pushovers were flown beyond that flap setting.

**Analysis:** The two extrema of a "pass" and a "fail" case will be discussed here. More examples can be found in Appendix C, which contains time histories of eight test points. In addition, and an example of a "shaped" maneuver and a trailing edge stall on a clean tailplane will be presented. Finally, the more advanced analysis techniques of co- and cross-plots will be introduced.

The pushover maneuver was designed to achieve high angles of attack at the tailplane dynamically. The tailplane angle of attack is given by Ref. 6.

$$\alpha_t = \alpha_{t0} + \Delta\alpha_t = [\alpha_w - \varepsilon - i_t] + \left[ \Delta\alpha_w \left( 1 - \frac{\partial \varepsilon}{\partial \alpha} \right) + \frac{ql_t}{V} \right],$$

where  $\alpha_{t0}$  is the trim (steady state) angle of attack and  $\Delta\alpha_t$  is the dynamic component. The change in wing angle of attack is denoted  $\Delta\alpha_w$ , and  $l_t$  is the distance from the CG to the tail center of lift. The  $(\partial \varepsilon / \partial \alpha)$  values vary from 0.4–0.7 as a function of  $\delta F$  for the Twin Otter. Therefore, the dynamic tailplane angle of attack may be increased primarily by increasing the pitch rate or reducing the speed. Moreover, high flap settings and high speed increase  $\alpha_{t0}$ .

For ease of discussion, it is prudent to define some terminology. Let a pushover maneuver where the values of  $\alpha_t$  are far from  $\alpha_{t\_stall}$ , be considered a "non-critical" pushover. Likewise, denote a case where the values of  $\alpha_t$  are close to  $\alpha_{t\_stall}$  as "critical". For a target pitch rate, the most non-critical pushover therefore occurs at zero flap deflection and high speed. Conversely, the most critical is with full flap deflection and at a low speed.

Figure 50 illustrates a limited set of the time histories for the most non-critical case with no ice. Note that this was the very first set of pushover maneuvers during this flight test series. The three pushovers were flown to increasing lower G; specifically, the task was to increase the target  $q$ :  $q_{target} = -5$  deg/s,  $-10$  deg/s and required  $q$  to achieve 0G. The pitch rate mimicked the vertical acceleration, albeit not perfectly. The target speed was  $VIAS = 1.5V_s = 100$  kts. In all cases, the pilot accurately hit  $q_{target}$  (or  $N_z$ ) at the  $\theta_{target} \cong -1^\circ$  but under flew the speed.\* The most negative  $\alpha_t$  was  $-6^\circ$ , far from stall, and the most negative  $C_{l\_Tail}$  was  $-0.3$ .

Note that in Figure 50, both  $\delta E$  &  $FYE$  and  $\delta E$  &  $q$  are co-plotted on the same graph. Co-plots of certain parameters are perhaps the best and most immediate way to interpret dynamic data. For example, a co-plot of  $\delta E$  &  $FYE$  immediately indicates whether or not a CFR has occurred. There are two inputs to the force measured at the yoke: (1) the pilot input and (2) the pressure-field around the elevator. If the elevator is fixed TED, yet the control force crosses the trim point, then it must be due solely to changes in the pressure field, and a CFR has been experienced. For this non-critical case, the push force remained fairly flat during the maneuver. Similarly, from a  $\delta E$  &  $q$  co-plot one can see whether the pitch rate response is damped or undamped. In this case, the response is damped; the most negative  $q$  peaked shortly after the elevator is deflected and then self-restores.

\* In subsequent test points, the information to the pilot was improved, and the target velocity was better met.

A critical pushover is depicted in Figure 51. With the Failed Boot ice shape at  $\delta F = 20^\circ$ , the target was to hit  $N_z = 0G$  at  $V = 55\text{kts} = 1.06Vs$ . While the pilot hit  $V_{target}$  at  $\theta_{target} \cong -5^\circ$  fairly well, the minimum  $N_z$  occurred only for a much steeper pitch angle,  $\theta \approx -30^\circ$ . For this configuration, the most negative  $\alpha_i$  was  $-14^\circ$ . The most negative  $C_{L-Tail}$  was  $-0.9$ ; the instability evidenced between  $t = 51\text{--}53$  sec suggests stall. This is confirmed by the tuft video. Also observe that the yoke force ( $FYE$ ) started to lighten as soon as the elevator was pushed TED. Indeed, during this maneuver, full control force reversals (CFR) were experienced. In fact, the control force crossed neutral at  $t = 17.6, 34.0$  and  $47.5$  sec while the elevator was fixed forward ( $\delta E \approx 10^\circ$ ). The  $\delta E$  &  $q$  co-plot also clearly indicated an undamped response; the decrease in pitch rate only ceased when the elevator was returned TEU.

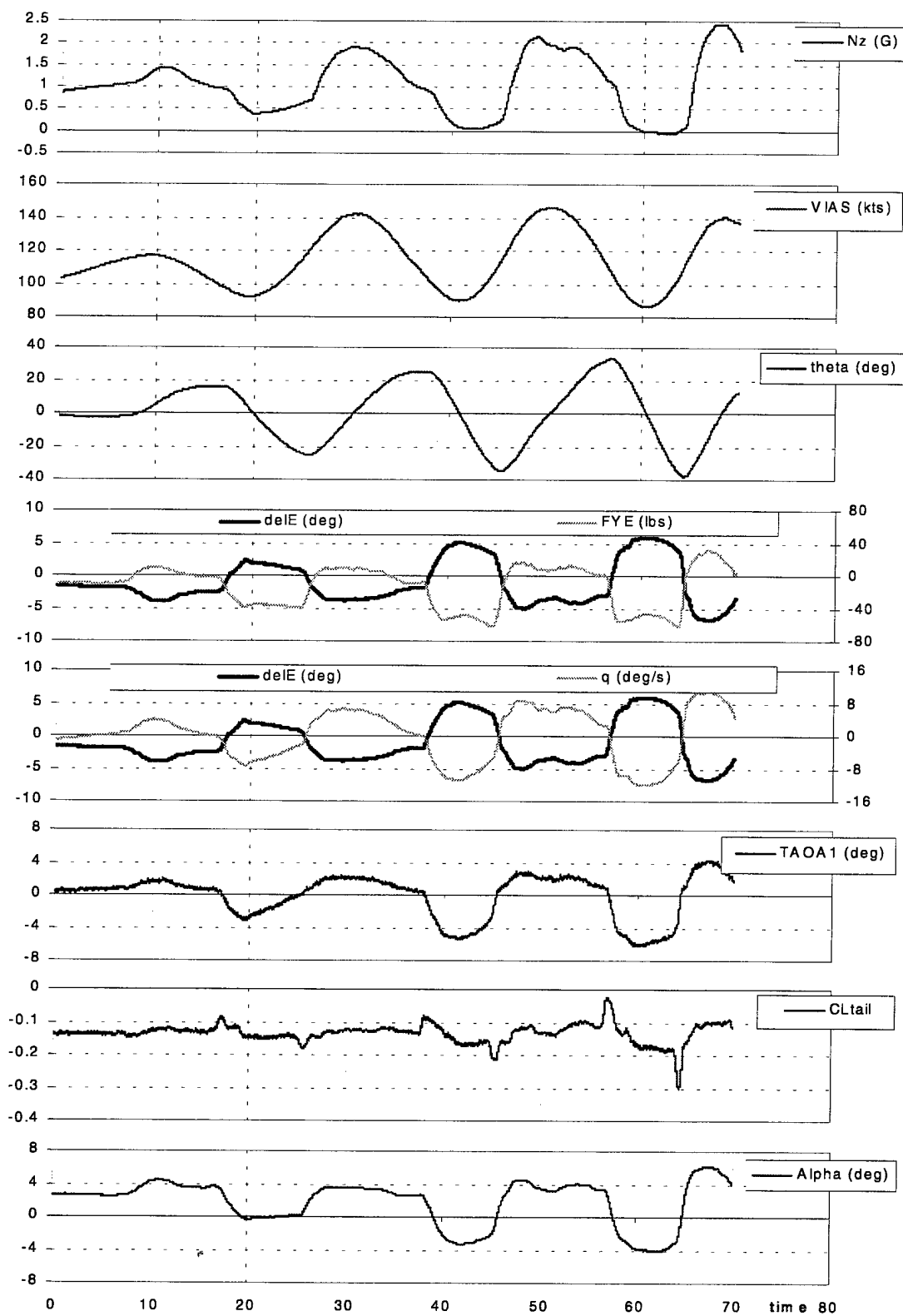


Figure 50. Non-critical pushover time histories: clean tail,  $\delta F = 0^\circ$  and  $V = 1.5V_s = 100$  kts.

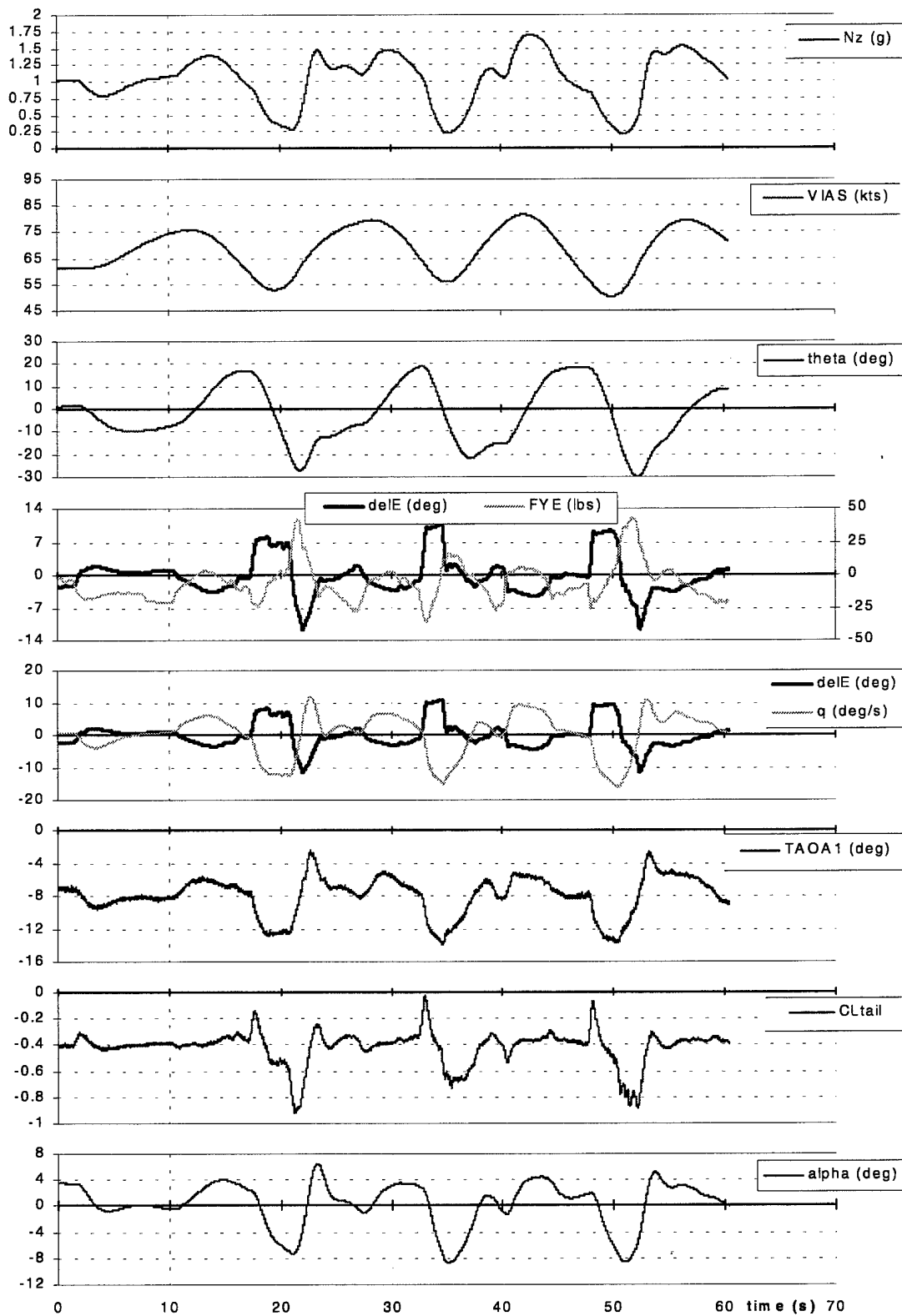


Figure 51. Critical pushover time histories: Failed Boot ice shape,  $\delta F = 20^\circ$  and  $V = 1.06V_s = 55\text{kts}$ .

### Shaped Maneuver

Figure 52 illustrates how a maneuver may be “shaped” to pass the no CFR criteria. At 18 sec, an adjustment of the elevator is sufficient to reattach the flow and cause the force to remain on the push side. The other two maneuvers show definite lightening and indicate a CFR.

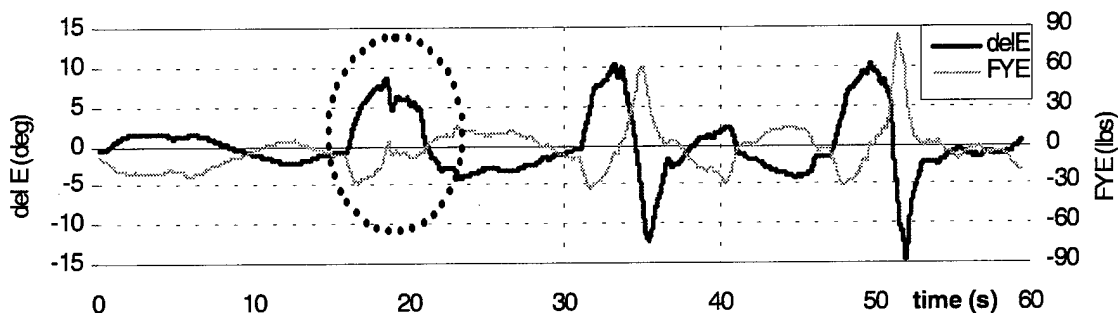
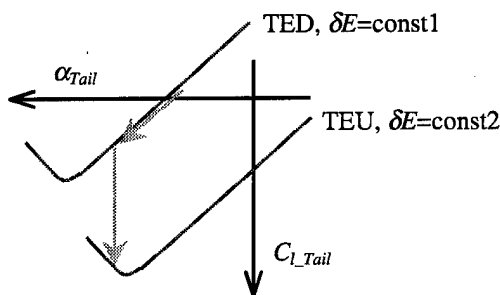


Figure 52. Example of elevator shaping during pushover maneuver.

### Trailing Edge Stall

The pushover maneuver has an additional challenge. During the pull up, the elevator deflects TEU suddenly. Cambering the tail increases the download capacity, but toward a reduced stall margin (see inset figure). If the tailplane were close to the stall margin, the rapid cambering might push  $\alpha_t$  through the stall point. Evidence of this is presented from the 1995 flight campaign. An extreme Baseline case of full flaps,  $\delta F = 40^\circ$ , low speed,  $VIAS = 50\text{kts} = 0.94V_s$  and high thrust,  $C_T = 0.23$ , is depicted in Figure 53. Note that this test point was flown near maximum thrust, not an insignificant factor for the Twin Otter. The trim condition is established for the first 12 sec. It should be noted that the pilot was actually pulling 30 lbs at this trim point because the trim tab had run out of authority (see Section 5.3.4); in the plot, this offset has been subtracted ( $FYE - FYE0$ ). The pilot then pushed the yoke forward to dive and gain speed. The pitch over portion was initiated at  $t = 27.5$  sec with the elevator push TED. The elevator is returned TEU at  $t = 30$  sec. The control force lightened, but clearly did not reverse. [The FYE data were clipped above a certain value, unfortunately.] In spite of the pull-up, however,  $N_z$  continued to decrease and reached its minimum at 31 sec. Moreover, the aircraft continued to gain speed and pitched over to  $\theta = -28^\circ$ . Examination of the pressure belt data indicates that immediately after the elevator was pulled TEU, the tailplane experienced a full stall starting from the trailing edge. **What is important to note here is that this pushover would have passed the CFR criterion, yet the tailplane had stalled.** There are more advanced techniques, however, that can identify tailplane stall. They are introduced next.



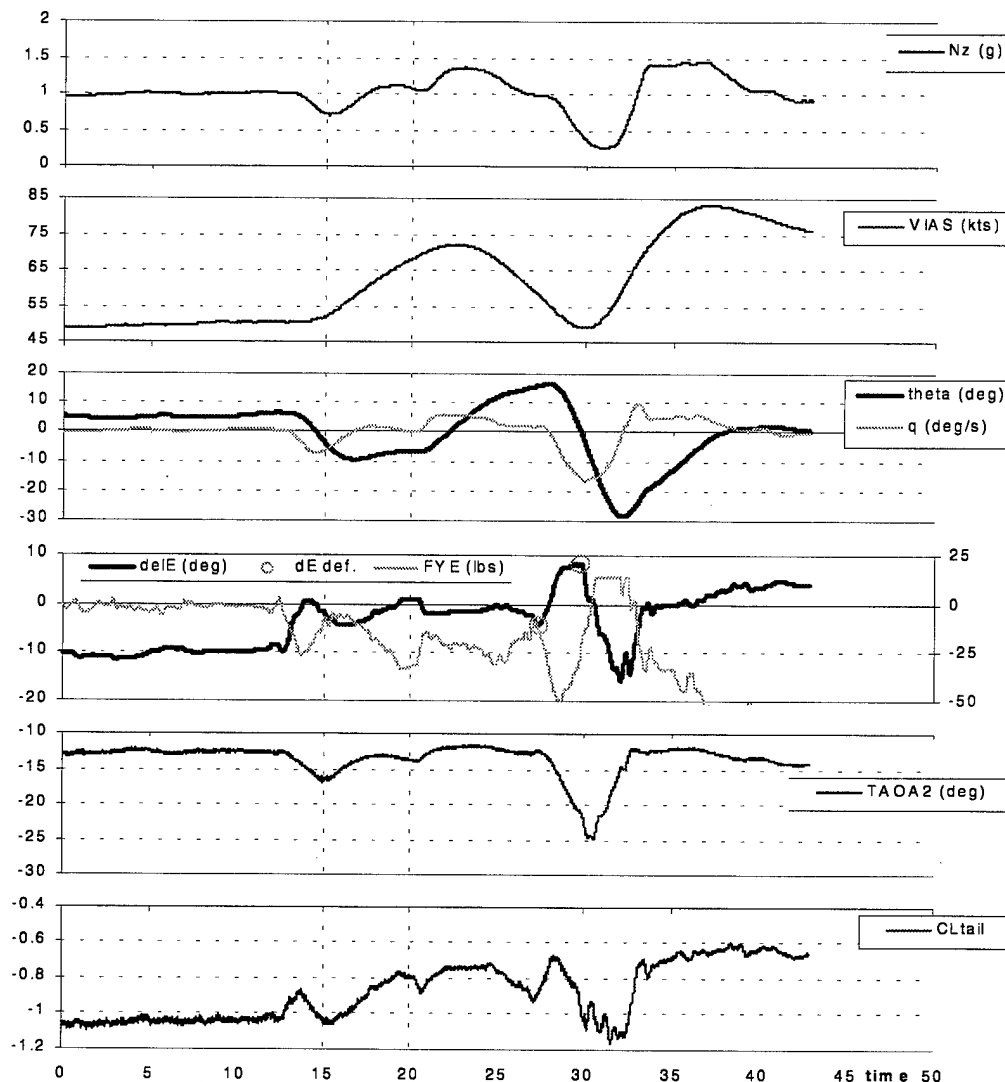


Figure 53. Example of a trailing edge tail stall. Baseline,  $\delta F = 40^\circ$ ,  $V = 0.94V_s = 50\text{kts}$ ,  $C_T = 0.23$ .

#### Advanced Analysis Methods

To examine some of the more advanced analysis techniques, the example of increasing flap deflection will be used. Three pushover test points, all with the Failed Boot ice shape and achieved conditions of  $N_z = 0G$  and  $VTAS = 80\text{kts}$  were flown with three flap deflections,  $\delta F = 0^\circ$ ,  $10^\circ$  and  $20^\circ$ . This advanced analysis will revisit some co-plots and introduce some cross-plots.

Figure 54 depicts the  $\delta E$  &  $FYE$  time histories for the three flap deflections. Note in particular the push and hold portions where the elevator went TED ( $\delta E$  increased). This occurred at the following times: for  $\delta F = 0^\circ$ ; 2–5, 22–25, and 42–45 sec; for  $\delta F = 10^\circ$ ; 14–17, 25–28 and 37–40 sec, and for  $\delta F = 20^\circ$ ; 22–24, 43–45 and 67–69 sec. One can see that as the elevator was pushed forward, the control force remained a nominally constant push (–40 lbs) for  $\delta F = 0^\circ$ , lightened to a point for  $\delta F = 10^\circ$ , and reversed, or crossed the neutral axis, for  $\delta F = 20^\circ$ . [The circles appearing in Figure 54 are for reference in Figure 57.] The  $\delta E$  &  $q$  time histories appear in Figure 55. One can see the pitch response is strongly damped for  $\delta F = 0^\circ$ , weakly damped for  $10^\circ$ , and undamped for  $20^\circ$ .

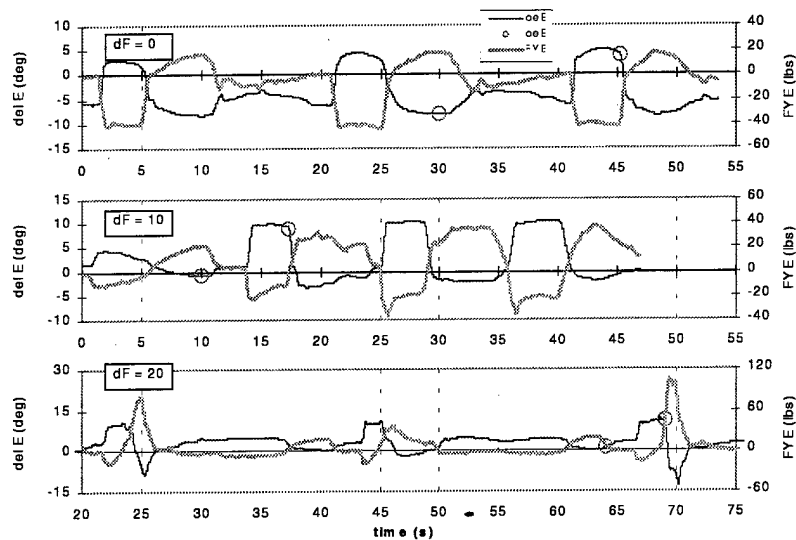


Figure 54. Co-plots of  $\delta E$  and  $FYE$  for pushover. Failed Boot,  $VTAS = 80\text{kts}$ , increasing flap deflection.

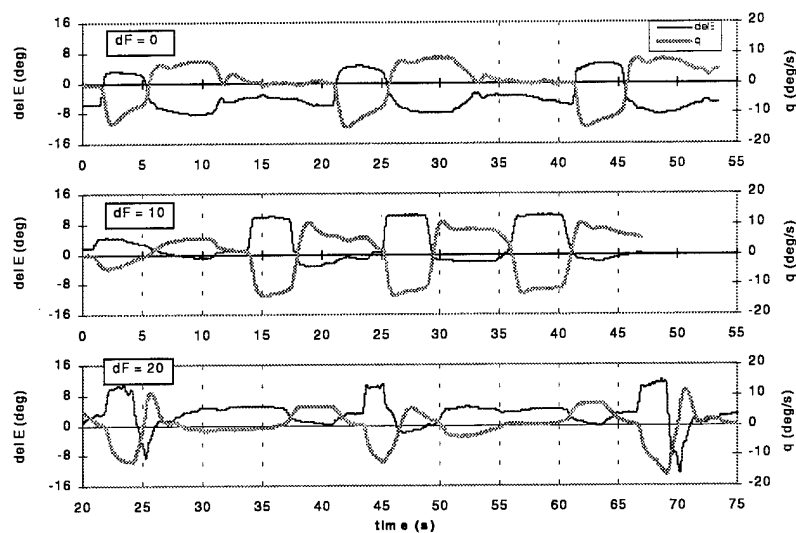


Figure 55. Co-plots of  $\delta E$  and  $q$  for pushover. Same data base as in Figure 54.

Perhaps a more elegant presentation of these data is via the cross-plot. The question posed is whether or not there is a distinct footprint in these cross-plots which would indicate problems. Before continuing with the effect of flap deflection on a contaminated leading edge, a well-behaved non-critical pushover is examined first. A set of cross-plots for the Baseline case at  $\delta F = 0^\circ$  and  $V = 1.5V_s = 100\text{kts}$  is presented in Figure 56. Time histories of these data are depicted in Figure 50; the particular pushover examined occurs between  $t = 53\text{--}68$  sec. Note, for this well-behaved case, the character of these cross-plots, both the  $q$  vs.  $\delta E$  and  $FYE$  vs.  $\delta E$ , exhibit nearly flat straight lines.

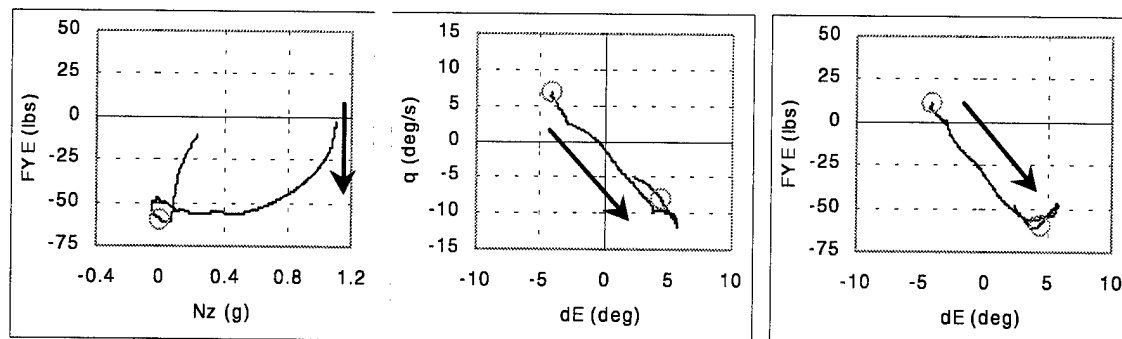


Figure 56. Cross-plots for Baseline case at  $\delta F = 0^\circ$  and  $V = 1.5V_s$ .

Now let us return to Failed Boot data presented in Figure 54 through Figure 55. Figure 57 displays the three corresponding cross-plots of a single pushover – those identified by the circles in Figure 54. The  $\delta F = 0^\circ$  case appears in the top row,  $\delta F = 10^\circ$  in the middle and  $\delta F = 20^\circ$  in the bottom row. Like any phase plot, the temporal information is lost. However, the circles, which correspond to the circles found on the  $\delta E$  &  $FYE$  co-plots from Figure 54, give some indication of events. The first circle marks the beginning of the maneuver – the maximum  $N_z$ . After this point, the elevator is pushed TED and the OG portion of the pushover begins. The second circle marks the point where the elevator is returned or pulled TEU. The arrows indicate the path from the first to the second circle. [Note that for the  $FYE$  vs.  $N_z$  cross-plot, only the push portion is indicated; only the second circle is included in these plots.]

Some of the interesting features of each cross-plot are discussed next.

**$FYE$  vs.  $N_z$  :** Data in this format have been presented by Ref. 14, and is used within the community fairly extensively. One key feature of this graph is to note on which side of the axis the elevator is returned. A circle in the upper half of the graph indicates a CFR. By noting the trend after the elevator is returned, one can also check for a stalled condition. If, after crossing the trim force, the data trend continues to the left, then the aircraft has not responded to the elevator TEU command. A plot of  $FYE$  vs.  $q$  yields similar information.

**$q$  vs.  $\delta E$  :** This graph highlights the pitch response to the elevator deflection. Of most interest is the lower right hand quadrant where the elevator is returned. For  $\delta F = 0^\circ$ , the short period is evidenced by the overshoot in  $q$  while  $\delta E$  is still moving TED. When the elevator is returned,  $q$  responds immediately. For  $\delta F = 10^\circ$ , the short period response is still evident, albeit much diminished. For  $\delta F = 20^\circ$ , on the other hand, the elevator traveled over  $10^\circ$  before any appreciable decrease in the magnitude of  $q$  was noted.

**$FYE$  vs.  $\delta E$  :** This cross-plot is an easy check of CFR. If, as the elevator returns across the trim force, the slope of the line is positive, then a CFR is indicated.



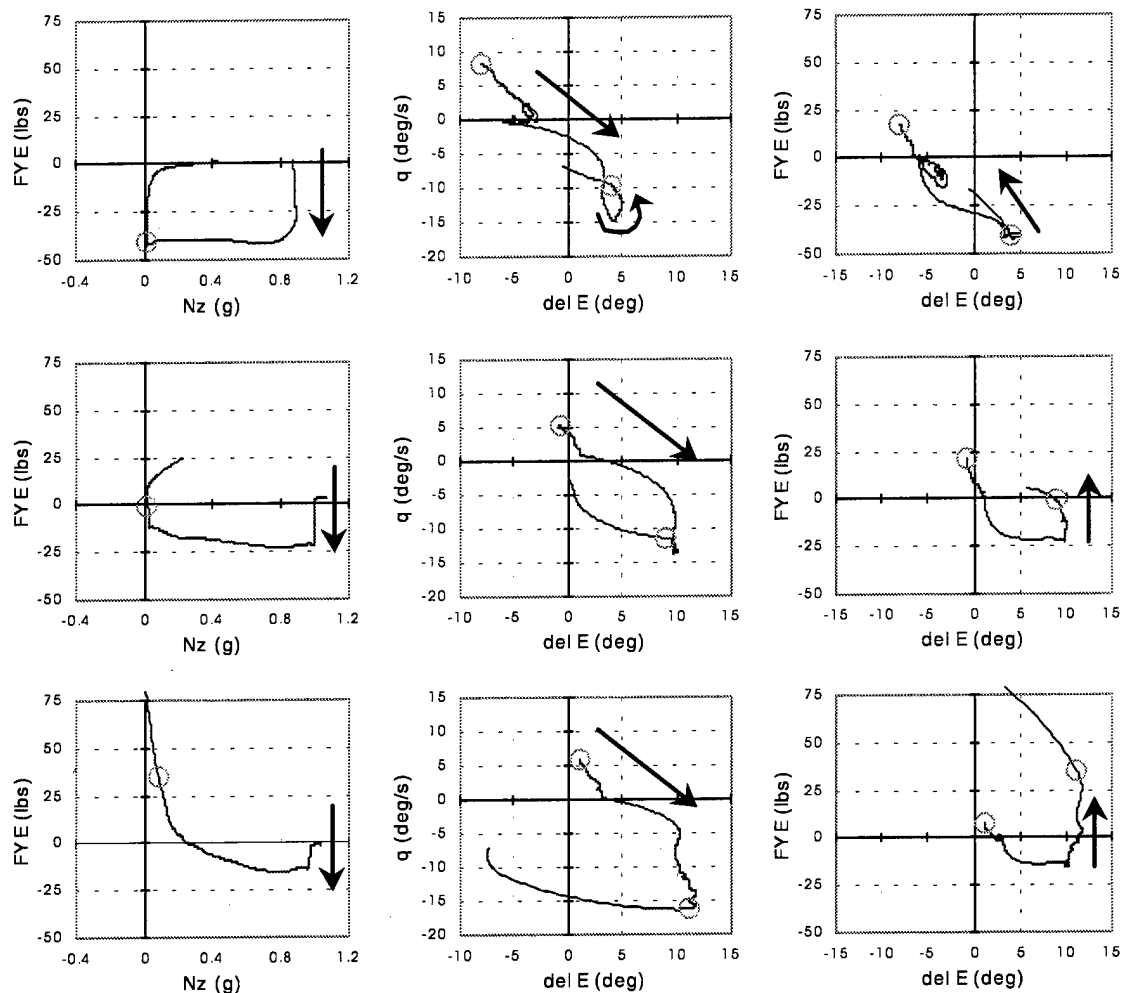


Figure 57. Cross-plots for same database as Figure 54. Top row is  $\delta F = 0^\circ$ , middle  $10^\circ$  and bottom  $20^\circ$ .

Recall the earlier discussion that the CFR criterion was inadequate for warning against a trailing edge stall. Figure 58 illustrates the  $FYE$  vs.  $N_z$  and  $q$  vs.  $\delta E$  cross-plots corresponding to the data set presented in Figure 53. From the  $FYE$  vs.  $N_z$  cross-plot, the elevator was clearly returned TEU prior to CFR; however, the subsequent negative slope of the line indicates that the aircraft did not respond immediately. The lower right-hand quadrant (indicated with the dashed box) of the  $q$  vs.  $\delta E$  cross-plot immediately indicates a lack of pitch response.

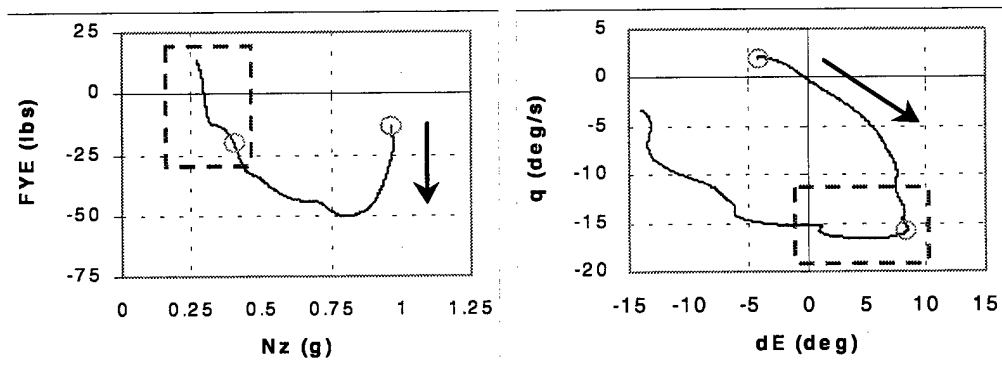


Figure 58. Cross-plots corresponding to data in Figure 53, the trailing edge stall pushover case.

### 6.1.6 Elevator Doublet

Elevator doublets demonstrate the effect of tailplane ice on the longitudinal stability and control. This maneuver is typically associated with a parameter estimation study. The discussion contained herein introduces the maneuver and discusses some of the aspects and features as related to pitch rate characteristics. Section 7 discusses the parameter estimation analysis.

**Description:** This maneuver consisted of a series of elevator inputs initiated from straight and level flight. The aircraft was trimmed for the target flap deflection, speed and thrust. One series of negative and positive deflections was made immediately followed by a second series whose amplitude was heightened and period shortened.

**Configuration:** All ice shapes, flap deflections, and speeds were flown. For the majority of cases, the moderate thrust setting of  $C_T = 0.10$  (0.05 per engine) was chosen; however, a higher setting of  $C_T = 0.18$  was also flown for a very limited number of test points. For the Failed Boot and S&C ice shapes, elevator doublets were not flown beyond  $\delta F = 30^\circ$ . Recall the corresponding pushovers were limited to  $\delta F = 20^\circ$ .

**Analysis:** The elevator doublet is directly compared to the pushovers previously shown. Figure 59 depicts an elevator doublet for the same aircraft configuration and flight condition (Baseline,  $\delta F = 0^\circ$ ,  $V = 1.5Vs$ ) as the pushover in Figure 50. Likewise, the elevator doublet presented in Figure 60 is similar to that of the pushover in Figure 51, Failed Boot shape at  $\delta F = 20^\circ$  and  $V = 1.06Vs$ . Perhaps the most direct comparison is between the second push and elevator TED portion of the elevator doublet to the push and elevator TED portion of the pushover. Finally, the most critical elevator doublet is examined in Figure 61. Recall that for steady level flight, the most negative  $\alpha_i$  occurs for a high flap setting and high speed. Appendix C contains additional elevator doublet data.

As the  $\delta E$  vs.  $FYE$  is the key relationship for the pushover,  $\delta E$  vs.  $q$  is key for the elevator doublet. The primary question concerns whether the pitch response is damped or if it continues to increase after the elevator has been frozen. As an illustration of a damped response, examine  $q$  and  $\delta E$  for the second "push and hold" portion of the elevator doublet depicted between  $t = 7-9$  sec in Figure 59. While the elevator was fixed at  $\delta E = 0.5^\circ$ , the  $q$ -magnitude increased ( $q$  decreased), peaked and receded. This peak occurred when the short period was excited. The  $q$ -magnitude then lessened because the pitch response was damped. An example of an undamped response is provided by all four of the responses in Figure 60. Again, focussing on the last push between 7-8 sec, one sees that the  $q$ -magnitude increases continuously the whole time the elevator is fixed TED at  $\delta E = -1^\circ$ . Only when the pilot returned the elevator to neutral did the  $q$  magnitude decrease.

For the non-critical case of Figure 59, the control force was flat and the pitch response damped. The minimum  $\alpha_i$  was  $-1.8^\circ$ , and the minimum  $C_{l\_Tail}$  was  $-0.4$ . Similar to the corresponding pushover, this elevator doublet clearly passed all tests. For the more critical case in Figure 60, the control force lightened and came very close to reversing on the last elevator push ( $t = 7.75$  sec). In addition, the pitch response is clearly undamped. The most negative  $\alpha_i = -7.5$  and  $C_{l\_Tail} = -0.7$ .

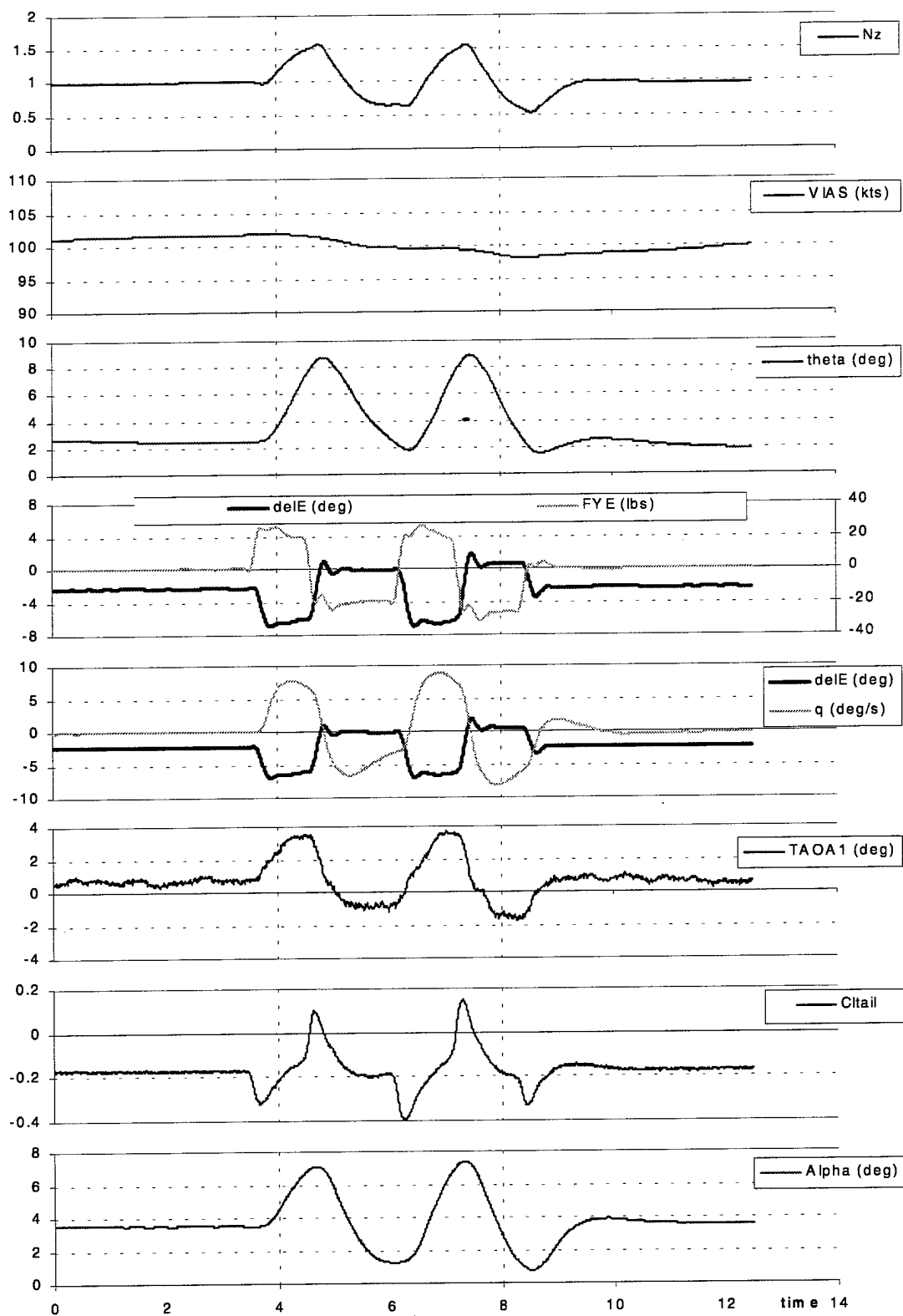


Figure 59. Elevator doublet for a clean tail,  $\delta F = 0^\circ$ ,  $V = 1.5V_s = 100\text{kts}$ .

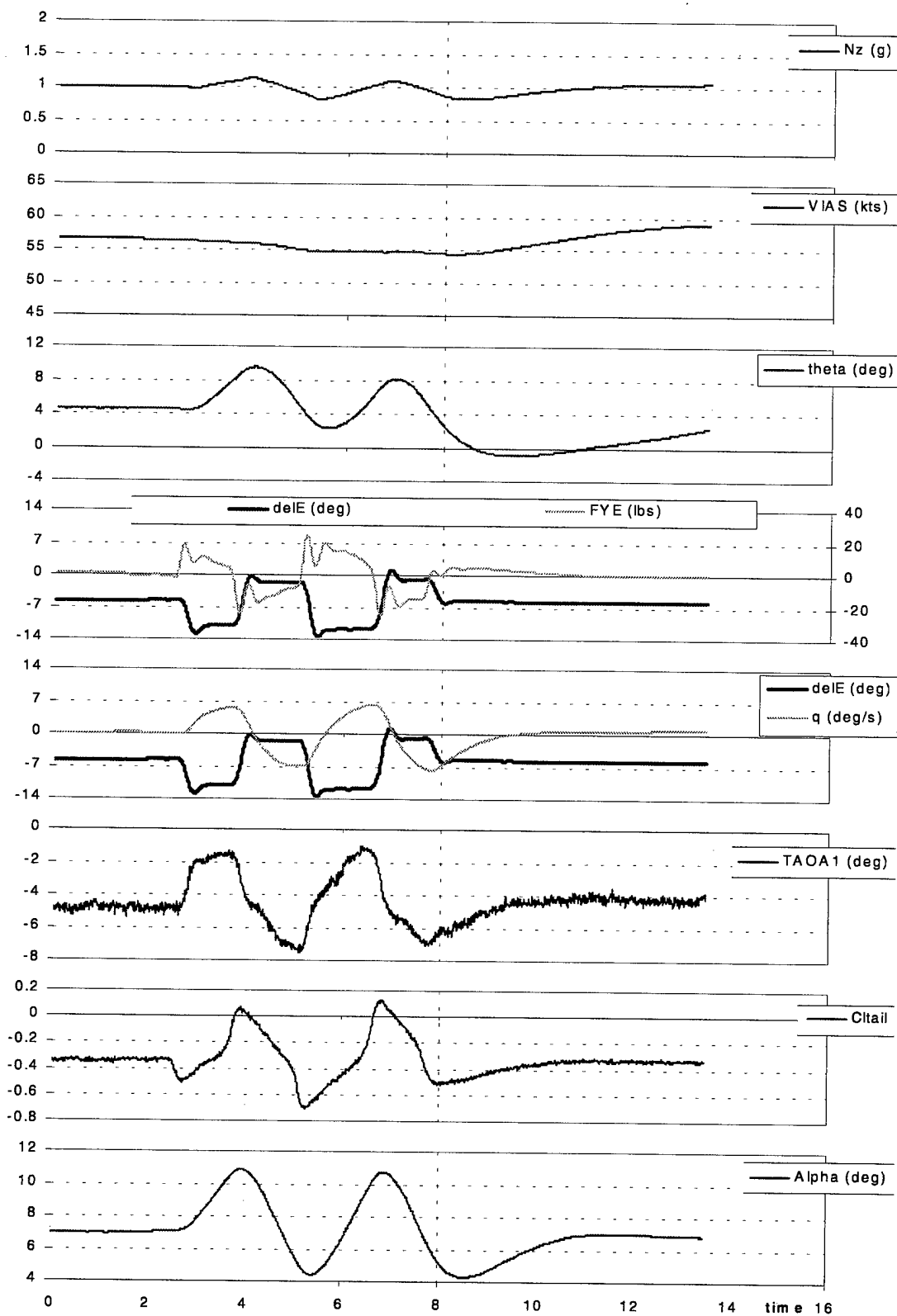


Figure 60. Elevator doublet for the Failed Boot,  $\delta F = 20^\circ$ ,  $V = 1.1V_S = 55 \text{ kts}$ .

The previous discussion allowed for a direct comparison of plots between the pushover and elevator doublet given an aircraft configuration. This comparison is discussed in Section 6.2. Now the  $q$  vs.  $\delta E$  co-plots and some corresponding cross-plots will be compared for the extremes of the elevator doublet parameter space. The time histories of these are depicted in Figure 61 for a clean and an iced shape. The Baseline configuration is compared to the worst-case ice shape, S&C, at flap deflections of zero and maximum flap deflection flown for the S&C ice shape,  $30^\circ$ . The speeds were nominally  $1.6Vs$ . Several items stand out from these plots. One is the relative similarity between three of the corners and the drastic difference for the worst case – S&C,  $\delta F = 30^\circ$ . Note for both Baseline cases and the S&C  $\delta F = 0^\circ$  cases that the pitch response is damped. In all cases the pitch response relaxes more on the nose down portion ( $\delta E$  moving positive or TED). For the S&C ice shape at  $\delta F = 30^\circ$ , however, the pitch response is undamped. The aircraft continues to increase its pitch rate magnitude until the elevator position is changed. The fluctuations of the  $\delta E$  plot indicate the difficulty in holding the elevator still. This is due to the unsteadiness of the separation bubble washing back and forth over the hinge point. Another thing to note is the elevator deflection at trim for the different ice shapes. For  $\delta F = 0^\circ$ , the elevator deflection is nominally the same,  $\delta E = -2.5^\circ$ , regardless of ice shape. For  $\delta F = 30^\circ$ , however,  $\delta E$  rises from  $7^\circ$  for the Baseline to  $-1^\circ$  for the S&C ice shape. The ice shape has caused an  $8^\circ$  loss of elevator authority.

Cross-plots are presented in the next two figures. As with the pushover data, the circles in Figure 61 denote the portion of time being cross-plotted. Note that for the elevator doublet, the first circle occurs with the elevator deflecting TED, not with the maximum  $N_z$ , as was the case for the pushover maneuver. Both Figure 62 and Figure 63 bring out some features that are not as easily picked up from the time history co-plots. For example, both the Baseline at  $\delta F = 30^\circ$  and S&C ice shape at  $\delta F = 0^\circ$  cross-plots indicate that the final push portion is only weakly damped.

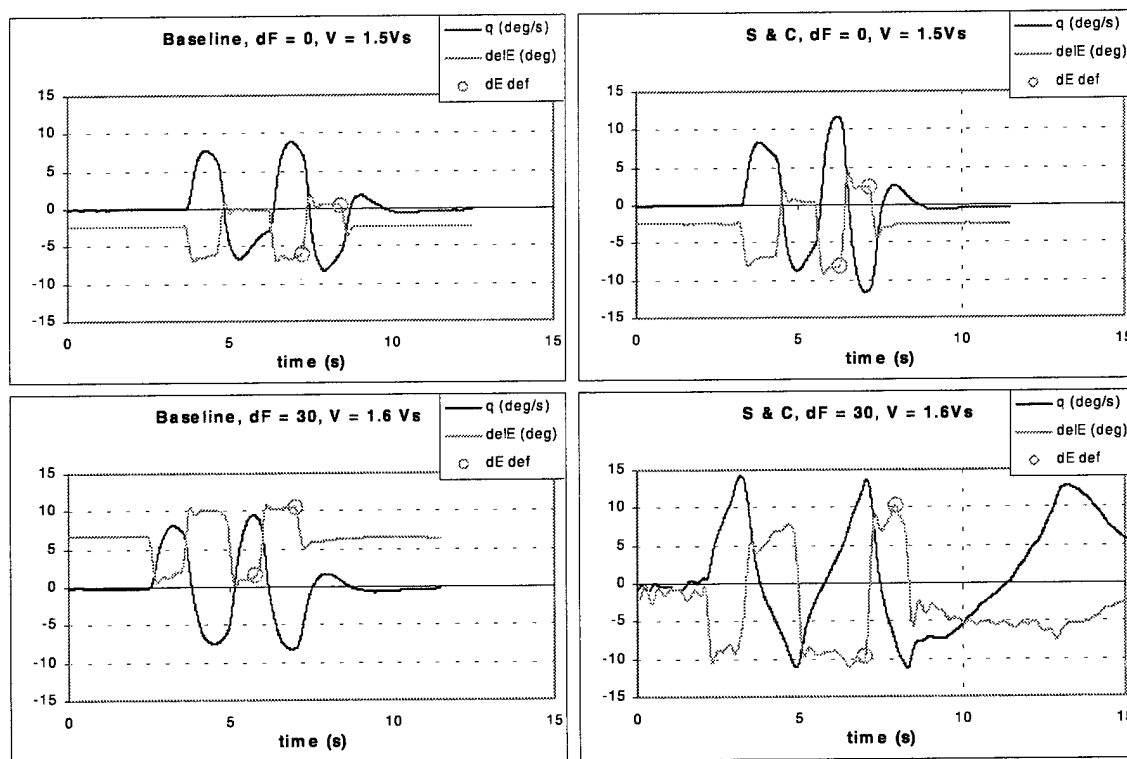


Figure 61. Pitch response and damping characteristics for extreme elevator doublet cases.

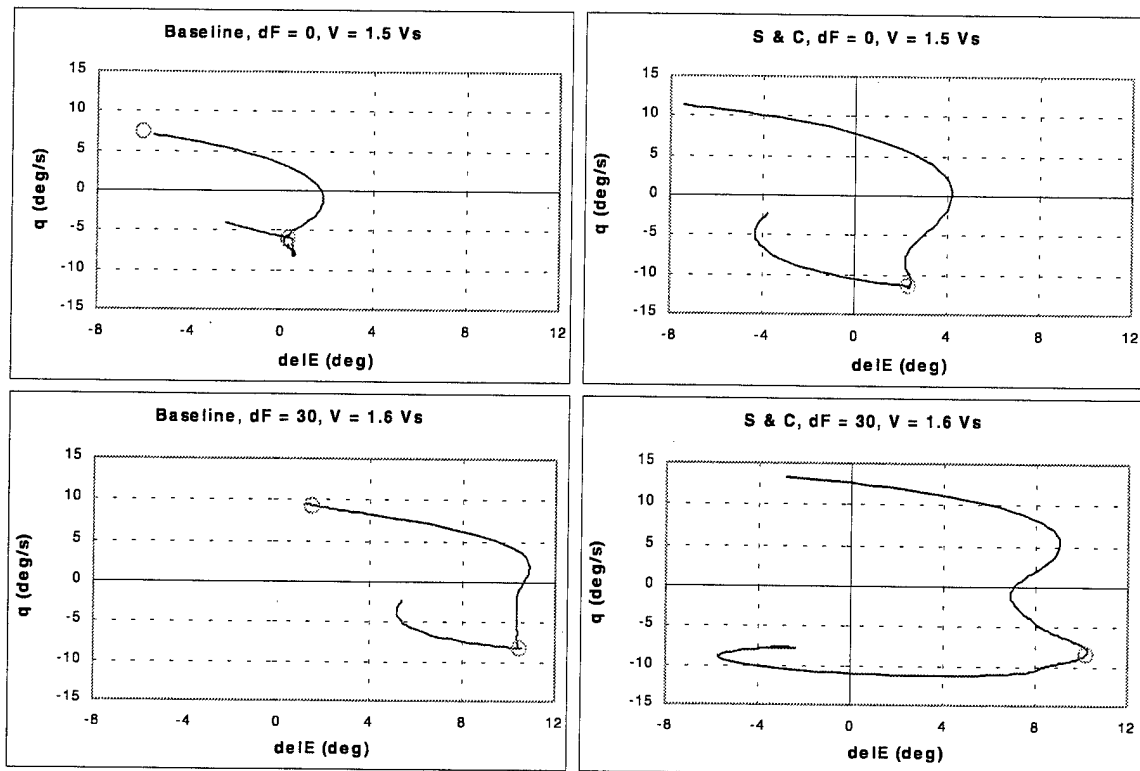


Figure 62. Cross-plots of  $q$  vs.  $\delta E$  for elevator doublet data from Figure 61.

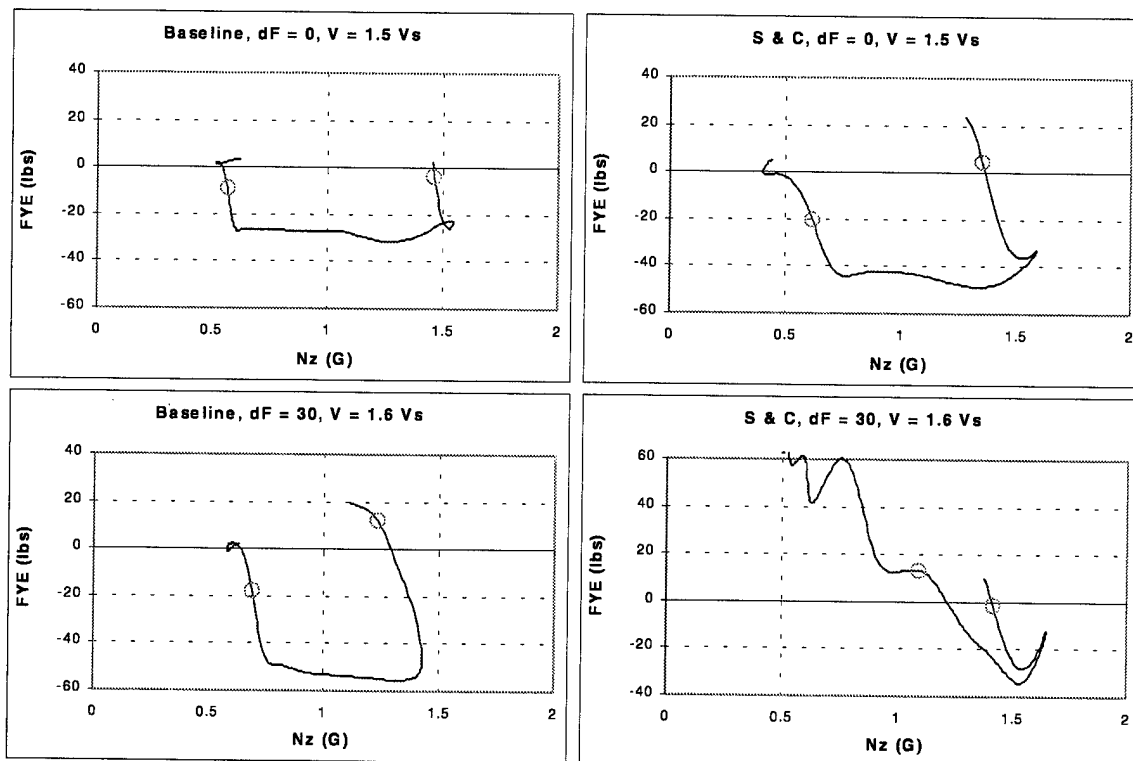


Figure 63. Cross-plots of  $N_z$  vs.  $FYE$  for elevator doublet data from Figure 61.

### 6.1.7 Balked Landing

This maneuver was born from the debriefing discussion during the first sequence of the Guest Pilot Workshop with the FAA and Transport Canada pilots (see Section 8). The question was raised concerning the distinction between stability and controllability, and its relationship to a typical piloting task. Thus, a closed-loop task was constructed to determine safe flight characteristics and controllability margins with an ice-contaminated tailplane.

**Description:** The balked landing maneuver consisted of a simulated instrument approach and go-around. This maneuver was flown at altitude and with "heads down." To simulate course and glide slope corrections, commands to change both rate of decent (ROD) and heading were made every 20 sec all the while maintaining a constant  $1.3V_s$  velocity. Specifically, heading changes of  $\pm 5^\circ$  off a reference heading, and RODs of  $-500 \pm 500$  fpm were ordered. The RODs required the pilot to adjust the thrust requirements. The idealized flight path appears as the dashed line in Figure 64. The 20 sec intervals required the pilot to make fairly aggressive control and thrust inputs. At the conclusion of the approach portion of the task, a go-around was commanded. Unlike the maneuvers discussed previously (open loop), the ability to determine whether or not the pilot actually met the targets closed the task loop.

**Configuration:** This maneuver was only flown with the Failed Boot ice shape with flaps set to  $\delta F = 10^\circ$ ,  $20^\circ$  and  $30^\circ$ . Test points were conducted with  $V = 1.3V_s$  and thrust set as required ( $C_T = 0-0.24$ ).

**Analysis:** In addition to the idealized task requirements, Figure 64 illustrates flight data from two pilots. The data set depicted in the left column was flown by a NASA pilot. One can see that this pilot met the task criteria within the 20 sec allotted. The data set in the right column was flown by a 600-hour guest pilot. This guest pilot was able to stay on task for the relatively low thrust requirements but encountered difficulty when near maximum thrust had to be added to attain level flight. Instead of leveling off, the aircraft lost 280 ft of altitude when the flow at the tailplane separated (the safety pilot recovered the aircraft). It is felt that this comparison highlights the fabled "dark and stormy night" scenario where there is a considerable pilot workload in addition to some level of fatigue at the end of a flight. Should the tailplane start to stall, would the pilot be able to recognize the situation, and respond quickly and appropriately?

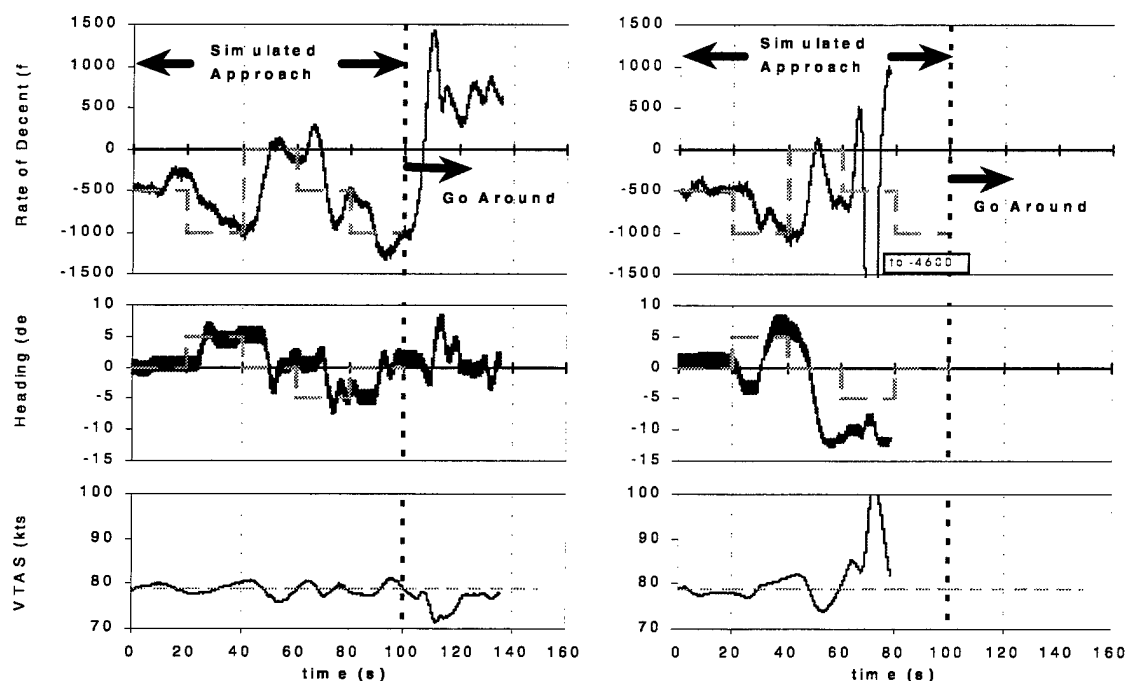


Figure 64. Balked landing tracking task.

### 6.1.8 A Case of Turbulence

The opportunity to document a "light to moderate" turbulence encounter arose during the guest pilot workshop. During a flight home, 16 sec of data were taken with the Failed Boot ice shape at zero flaps and 140kts. In Figure 65, it is compared to 13 sec of a steady, wings level flight for the same nominal conditions. Two key configuration differences are (1) a much higher thrust setting for the turbulent case,  $C_T = 0.15$ , as opposed to 0.09 for the quiescent case, and (2) significantly offset  $FYE$  values. For the quiescent case, the pilot was not allowed to change the trim from the lowest speed configuration. The corresponding difference in yoke force was -63 lbs (push). What is plotted, then, is the difference ( $FYE - FYE_0$ ), where  $FYE_0$  is the value at the start of the maneuver.

One can see the turbulence tossed the aircraft  $\pm 0.2G$ , with a corresponding pitch rate oscillation of approximately  $\pm 1^\circ/s$ . Also illustrated is the effect of the turbulence on the elevator and tailplane angle of attack. The standard deviation of the signal for the turbulence vs. quiescent case is  $0.125^\circ$  vs.  $0.040^\circ$  for  $\delta E$  and  $0.25^\circ$  vs.  $0.09^\circ$  for  $\alpha$ .

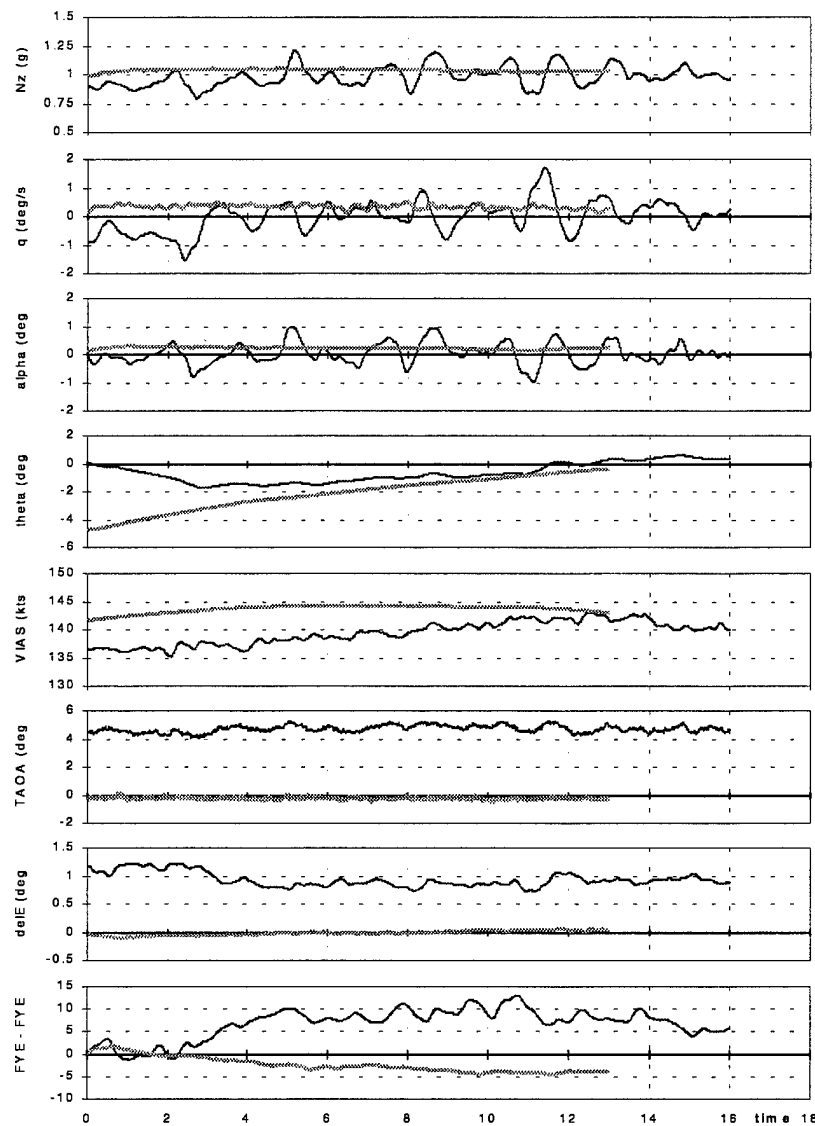


Figure 65. Comparison between quiescent and turbulent environment. Failed Boot,  $\delta F = 0^\circ$  flaps.



## 6.2 Comparison Between the Pushover and Elevator Doublet

The NASA/FAA Tailplane Icing Program contains the data to directly compare the pushover (PO) to the elevator doublet (ED). Six configurations were compared; two representative configurations are listed in Table 2. These configurations are the previously shown (1) Baseline,  $\delta F = 0^\circ$ ,  $V = 1.5V_s$  and (2) Failed Boot,  $\delta F = 20^\circ$ ,  $V = V_s$ . Recall that for the latter configuration, the Twin Otter failed both tests; it experienced a CFR during the pushover and an undamped pitch rate response during the elevator doublet. The excursion range, minimum values and a difference are compared. The range is the difference between the maximum and minimum values recorded during the test point, the minimum is simply the minimum value recorded, and the difference is that between the trim and minimum values. Note that under the Comparison of Minimums header, elevator deflection (*delE*) data appear. The values recorded are those of the elevator at its most TED position, *i.e.*, the maximum value.

For the range data, ED/PO represents the relative excursion percentage of the elevator doublet compared to the pushover. In all cases, except for  $C_m$ , the elevator doublet range excursions are less than those of the pushover. Furthermore, the pitch, speed and altitude excursions are significantly lower, less than 20%. Neither the  $N_z$ ,  $q$  nor *FYE* ranges exceed those of the pushover. The  $C_m$  range is larger for the elevator doublet because the nature of the maneuver requires a step input to the elevator.

For the minimum and difference data, PO-ED represents the difference between the two maneuvers. While the tailplane angles of attack are not as negative during the elevator doublet as for the pushover and their difference from trim is not as great, the tail loading factors, minimum  $C_{l\_Tail}$  and  $\Delta C_{l\_Tail}$ , are comparable. Note from the *delE* data that during the pushover, the tailplane is much less cambered than for the elevator doublet. Recall the less the camber, the greater the stall margin (Figure 12). Therefore, it is the combination of  $\alpha_x$  and  $\delta E$  that determines the aircraft's longitudinal stability, not large  $\alpha_x$  alone. This combination is manifest in the  $C_{l\_Tail}$  value.

### Baseline, $\delta F = 0$ , $V = 1.5V_s = 100\text{kts}$

#### Comparison of Ranges:

	PO	ED	ED/PO
theta (deg)	70	7	0.10
FYE (lbs)	94	58	0.62
VIAS (kts)	60	4	0.07
alt (ft)	925	38	0.04
$N_z$ (g)	2.5	1	0.40
$q$ (deg/s)	23	17	0.74
<i>delE</i> (deg)	13	9	0.69
$C_m$ (about CG)	0.1	0.4	4.00

#### Comparison of Minimums:

	PO	ED	PO-ED
alpha (deg)	-4	0.7	-4.7
TAOA (deg)	-8	-3	-5.0
$C_{l\_Tail}$	-0.3	-0.4	0.1
<i>delE</i> (max)	6	0.5	

#### Comparison of Differences:

	PO	ED	PO-ED
$\Delta(\text{alpha})$ deg	6.6	2.7	3.9
$\Delta(\text{TAOA})$ deg	6.6	2.5	4.1
$\Delta(C_{l\_Tail})$	0.2	0.2	0

### Failed Boot, $\delta F = 20$ , $V = V_s = 55\text{kts}$

#### Comparison of Ranges:

	PO	ED	ED/PO
theta (deg)	50	10	0.20
FYE (lbs)	80	50	0.63
VIAS (kts)	30	5	0.17
alt (ft)	480	60	0.13
$N_z$ (g)	1.5	0.3	0.20
$q$ (deg/s)	28	14	0.50
<i>delE</i> (deg)	23	15	0.65
$C_m$ (about CG)	0.5	0.7	1.40

#### Comparison of Minimums:

	PO	ED	PO-ED
alpha (deg)	-9	4	-13.0
TAOA (deg)	-14	-7	-7.0
$C_{l\_Tail}$	-0.9	-0.7	-0.2
<i>delE</i> (max)	10	-1	

#### Comparison of Differences:

	PO	ED	PO-ED
$\Delta(\text{alpha})$ deg	12.2	2.6	9.6
$\Delta(\text{TAOA})$ deg	7	2.5	4.5
$\Delta(C_{l\_Tail})$	0.5	0.4	0.1

Table 2. Pushover – elevator doublet comparison.

Now that some quantitative differences between these two maneuvers have been established, the next question concerns a pass/fail criterion. To attempt to answer this question, a Pass/Fail Map was constructed for both the control force and pitch response criteria. These judgements were made on one set of pushover maneuvers. Caution: this map attempts to present a 4-D data set in a 2-D plane. The three inputs are  $\delta F$ , minimum  $VTAS/V_s$  and minimum G-load for each maneuver. The output has three levels: pass, marginal and fail for each criterion. In color copies of this map, note that blue italic text corresponds to a pass, black to a marginal response and bold red to a fail. Careful inspection of this map will reveal a nearly one-to-one correspondence between the two criteria; *i.e.*, they are nearly interchangeable.

The control force rating examined the relationship between  $FYE$  and  $\delta E$ . The pass level is denoted by *P*; this means the control force remained nominally flat while the elevator was deflected TED. The marginal level is denoted CFL; this means the control force lightened while the elevator was moving TED. This level was further subdivided into two categories: a weak CFL (wCFL), which means that the force lightened, but only to some point shy of neutral, and a strong CFL (sCFL), which means that the force crossed the axis within a second of the elevator returning TEU. Finally for the fail level, a **CFR** means that the force crossed the axis while the elevator was fixed TED. This level is also presented in bold face in Table 3. For the pitch response rating,  $q$  and  $\delta E$  were examined. For this rating, the three categories were damped *D* for pass, weakly damped wD for marginal and undamped *U* for fail.

Table 3 presents a  $\delta F$  vs.  $VTAS/V_s$  chart for each of the ice shapes (the Baseline case passed all configurations). The map on this plane consists of the above rating with the G-load next to it in parentheses. For example, for the Failed Boot ice shape at  $\delta F = 20^\circ$  and  $VTAS/V_s = 1.4$ , the entry is **CF(L.5,R.2)**. This means that for a 0.5G pushover, a CFL was experienced, but when it went to 0.2G, the response was a CFR. For the pitch response of the exact same data set, the entry is **wD(.5), U(.2)**. This means that the response was weakly damped during the 0.5G pushover, and undamped for the 0.2G maneuver.

As can be seen from Table 3, these rating criteria yield nearly identical results. The pitch response criteria will yield the same information as the control force response.

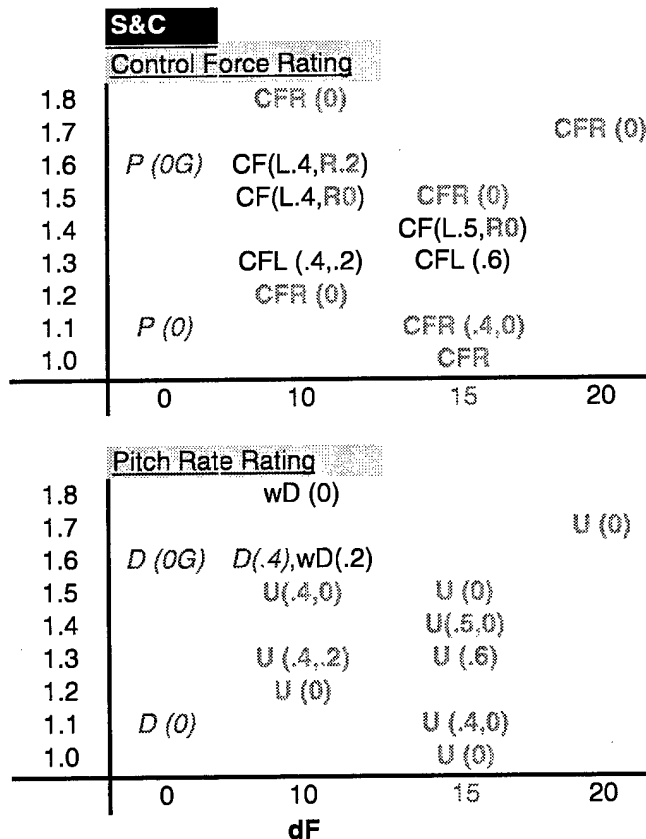
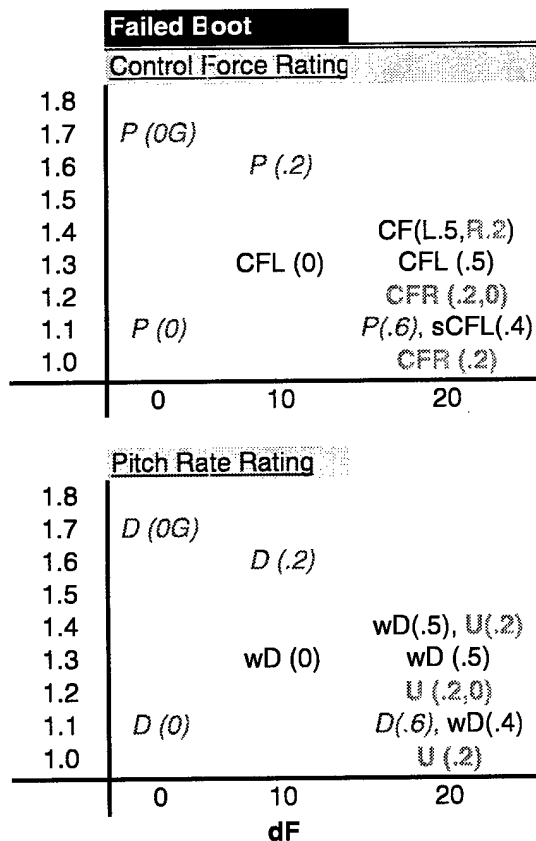
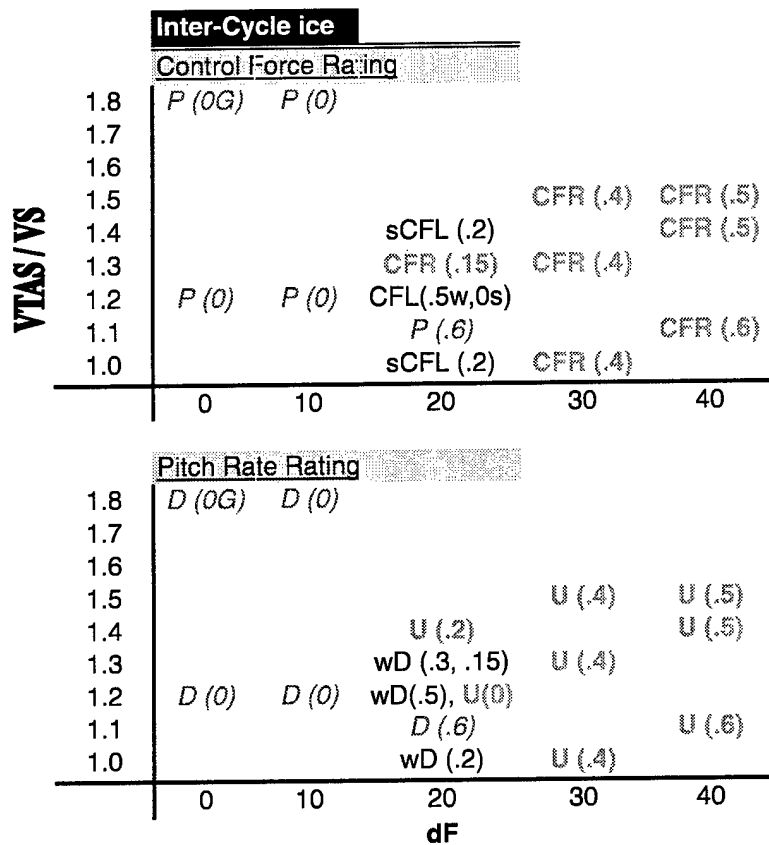


Table 3. Pass/Fail maps for both the control force and pitch response ratings during a pushover maneuver.

### 6.3 Repeatability Analysis for the Pushover

This section introduces an analysis of the pushover data introduced in Section 6.1.5 and includes a precision and accuracy study.

An important question regarding the pushover is how precisely it must be flown. If, for example, a point is flown five knots below the lowest target speed and a control force reversal is experienced, should the aircraft be certified if it would have passed at the target speed? What if the point is flown five knots too fast? In general, what magnitude of error is tolerable, and what is not? It is beyond the provision of this report to provide comment on such guidelines. What can be discussed herein, however, are the variations experienced by one NASA pilot flying the Twin Otter aircraft.

The nature in which most of these pushovers were flown allows for such a repeatability analysis. Within each test point three parabolas were flown, each targeting the same conditions of pitch rate (and correspondingly, vertical acceleration), speed and pitch angle. If the three parabolas can be superimposed on each other and synchronized to a distinguishing feature, then a point-by-point repeatability analysis can be conducted.

The distinguishing feature was chosen to be the vertical acceleration  $N_z$ . This choice of an output parameter was based on the fact that the criteria for the pushover maneuver is written to this parameter, and the fact that it has obvious demarcations between maneuvers. The choice of the input parameter, elevator deflection, was not chosen because it was not "clean" in that the elevator was moved differently for different configurations. This choice would have required more filters or decisions to properly define the maneuver.

Reported herein are precision and accuracy analyses for a range of critical and non-critical configurations. This section starts with a detailed description of the analysis.

#### 6.3.1 Description of the Analysis

The goal is to superimpose the three maneuvers of each test point on one axis. It was decided that a maneuver shall begin and end with the pull up, *i.e.*, from maximum  $N_z$  to maximum  $N_z$ . This choice also puts the dynamics of interest in the middle of the maneuver. Once the three maneuvers are properly defined, each is scaled to run from 0 to 1. Typically, maneuvers lasted 9–15 sec; within a given configuration, the variation was usually within 2 sec. The three individual maneuvers, plus their average, are depicted in Figure 66 for a non-critical configuration that demonstrated no CFR, and therefore easily "passed" the certification criteria: Inter-Cycle Ice with  $\delta F = 0^\circ$  and  $V = 1.5V_S$ .

It became apparent that simply identifying the end points was insufficient; the minimum scaled  $N_z$  appeared anywhere from 50% to 80% of the total time; therefore, it needed to be fixed as well. The optimal place to fix the scaled  $N_{z\_min}$  is the average  $N_{z\_min}$  location of the three maneuvers under consideration. For the example in Figure 66, the choice of 50% was made. The full procedure is then:

- 1) Find the actual times of the two  $N_{z\_max}$ ,  $t_0$  and  $t_1$ , to determine the period  $T$ .
- 2) Find the actual time of  $N_{z\_min}$ ,  $t_{min}$ .
- 3) To fix the scaled time of  $N_{z\_min}$  at 0.5, subtract  $0.5 T$  from  $t_{min}$  to find the new start time,  $t_0'$ . Add  $T$  to the new start time to find the new end time,  $t_1'$ .
- 4) With the bounds of the maneuver determined, scale the actual time,  $t$ , in this manner:  
$$t_{scaled} = (t - t_0') / (t_1' - t_0').$$
 And, of course,  $t_{scaled}(N_{z\_min}) = 0.5 = (t_{min} - t_0') / (t_1' - t_0')$ .

Once the traces are scaled and synchronized, statistical analyses may be performed. To make the task of directly comparing all three scaled time traces more manageable, the time axis was subdivided into equidistant bins. For this exercise, the number of maneuvers,  $N_{man} = 3$ , and the number of bins,  $N_{bin} = 20$ , which left the number of points per bin,  $N_{siz} \approx 70$ . Let  $Q(i,j,k)$  represent the  $i^{th}$  point of the  $j^{th}$  maneuver in the  $k^{th}$  bin for a quantity  $Q$ . The scaled data within a bin were averaged, and the average value was placed at the center of that bin. This was done for each of the three maneuvers.

$$\bar{Q}(j, k) = \frac{1}{N_{siz}} \sum_{i=1}^{N_{siz}} Q(i, j, k)$$

Within a bin, the values of the three averages were themselves averaged to determine the overall average for that time step.

$$\bar{\bar{Q}}(k) = \frac{1}{N_{man}} \sum_{j=1}^{N_{man}} \bar{Q}(j, k)$$

As seen in Figure 66, the overall average for each quantity is represented with the thick blue line. This line is simply a straight-line fit through the  $\bar{\bar{Q}}$ . The error bars within each bin,  $s(k)$ , come from taking the standard deviation of the three differences between each trace average and the overall average.

$$s(k) = \left[ \frac{\sum_{j=1}^{N_{man}} (\bar{Q}(j, k) - \bar{\bar{Q}}(k))^2}{N_{man} - 1} \right]^{1/2}$$

The final error,  $\bar{s}$ , is the average of all of the bins.

$$\bar{s} = \frac{1}{N_{bin}} \sum_{k=1}^{N_{bin}} s(k)$$

To isolate the target portion of the maneuver and eliminate the entry and exit variations, the values centered around the  $N_{z_{min}}$  bin can be averaged. The quantity  $\bar{s}_{tar}$  is defined similarly to  $\bar{s}$ , but only averaged over the immediate target neighborhood. Let  $k_0$  define the bin which contains  $N_{z_{min}}$ , and  $n$  define the number of bins in the neighborhood.

$$\bar{s}_{tar} = \frac{1}{n} \sum_{k=k_0 - \frac{n}{2}}^{k_0 + \frac{n}{2}} s(k)$$

### 6.3.2 Description of the Results

For the Inter-Cycle ice case presented in Figure 66, the  $\bar{s}_{tar}$  value was averaged from  $t_{scaled} = 0.375$ – $0.625$ . This neighborhood is depicted with the vertical dashed lines.

In Table 4, both the  $\bar{s}_{tar}$  and  $\bar{s}$  errors are listed for the above and several other configurations. These are divided into cases where no CFR was experienced (non-critical) and cases where CFR was experienced (critical). Focussing on the  $\bar{s}_{tar}$  values, Table 4 suggests that  $N_z$  was very repeatable regardless of the maneuver criticality. On the other hand, the repeatability of  $q$ ,  $V$  and to some extent  $\theta$  was effected by criticality. Note that the speed was normalized by its target,  $V/V_{target}$ .

With the average values established, the accuracy of achieving the targets may now be addressed. The accuracy shall be defined as the difference (Dif) between the average of the  $k_0$  bin (Actual) and the target quantity (Target),  $|\bar{Q}(k_0) - Q_{target}|$ . Again, the speed was normalized by its target,  $\%Dif = |(\bar{V}(k_0) - V_{target})/V_{target}| * 100$ . These values are presented in Table 5. The results suggest the pilot was able to achieve the target  $N_z$  to within 0.1G, regardless of difficulty performing the maneuver. The pilot averaged 5% accuracy in hitting  $V_{target}$ . Theta was clearly the most difficult target to meet. The average of the values reported is  $-18^\circ$  off target. Typically, to achieve the target  $N_z$ , the Twin Otter had to be in a dive, not at the horizon.

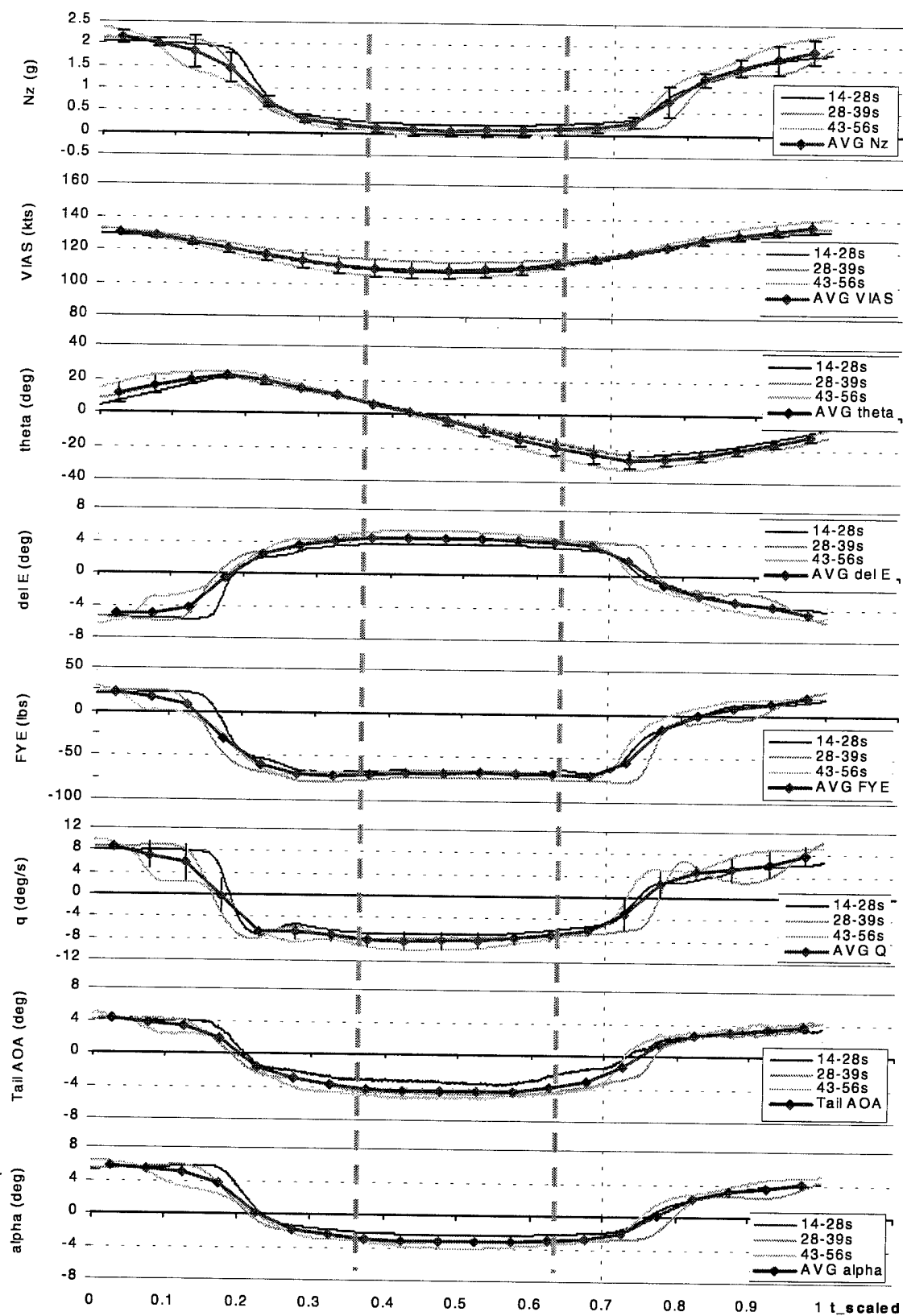


Figure 66. Three maneuvers (thin lines) and their average (thick line) vs. scaled time for an Inter-Cycle ice,  $\delta F = 0^\circ$ ,  $V = 1.5V_s = 100\text{kts}$  test point. Error bars are indicated on select traces.

Configuration Ice Shape, $\delta F$ , V/Vs	$N_z$ (G)		$q$ (deg/s)		$V/V_{target}$ (%)		theta (deg)	
	$\bar{s}_{tar}$	[ $\bar{s}$ ]	$\bar{s}_{tar}$	[ $\bar{s}$ ]	$\bar{s}_{tar}$	[ $\bar{s}$ ]	$\bar{s}_{tar}$	[ $\bar{s}$ ]
No CFR								
IC, 0°, 1.5	0.12	[0.17]	1.2	[1.5]	4.2	[3.1]	2.8	[3.1]
FB, 0°, 1.5	0.09	[0.24]	0.9	[2.0]	5.0	[7.2]	2.5	[4.0]
SC, 0°, 1.5	0.05	[0.21]	0.5	[1.9]	3.1	[3.6]	1.4	[2.6]
Ba, 20°, 1.0	0.06	[0.07]	1.0	[1.1]	2.0	[4.9]	1.5	[1.5]
IC, 20°, 1.0	0.06	[0.05]	1.2	[1.0]	3.5	[2.4]	1.7	[1.3]
CFR								
IC, 40°, 1.0	0.07	[0.09]	1.9	[1.7]	9.1	[7.5]	2.6	[3.2]
FB, 20°, 1.15	0.07	[0.12]	2.4	[2.3]	2.6	[5.2]	1.8	[3.2]
FB, 20°, 1.0	0.08	[0.19]	2.9	[3.4]	5.1	[8.2]	8.3	[5.6]
SC, 15°, 1.0	0.24	[0.24]	3.5	[3.4]	6.7	[6.9]	2.5	[4.2]
SC, 20°, 1.0	0.10	[0.12]	2.3	[1.7]	8.5	[9.3]	3.5	[3.5]

Table 4. Repeatability analysis – precision levels for several flight conditions to minimum  $N_z$ .

Configuration Ice Shape, $\delta F$ , V/Vs	$N_z$ (G)			VIAS (kts)			theta (deg)		
	Actual	Target	Dif	Actual	Target	%Dif	Actual	Target	Dif
No CFR									
IC, 0°, 1.5	0.07	0	0.07	108	100	8.0	-4.2	3	-7.2
FB, 0°, 1.5	-0.07	0	-0.07	102	100	2.0	-12.5	3	-15.5
SC, 0°, 1.5	0.05	0	0.05	105	100	5.0	5.5	3	2.5
Ba, 20°, 1.0	0.22	0.17	0.05	57	55	3.6	-25.9	3	-28.9
IC, 20°, 1.0	0.31	0.25	0.06	60	55	9.1	-20.7	3	-23.7
CFR									
IC, 40°, 1.0	0.58	0.50	0.08	55	55	0.0	-15.7	-4	-11.7
FB, 20°, 1.15	0.15	0.17	-0.02	66	65	1.8	-18.4	-0.5	-17.9
FB, 20°, 1.0	0.24	0.17	0.07	56	55	1.3	-18.3	3	-21.3
SC, 15°, 1.0	0.01	0	0.01	58	55	5.4	-23.3	5	-28.3
SC, 20°, 1.0	0.34	0.25	0.09	62	55	12.7	-23.9	3	-26.9

Table 5. Repeatability analysis – accuracy of achieving the target values for non-critical and critical cases.

## 6.4 Dynamic Maneuvering Conclusions

Several types of dynamic maneuvers were flown during the NASA/FAA Tailplane Icing Program. The primary interest was to study the pushover maneuver. A potential alternate maneuver, the elevator doublet, was also studied. In addition to these two maneuvers which intentionally manipulated the elevator, several other conceptually simplified maneuvers were flown. These maneuvers were three types of transitions – increasing flaps, speed and thrust – flown to isolate their effect of the tailplane. Each of these transitions, by itself, drove an ice-contaminated Twin Otter horizontal tailplane toward stall. It should be noted that a thrust increase might not affect other aircraft as adversely; the phenomenon observed for the Twin Otter is believed to be caused by the thrust line positioned above the CG.

A tail stall occurs, of course, when the tailplane angle of attack,  $\alpha_t$ , exceeds the stall angle,  $\alpha_{t\_stall}$ . The elevator deflection,  $\delta E$ , also plays a role in determining the stall angle. For example, the stall point of a more cambered airfoil occurs with more downward lift but at a reduced stall angle. A high flap deflection always corresponds to a more negative tail angle of attack. However, it was also noted that there are opposite trends in the speed criteria for extreme tail angles depending on whether the aircraft is in a steady state or dynamic maneuver. For steady, wings level flight, high speed will drive  $\alpha_{to}$  more negative. During maneuvering, on the other hand, the dynamic component becomes dominant,  $\Delta \alpha_t$ . This corresponds to low speeds and high pitch rates. With these thoughts in mind, the single variable paths to stall will be discussed first, then the pushover and elevator doublet maneuvers.

### 6.4.1 Transition Maneuvers

The flap transition is clearly a path toward stall. Flap deflection drives the tailplane toward stall by making  $\alpha_{w/c}$  more negative. The downwash remains nominally constant because  $C_{L\_w/c}$  remains nominally constant. To maintain speed, the elevator moves TED which increases the stall margin slightly, but the dominant factor is the substantial decrease in  $\alpha_{w/c}$ , which drives the  $\alpha_t$  more negative.

The mechanism driving the speed transition toward stall, on the other hand, is less obvious. A microscopic view of the data is necessary since looking at only the gross trends of a nominally constant  $\alpha_t$  and a slight  $\delta E$  deflection TED suggest that the stall margin should increase. A careful inspection of the oscillations in the  $\alpha_t$  data coupled with the  $\delta E$  data, revealed that the most negative extremes of the  $\alpha_t$  trace drive the tail toward stall, whereas the least negative extremes increase the stall margin. For this extreme case, the tailplane is going into and out of stall.

For the full stall of the thrust transition, the features are again subtle. The  $\alpha_{w/c}$  decreased about  $2^\circ$  with a slight decrease ( $-11^\circ$  to  $-12^\circ$ ) in the  $\alpha_t$ . To maintain speed, the elevator was required to move TEU. With this, the stall margin decreased and the plane plunged into a full tail stall.

### 6.4.2 Dynamic Maneuvers

The main focus of the study was on the pushover. To this end, nearly 400 pushover maneuvers were flown in a manner consistent with the FAA ANM-100 memorandum<sup>Error! Bookmark not defined.</sup>. Note that in the ANM-100 description, the pushover maneuver begins with the elevator TED deflection and ends with the minimum load factor. The pass/fail criteria are that (1) a push control force is required throughout the maneuver (to minimum-G) and (2) "the airplane should demonstrate suitable controllability and maneuverability throughout the maneuver with no force reversal and no tendency to diverge in pitch". For this series of flight tests, it was interpreted that the "maneuver" ended when the elevator was returned TEU.

Time history analyses immediately indicate how well the pilot met the target conditions of the maneuver ( $N_z$ ,  $V$ ,  $\theta$ ) and whether or not a control force reversal (CFR) was experienced. This was determined by inspecting the co-plot of  $\delta E$  &  $FYE$ ; a CFR occurred when the control force crossed the neutral axis (or trim point) while the elevator was fixed TED, prior to the elevator return TEU. As expected, the incidence of CFRs for the pushover increased with:



- (1) increasing ice shape severity,
- (2) increasing flap deflection,
- (3) decreasing normal load factor, and
- (4) decreasing speed.

Data were presented demonstrating that merely looking for a CFR is a good but not fully inclusive indicator of whether or not the tailplane stalled or had undamped characteristics. In fact, these data confirmed the ANM-100 guidance to note the "tendency to diverge in pitch". That is, inspecting  $q$  vs.  $t$  for an undamped response seemed to be a slightly more robust indicator of a destabilized tailplane than the CFR. More conclusive results are obtained by the following more advanced analyses:

- (1)  $q$  vs.  $\delta E$  – Examine the pitch rate response after the elevator is returned TEU. If stalled, the elevator could travel quite a distance before the pitch rate starts to return to zero. This would also appear as a reduced elevator effectiveness,  $C_{m\delta E}$ .
- (2)  $N_z$  vs.  $FYE$  – Check the slope of the line after the elevator is returned TEU and after it crosses the trim point. If stalled, the aircraft will continue toward OG regardless of the force applied by the pilot to return toward 1G flight.

Also presented were two examples of special cases. One was of a "shaped" maneuver that erroneously passed the CFR criteria because the elevator was deflected slightly but sufficiently to maintain flow attachment. The other example passed the CFR criteria but stalled after the elevator deflection TEU. The flow remained attached *until* the elevator was pulled TEU and the tailplane became more cambered. It should be noted that this example failed the pitch rate response criterion. Analysis of the  $q$  vs.  $\delta E$  and  $N_z$  vs.  $FYE$  cross-plots helped resolve this issue. More examples of pushovers can be found in Appendix C.

Since the pushover was a difficult maneuver to fly accurately, a repeatability analysis was synthesized to determine the variations in how well the NASA pilot was able repeat the maneuver and how accurately he simultaneously hit the three targets. The severity of the ice shape did not seem to play a major role in how accurately he met the targets, although it did, to some extent, affect the repeatability of the velocity and pitch attitude. The pilot met the  $N_{z\_min}$  objective within  $\pm 0.1G$ . The simultaneous  $VIAS$  varied but was typically within about 5% of  $V_{target}$ . The most difficult target to meet simultaneously with  $N_{z\_min}$  was  $\theta$ . For the Twin Otter, this was typically  $-20^\circ$  beyond the trim  $\theta$ .

Part of the request from the FAA was to investigate potential alternate maneuvers to the pushover. To this end, elevator doublets were flown. Of course, the elevator doublet is typically flown for parameter estimation studies, but it seems to have applicability for tailplane stall certification as well; this maneuver could also destabilize the tailplane. Appendix C also contains a number of elevator doublet time histories. One issue that needs to be addressed for the elevator doublet, or any alternate maneuver, is that of "equivalency" to the pushover. That is, what is the relevant parameter for comparison?

For the elevator doublet, as with the pushover, examining either the  $\delta E$  &  $FYE$  or  $\delta E$  &  $q$  co-plots yielded essentially the same conclusion as to whether or not the tailplane destabilized; again, the pitch rate response,  $q$ , seems to be a more robust indicator. Based on an undamped response, it was found, as expected, that the elevator doublet was most likely to fail with:

- (1) increasing ice shape severity,
- (2) increasing flap deflection, and
- (3) increasing speed.

The pushover and elevator doublet maneuvers were compared directly for the same aircraft configurations and flight conditions. A test point that destabilized the tailplane for the pushover also destabilized the tailplane for the elevator doublet, even though the pushover generated much more negative tailplane angles of attack. What became apparent is that the extreme  $\alpha_i$  values alone are not an adequate indicator of impending tail stall, but rather the combination of  $\alpha_i$  and  $\delta E$  that drive the tailplane toward stall. For the Twin Otter, this seems to translate to an equivalency parameter of  $C_{l\_Tail}$ . This should be checked with other aircraft, however.

A further investigation of the difference, if any, between the control force and pitch response criteria was conducted. The two criteria were compared directly using the pushover data. A nearly one-to-one correspondence was observed for all ice shapes, flap deflections and speeds. In other words, for a given data set, if a CFR is observed, then so is an undamped pitch response. **For the Twin Otter, the control force and pitch rate response criteria yield nearly the same results.** Further analysis of any discrepancies indicated that the pitch response was the more robust measure.

In summary, it was found that for the Twin Otter, the same certification pass/fail decisions could be made using the elevator doublet rather than the pushover. In general, the elevator doublet is an easier and safer maneuver to fly. Summarized in Table 6 are the advantages and disadvantages of the pushover compared to the elevator doublet. **It would be of great interest to investigate the response of other aircraft to both the pushover and elevator doublet.**

	Pushover	Elevator Doublet
Advantages	<ul style="list-style-type: none"> <li>• Flight to 0G does not require instrumentation to detect.</li> <li>• Control Force Reversal criteria straightforward to detect PROVIDED the maneuver is flown properly.</li> </ul>	<ul style="list-style-type: none"> <li>• Excursions are <math>1 \pm 0.5G</math></li> <li>• Much less risky than Pushover; much easier to recover from a stall.</li> <li>• Easier to fly; less pilot variability; not susceptible to shaping.</li> </ul>
Disadvantages	<ul style="list-style-type: none"> <li>• Excursions are <math>1 \pm 1.1G</math></li> <li>• Flight to less than 0G requires instrumentation for documentation.</li> <li>• Difficult to hit all three targets (<math>N_z</math>, <math>V</math> &amp; <math>\theta</math>) as aircraft tracks through horizon.</li> <li>• Possible to manipulate the elevator to keep flow attached.</li> <li>• If tail stalls, aircraft will be in a difficult position for recovery (<math>\theta \approx -40^\circ</math>, near VFE).</li> <li>• Concern for fluid system operations during 0G flight (e.g., hydraulics, fuel, oil).</li> </ul>	<ul style="list-style-type: none"> <li>• Hardware required to measure pitch rate and elevator deflection.</li> </ul>

**Table 6. Comparison of the advantages and disadvantages for both the pushover and elevator doublet.**

## 7.0 Parameter Estimation Analysis

Elevator doublet maneuver test points were added to the test matrix in Flight 97-39 as a potential alternate maneuver for discerning icing effects on tailplane performance. The benefit of the maneuver was twofold. Prior experience with the elevator doublet suggested it could also be used for pilot evaluation of the aircraft response. In addition, the elevator doublet maneuver can be used in parameter estimation analyses to derive mathematical aerodynamic models and stability and control derivatives of the aircraft. The focus of this section is to provide the results of the parameter estimation analysis on the Twin Otter with the various levels of contamination.

### 7.1 Flight Test Procedures

The elevator doublet maneuver was a series of elevator inputs initiated from straight and level flight. The aircraft was trimmed for the target flap deflection, speed and thrust. The elevator input was a near perfect classic square wave consisting of two doublet cycles followed by 6 to 10 sec of no control input. Elevator doublets were conducted with all ice shapes and covered the speed range for the flap settings tested. For the majority of cases, the moderate thrust setting of  $C_T = 0.10$  (0.05 per engine) was chosen; however, a higher setting of  $C_T = 0.18$  was also flown for a very limited number of test points. For the Failed Boot and S&C ice shapes, elevator doublets were not flown beyond  $\delta F = 30^\circ$ .

Since the elevator doublet was also used for pilot evaluation, the maneuvers were of relatively large amplitude. The incremental angle of attack range typically varied  $\pm 3^\circ$  to  $\pm 5^\circ$ ; while, the incremental normal acceleration often varied  $\pm 0.5G$  from 1G flight. The maneuvers are also discussed in Section 6.1.6, and were very similar to those previously performed for and documented in Ref. 3.

Table 7 shows the tailplane ice and aircraft configuration where data maneuvers were performed. A complete matrix of data was obtained for the  $0^\circ$ ,  $10^\circ$ ,  $20^\circ$ , and  $30^\circ$  flap settings. Data were also obtained for the Baseline and Inter-Cycle ice configurations with the flaps at  $40^\circ$ . For the S&C ice configuration, additional data were obtained at the  $15^\circ$  and  $25^\circ$  flap settings. Except for the Baseline data with the higher thrust coefficient of 0.18, an "X" in the table represents 3 to 4 maneuvers over the angle of attack range. At the higher thrust setting, the "x" represents 1 to 2 maneuvers at the high angle of attack for each flap setting. Because of the limited quantity of the data with higher thrust, it will not be presented with the results. The remaining data were all obtained with the same lower thrust setting. For the aft CG baseline data, a linear aerodynamic correction was applied to the static stability parameter and to the elevator control parameter to correct them to the forward CG for data presentation.

Data will be presented at the  $0^\circ$ ,  $10^\circ$ ,  $20^\circ$ ,  $30^\circ$ , and  $40^\circ$  flap settings as the effects of tailplane icing are more prominent when the various ice configurations are viewed at a common flap setting.

Tail Configuration	CG	$C_T$	Flap Deflection (deg)						
			0	10	15	20	25	30	40
Clean	AFT	0.10	X	X		X		X	X
Clean	FWD	0.18	x	x		x		x	x
Clean	FWD	0.10	X	X		X		X	X
Inter-Cycle ice	FWD	0.10	X	X		X		X	X
Failed Boot Ice	FWD	0.10	X	X		X		X	
S&C Ice	FWD	0.10	X	X	x	X	x	X	

Table 7. Conditions for the parameter estimation maneuvers.

## 7.2 Method of Analysis for Parameter Estimation

A parameter estimation analysis of the flight data was performed using version 2.3.4 of pEst, a parameter estimation program similar to an earlier version in Ref. 15. The pEst program is an interactive, nonlinear program for the analysis of dynamic systems. This analysis used the standard pEst user routines that define the aircraft six-degree-of-freedom nonlinear set of differential equations. However, full coupling of the equations was not needed as the maneuvers were performed in a decoupled manner. This allowed the aerodynamic part of the equations to be split into a longitudinal subset, while the inertial part of the equations maintained their full nonlinearity. For the longitudinal subset, the elevator time history measurement was the only input control variable. The output control variables consisted of state variables and additional response variables. The state variables used were angle of attack, pitch angle, and pitch rate. The additional time responses used were normal acceleration, axial acceleration, and pitch angular acceleration. The measured lateral-directional response variables were also used to supplement the inertial part of the equations. Dynamic pressure and velocity varied with time throughout the analysis.

The parameters used to define the longitudinal aerodynamic model contained the standard longitudinal partial derivatives that are often referred to as stability and control derivatives. In addition, the angle of attack squared parameters for pitching moment and axial force were used to better model the large size of the maneuvers. The results of the pEst analysis were sets of longitudinal parameters for each maneuver. The resulting parameters are a best value averaged over the oscillation range of the maneuver. For example, for maneuvers where angle of attack oscillated  $\pm 5^\circ$ , the resulting parameters are the averaged values over the  $10^\circ$  angle of attack range. For plotting presentation, the parameters are then plotted versus the average angle of attack for each maneuver.

It should be noted that the analysis process works best when the model used is consistent with the vehicle characteristics. The mostly linear aerodynamic model used for the analysis is very adequate to describe the piecewise linear behavior exhibited by a conventional configuration below its stall angles of attack. However, when the wing flaps are deployed much more than about  $20^\circ$ , the resulting separated flow induces a modeling error that shows up as scatter in the parameter results.

The analysis process consisted of an initial analysis of all the maneuvers followed by a final analysis. The initial analysis used starting values from the prior maneuver in sequence and yielded a complete set of the longitudinal derivatives. The data were then plotted as a function of angle of attack for each flap position and tail ice condition. Trends from the initial analysis were used as starting values and predicted reference values for the final analysis. A low weighting was placed on the predicted values to lessen the scatter in the final results. Care was taken to limit the cost due to the weighted predictions to approximately 2% of the total cost function. Data from a small number of the maneuvers were not used because the analysis was not able to obtain an acceptable fit between the measured and the calculated responses.

## 7.3 Results

The stability and control characteristics of the Twin Otter have been previously documented in Ref. 3. This analysis expands on the prior results by presenting the effects of tailplane icing using three ice shapes and with wing flap extensions as high  $\delta F = 40^\circ$ .

A very basic review of the effects of tailplane icing on the flight data will enhance interpretation of the parameter results. Moving the CG forward requires the horizontal tail to produce more down load to balance (trim) the aircraft. Deploying the flaps creates a negative pitching moment that also requires the horizontal tail to produce more down load to trim the aircraft. Thus for a given CG and flap position, the elevator or engine thrust can be modulated to attain the desired angle of attack or velocity. As most of the parameter estimation data were at the same CG, thrust was at a constant setting, and the flaps were at discrete settings, the elevator was the only remaining longitudinal control. Thus, as the various ice shapes were placed on the horizontal tail, a rough measure of the degradation in the tail's ability to generate a down force was the elevator position ( $\delta E$ ). However, the elevator required for trim varies with flap deflection because the flaps also change the flow angle into the horizontal tail. While this negates using the absolute value of  $\delta E$  as metric, the incremental value between the ice free tail and the various ice shapes can still be a

valid metric within the linear load range of the horizontal tail. Incremental  $\delta E$  is not a valid metric when the horizontal tail is close to stall. For the forward CG and thrust coefficient  $C_T = 0.10$ , the additional  $\delta E$  required to maintain angle of attack as a function of flap position is shown in Figure 67 for the various ice shapes. Note that the Baseline configuration is the zero elevator axis. Given the qualifications of this plot, it is noted that the Inter-Cycle ice had no effect (within the plot resolution) on the horizontal tail's ability to produce down load until the flaps were deflected past  $\delta F = 20^\circ$ . Likewise the Failed Boot and S&C ice shapes had only a limited effect until the flaps were deflected beyond  $\delta F = 10^\circ$ . While the figure is only valid prior to tailplane stall, the maneuvers for parameter estimation were also conducted without encountering tailplane stall. Assuming the parameter variation with ice shapes follows the trends of Figure 67, only slight changes in the parameters will result at the lower flap settings where the ice shapes have only a limited effect on the function of the horizontal tail.

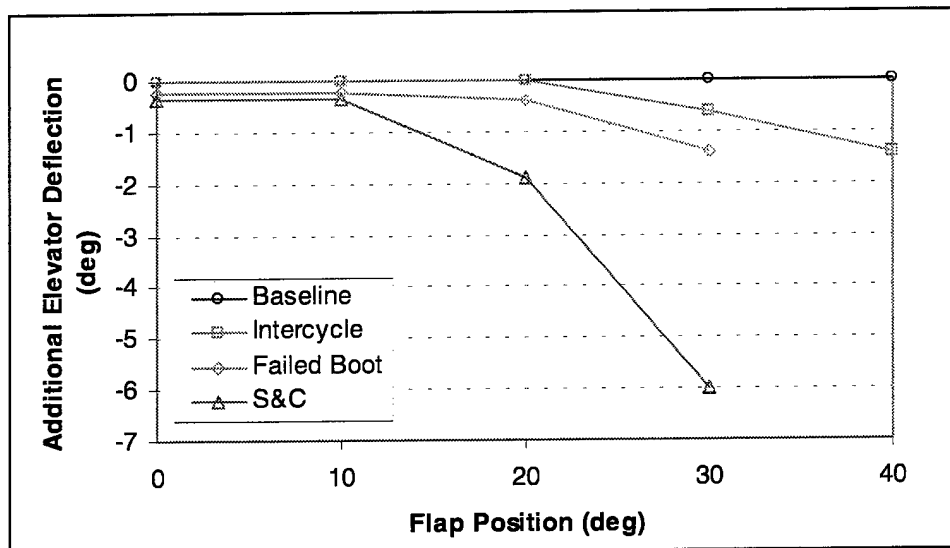


Figure 67. Additional elevator required to trim.

While the tailplane ice caused a significant degradation of the general flying qualities in the areas of buffet and the associated control wheel shaking, its effects were explicit in a relatively small number of parameters. The elevator control effectiveness,  $C_{m\delta E}$ , was the principal parameter. The effects were also apparent in the longitudinal static stability parameter,  $C_{m\alpha}$  and the pitch damping parameter,  $C_{mq}$ . While lesser effects could be inferred from the axial and normal force parameters, the effects were generally of limited significance to the flying qualities and, thus, are not be presented. Angle of attack typically oscillated over a  $6^\circ$  to  $10^\circ$  range; while the elevator control inputs oscillated over a  $10^\circ$  to  $14^\circ$  range. The analysis returns the best value of the parameter averaged over the oscillation range. Thus as tailplane stall was approached, the parameters were only marginally degraded as only the nose down limits of the elevator doublets were near tailplane stall. While smaller doublets would have been more desirable for the parameter analysis, the doublets analyzed for this study needed to be large for pilot evaluation.

The resulting parameters obtained near  $\delta F = 0^\circ$  setting are shown in Figure 68. Of significance is the approximately 8% reduction in  $C_{m\delta E}$  with either the Failed Boot or S&C ice shapes. The effects on  $C_{m\alpha}$  and  $C_{mq}$  due to the ice shapes are within the scatter of the data. The reduction in  $C_{m\alpha}$  at angles of attack greater than  $7^\circ$  is related to the wing characteristics.

Figure 69 presents the data obtained with  $\delta F = 10^\circ$ . The data again show an approximate 8% reduction in  $C_{m\delta E}$  with either the Failed Boot or S&C ice shapes, and there is also about a 4% reduction in  $C_{m\delta E}$  due to the Inter-Cycle ice shape. Slight reductions in  $C_{m\alpha}$  and  $C_{mq}$  are also starting to become apparent.

With the  $\delta F = 20^\circ$  flap setting, (Figure 70) the parameter variations with ice shape become more dramatic. The reductions in the elevator control effectiveness parameter,  $C_{m\delta E}$ , are about a 10% for the Inter-Cycle ice, 17% for the Failed Boot ice, and 27% for the S&C ice. The static stability parameter,  $C_{m\alpha}$ , becomes unstable (positive values) at the higher angles of attack (lower speeds) for both the Failed Boot and the S&C ice shapes.  $C_{mq}$  shows reduced pitch damping for the S&C ice shapes at the lower angles of attack.

At the  $\delta F = 30^\circ$  flap setting (Figure 71), the effects of ice on the horizontal tail significantly degrade the flying qualities.  $C_{m\delta E}$  is reduced about 10% for the Inter-Cycle ice shape, 22% for the Failed Boot ice shape, and 33% for the S&C ice shape. The effects on  $C_{m\alpha}$  are not explicit for the Inter-Cycle or Failed Boot ice shapes. For the S&C ice shape,  $C_{m\alpha}$  becomes statically unstable above about  $-2^\circ$  angle of attack. The analysis of  $C_{mq}$  is strongly effected by the separated flow from the flaps and contains enough scatter to mask any trends in the data.

With  $\delta F = 40^\circ$  (Figure 72), data were obtained for only the Baseline configuration and with the Inter-Cycle ice shape. With the Inter-Cycle ice shape,  $C_{m\delta E}$  shows a strong reduction as angle of attack is decreased (increasing airspeeds). This reduction is about 30% at  $-4^\circ$  angle of attack. The trends in  $C_{m\alpha}$  and  $C_{mq}$  are not apparent.

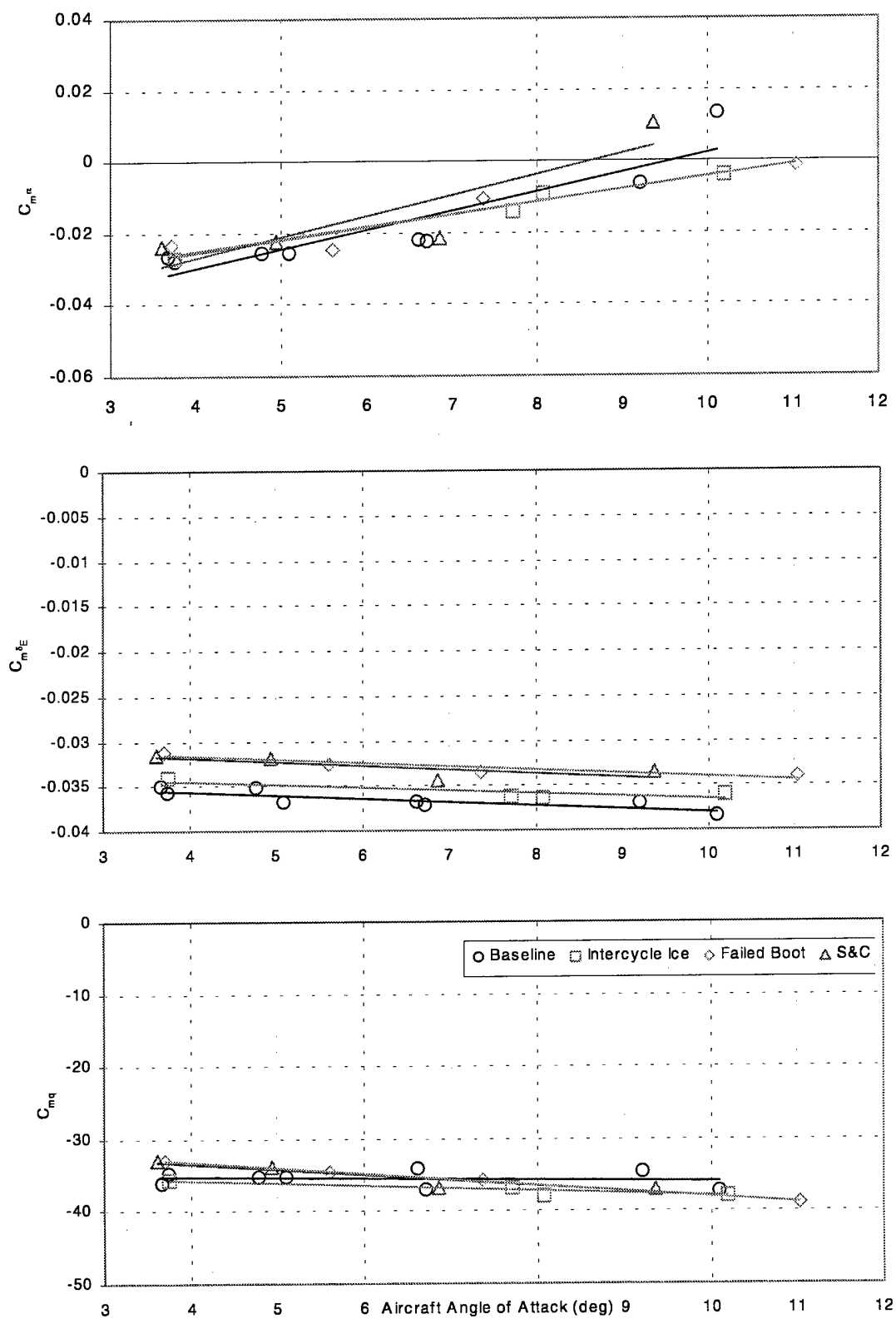


Figure 68. Icing effects on pitching moment derivatives,  $\delta F = 0^\circ$ .

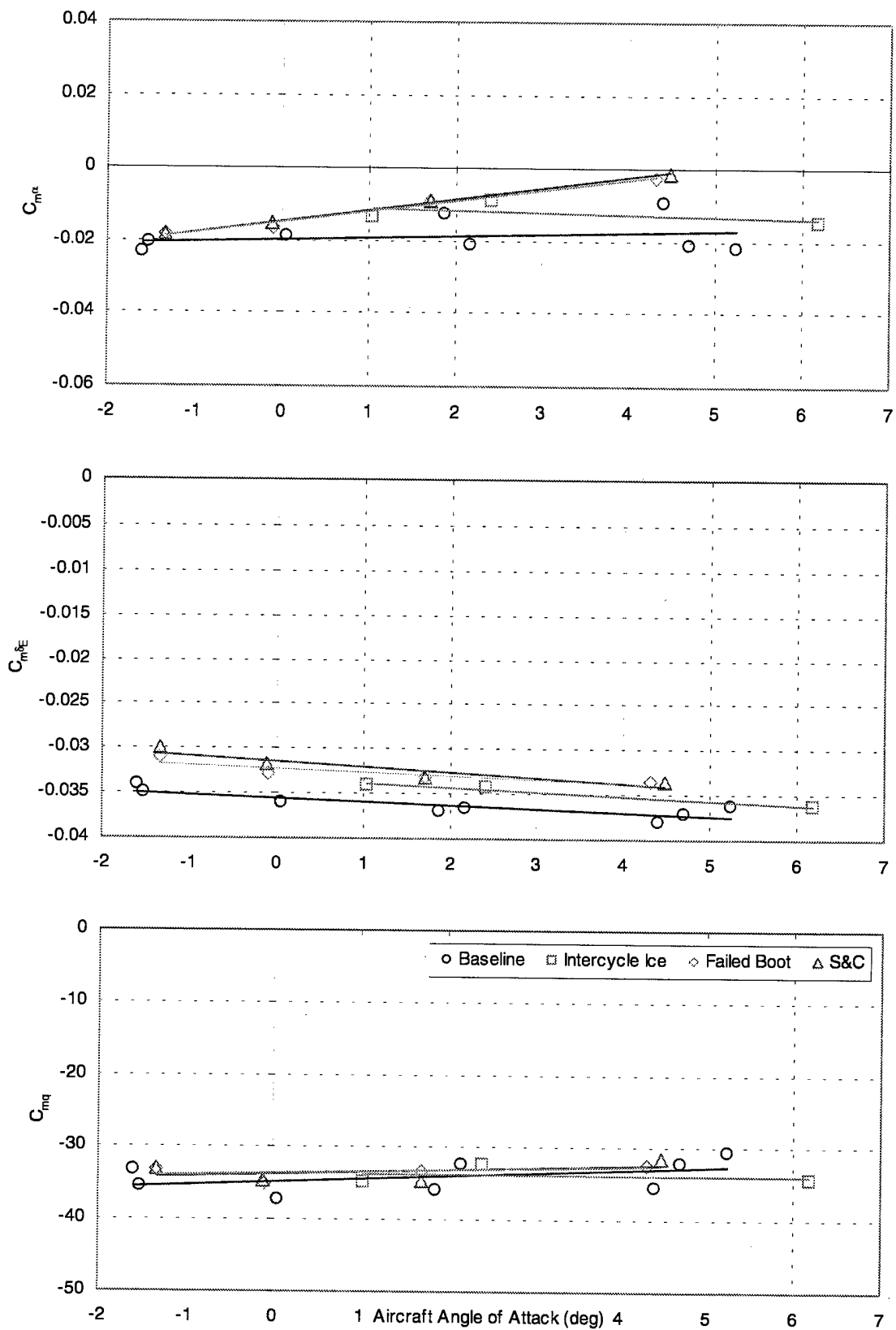


Figure 69. Icing effects on pitching moment derivatives,  $\delta F = 10^\circ$ .



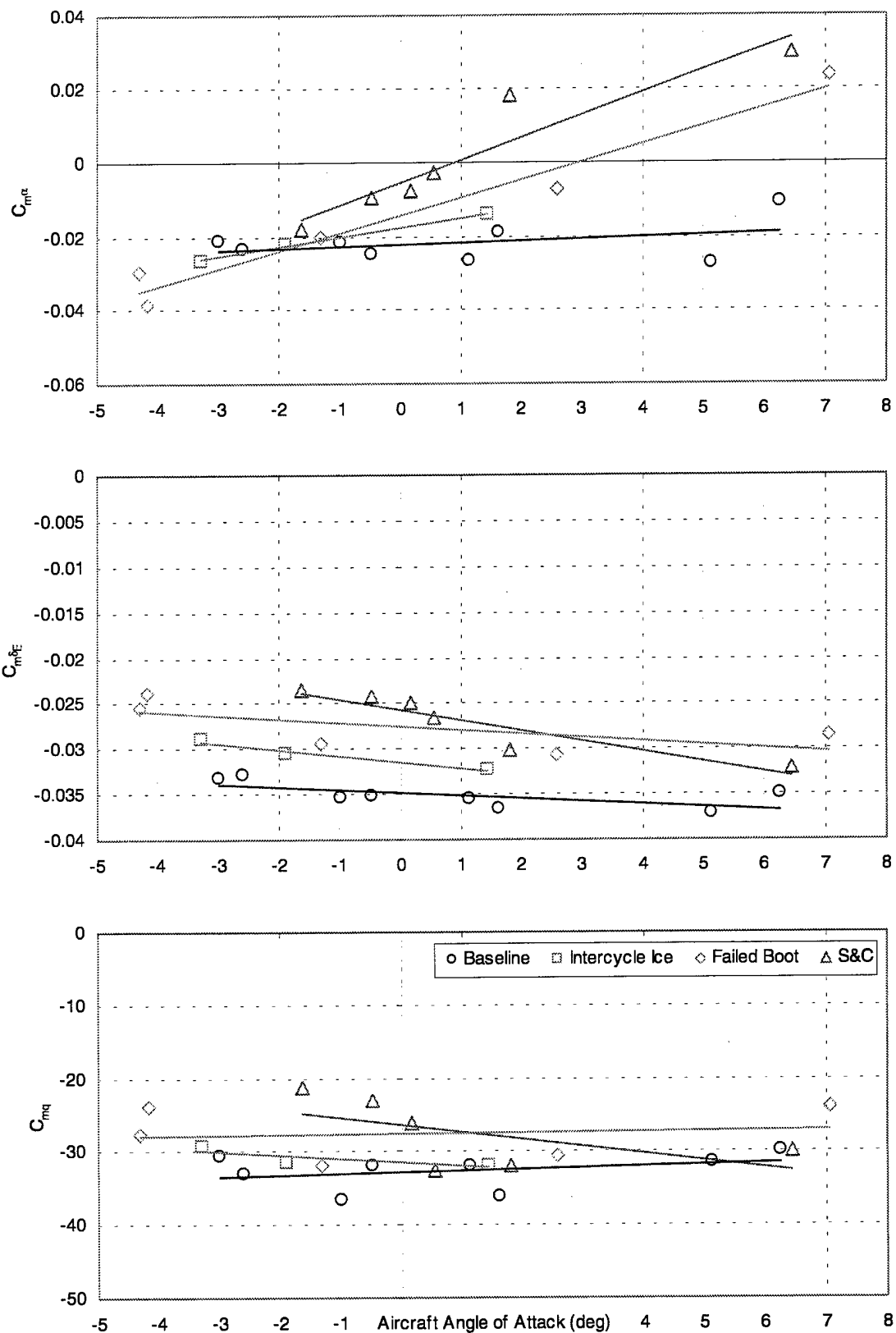


Figure 70. Icing effects on pitching moment derivatives,  $\delta F = 20^\circ$ .

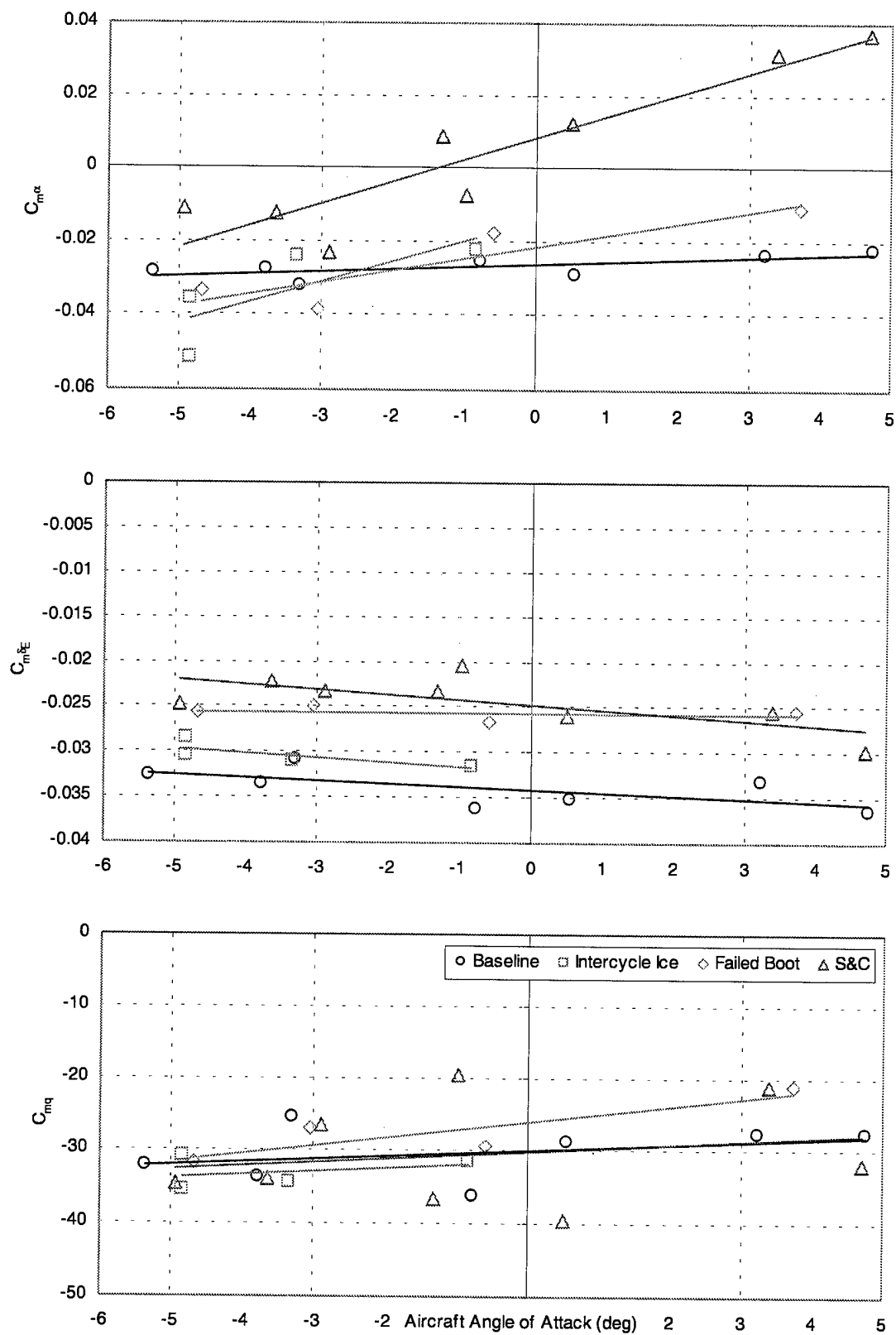


Figure 71. Icing effects on pitching moment derivatives,  $\delta F = 30^\circ$ .

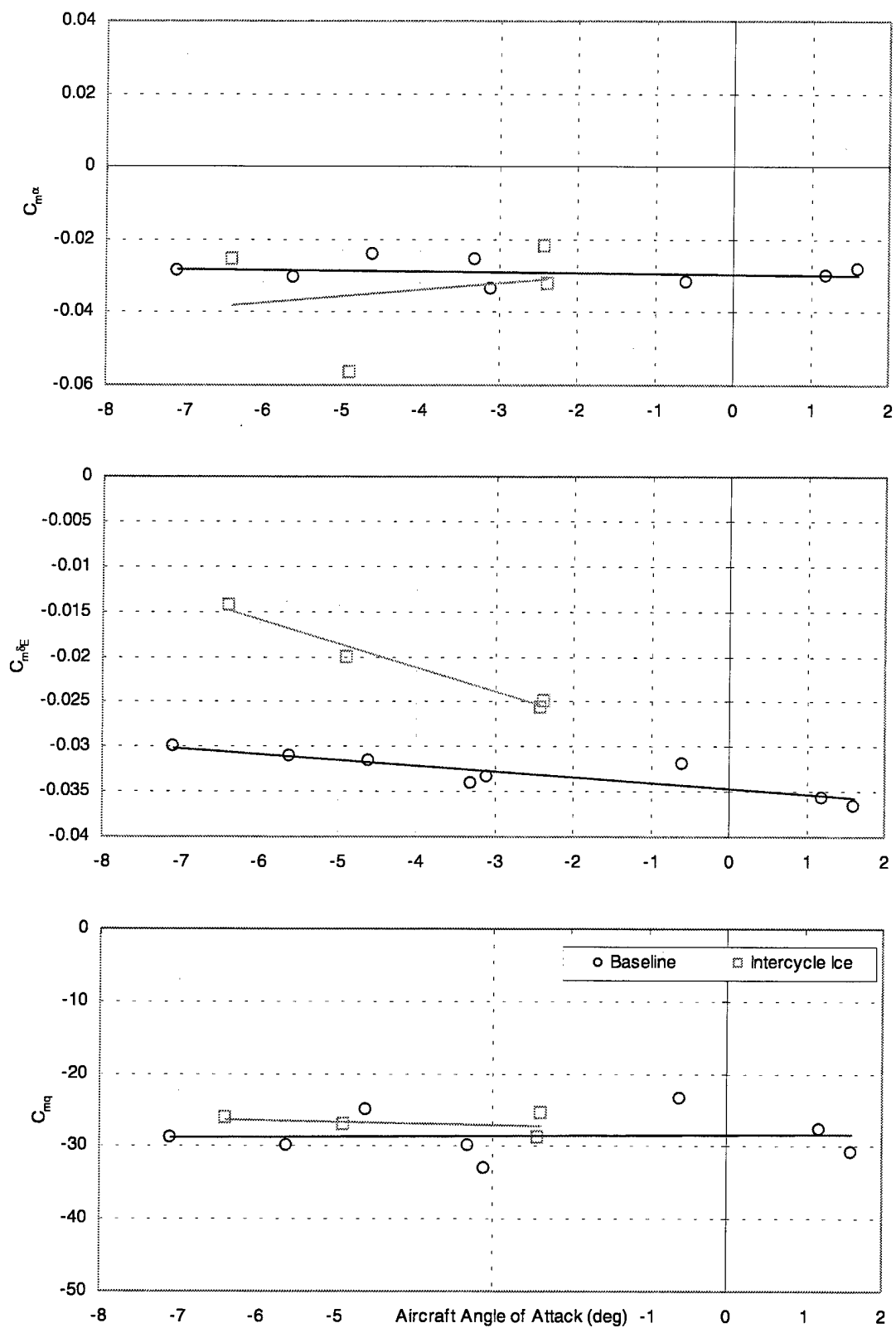


Figure 72. Icing effects on pitching moment derivatives,  $\delta F = 40^\circ$ .

## 7.4 Parameter Estimation Conclusions

A parameter analysis of the flight data was used to quantify the degradation resulting from Inter-Cycle, Failed Boot, and the S&C ice shapes attached to the leading edge of the Twin Otter tailplane. The analysis was conducted as a function of angle of attack with flap settings as high as  $\delta F = 40^\circ$ .

The Inter-Cycle ice shape was shown to slightly degrade the baseline airplane. Up through  $\delta F = 10^\circ$ , the effects of the Inter-Cycle ice were minimal. With  $\delta F = 20^\circ$  and  $\delta F = 30^\circ$  the elevator control effectiveness was reduced about 10%, while changes in static stability and pitch damping were small. With  $\delta F = 40^\circ$ , the Inter-Cycle ice shape began to significantly decrease the elevator control effectiveness.

The Failed Boot ice shape showed a larger degradation. The ice shape effects were minimal up through  $\delta F = 10^\circ$  flap setting with the primary effect being about an 8% decrease in elevator control effectiveness. The elevator control effectiveness dropped by 17% at  $\delta F = 20^\circ$  and by 27% at  $\delta F = 30^\circ$ . Significant reductions in static stability are also apparent.

The S&C ice shape yielded the largest degradation shown in the parameters. At  $\delta F = 0^\circ$  and  $\delta F = 10^\circ$ , the primary effect was about an 8% decrease in elevator control effectiveness. The elevator control effectiveness was reduced by 27% at  $\delta F = 20^\circ$  and by 33% at  $\delta F = 30^\circ$ . At both  $\delta F = 20^\circ$  and  $\delta F = 30^\circ$ s, the vehicle became strongly statically unstable with increasing angle of attack. Trends in pitch damping were less certain due to data scatter.

## 8. Guest Pilot Workshop

At the conclusion of the flight tests, a Guest Pilot Workshop was conducted to provide a forum to rapidly disseminate valuable lessons learned in the Tailplane Icing Program to the user community and to gather flight data using non-TIP pilots. An international group representing various facets of the aviation industry – aviation regulatory agencies, aircraft manufacturers and aviation media pilots/reporters – were invited. In total, 15 guest pilots and engineers had the opportunity to fly the NASA Twin Otter with the Failed Boot ice shape on the tail and experience the unique flying qualities of an aircraft with an ice-contaminated tailplane. The purpose of this section is to provide an overview of the workshop and show results from a handling qualities assessment of the simulated approach and balked landing maneuver under specified conditions.

### 8.1 Attendees

A total of 15 guest pilots and engineers attended the workshop. Table 8 lists the affiliation of each guest pilot that attended the workshop. Due to the relatively short duration time of each flight, the workshop was divided into three sequences to reduce the wait time for each guest pilot. The attendees for the first sequence were the FAA, Transport Canada, and non-TIP NASA pilots. Attendees for the second sequence covered the airframe manufacturers. The final sequence was devoted to the aviation media pilots.

Sequence 1	Sequence 2	Sequence 3
FAA, Test Pilot	Bombardier, Test Pilot	"Airline Pilot", Pilot
FAA, Test Pilot	Bombardier, Design Engineer/Pilot	"Airline Pilot", Pilot/Reporter
Transport Canada, Test Pilot	Cessna, Design Engineer/Pilot	"Aviation Week", Pilot/Reporter
NASA, Test Pilot	Raytheon, Design Engineer/Pilot	"Commercial & Business Aviation", Pilot/Reporter
	Raytheon, Test Pilot	"Flying Magazine", Pilot/Reporter
		"Professional Pilot", Pilot/Reporter

Table 8. Guest pilot attendees.

### 8.2 Guest Pilot Workshop Flight Test Procedures and Maneuvers

Guest pilots performed each maneuver listed below from the left seat with a NASA safety pilot occupying the right seat. The data acquisition system was running during all maneuvers. The video cameras recorded the horizon, pilot control inputs as well as comments, and tailplane tuft activity while performing test maneuvers.

In order to provide a useful experience for multiple pilots in one flight session, a truncated test matrix was developed from the full test matrix to demonstrate the findings of the TIP. The maneuvers were:

- Data Compatibility
- Flap Transitions and Elevator Doublets
- Steady Heading Sideslips
- Wind up turns
- Constant Airspeed Thrust Transitions
- Pushover Maneuvers
- Simulated Instrument Approach and Balked Landing

(For more detail on maneuver description, see Section 6).

At the conclusion of the demonstration flight, debriefings were held and recorded with the intent of capturing immediate pilot impressions. NASA received written reports on the workshop from most participants that contained the following information on:

- unusual or unexpected flight characteristics observed during the course of the demonstration program
- suggestions to improve the technical content of NASA's tailplane icing research program

- impressions of the pushover maneuver vs. the simulated approach task or repeat doublet maneuvers for assessing safe flight characteristics

### 8.3 Handling Qualities Assessment

The simulated approach and balked landing maneuver was developed after the first sequence of guest pilots. The discussion in those debriefings suggested that there needed to be a task-oriented maneuver to assess the reduced tail-plane performance. The simulated instrument approach and balked landing maneuver was provided two mission task elements (MTE) that could be used for handling qualities assessment. The maneuver was flown at altitude and with "heads down." To simulate course and glide slope corrections, commands to change both rate of descent (ROD) and heading were made every 20 seconds all the while maintaining a constant 1.3Vs velocity. Specifically, heading changes of  $\pm 5^\circ$  off a reference heading, and RODs of 0, 500, or 1000 ft/min were ordered. The expected tolerance in ROD was  $\pm 100$  ft/min. The RODs required the pilot to adjust the throttle setting. See Figure 64 for the idealized flight path (dashed line). The 20 sec intervals required the pilot to make fairly aggressive control and thrust inputs. At the conclusion of the simulated approach MTE, a go-around was commanded. The go-around was accomplished by increasing thrust and raising the nose without changing the flap configuration. After the pilot accomplished a steady positive rate of ascent, the flaps were raised. The pilot immediately ranked the Twin Otter's flying qualities based on the Cooper-Harper handling qualities rating scale (Figure 73) for the approach MTE and go-around MTE. This maneuver was only flown with the Failed Boot ice shape and with flaps set to  $\delta F = 20^\circ$  and  $30^\circ$ .

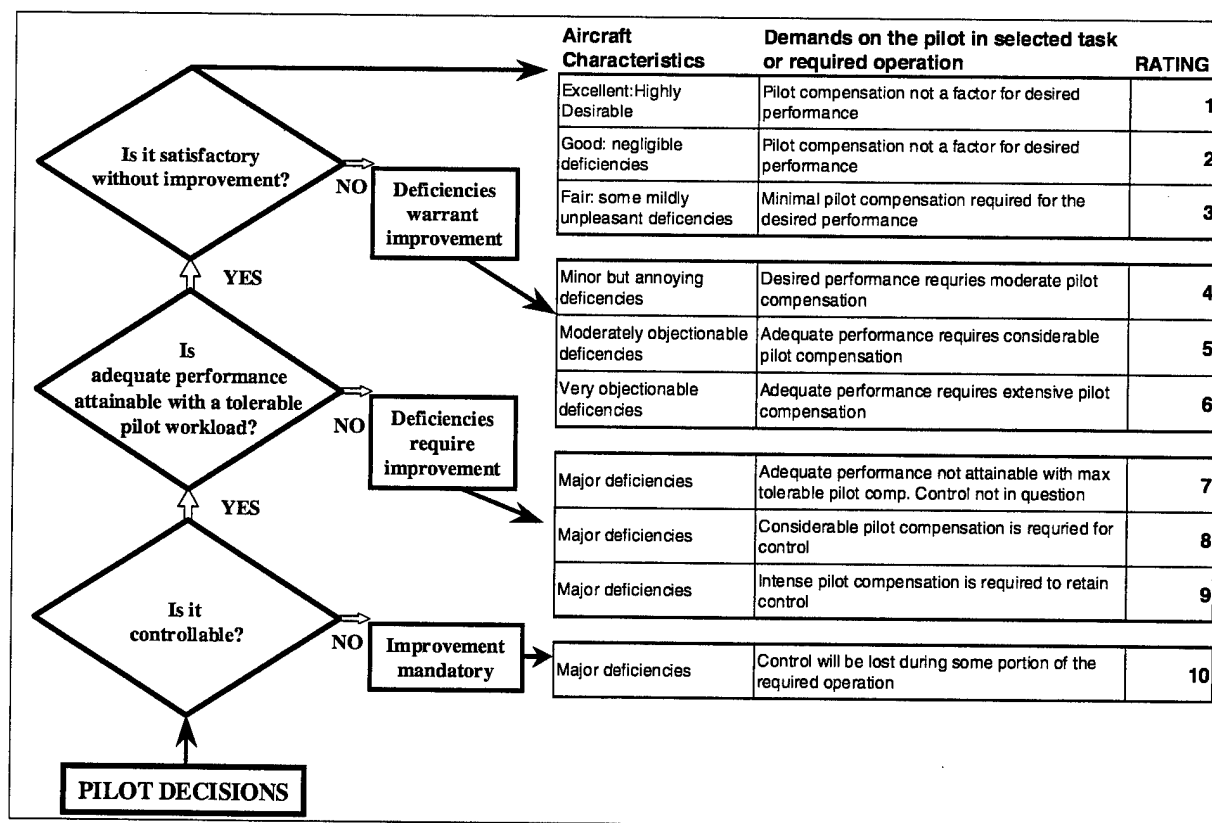


Figure 73. Cooper-Harper handling qualities rating flow chart.

The handling qualities ratings (HQR) for five of the guest pilots and the average value are shown in Figure 74. Separate ratings were given for the simulated instrument approach and go-around MTE's with the aircraft configured with flaps at  $\delta F = 20^\circ$  and at  $\delta F = 30^\circ$ . By doing so, it is clearly seen that the handling qualities of aircraft with  $\delta F = 20^\circ$

are much better than the handling qualities of the aircraft with at  $\delta F = 30^\circ$ . Likewise, in both flap cases examined, it can be seen that the go-around MTE required more pilot compensation than the approach MTE.

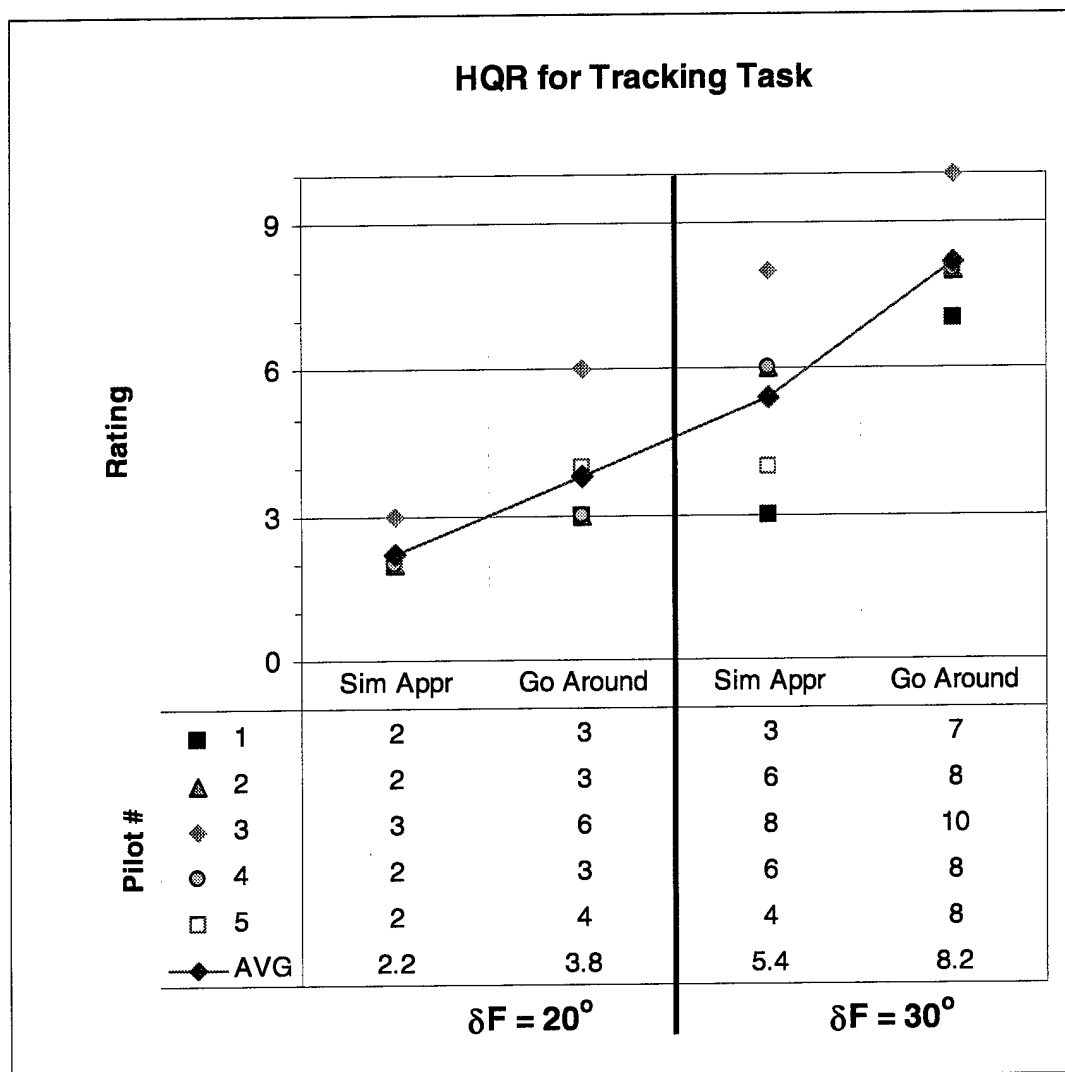


Figure 74. Cooper-Harper ratings for approach and go-around MTE.

The significance of these HQRs is the agreement of the pass/fail criteria set up in the elevator doublet analysis. With the Failed Boot ice shape on the tail, CFR's were experienced during elevator doublets with  $\delta F = 30^\circ$ , but not with  $\delta F = 20^\circ$ . Likewise, the HQR for the  $\delta F = 30^\circ$  suggested that there were major deficiencies in the aircraft characteristics that required considerable pilot compensation to control the aircraft during the go-around task. However, the HQR for the  $\delta F = 20^\circ$  case, suggested that there were minor but annoying deficiencies in the aircraft characteristics.

## 9. Concluding Remarks

The purpose of this section is to provide general comments and conclusions on the entire project and draw connections across the previous sections.

### 9.1 Data Analysis Techniques

The flight data acquired in the TIP included steady-state 1G test points and dynamic maneuvering test points about the pitch axis with the intention of increasing the steady-state tailplane angle of attack. Data from the steady-state test points were analyzed through visual inspection of trends of a variety of parameters. Likewise, data from the dynamic maneuvering test points were also analyzed through visual inspection of time history plots, co-plots, and cross-plots of selected variables. In addition to these visual inspection analysis techniques, a computational analysis method was used with a subset of the dynamic maneuvering test points to estimate stability and control coefficients for a mathematical model that was representative of the test aircraft. Lastly, a different subset of the dynamic maneuvering test points was analyzed using visual inspections of pilot rankings of the aircraft flying qualities.

Each of these methods proved useful in some capacity by depicting the degradation in iced tailplane performance and the resultant degradation in flight dynamics and handling qualities.

- For the steady state data, two key methods were developed that indicated degradation in tailplane performance and control anomalies. First, the difference in the elevator deflection ( $\delta E$ ) required for speed for the clean and iced case for consistent aircraft configuration (CG,  $\delta F$ ,  $C_T$ , landing gear, etc) clearly indicated significant tailplane performance losses. Second, the difference in elevator hinge moment ( $C_{He}$ ) required for speed for a clean and iced case for a consistent aircraft configuration, indicated tailplane performance losses and provided insight as to impending controllability problems.
- For all of the dynamic maneuvering data, visual inspection of time history co-plots of stick force and elevator deflection ( $FYE$  &  $\delta E$ ), and pitch rate and elevator deflection ( $q$  &  $\delta E$ ), were key in the assessment of control force anomalies and the reduced pitch damping characteristics of an iced tailplane. This technique was improved by examining cross-plots of stick force versus normal acceleration ( $FYE$  vs.  $N_z$ ) and pitch rate versus elevator deflection ( $q$  vs.  $\delta E$ ). These techniques clearly indicated control force lightening and reversal, reduced pitch damping when the elevator was in the TED position, and reduced elevator effectiveness.
- For the elevator doublet maneuvers, the estimation of stability and control parameters proved useful by providing numerical values reflecting the reduced stability and control coefficients due to tailplane icing. The results clearly showed a reduced elevator effectiveness ( $C_{m\delta E}$ ) and static longitudinal stability ( $C_{m\alpha}$ ) as ice shape severity increased and tailplane AOA increased due to flap deflection. This analysis method did not reveal significant changes in the pitch damping derivative ( $C_{mq}$ ), which were revealed by the visual techniques described above. This is likely a result of the time periods examined for each analysis method. The technique used by pEst estimated stability and control coefficients that best represented the entire doublet maneuver – both pitch up and pitch down. The visual technique focused on the part of the maneuver when the elevator was fixed TED and the tailplane AOA was most negative. Since the pEst technique fitted the whole maneuver, the values may not be representative of events that took place within only part of the maneuver. Therefore, the  $C_{mq}$  results from pEst may not accurately reflect the damping characteristics at the most critical condition for the tailplane. To improve these results, maneuvers with smaller amplitudes could be developed specifically to explore this flight regime.
- For the simulated approach and balked landing, the handling qualities results provided numerical indicators of the reduction of the pilot's ability to accomplish a specified task with an iced tailplane. These results are very significant since they provide insight into the ultimate question with an iced tailplane – how well can a pilot accomplish a task with the aircraft in the potentially critical condition? Inherently, the ratings provide feedback on whether the aircraft has deficiencies that are tolerable or require improvement. Another significant aspect of this analysis method is that it employs a maneuver that is part of the normal flight operation.



## 9.2 Maneuvers

The maneuvers chosen in this flight project ranged from steady state to dynamic maneuvers. Each type had value as revealed through the analysis techniques described above. The dynamic maneuvers provided a means to push the  $\alpha_i$  beyond the steady state values  $\alpha_{i0}$  by some increment,  $\Delta\alpha_i$ . The increment depended on  $\alpha_{wing}$ ,  $V$  and  $q$  and was largest in magnitude for the minimum-G pushover maneuver at low speeds. However, for a given ice shape, the tailplane stall margin is not only a function of the  $\alpha_i$  but also  $\delta E$ . With the pushover maneuver, the elevator is TED, which by itself increases the tail stall margin. But since the  $\Delta\alpha_i$  is large in the pushover maneuver at low speeds, the combined change in  $\alpha_i$  and  $\delta E$  indicated ice-contaminated tail stall characteristics typically at lower flap settings than the other dynamic and steady state maneuvers. This may appear as an added level of conservatism, but it should be clearly noted that the  $\delta E$  during the pushover is not in a position likely to be observed in normal flight operations. The elevator doublet provided information on tailplane performance degradation equivalent to the pushover at similar configurations by analyzing the pitch response characteristics. During the push part of the elevator doublet,  $\delta E$  was less trailing edge down, and exhibited stalling tendencies at a less negative  $\alpha_i$  than the pushover. Thrust transitions and the balked landing maneuvers were performed with a more appropriate  $\delta E$  and also revealed deficiencies due to the tailplane icing, but the aircraft was configured with larger flap settings than the pushover. In summary, each of these maneuvers can provide an indication of reduced tailplane performance. The difficulty is not in the choice of the maneuver, but in determining the threshold of acceptability that is universally applicable and widely acceptable. Determining thresholds was never the intent of this project and the nature of these results are far too limited to suggest those thresholds.

## 9.3 Aircraft Configuration

Results presented in this report are for one specific aircraft – a modified DHC-6 Twin Otter, and as such, the absolute values in parameters such as  $\alpha_i$  are limited to this aircraft. Likewise, it is not possible without further study to comment on aspects of tailplane design or other aircraft features such as wing and tail positions, wing and tail sweep and taper, airfoil sections, or propulsion system type. Generalizations on design aspects such as those would require a different means than the type of experimental testing performed in this project.

However, there are some aspects of aircraft configuration to which comments can be made. Since the data were collected over a wide range of configurations on the Twin Otter, some general insights were gained on critical and non-critical aircraft configurations for tailplane stall with respect to a few of the maneuvers flown. These generalizations are listed in Table 9. In all cases, the forward CG and maximum flap deflection are critical to achieving the greatest demand on the horizontal tailplane. Likewise, the aft CG and minimum flap deflection were non-critical in all cases. Airspeeds varied depending on the maneuver used for testing. Regarding thrust settings, it is logical that the criticality of high thrust was caused by the vertical displacement of the thrust line above the CG in the case of the Twin Otter. So the  $C_T$  listed in the table are likely to be limited to similar high thrust line aircraft. This table may serve to reduce tests for tailplane icing sensitivity at the non-critical aircraft configuration.

Maneuver	Critical	Non-Critical
Steady wings level 1G	CG=fwd, $\delta F$ =max, $V=V_{FE}$ , $C_T$ =max	CG=aft, $\delta F$ =0, $V=V_S$ , $C_T$ =min
Pushover	CG=fwd, $\delta F$ =max, $V=V_S$ , $C_T$ =max, $N_z$ =min	CG=aft, $\delta F$ =0, $V=V_{cruise}$ , $C_T$ =min, $N_z$ >min
Elevator doublet	CG=fwd, $\delta F$ =max, $V=V_{FE}$ , $C_T$ =max	CG=aft, $\delta F$ =0, $V=V_S$ , $C_T$ =min
Thrust transition	CG=fwd, $\delta F$ =max, $V=V_{FE}$ , $C_T$ =max	CG=aft, $\delta F$ =0, $V=V_S$ , $C_T$ =min

Table 9. Critical and non-critical aircraft configurations for tailplane stall.

#### 9.4 Closing Commentary

The body of knowledge on ice-contaminated tailplane stall has been significantly advanced through the NASA/FAA Tailplane Icing Program by gaining a better understanding of the basic aeroperformance issues of a tailplane and the aerodynamic characteristics of the pushover and several alternate maneuvers. Although the progress made in this program was noteworthy, it did not provide answers to some of the key questions that remain about ice-contaminated tailplane stall. Some of these questions are:

- What aircraft design aspects yield a greater or lesser susceptibility to ICTS?
- What experimental techniques or computational tools can be used in the design phases to screen susceptibility to ICTS?
- What aspects of the ice contamination cause critical degradation of tailplane performance?
- What are universally applicable and widely acceptable pass/fail criteria for flight test maneuvers that screen susceptibility to ICTS?

Although these are very difficult questions to provide absolute answers, efforts are in progress at NASA, the FAA and other organizations to improve the state of our knowledge and perhaps give guidance to answering some of these difficult questions.

## 10. References

- 1 Ratvasky, T.P., *NASA/FAA/OSU Tailplane Icing Program Requirements Document*, May 1994.
- 2 Ranaudo, R.J., Baterson, J.G., Reehorst, A.L., Bond, T.H. & O'Mara, T.M., *Determination of Longitudinal Aerodynamic Derivatives Using Flight Data From an Icing Research Aircraft*, AIAA Paper 89-0754, NASA TM 101427, 1989.
- 3 Ratvasky, T.P. & Ranaudo, R.J., *Icing Effects on Aircraft Stability and Control Determined from Flight Data, Preliminary Results*. AIAA Paper 93-0398, NASA TM 105977, 1993.
- 4 Jordan, J.L., Platz, S.J. & Schinstock, W.C., *Flight Test Report of the NASA Icing Research Airplane*, KSR 86-01, Kohlman Systems Research, Inc., Lawrence KS, NASA CR-179515, 1986.
- 5 Pfeiffer, N.J., *Wake Rake Studies Behind a Swept Surface, Canard Aircraft*, Beechcraft Report, Sept. 1993.
- 6 Etkin, Bernard, *Dynamics of Flight – Stability and Control*, John Wiley & Sons, 1982.
- 7 Perkins, C.D. & Hage, R.E., *Airplane Performance Stability and Control*, John Wiley & Sons, 1949.
- 8 Ingelman-Sundberg, M. & Trunov, O.K., *Wind Tunnel Investigation of the Hazardous Tail Stall Due to Icing*, Swedish-Soviet Working Group Report No. JR-2, 1979.
- 9 Hiltner, D., McKee, M. & La Noé, K., *DHC-6 Twin Otter Tailplane Airfoil Section Testing In The Ohio State University 7'x10' Wind Tunnel*, NASA/CR—2000-209921/VOL1, 2000.
- 10 Gregorek, G.M., Dreese, J.J., & La Noé, K., *Additional Testing of the DHC-6 Twin Otter Iced Airfoil Section at the Ohio State University 7'x10' Low Speed Wind Tunnel*, NASA/CR—2000-209921/VOL2, 2000.
- 11 Dickson, B., *Aircraft Stability and Control for Pilots and Engineers*, Sir Isaac Pitman & Sons LTD, 1968.
- 12 Obert, E., *Low-Speed Stability and Control Characteristics of Transport Aircraft With Particular Reference to Tailplane Design*, AGARD Take-off and Landing, Jan 01, 1975.
- 13 Wojnar, Ronald T., *Recommended Method of Identification, Susceptibility to Ice Contaminated Tailplane Stall*, FAA Memorandum ANM-100, Apr 29, 1994.
- 14 Trunov, O.K. & Ingelman-Sundberg, M., *On the Problem of Horizontal Tail Stall Due to Ice*, Swedish-Soviet Working Group Report No. JR-3, 1985.
- 15 Murray, James E. & Maine, Richard E., *pEst Version 2.1 User's Manual*, NASA TM-88280, 1987.

## Appendix A. Flight Test Summaries, Research Aircraft, Ice Shapes and Instrumentation

Flight Date	Flight No.	Tail Config	CG	Comment
14-Sep-95	FLT 95-12	Baseline	fwd	A/C systems check in 0G
27-Sep-95	FLT 95-13	Baseline	fwd	SWL, steady pull up
28-Sep-95	FLT 95-14	Baseline	fwd	SWL
29-Sep-95	FLT 95-15	Baseline	fwd	SWL
02-Oct-95	FLT 95-16	Baseline	fwd	SWL, DC added
03-Oct-95	FLT 95-17	Baseline	fwd	SWL, CHK added
10-Oct-95	FLT 95-18	Baseline	fwd	CHK points only, called back
10-Oct-95	FLT 95-19	Baseline	fwd	SWL, CTL=0
11-Oct-95	FLT 95-20	Baseline	fwd	SHSS
11-Oct-95	FLT 95-21	Baseline	fwd	SHSS
12-Oct-95	FLT 95-22	Baseline	fwd	SHSS
17-Oct-95	FLT 95-23	Baseline	fwd	PO
18-Oct-95	FLT 95-24	Baseline	fwd	PO
19-Oct-95	FLT 95-25	Baseline	fwd	PO
20-Oct-95	FLT 95-26	Baseline	fwd	PO
23-Oct-95	FLT 95-27	Baseline	fwd	PO CTL=0
23-Oct-95	FLT 95-28	Baseline	fwd	PO, TPR, WT
25-Oct-95	FLT 95-29	Baseline	fwd	SWL, SHSS
26-Oct-95	FLT 95-30	Baseline	fwd	Alt maneuvers, SR, go-around, PO max thrust
26-Oct-95	FLT 95-31	Baseline	fwd	Alt maneuvers, SR, go-around, PO max thrust
30-Oct-95	FLT 95-32	Baseline	fwd	air-air video document of maneuvers

Table A-1. 1995 flight test summary.

Flight Date	Flight No.	Tail Config	CG	Comment
10-Jul-97	FLT 97-31	Baseline	fwd	Trailing Cone Flt
23-Jul-97	FLT 97-32	Baseline	fwd	bad ZOCs
23-Jul-97	FLT 97-33	Baseline	fwd	bad ZOCs
24-Jul-97	FLT 97-34	Baseline	fwd	bad ZOCs
25-Jul-97	FLT 97-35	Baseline	fwd	bad ZOCs
19-Aug-97	FLT 97-36	Baseline	fwd	ZOC's repaired
20-Aug-97	FLT 97-37	Baseline	fwd	
21-Aug-97	FLT 97-38	Baseline	aft	
21-Aug-97	FLT 97-39	Baseline	aft	
26-Aug-97	FLT 97-40	Inter-Cycle ice	fwd	
02-Sep-97	FLT 97-41	Inter-Cycle ice	fwd	thrust transition developed
05-Sep-97	FLT 97-42	Inter-Cycle ice	fwd	
05-Sep-97	FLT 97-43	Inter-Cycle ice	fwd	
13-Sep-97	FLT 97-44	Failed Boot Ice	fwd	
17-Sep-97	FLT 97-45	Failed Boot Ice	fwd	full tail stall
18-Sep-97	FLT 97-46	Failed Boot Ice	fwd	
18-Sep-97	FLT 97-47	Failed Boot Ice	fwd	air-air video document of maneuvers
22-Sep-97	FLT 97-48	S&C Ice	fwd	
22-Sep-97	FLT 97-49	S&C Ice	fwd	
24-Sep-97	FLT 97-50	S&C Ice	fwd	
24-Sep-97	FLT 97-51	S&C Ice	fwd	
26-Sep-97	FLT 97-52	Baseline	fwd	limited repeat w/ good ZOCs
06-Oct-97	FLT 97-53	Failed Boot Ice	fwd	Guest Pilot Workshop I
07-Oct-97	FLT 97-54	Failed Boot Ice	fwd	Guest Pilot Workshop I
15-Oct-97	FLT 97-55	Failed Boot Ice	fwd	develop balked landing
21-Oct-97	FLT 97-56	Failed Boot Ice	fwd	Guest Pilot Workshop II
23-Oct-97	FLT 97-57	Failed Boot Ice	fwd	Guest Pilot Workshop II
28-Oct-97	FLT 97-58	Failed Boot Ice	fwd	Guest Pilot Workshop III
28-Oct-97	FLT 97-59	Failed Boot Ice	fwd	Guest Pilot Workshop III
30-Oct-97	FLT 97-60	Failed Boot Ice	fwd	Guest Pilot Workshop III

Table A-2. 1997 flight test summary.

Characteristic	Low	High
Mass, kg	4,510	4,970
Inertia		
IX, kg-m <sup>2</sup>	26,190	26,660
IY, kg-m <sup>2</sup>	33,460	34,650
IZ kg-m <sup>2</sup>	47,920	51,650
IXZ, kg-m <sup>2</sup>	1,490	1,560
<b>Wing:</b>		
Area, m (ft)	39.02 (422.5)	
Aspect Ratio	10.06	
Span, m (ft)	19.81 (65.0)	
Mean Geometric Chord, m (ft)	1.98 (6.5)	
Airfoil Section	"DeHavilland High Lift" 17% thickness	
<b>Horizontal Tail:</b>		
Area, m (ft)	9.10 (98.18)	
Aspect ratio	4.35	
Span, m (ft)	6.30 (20.67)	
Mean geometric chord, m (ft)	1.45 (4.75)	
Airfoil section	NACA 63 <sub>A</sub> 213	
Tail Volume, V <sub>H</sub>	0.91	

Table A-3. Physical characteristics of research aircraft.

Parameter	Sensor	Range	Resolution (16 bit)
AX & AY	Sundstrand QA-700	± 1G	0.00003G
AZ	Sundstrand QA-700	+3G, -1G	0.00006G
p, q, r	Humphrey RG02-2324-1	± 60 °/s	0.0018 °/s
φ	Humphrey VG24-0636-1	± 90°	0.0027°
θ	Humphrey VG24-0636-1	± 60°	0.0018°
α aircraft	Rosemount 858 probe	± 15°	NA
β aircraft	Rosemount 858 probe	± 15°	NA
V aircraft, airspeed	Rosemount 542K2	0 to 190 knots	0.01 knots
Altitude	Rosemount 542K2	0 to 15,000 ft	8.2 ft
OAT	Rosemount 102AU1P	-20° to 30° C	0.041° C
δA <sub>L</sub> & δA <sub>R</sub>	SAC series 160	+19°, -16°	0.0091°
δE	SAC series 160	+14°, -26°	0.0128°
δR	SAC series 160	±16°	0.0080°
δF	SAC series 160	0 to 40°	0.0091°
Tail Flow Probe	Scannivalve ZOC14IPTCU/8DPx	± 0.72 psi	4.4 e-5 psi
Tail Pressure Belt	Scannivalve ZOC14IPTCU/32Px	0-0.72 psi	2.2e-5 psi

Table A-4. Instrumentation specifications.

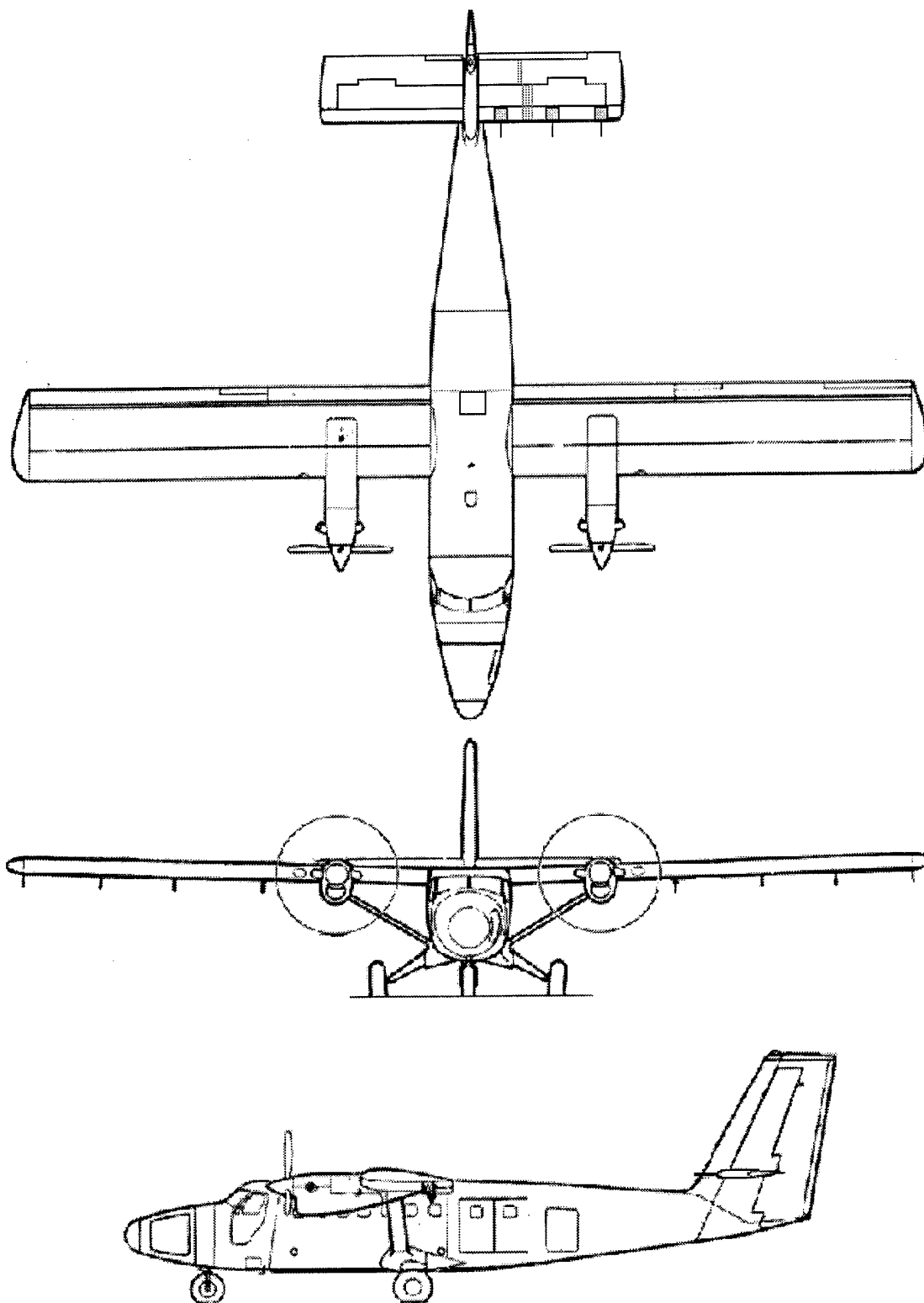
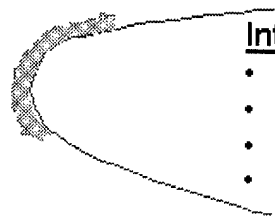
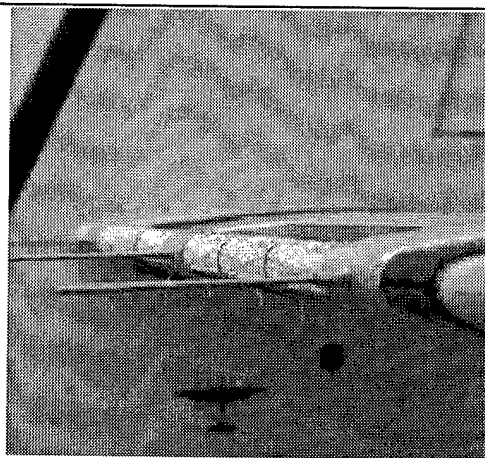


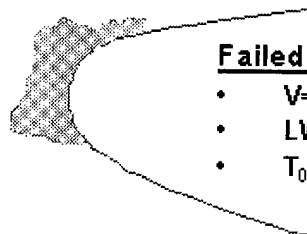
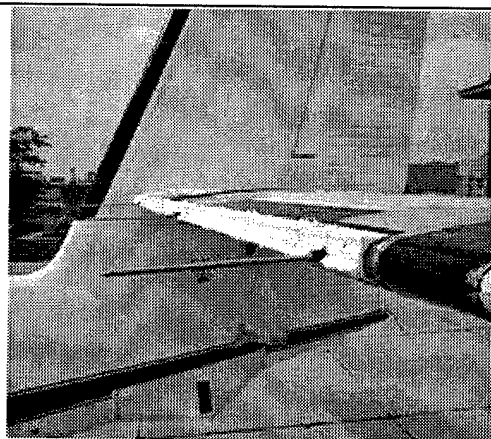
**Figure A-1. NASA Glenn Research Center Icing Research Aircraft.**



**Inter-cycle IRT Shape**

- $V=135$  kts,  $\alpha=-2.9^\circ$
- $LWC=0.5g/m^3$ ,  $MVD=20\mu m$
- $T_0=-4^\circ C$
- time=15 min, with boot cycle every 3 minutes

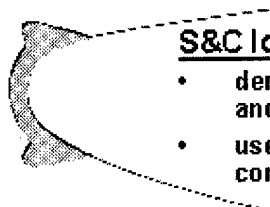
**Figure A-2. Inter-Cycle Ice on tailplane.**



**Failed Boot IRT Shape**

- $V=135$  kts,  $\alpha=-2.9^\circ$
- $LWC=0.5g/m^3$ ,  $MVD=20\mu m$
- $T_0=-4^\circ C$ , time=22 min

**Figure A-3. Failed Boot Ice on tailplane.**



#### S&C Ice Shape

- derived from in-flight photos and AD S-4
- used in previous stability & control flight tests

Figure A-4. S&C Ice on tailplane.

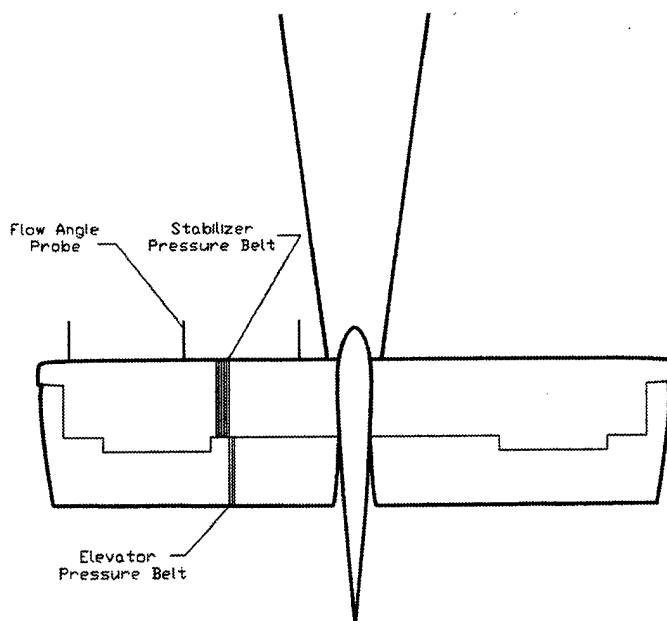
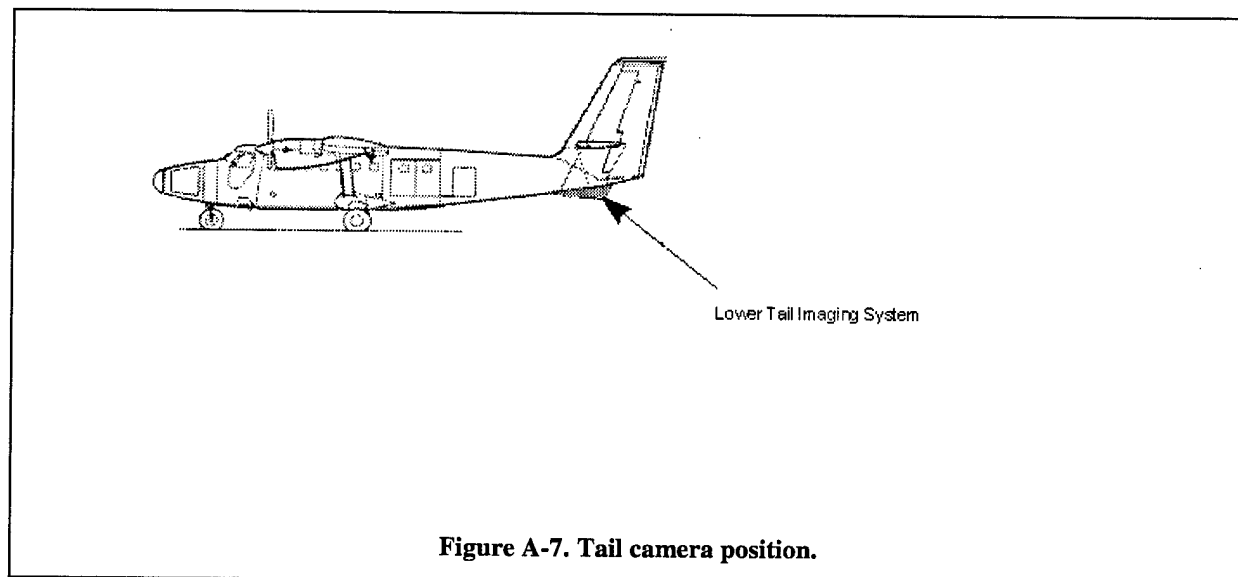
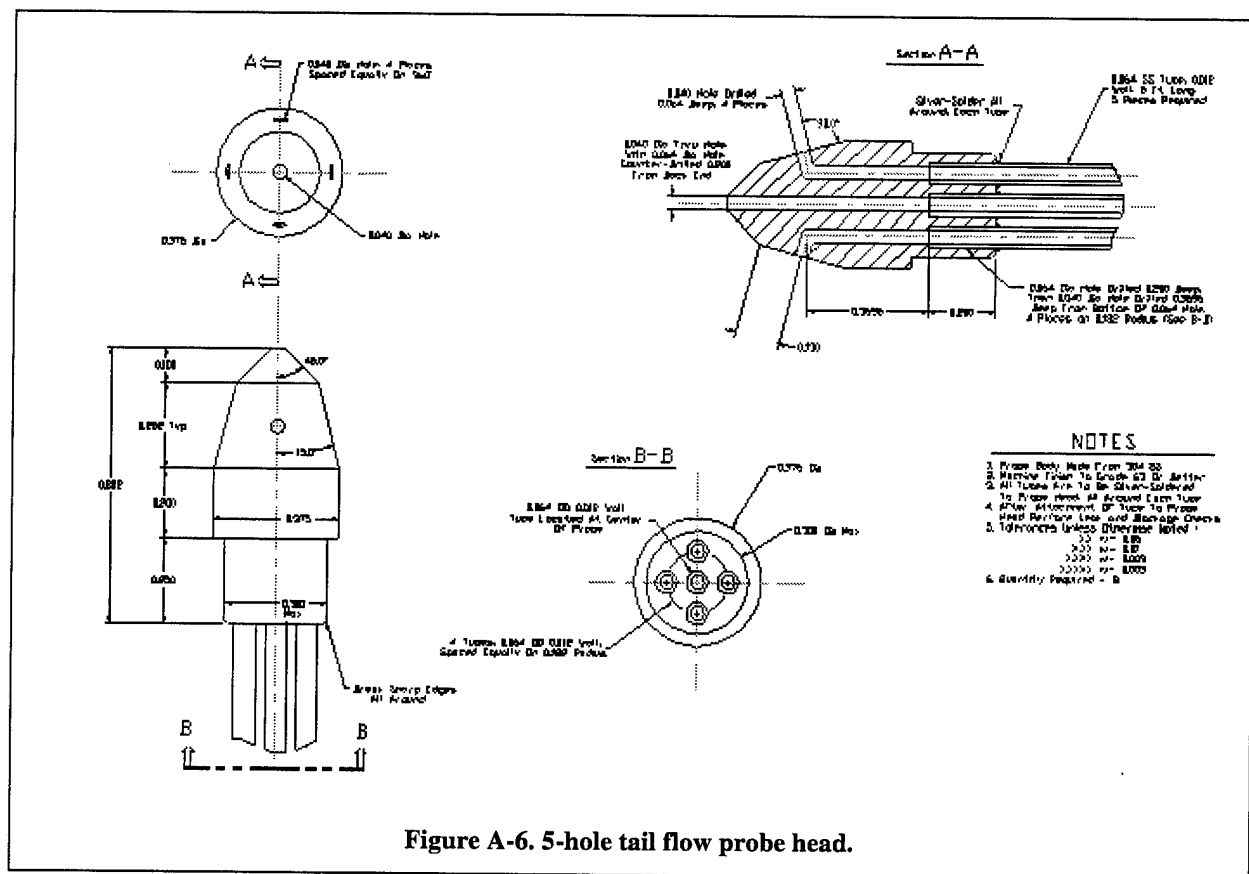


Figure A-5. Tail flow probes and pressure belt.





## Appendix B. Select Steady State Data Plots

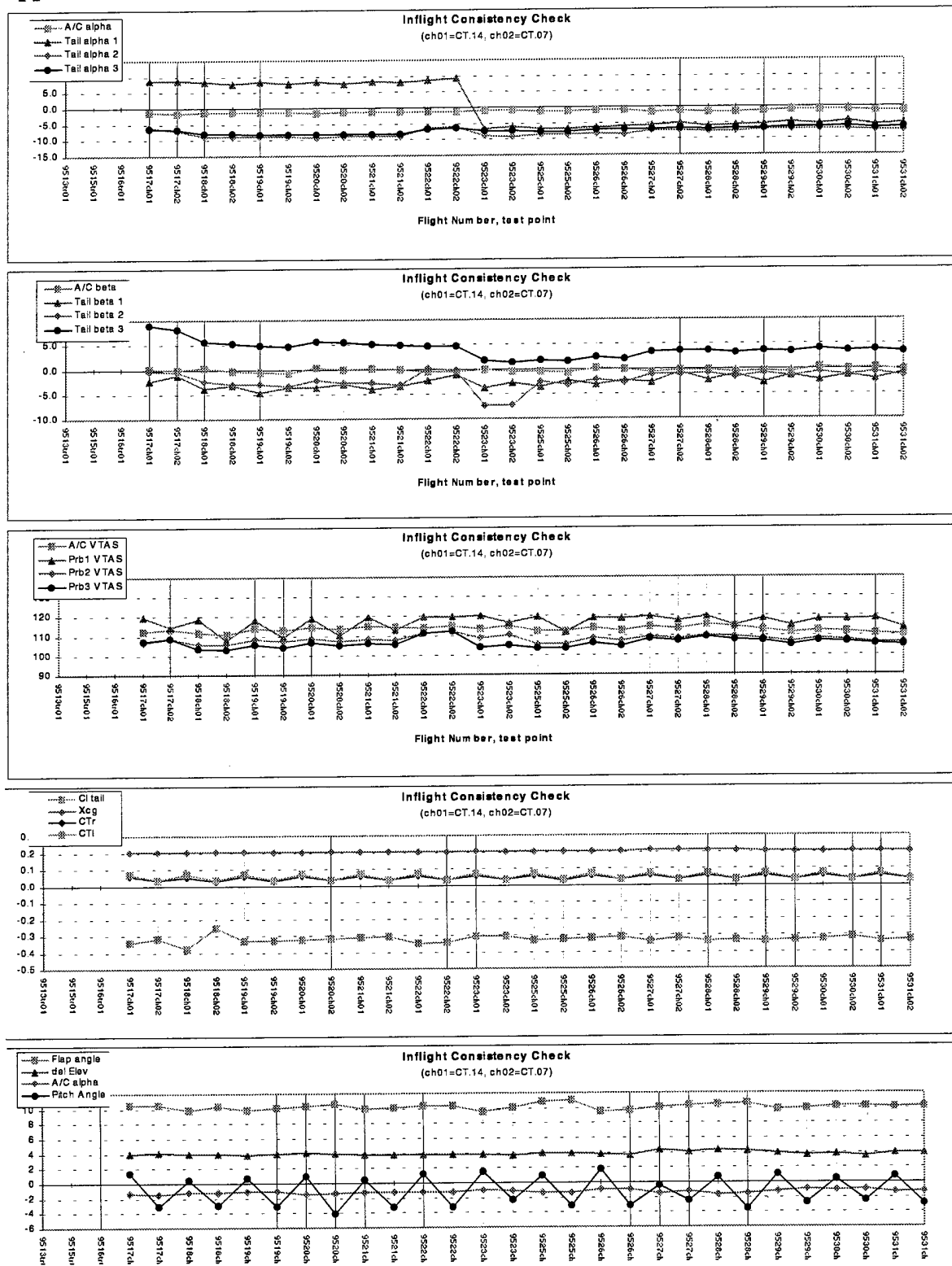


Figure B-1. 1995 data consistency results.

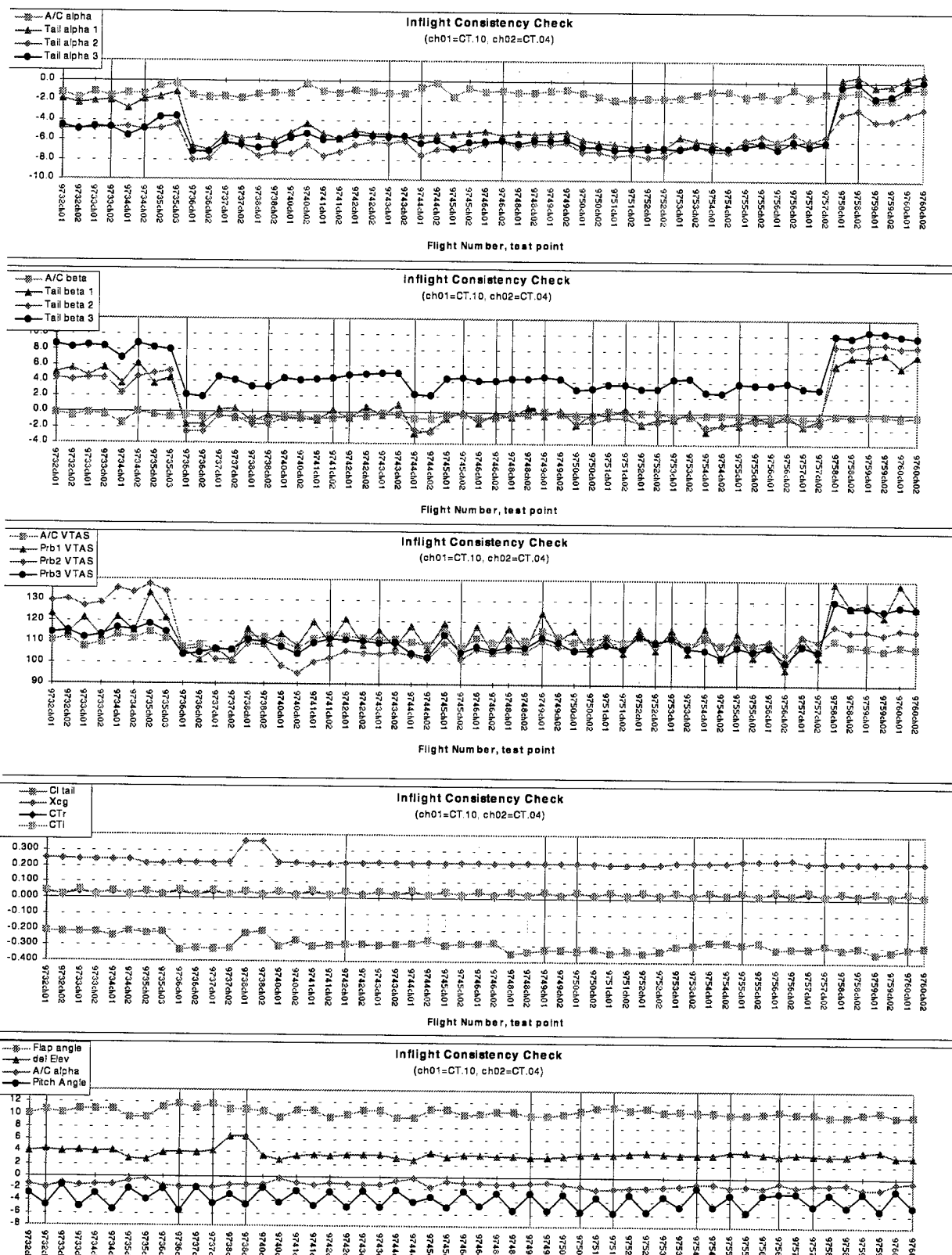


Figure B-2. 1997 data consistency results.

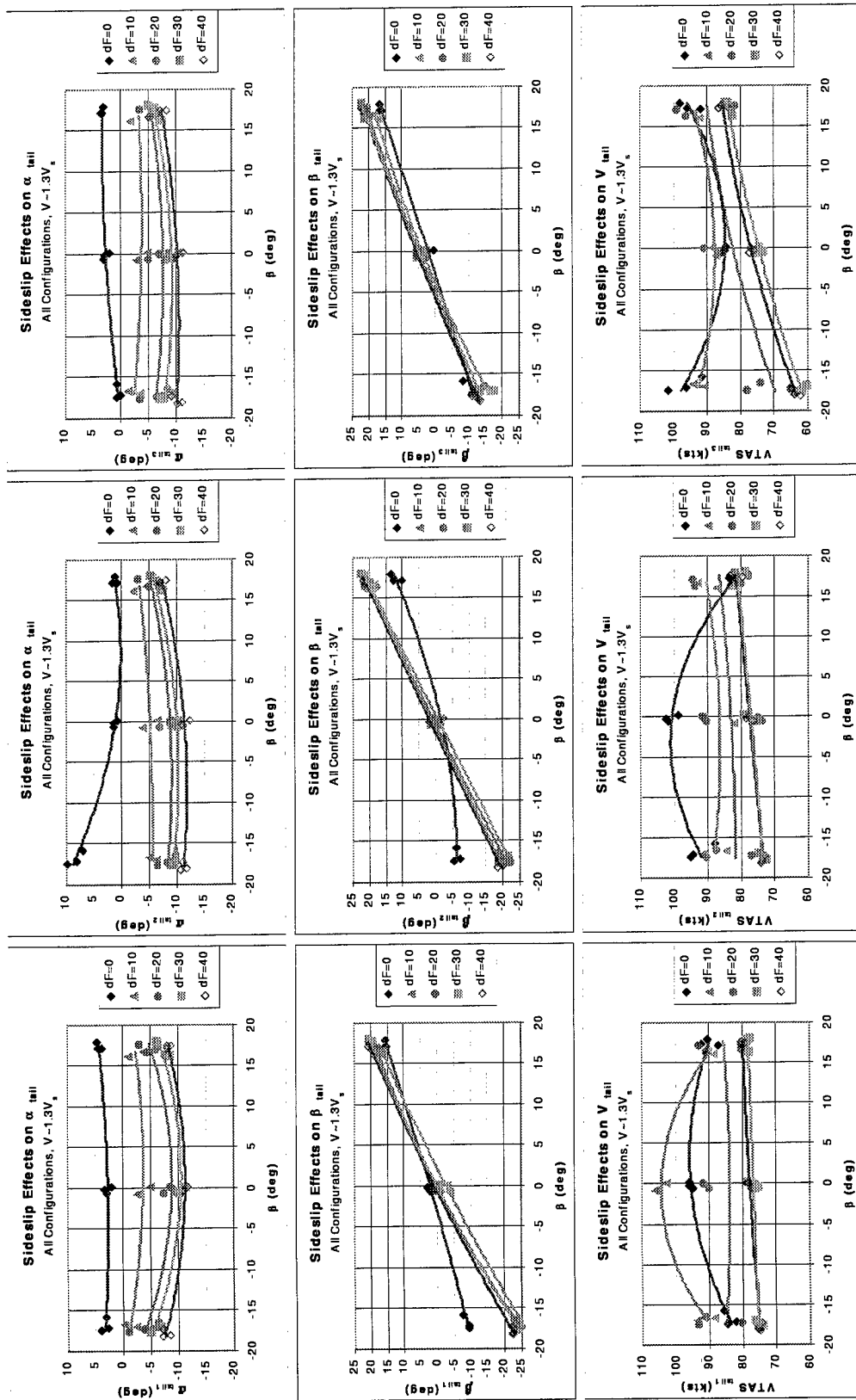
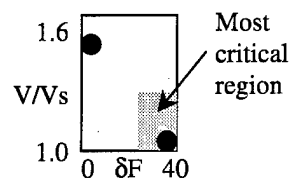


Figure B-3. Tail flow field during SHSS maneuvers.

## Appendix C. Time Histories of Select Dynamic Maneuvers

This appendix contains the time histories of 20 quantities for select test points. Two test points for each of the ice contamination cases are presented for both the pushover and elevator doublet maneuvers. For the thrust transition, only the extreme Baseline and Failed Boot cases are shown. These points were chosen to allow comparisons across several different parameters, including head-to-head comparisons of the pushover and elevator doublet. Note that there are two pages per figure. Also note that the velocities from the three tailplane probes ( $V_{probe}$ ) are true air speeds measured in knots, regardless of how indicated.

Also provided is a parameter space finder box for each ice contamination and maneuver case. As depicted in the figure on the right, the axes of this space are the flap deflection and the speed. For each maneuver, the most critical corner of this space is identified with a gray box. The dots mark where the two test points reside. As the flyable parameter space shrinks, so does the parameter box. The particular example depicted is of the Baseline pushover. The most critical region is at higher flap deflections and lower speed. The two test points indicated occurred at  $(\delta F, V/V_s) = (0, 1.5)$  and  $(40, 1.0)$ .



### List of Figures

Figure C-1. Pushover, Baseline,  $\delta F = 0^\circ$ ,  $VIAS = 1.50V_s = 100\text{kts}$ .

Figure C-2. Pushover, Baseline,  $\delta F = 40^\circ$ ,  $VIAS = 1.06V_s = 55\text{kts}$ .

Figure C-3. Pushover, Inter-Cycle Ice,  $\delta F = 0^\circ$ ,  $VIAS = 1.50V_s = 100\text{kts}$ .

Figure C-4. Pushover, Inter-Cycle Ice,  $\delta F = 40^\circ$ ,  $VIAS = 1.06V_s = 55\text{kts}$ .

Figure C-5. Pushover, Failed Boot,  $\delta F = 20^\circ$ ,  $VIAS = 1.33V_s = 75\text{kts}$ .

Figure C-6. Pushover, Failed Boot,  $\delta F = 20^\circ$ ,  $VIAS = 0.97V_s = 55\text{kts}$ .

Figure C-7. Pushover, S&C,  $\delta F = 0^\circ$ ,  $VIAS = 1.5V_s = 100\text{kts}$ .

Figure C-8. Pushover, S&C,  $\delta F = 20^\circ$ ,  $VIAS = 0.97V_s = 55\text{kts}$ .

Figure C-9. Elevator doublet, Baseline,  $\delta F = 0^\circ$ ,  $VIAS = 1.50V_s = 100\text{kts}$ .

Figure C-10. Elevator doublet, Baseline,  $\delta F = 40^\circ$ ,  $VIAS = 1.06V_s = 55\text{kts}$ .

Figure C-11. Elevator doublet, Inter-Cycle Ice,  $\delta F = 30^\circ$ ,  $VIAS = 1.59V_s = 85\text{kts}$ .

Figure C-12. Elevator doublet, Inter-Cycle Ice,  $\delta F = 40^\circ$ ,  $VIAS = 1.63V_s = 85\text{kts}$ .

Figure C-13. Elevator doublet, Failed Boot,  $\delta F = 30^\circ$ ,  $VIAS = 1.59V_s = 85\text{kts}$ .

Figure C-14. Elevator doublet, Failed Boot,  $\delta F = 30^\circ$ ,  $VIAS = 1.03V_s = 55\text{kts}$ .

Figure C-15. Elevator doublet, S&C,  $\delta F = 20^\circ$ ,  $VIAS = 0.97V_s = 55\text{kts}$ .

Figure C-16. Elevator doublet, S&C,  $\delta F = 30^\circ$ ,  $VIAS = 1.40V_s = 75\text{kts}$ .

Figure C-17. Thrust transition, Baseline,  $\delta F = 0^\circ$ ,  $VIAS = 1.20V_s = 80\text{kts}$ .

Figure C-18. Thrust transition, Baseline,  $\delta F = 40^\circ$ ,  $VIAS = 1.63V_s = 85\text{kts}$ .

Figure C-19. Thrust transition, Failed Boot,  $\delta F = 0^\circ$ ,  $VIAS = 1.20V_s = 80\text{kts}$ .

Figure C-20. Thrust transition, Failed Boot,  $\delta F = 40^\circ$ ,  $VIAS = 1.63V_s = 85\text{kts}$ .

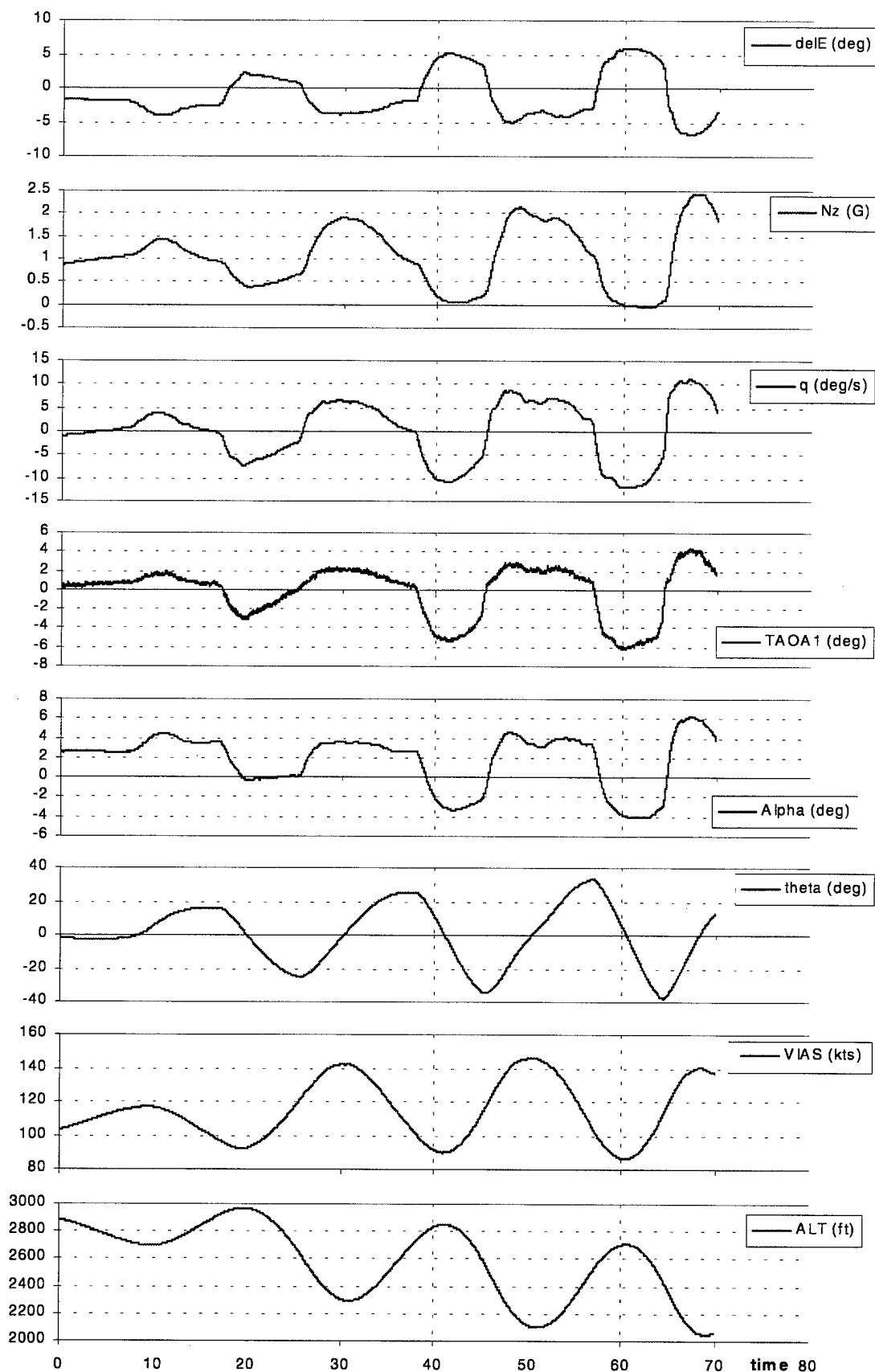


Figure C-1a. Pushover, Baseline,  $\delta F = 0^\circ$ , VIAS = 1.50Vs = 100kts.

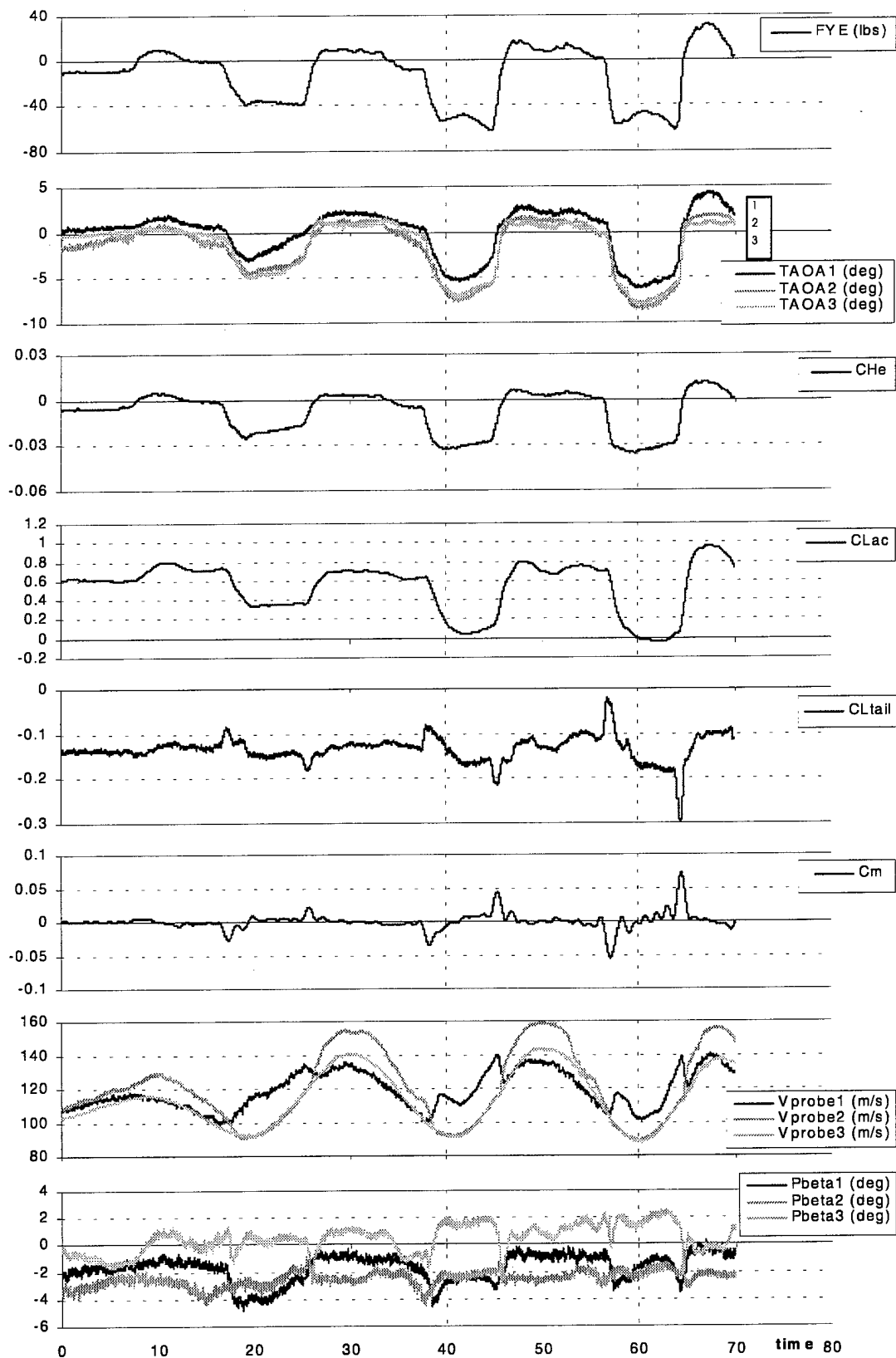


Figure C-1b. Pushover, Baseline,  $\delta F = 0^\circ$ ,  $VIAS = 1.50 V_s = 100 \text{ kts}$ .

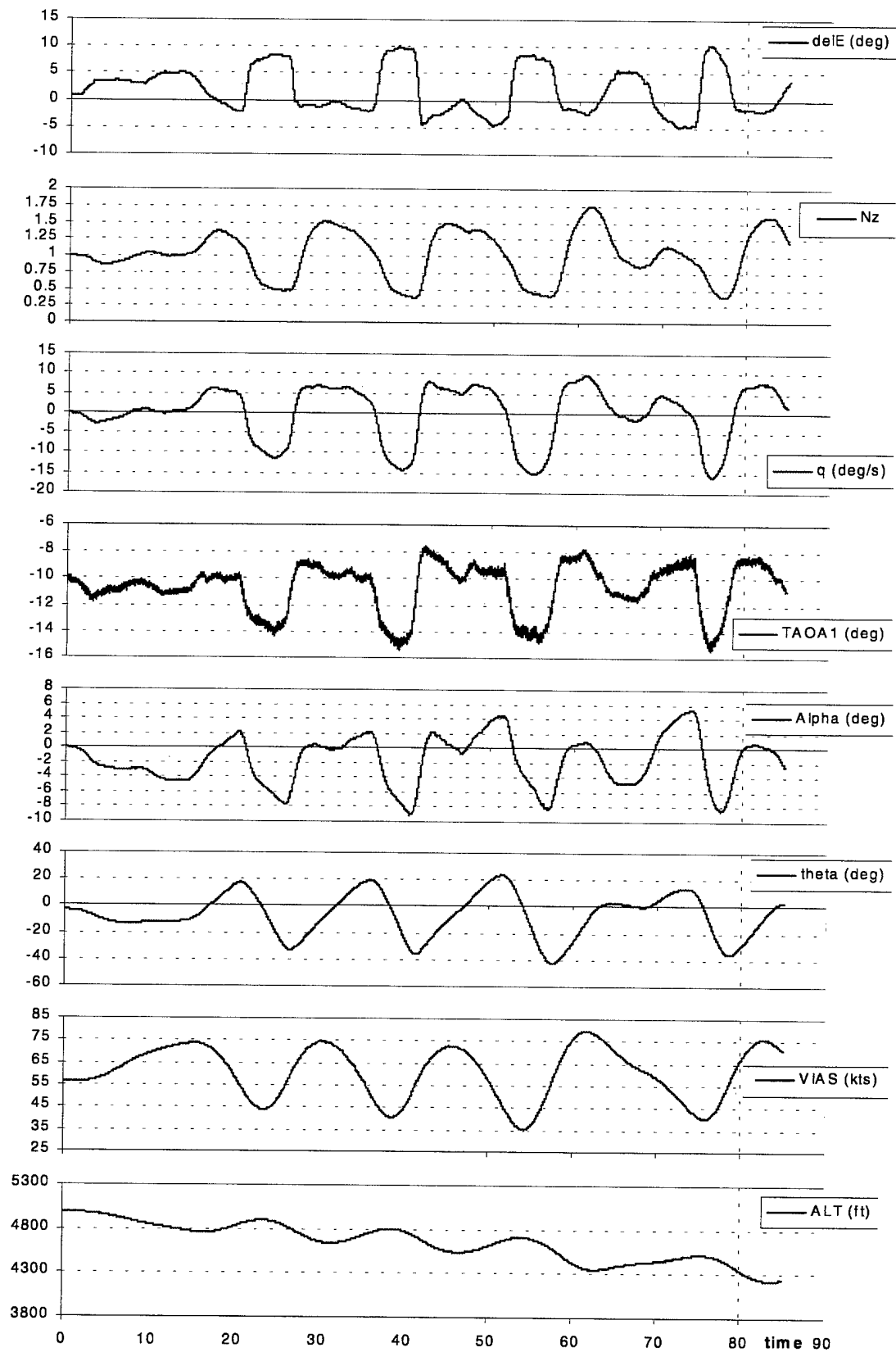


Figure C-2a. Pushover, Baseline,  $\delta F = 40^\circ$ , VIAS = 1.06Vs = 55kts.



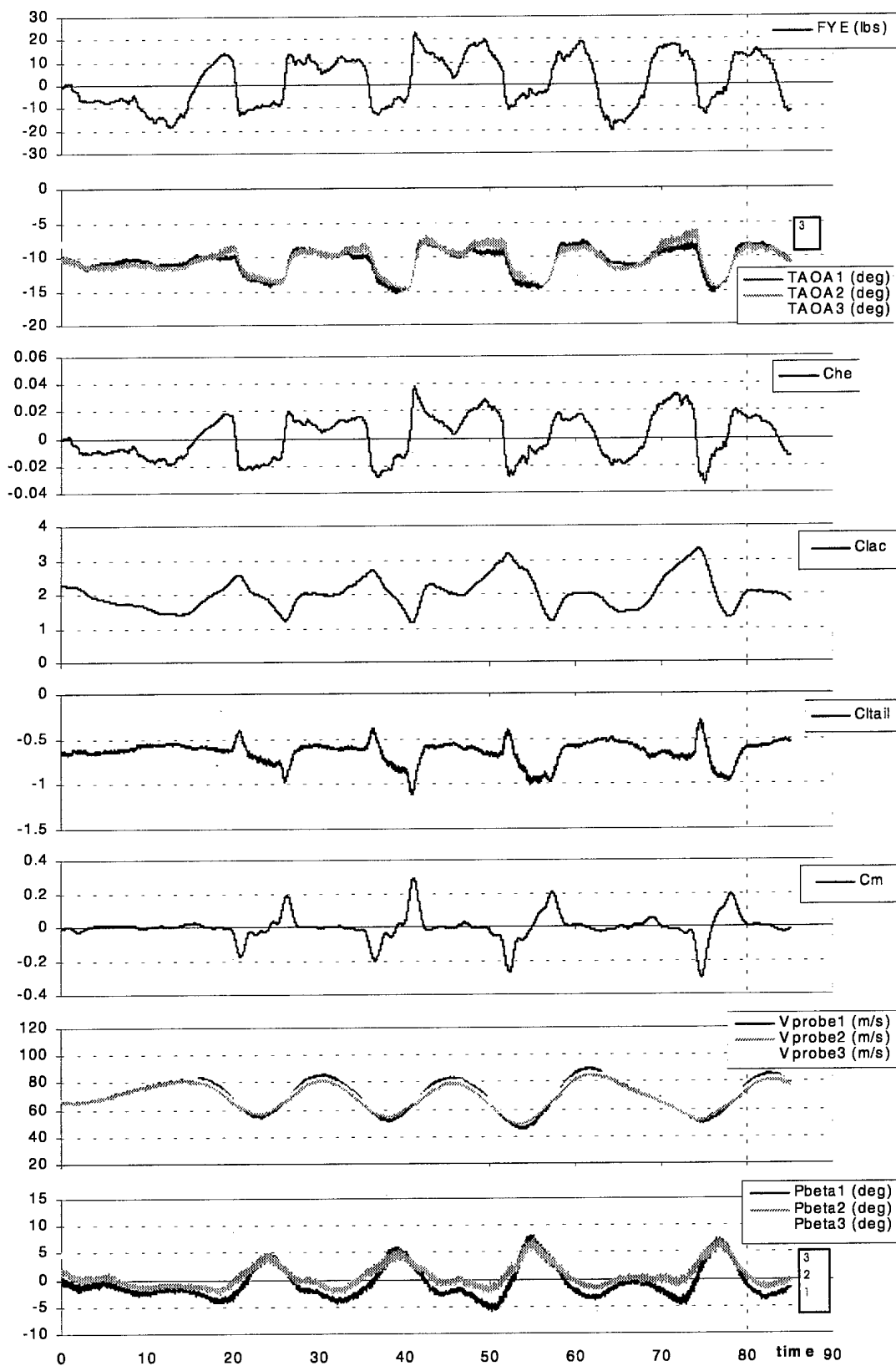


Figure C-2b. Pushover, Baseline,  $\delta F = 40^\circ$ , VIAS = 1.06Vs = 55kts.

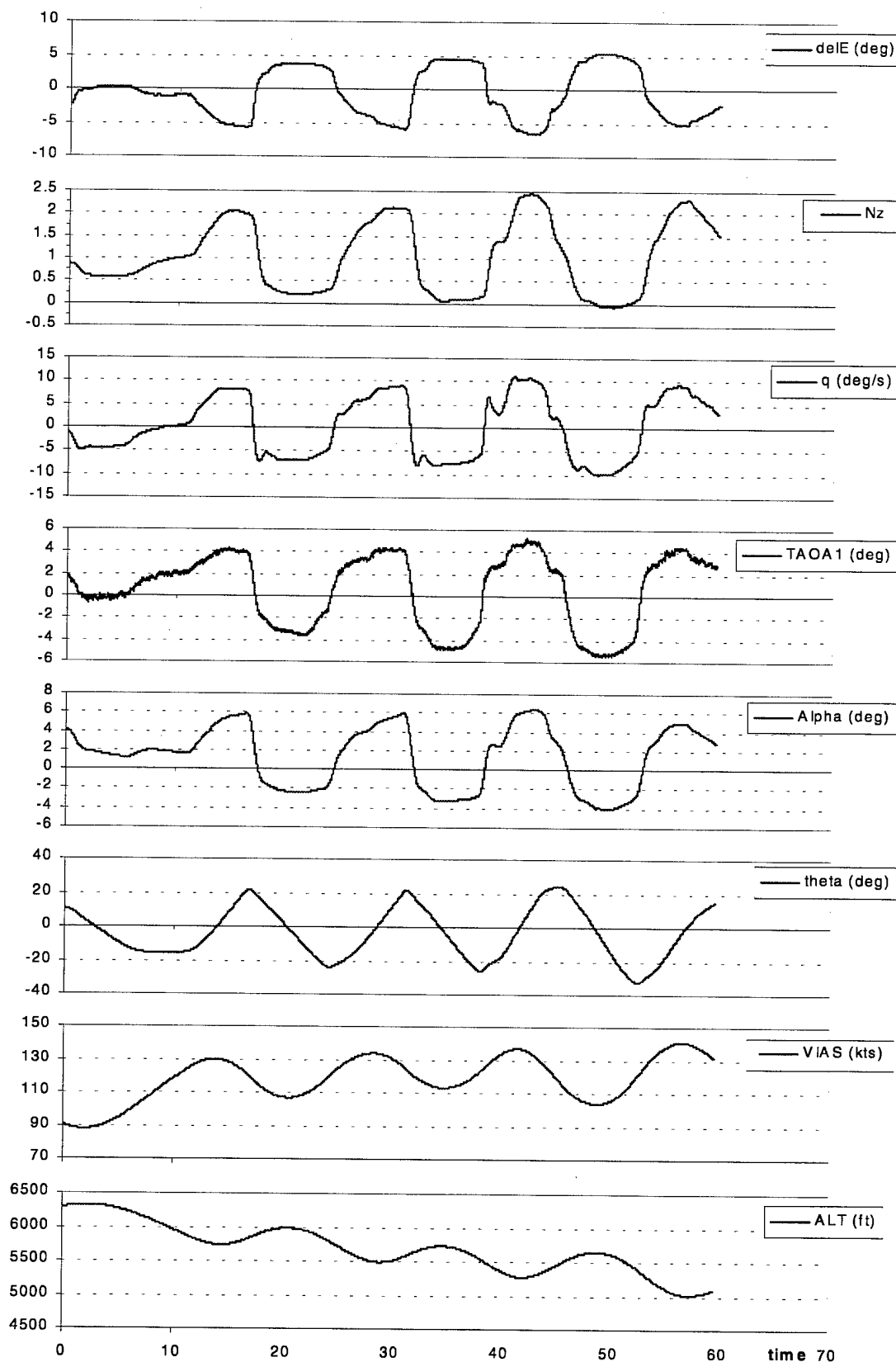


Figure C-3a. Pushover, Inter-Cycle Ice,  $\delta F = 0^\circ$ , VIAS = 1.50Vs = 100kts.

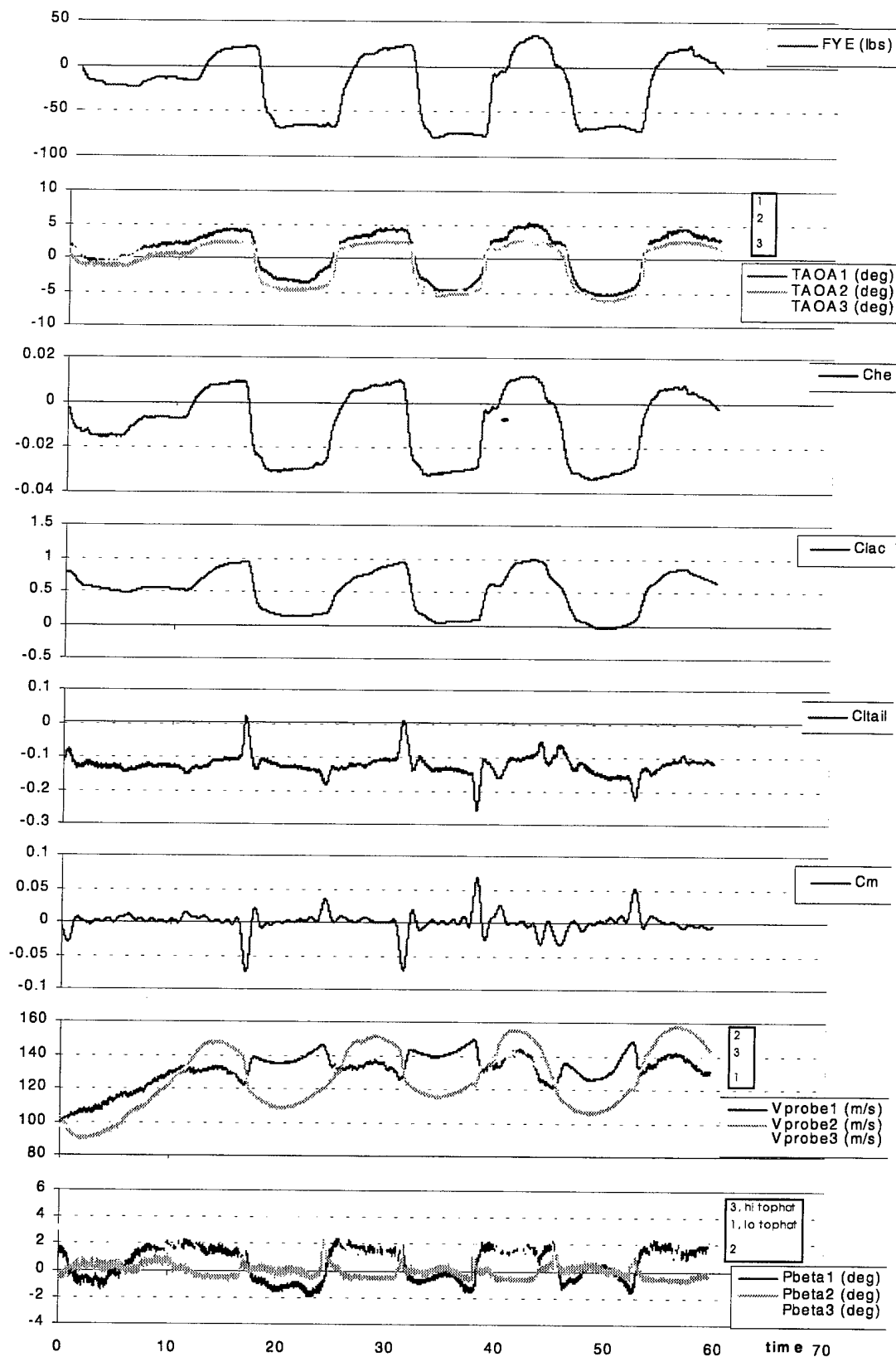


Figure C-3b. Pushover, Inter-Cycle Ice,  $\delta F = 0^\circ$ , VIAS = 1.50Vs = 100kts.

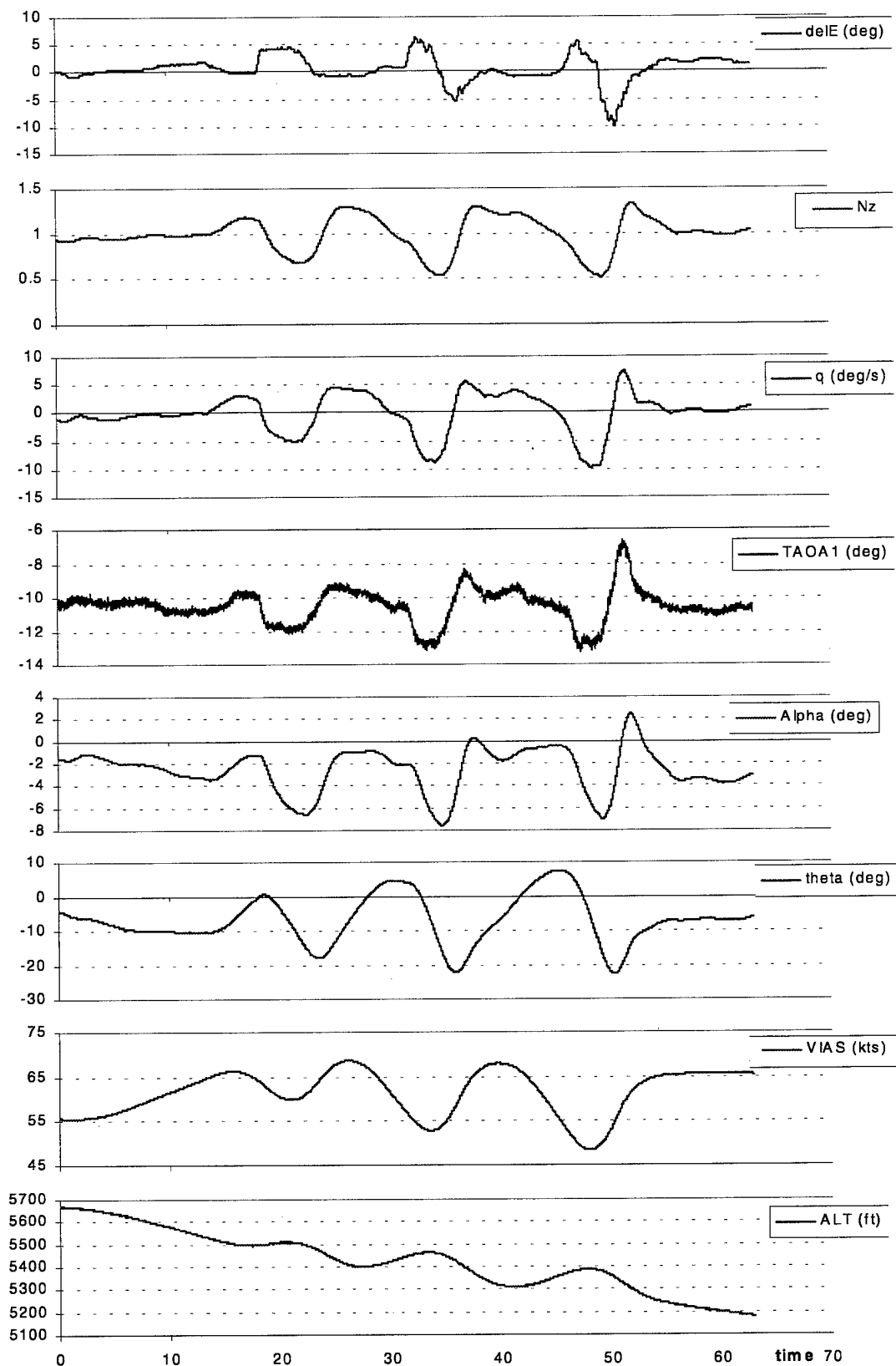


Figure C-4a. Pushover, Inter-Cycle Ice,  $\delta F = 40^\circ$ , VIAS = 1.06Vs = 55kts.

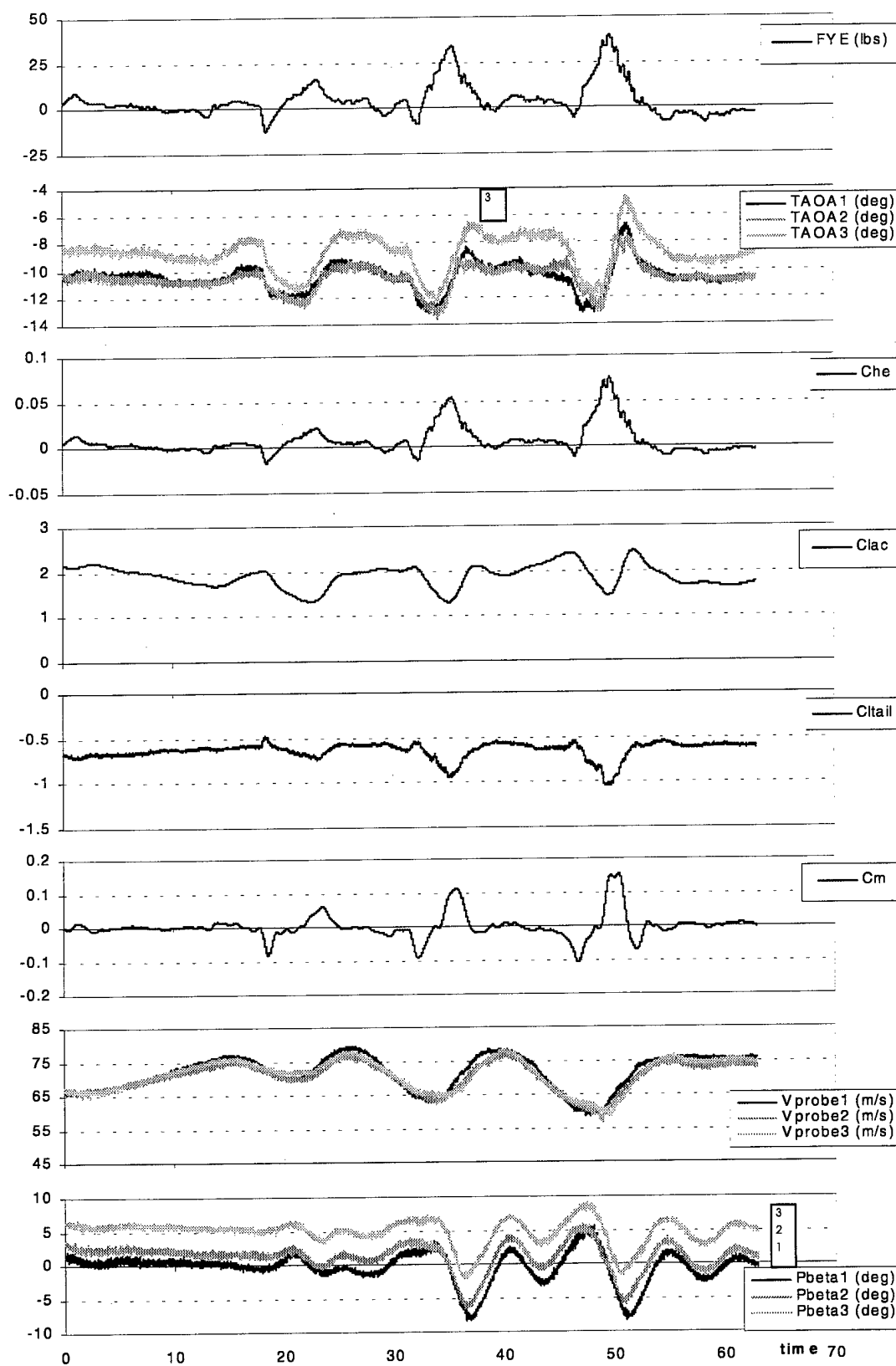


Figure C-4b. Pushover, Inter-Cycle Ice,  $\delta F = 40^\circ$ , VIAS = 1.06Vs = 55kts.

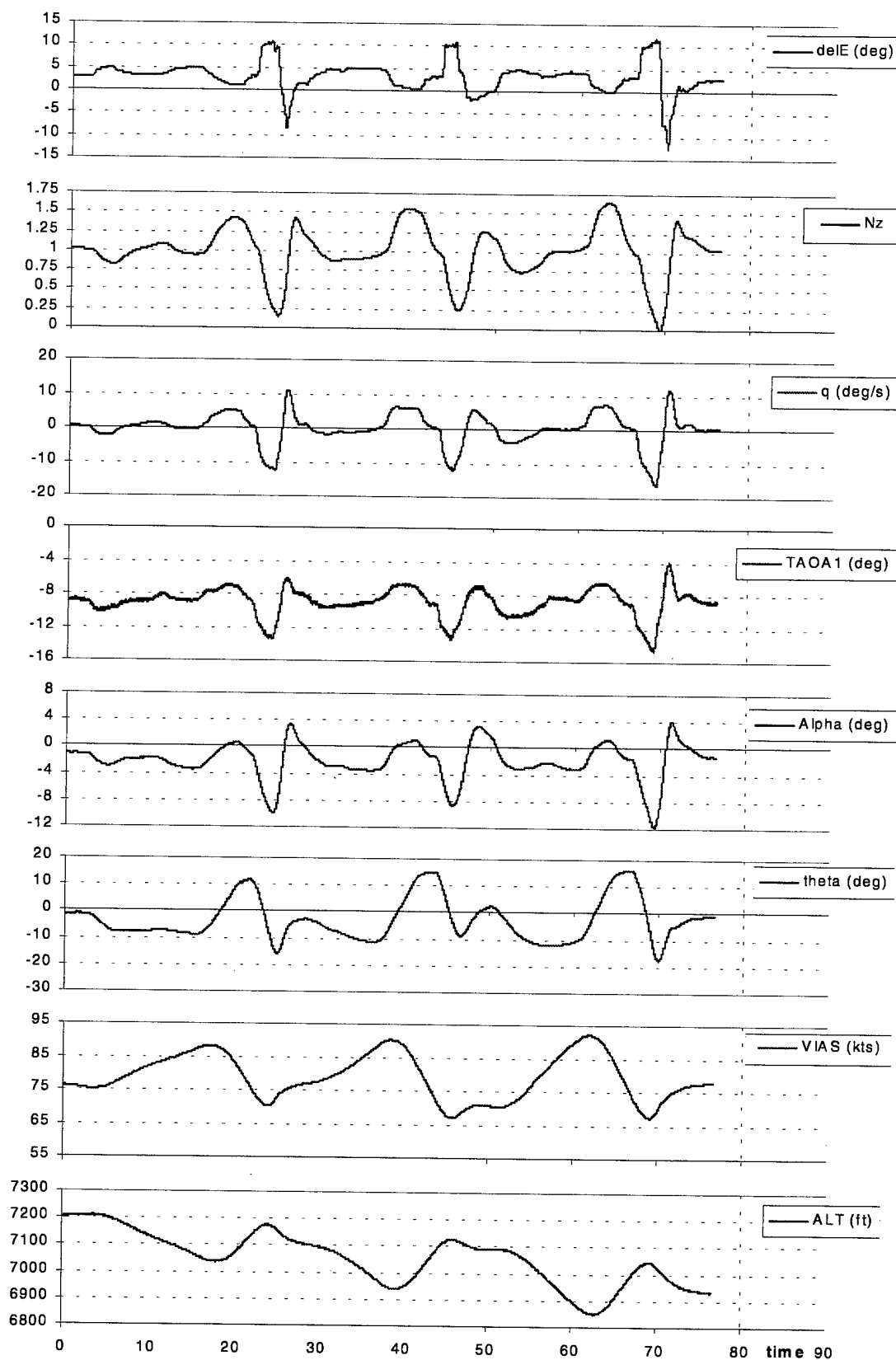


Figure C-5a. Pushover, Failed Boot,  $\delta F = 20^\circ$ , VIAS =  $1.33V_s = 75\text{kts}$ .

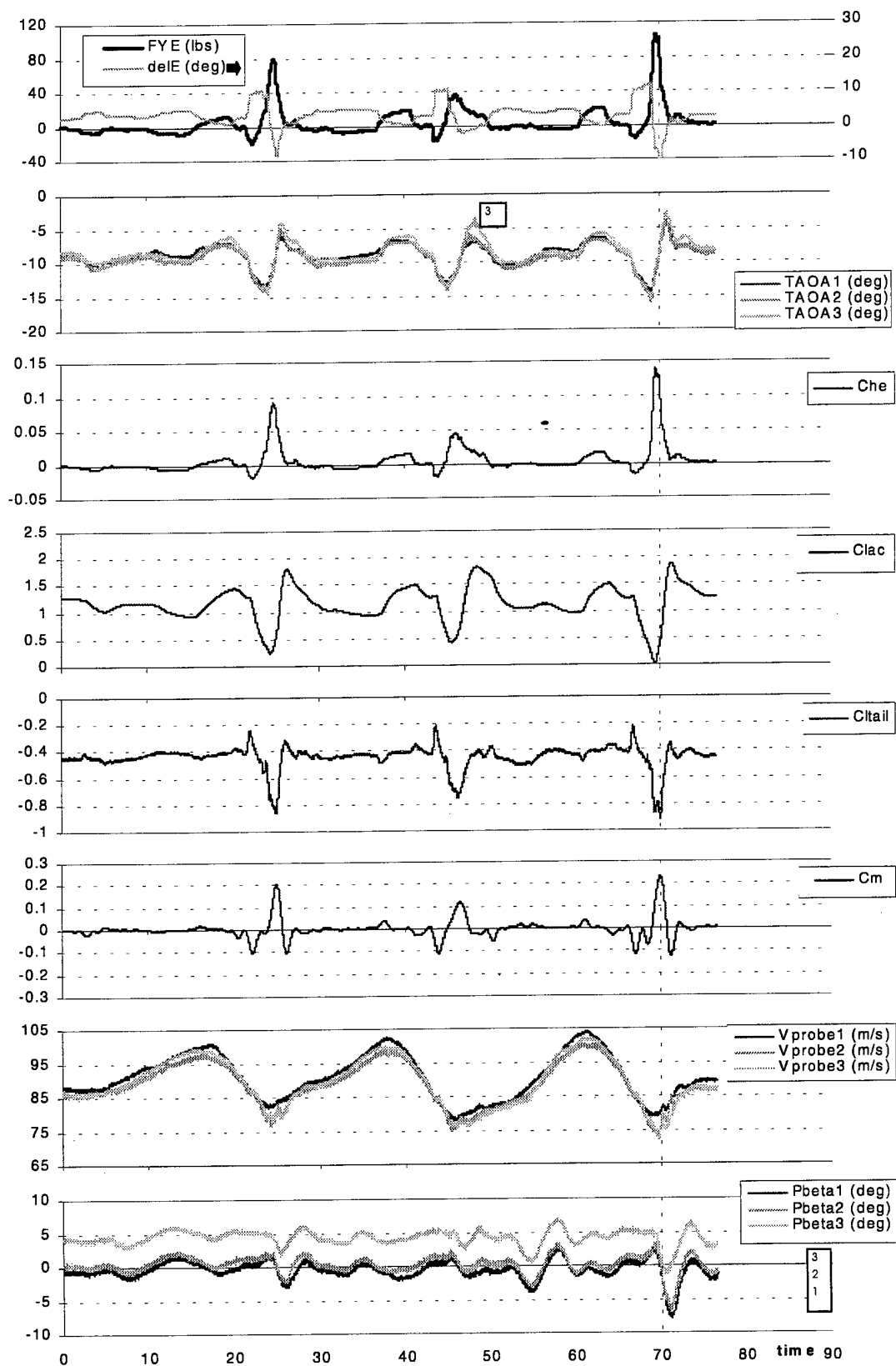


Figure C-5b. Pushover, Failed Boot,  $\delta F = 20^\circ$ , VIAS = 1.33Vs = 75kts.

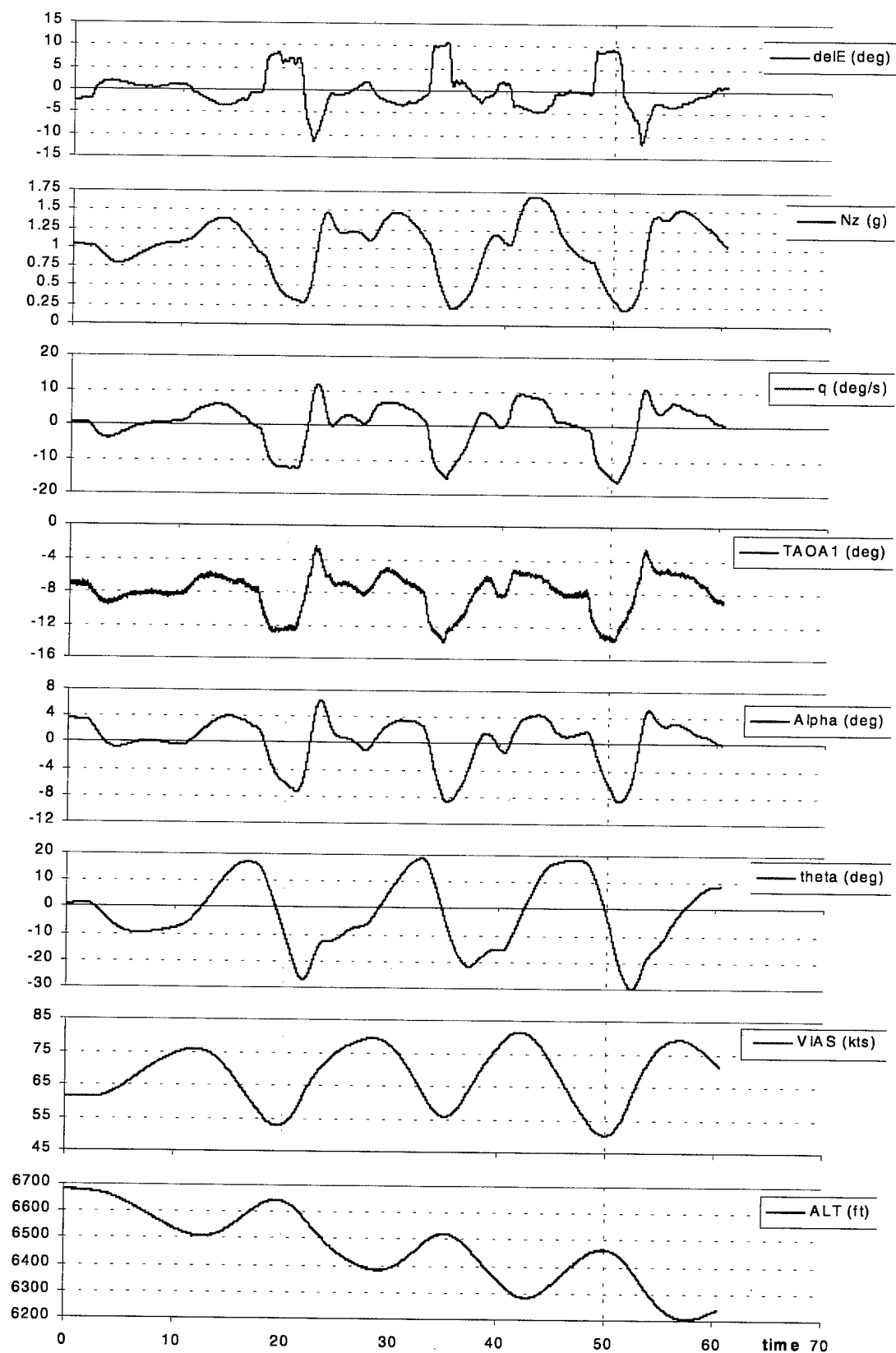


Figure C-6a. Pushover, Failed Boot,  $\delta F = 20^\circ$ , VIAS =  $0.97V_s = 55\text{kts}$ .



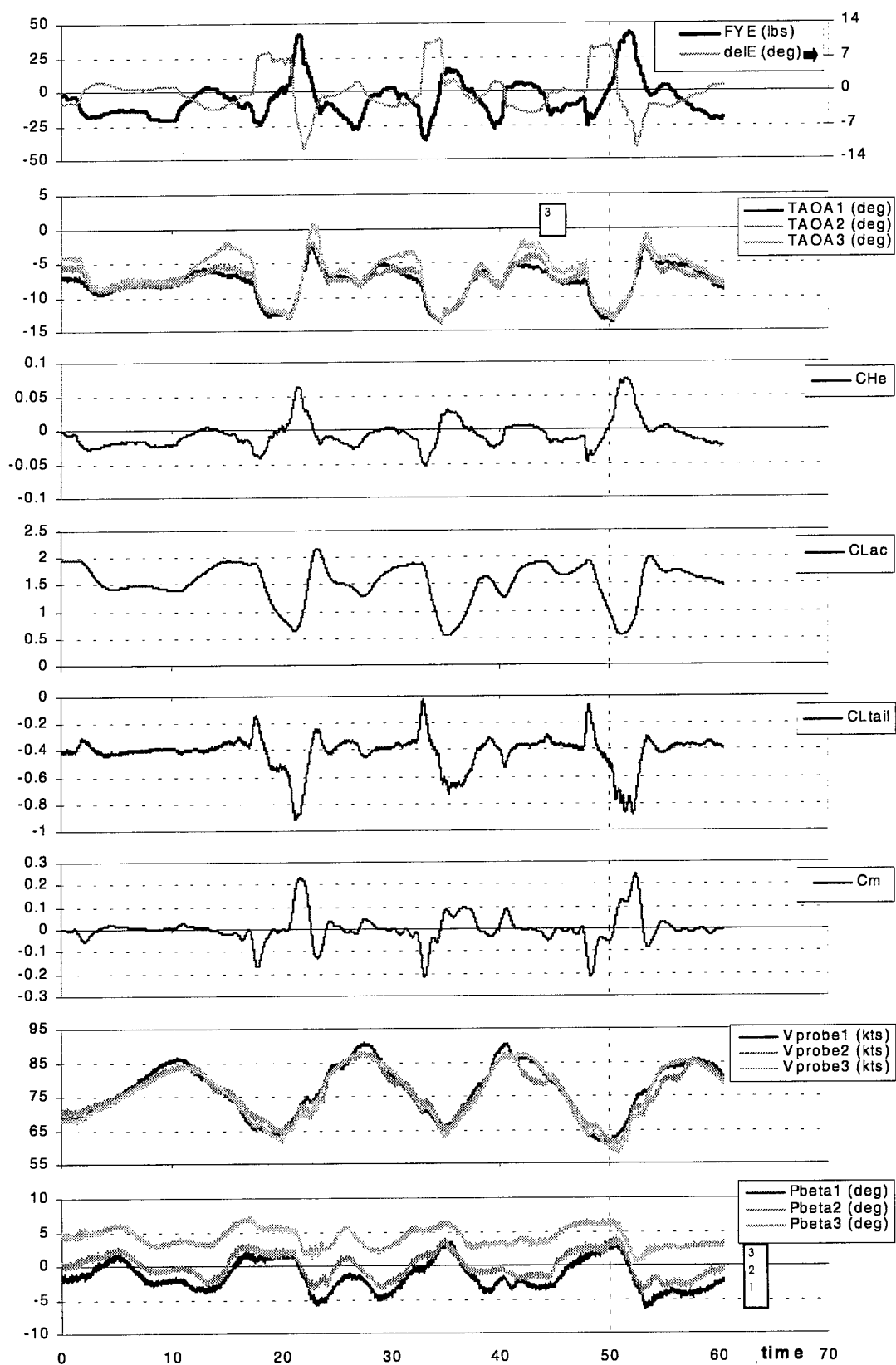


Figure C-6b. Pushover, Failed Boot,  $\delta F = 20^\circ$ , VIAS =  $0.97V_s = 55\text{kts}$ .

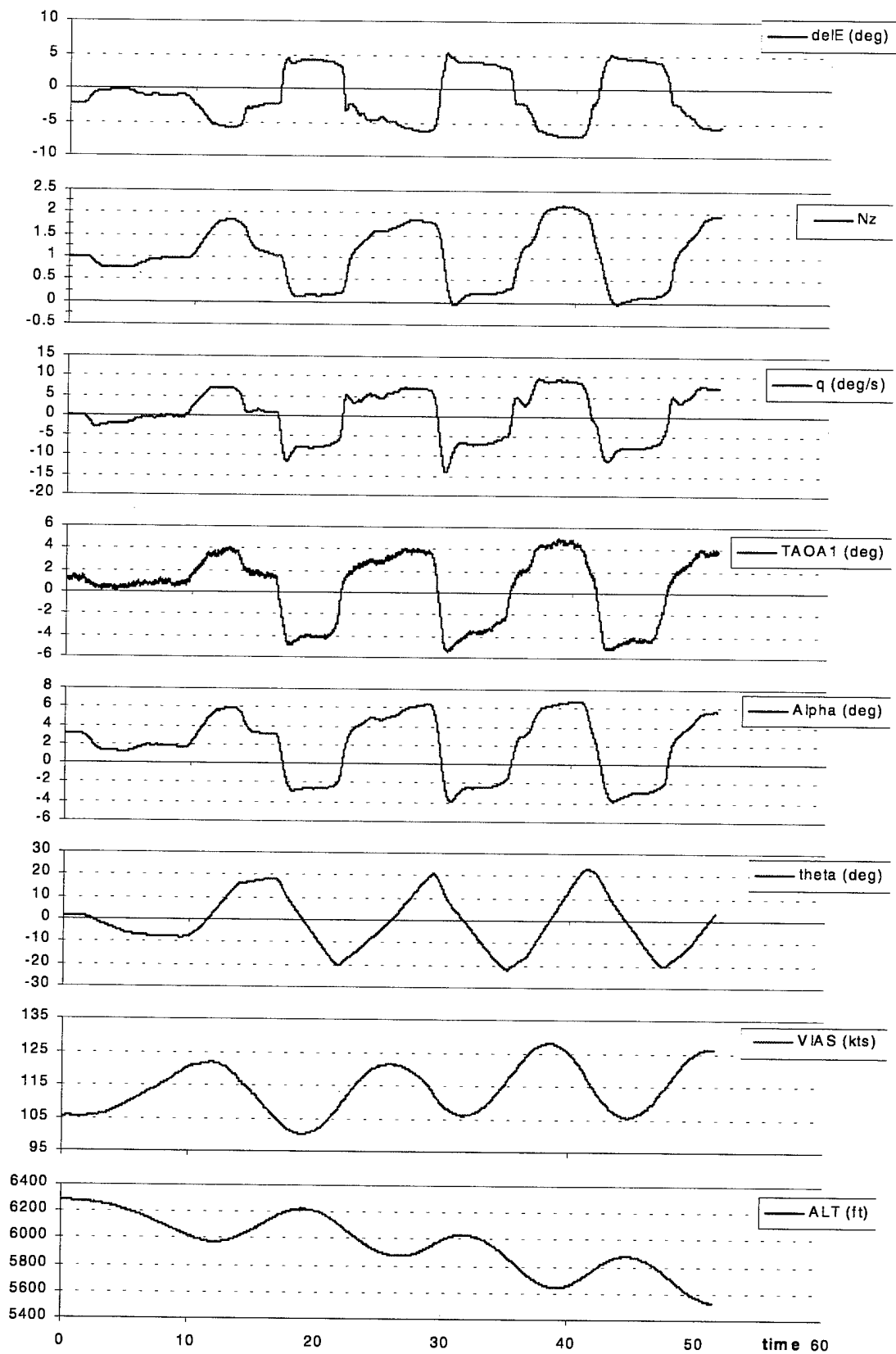


Figure C-7a. Pushover, S&C,  $\delta F = 0^\circ$ , VIAS = 1.50Vs = 100kts.

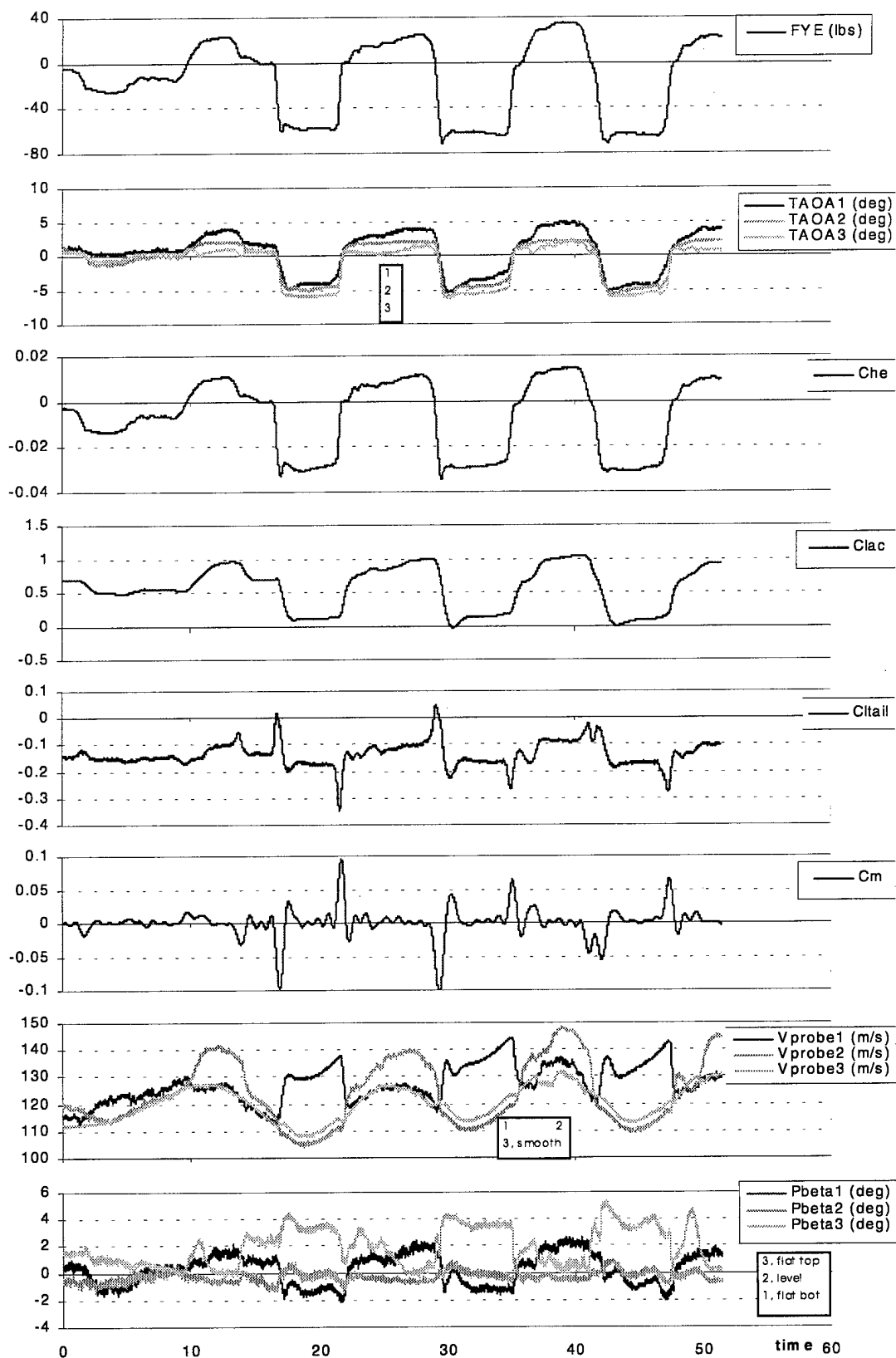


Figure C-7b. Pushover, S&C,  $\delta F = 0^\circ$ , VIAS = 1.50Vs = 100kts.

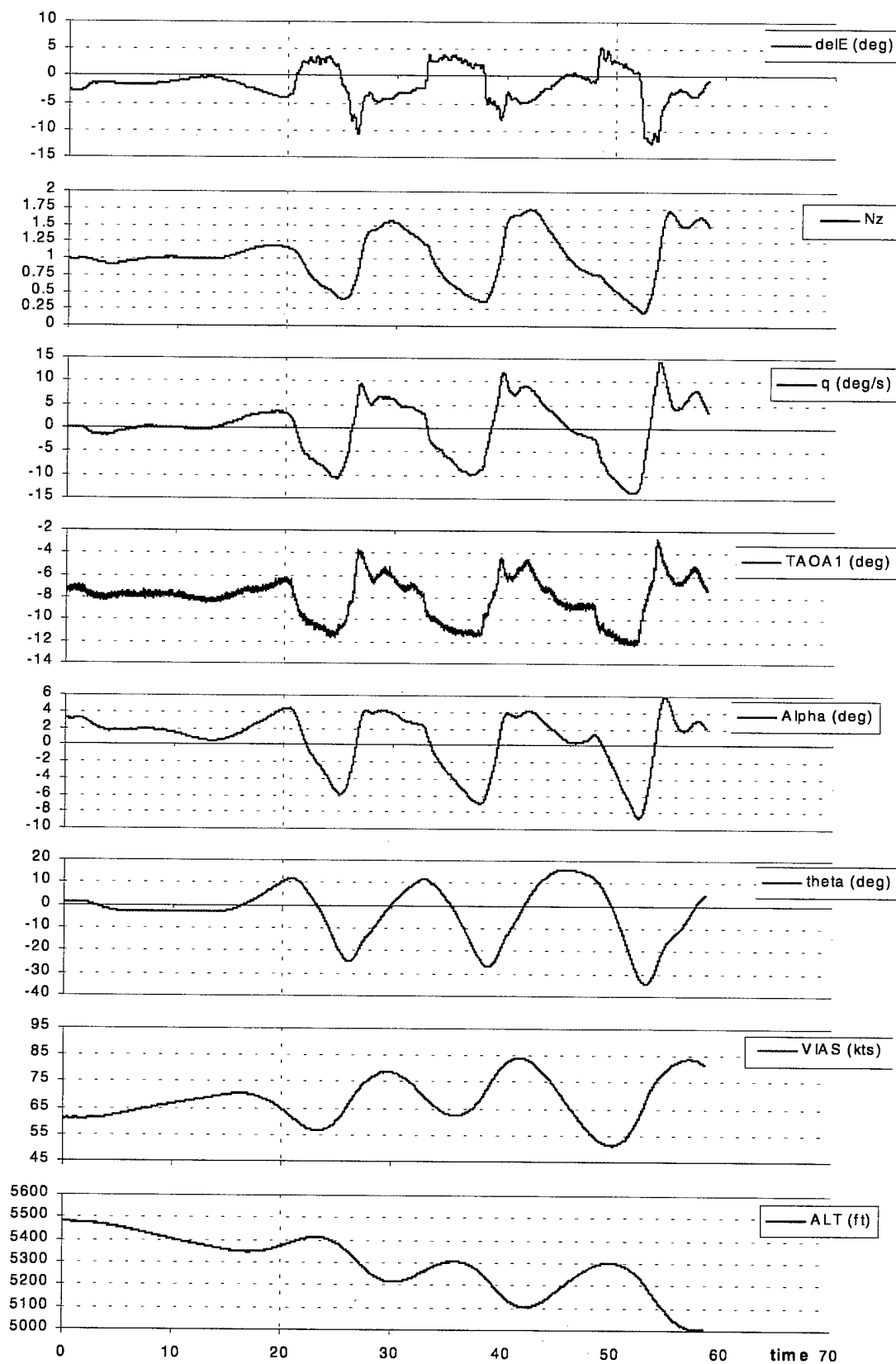


Figure C-8a. Pushover, S&C,  $\delta F = 20^\circ$ , VIAS =  $0.97V_s = 55\text{kts}$ .

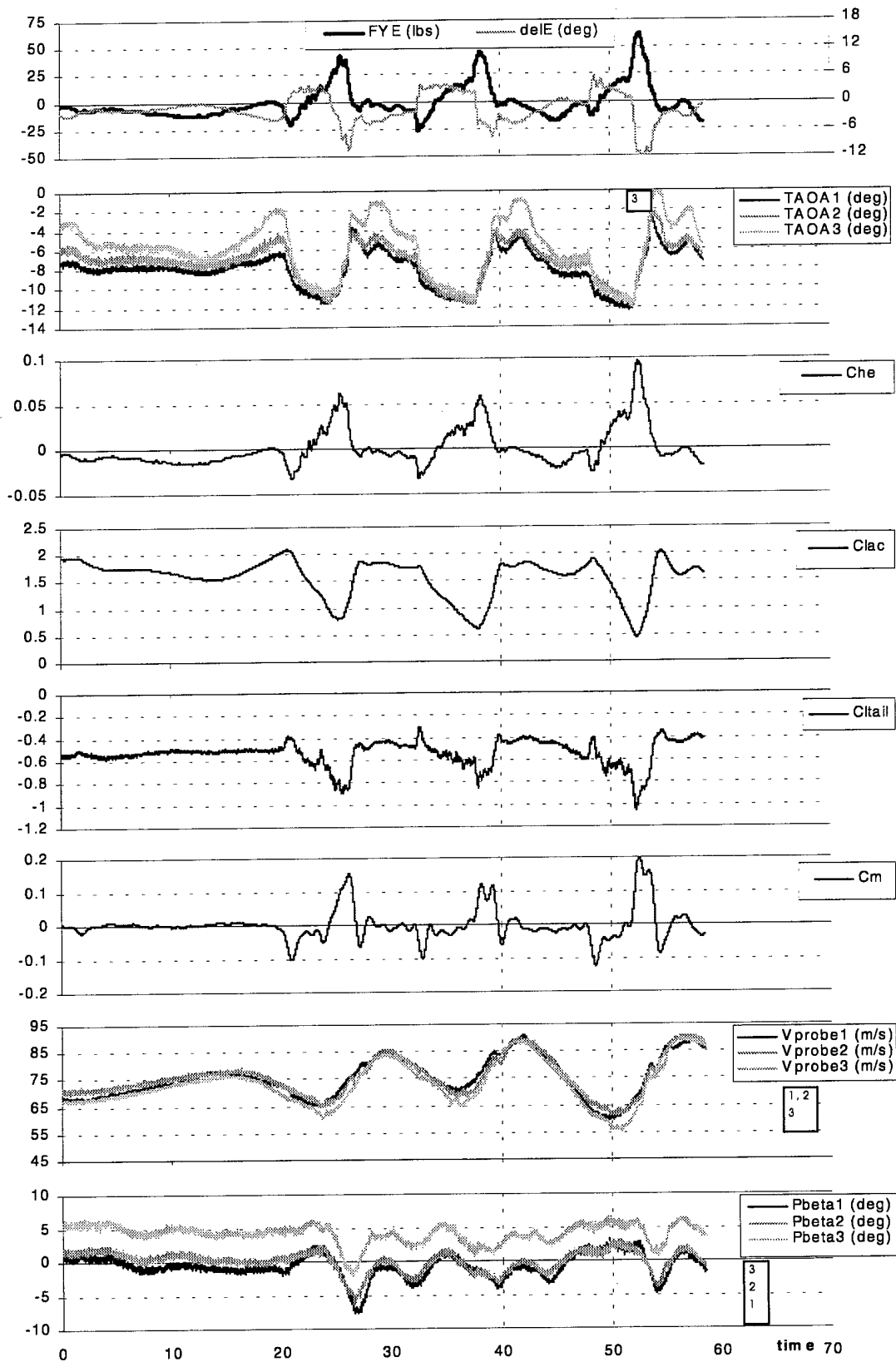


Figure C-8b. Pushover, S&C,  $\delta F = 20^\circ$ , VIAS =  $0.97V_s = 55\text{kts}$ .

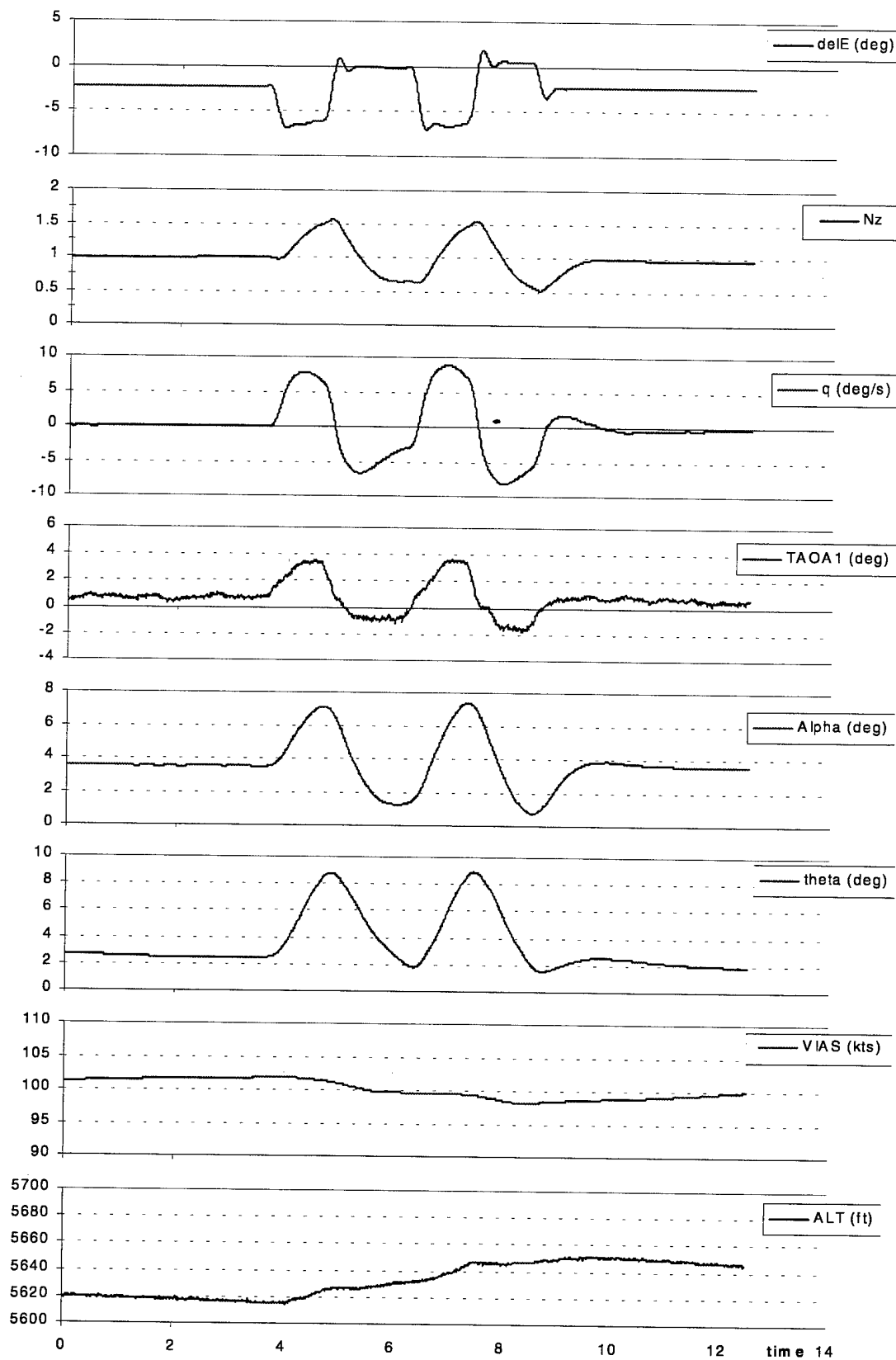


Figure C-9a. Elevator doublet, Baseline,  $\delta F = 0^\circ$ , VIAS = 1.50Vs = 100kts.

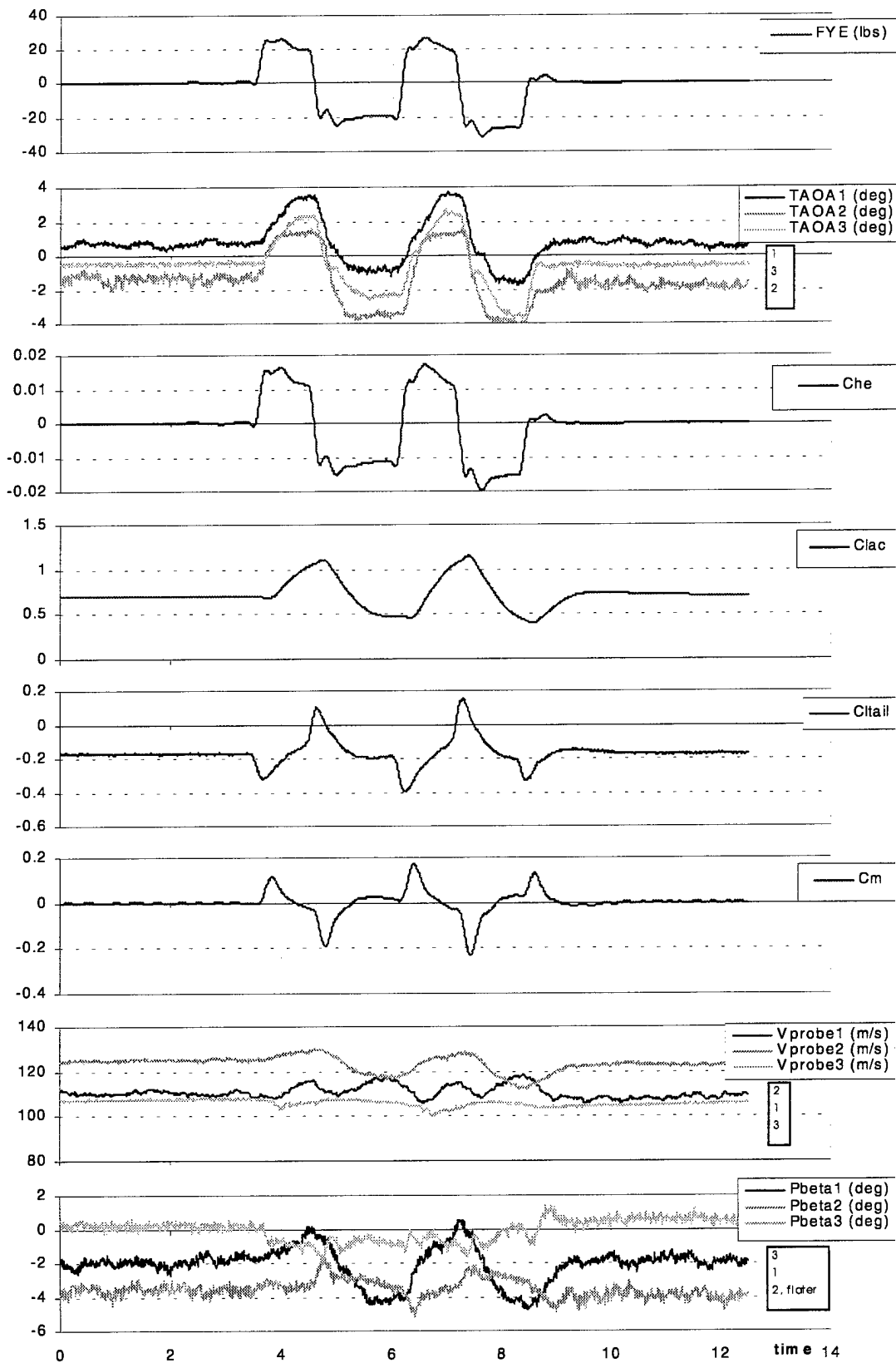


Figure C-9b. Elevator doublet, Baseline,  $\delta F = 0^\circ$ , VIAS = 1.50Vs = 100kts.

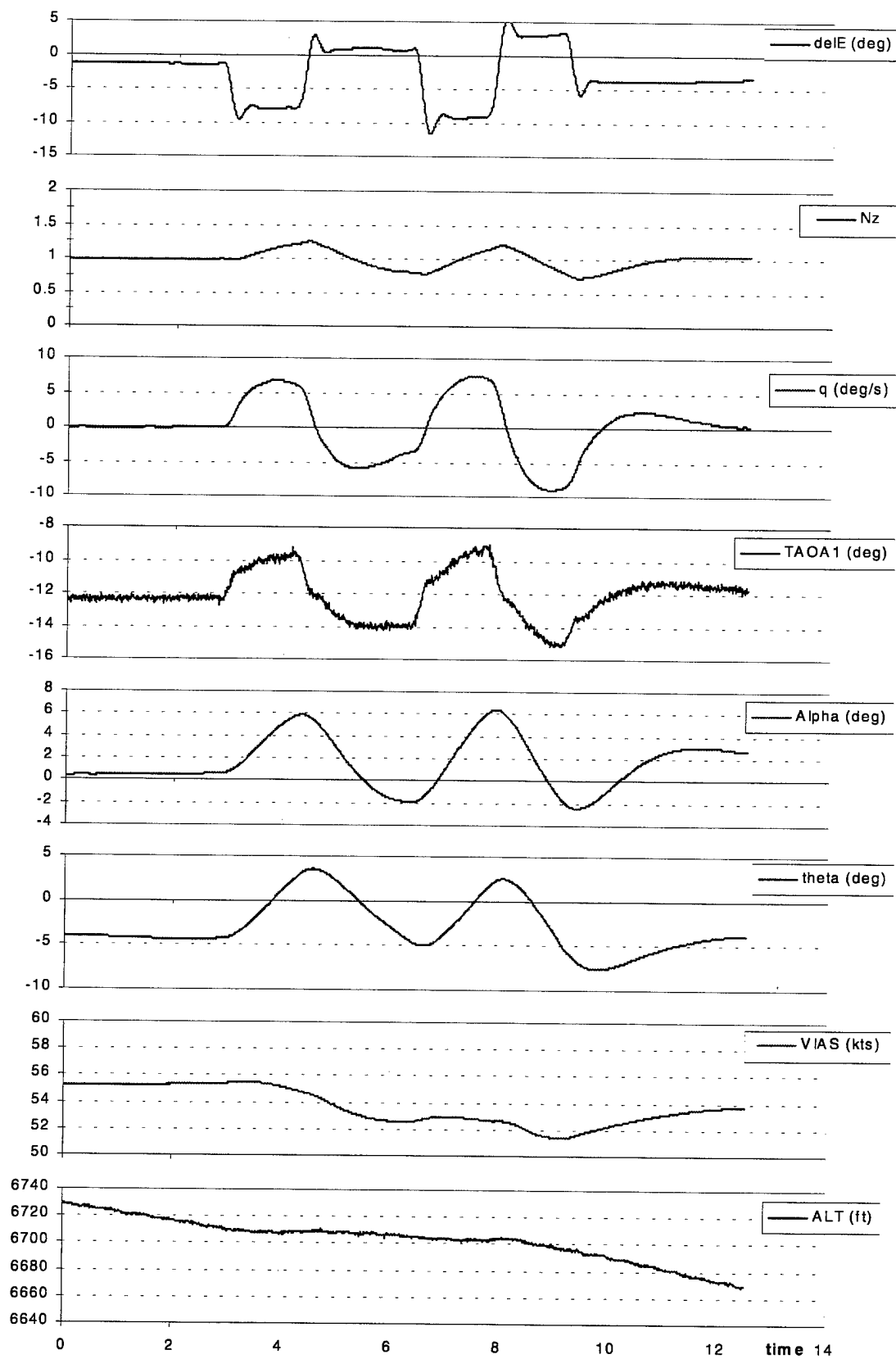


Figure C-10a. Elevator doublet, Baseline,  $\delta F = 40^\circ$ , VIAS = 1.06Vs = 55kts.



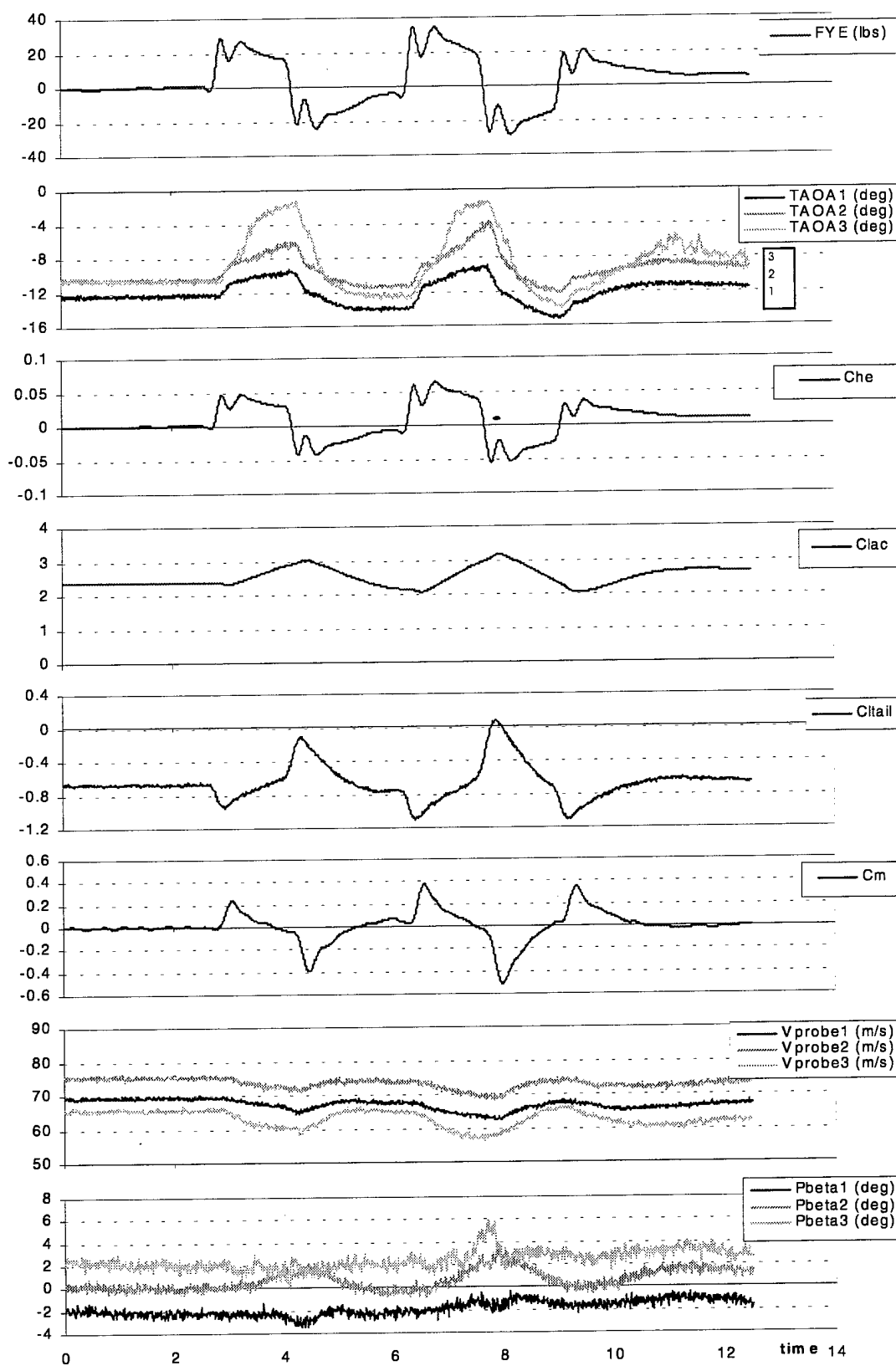


Figure C-10b. Elevator doublet, Baseline,  $\delta F = 40^\circ$ , VIAS =  $1.06V_s = 55\text{kts}$ .

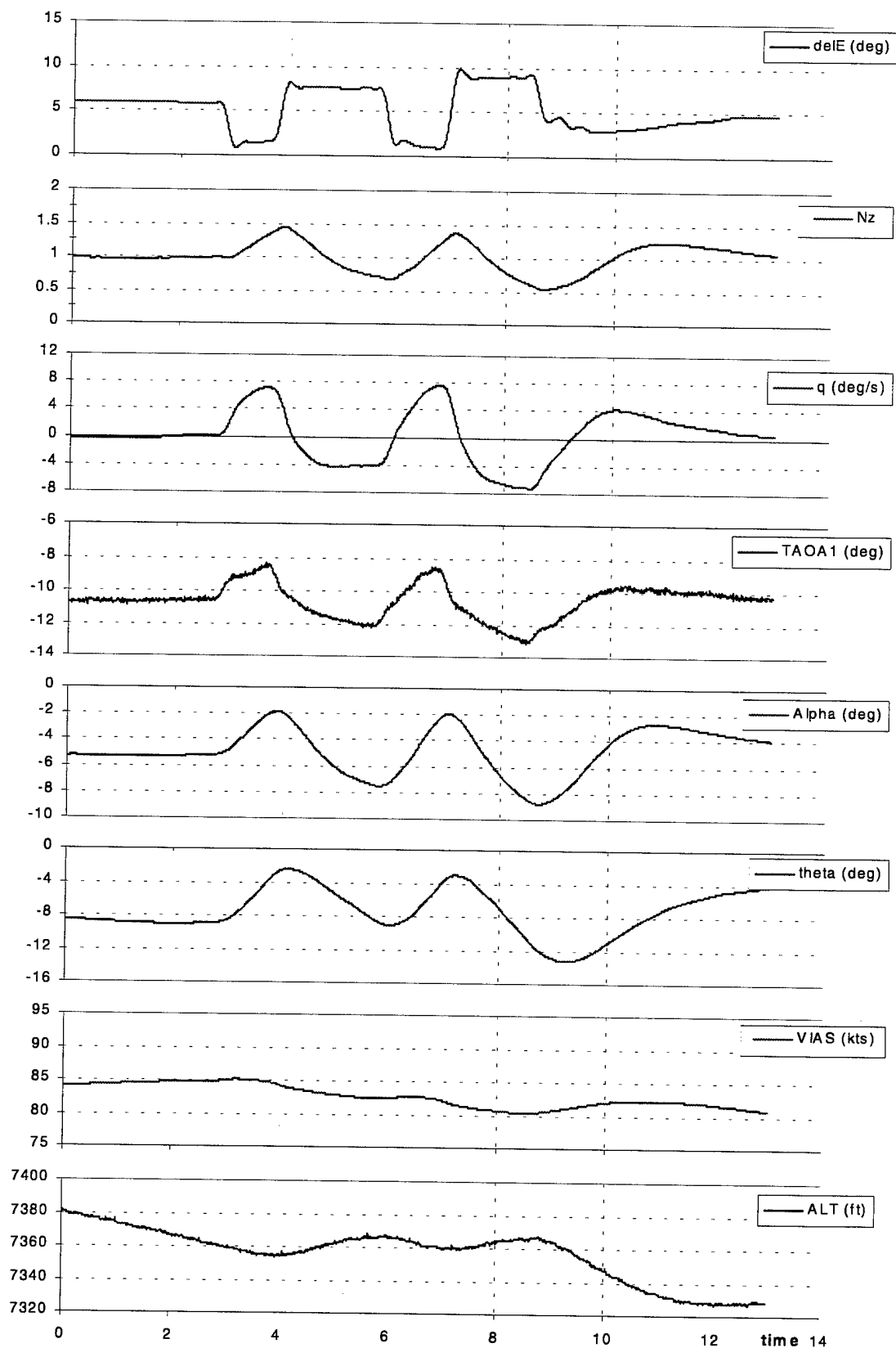


Figure C-11a. Elevator doublet, Inter-Cycle Ice,  $\delta F = 30^\circ$ , VIAS =  $1.59V_s = 85\text{kts}$ .

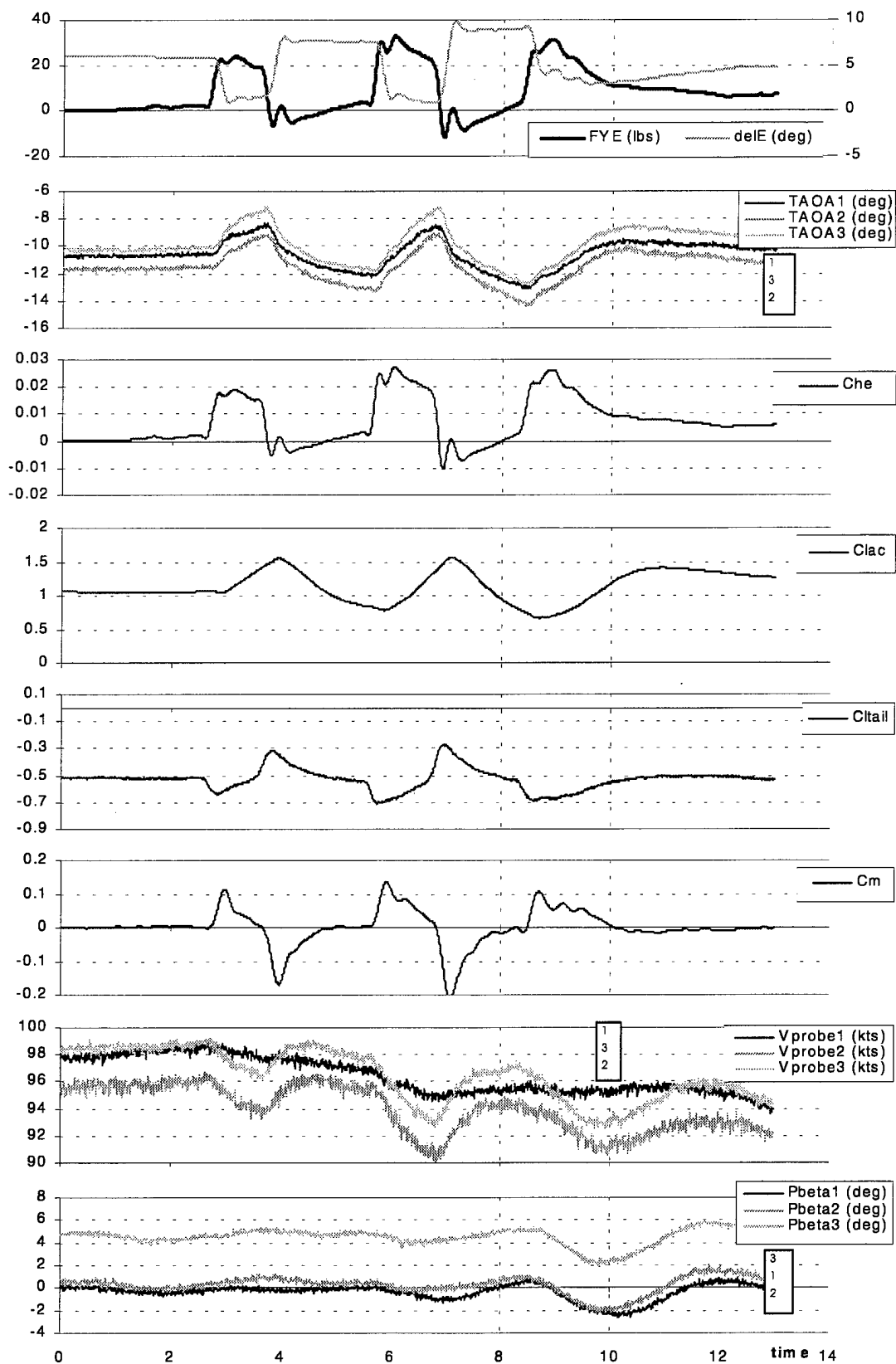


Figure C-11b. Elevator doublet, Inter-Cycle Ice,  $\delta F = 30^\circ$ , VIAS = 1.59Vs = 85kts.

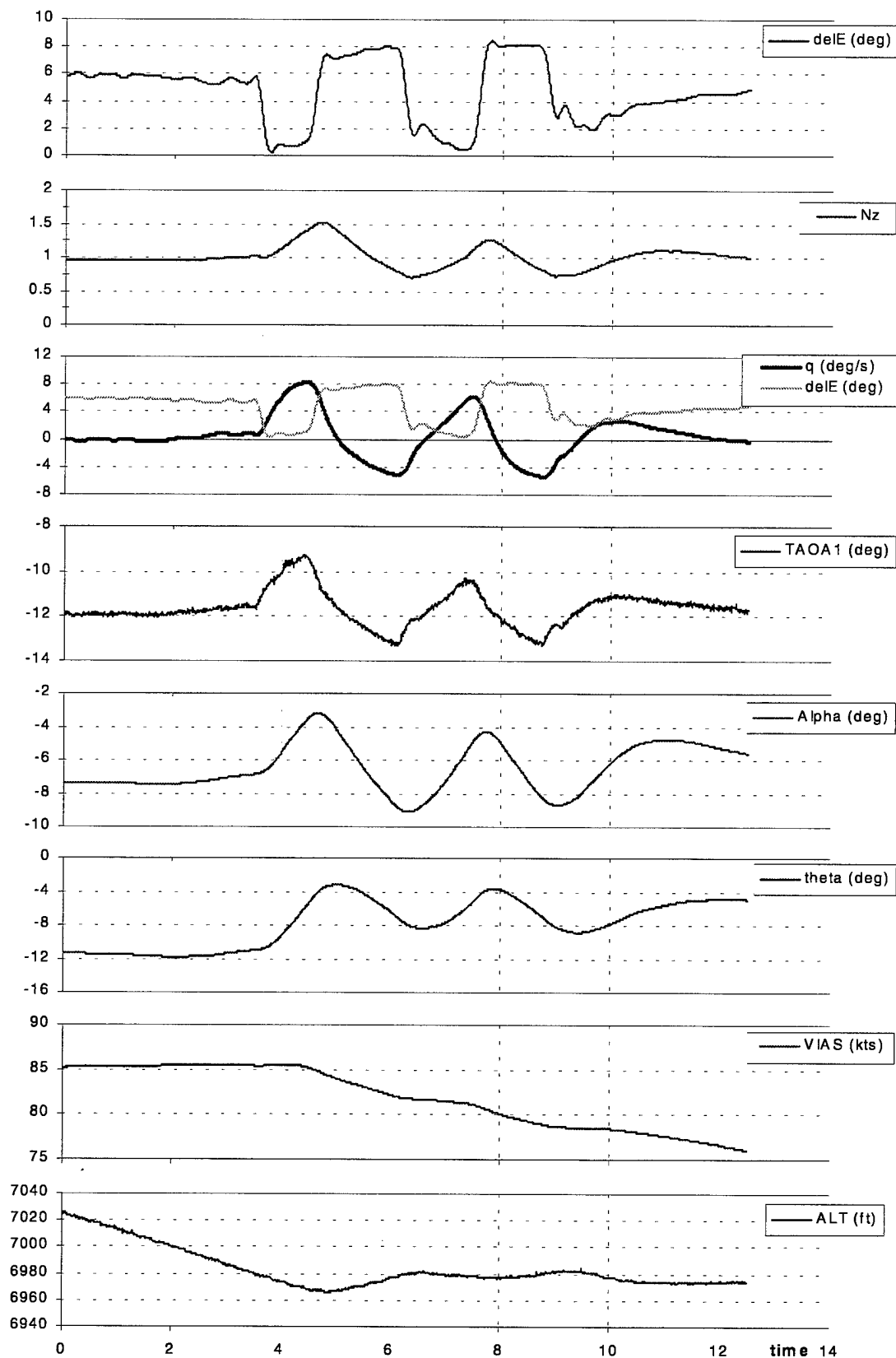


Figure C-12a. Elevator doublet, Inter-Cycle Ice,  $\delta F = 40^\circ$ , VIAS = 1.63Vs = 85kts.

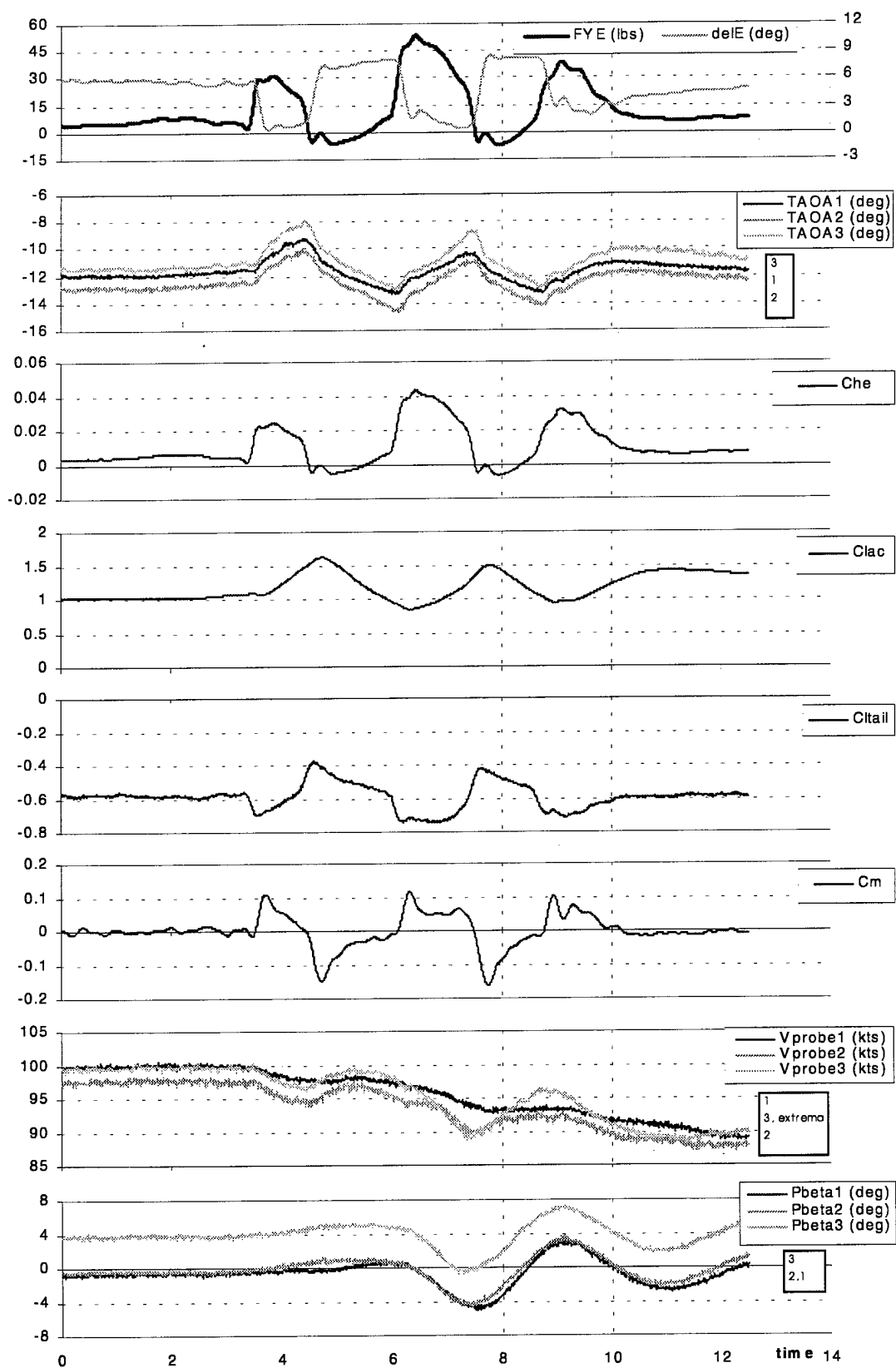


Figure C-12b. Elevator doublet, Inter-Cycle Ice,  $\delta F = 40^\circ$ , VIAS = 1.63Vs = 85kts.

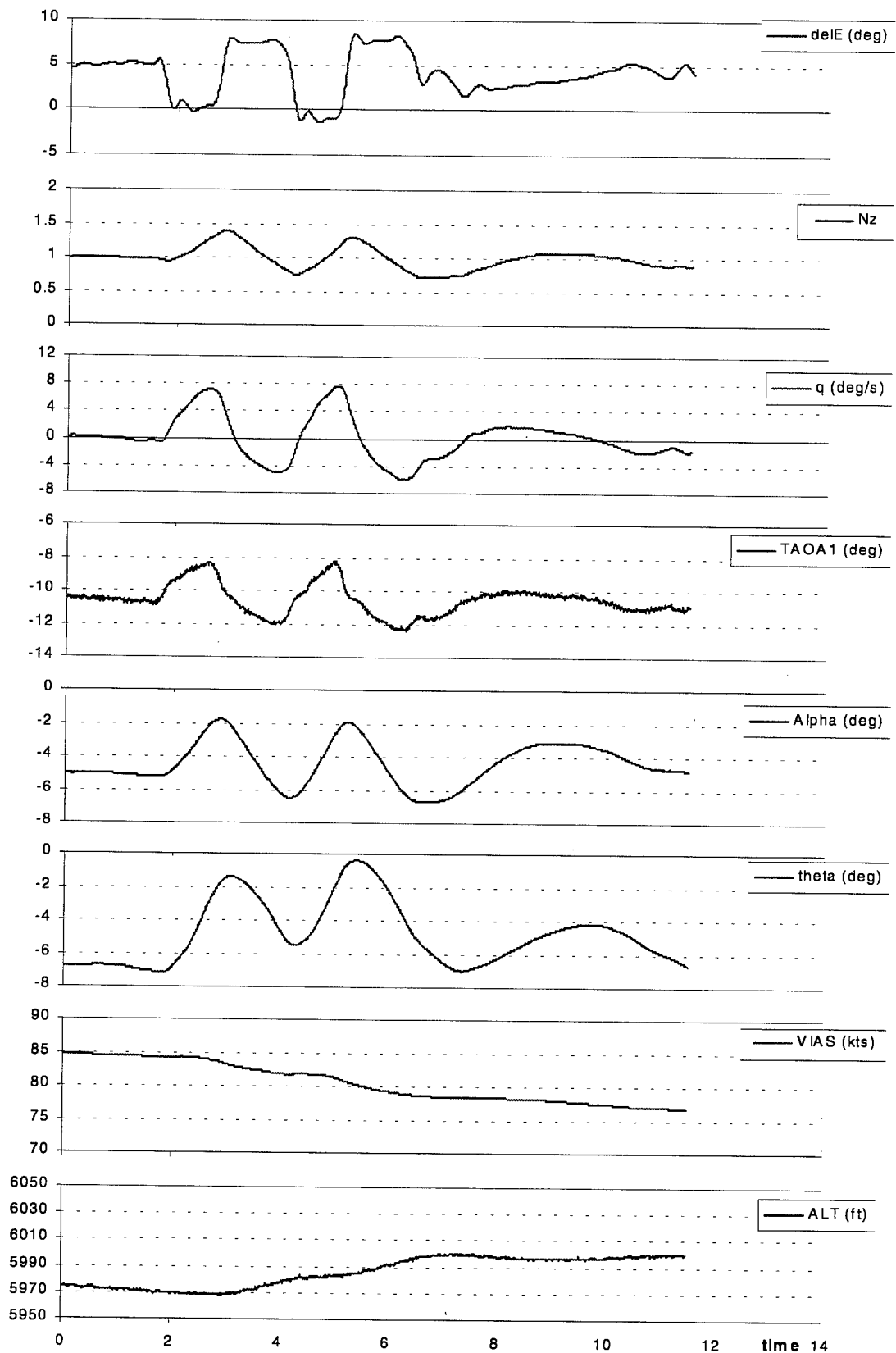


Figure C-13a. Elevator doublet, Failed Boot,  $\delta F = 30^\circ$ , VIAS =  $1.59V_s = 85\text{kts}$ .

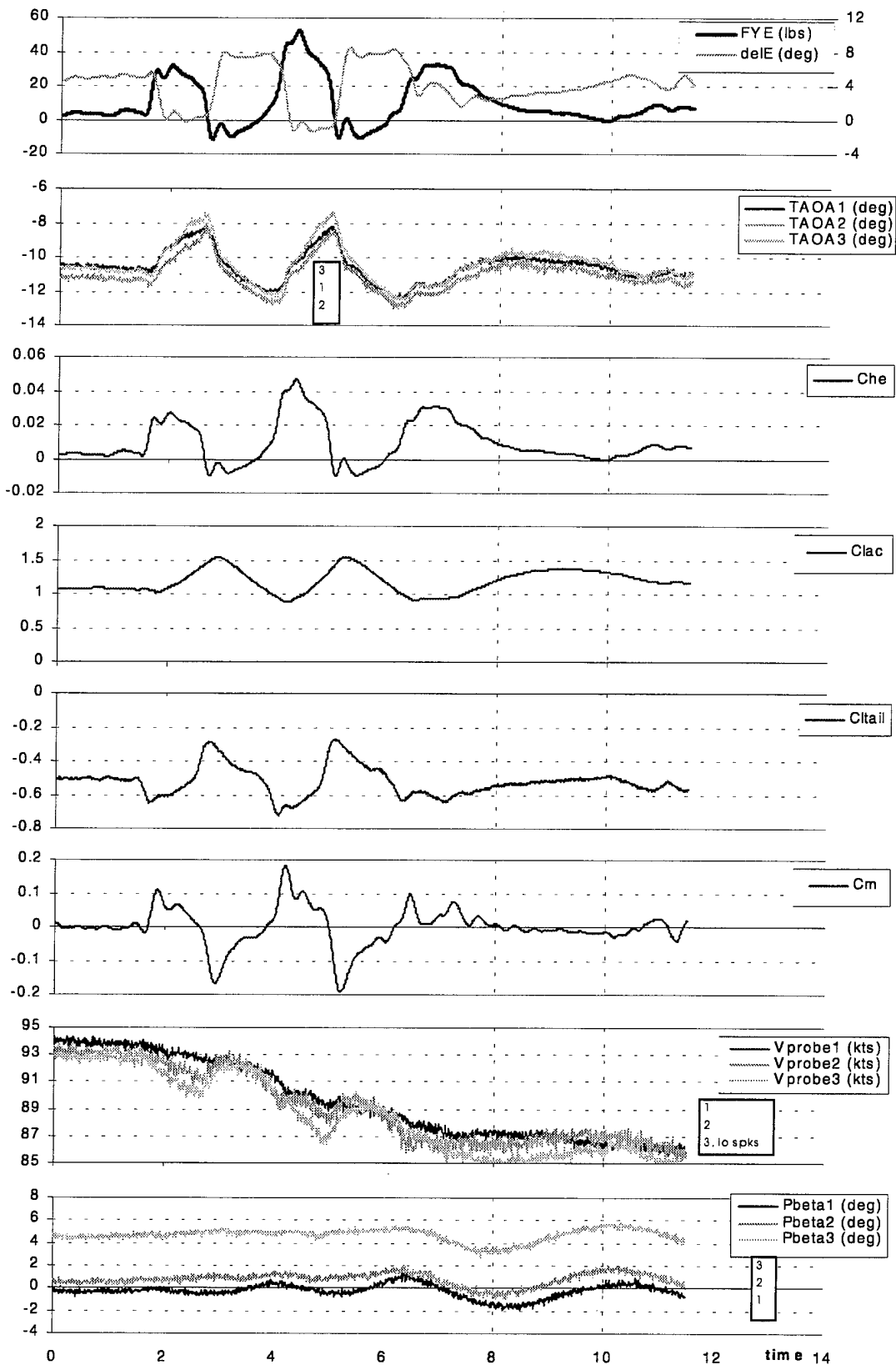


Figure C-13b. Elevator doublet, Failed Boot,  $\delta F = 30^\circ$ , VIAS =  $1.59V_s = 85\text{kts}$ .

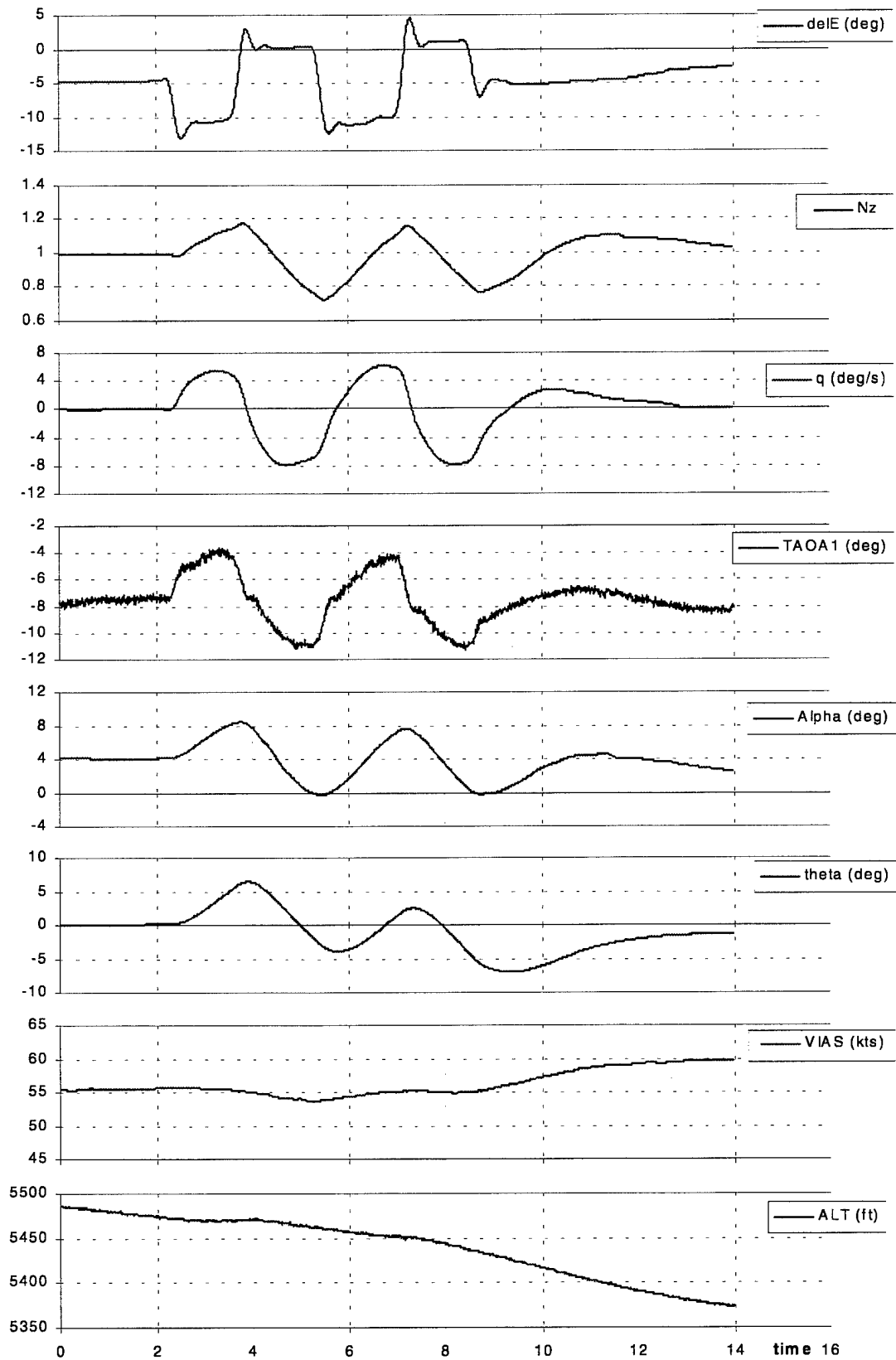


Figure C-14a. Elevator doublet, Failed Boot,  $\delta F = 30^\circ$ , VIAS = 1.03Vs = 55kts.



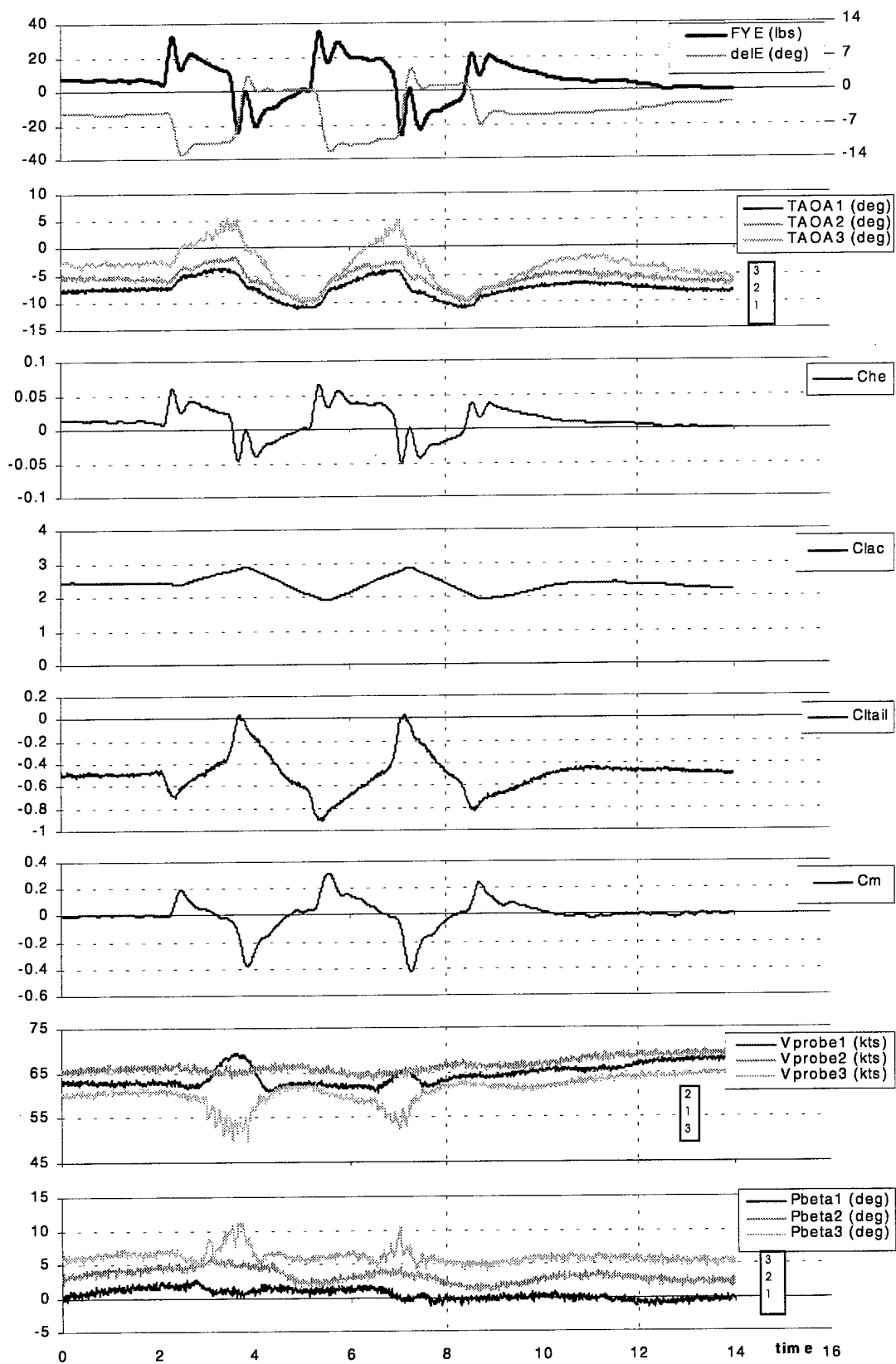


Figure C-14b. Elevator doublet, Failed Boot,  $\delta F = 30^\circ$ ,  $VIAS = 1.03V_s = 55\text{kts}$ .

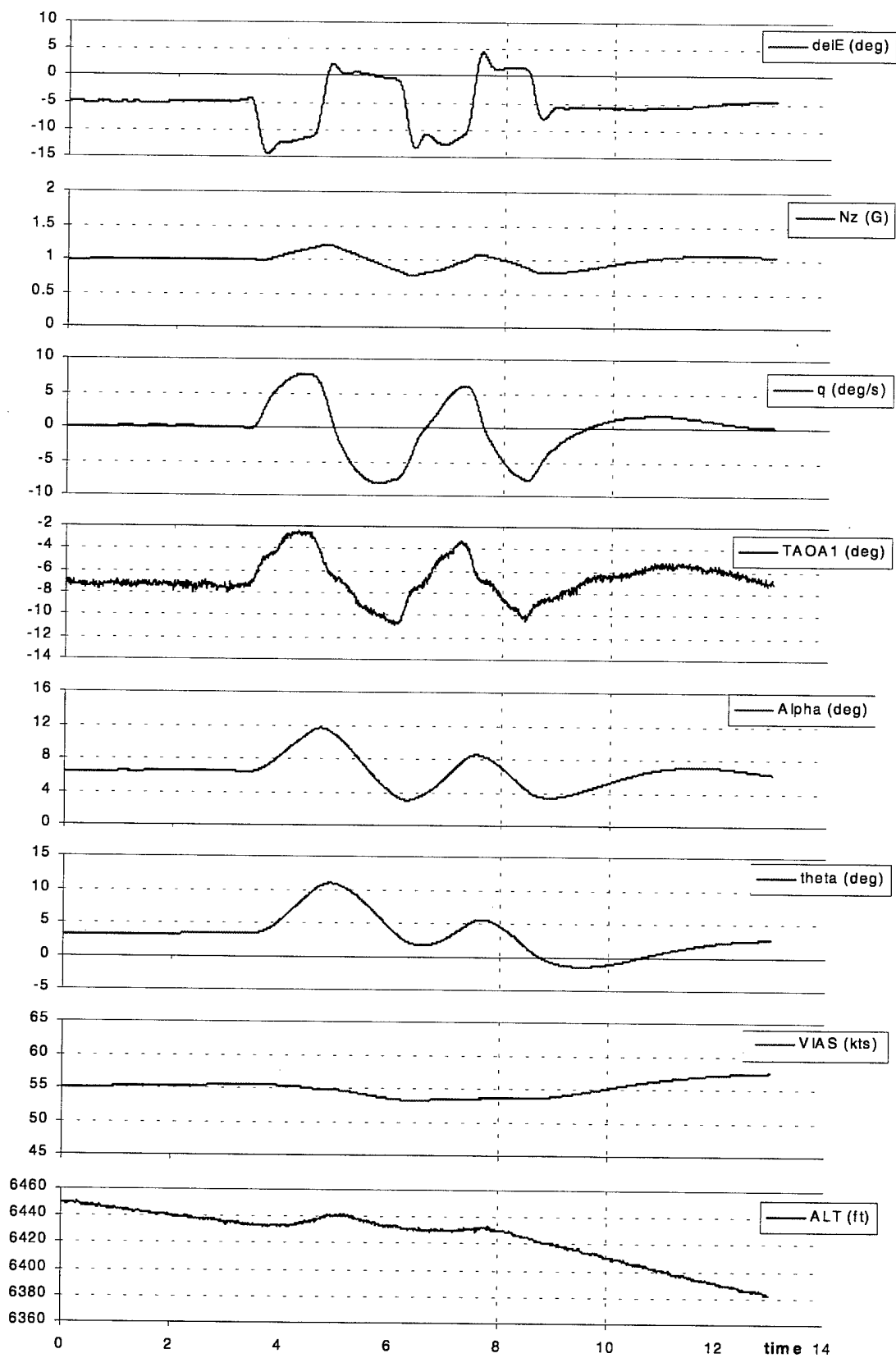


Figure C-15a. Elevator doublet, S&C,  $\delta F = 20^\circ$ , VIAS =  $0.97V_s = 55\text{kts}$ .

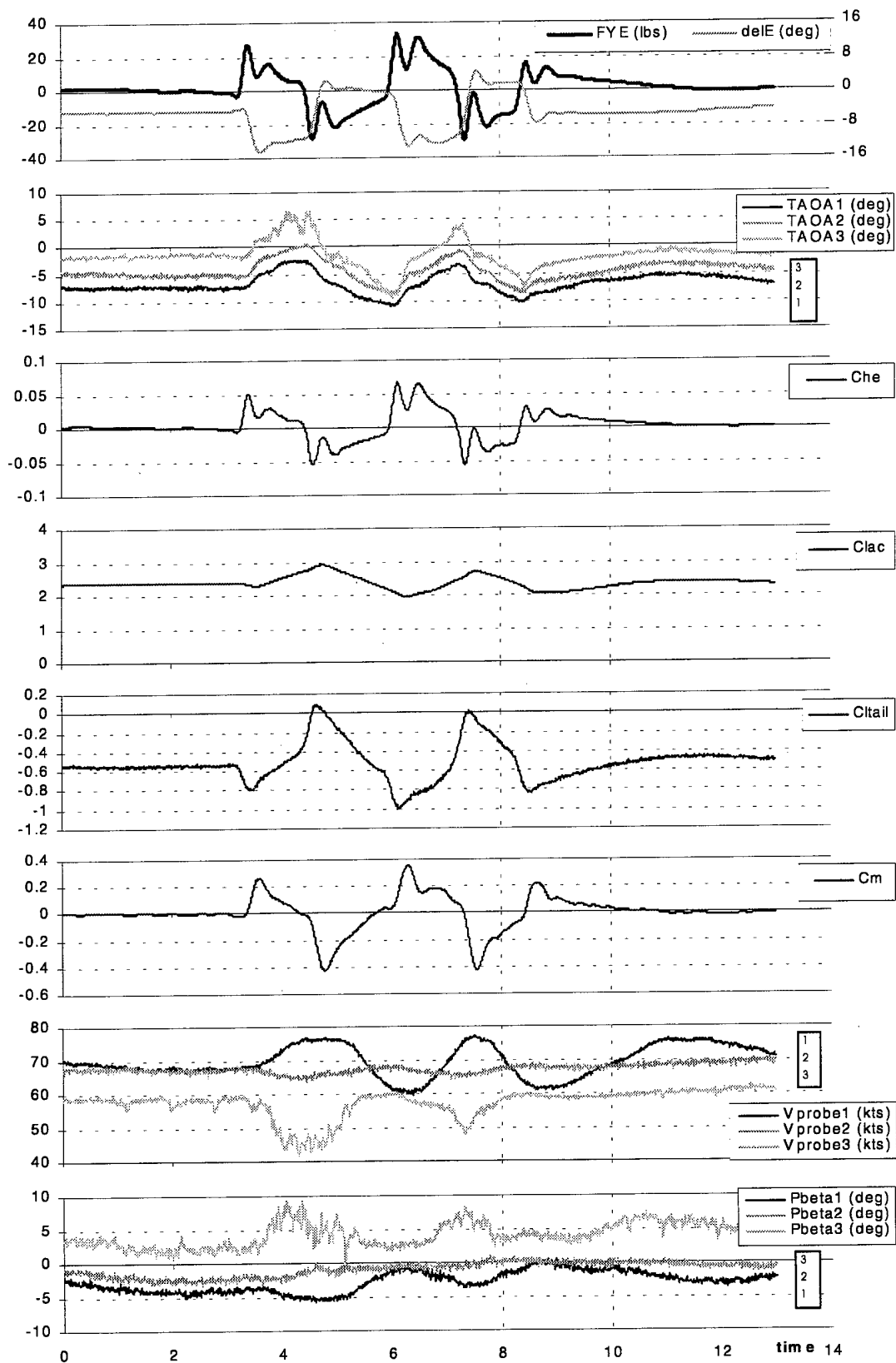


Figure C-15b. Elevator doublet, S&C,  $\delta F = 20^\circ$ , VIAS =  $0.97V_s = 55\text{kts}$ .

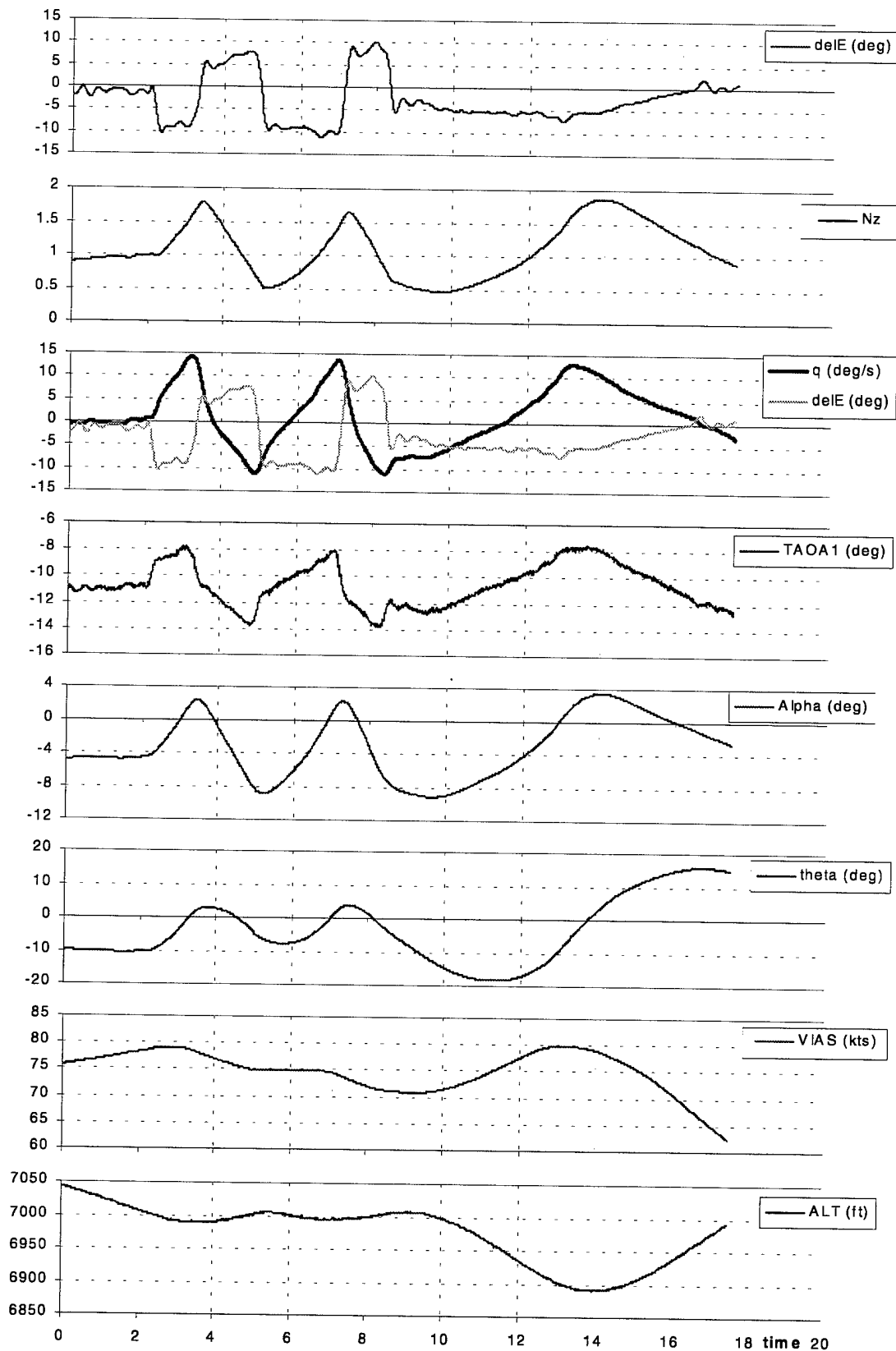


Figure C-16a. Elevator doublet, S&C,  $\delta F = 30^\circ$ , VIAS = 1.40Vs = 75kts.

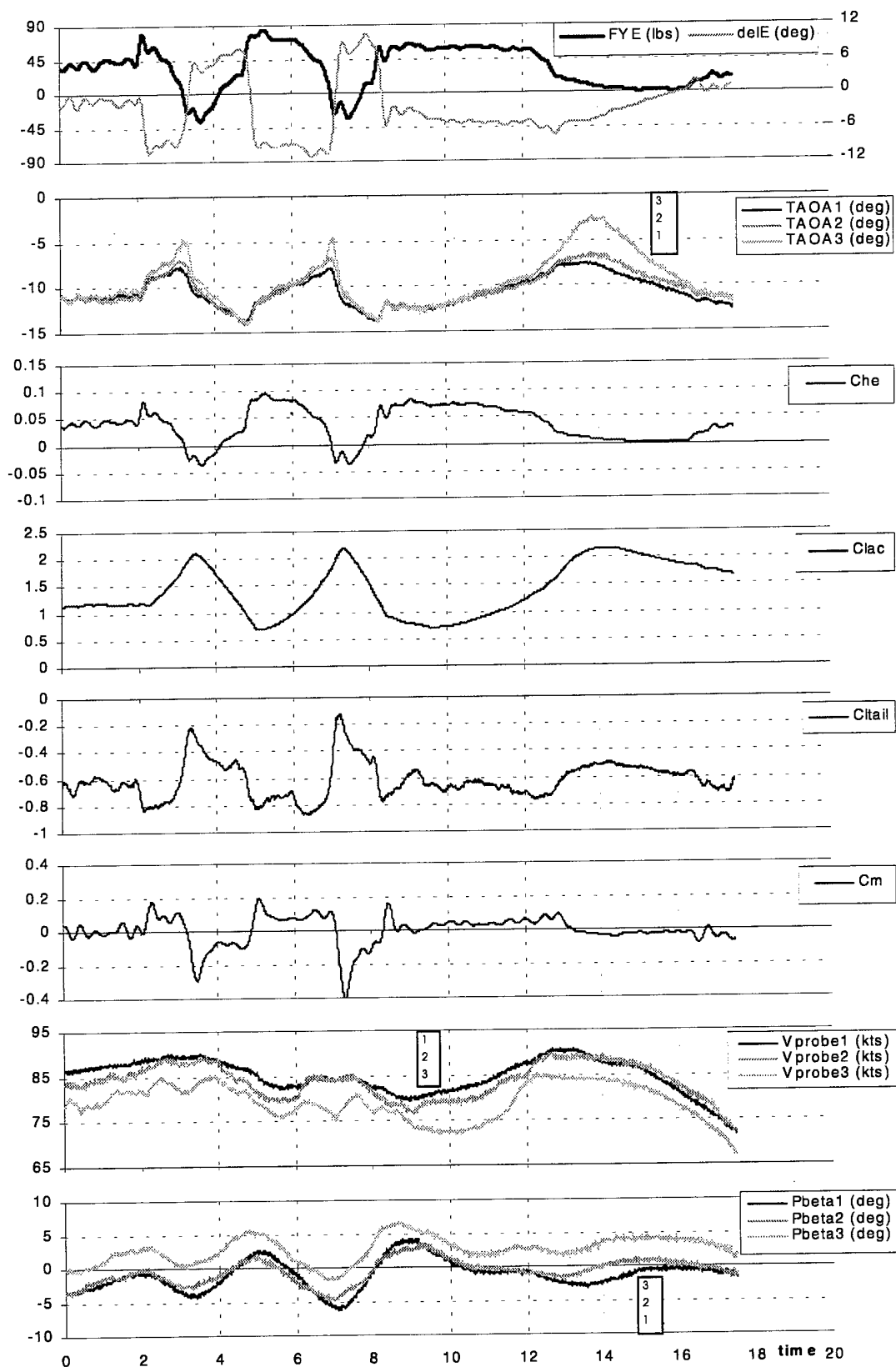


Figure C-16b. Elevator doublet, S&C,  $\delta F = 30^\circ$ , VIAS =  $1.40V_s = 75\text{kts}$ .

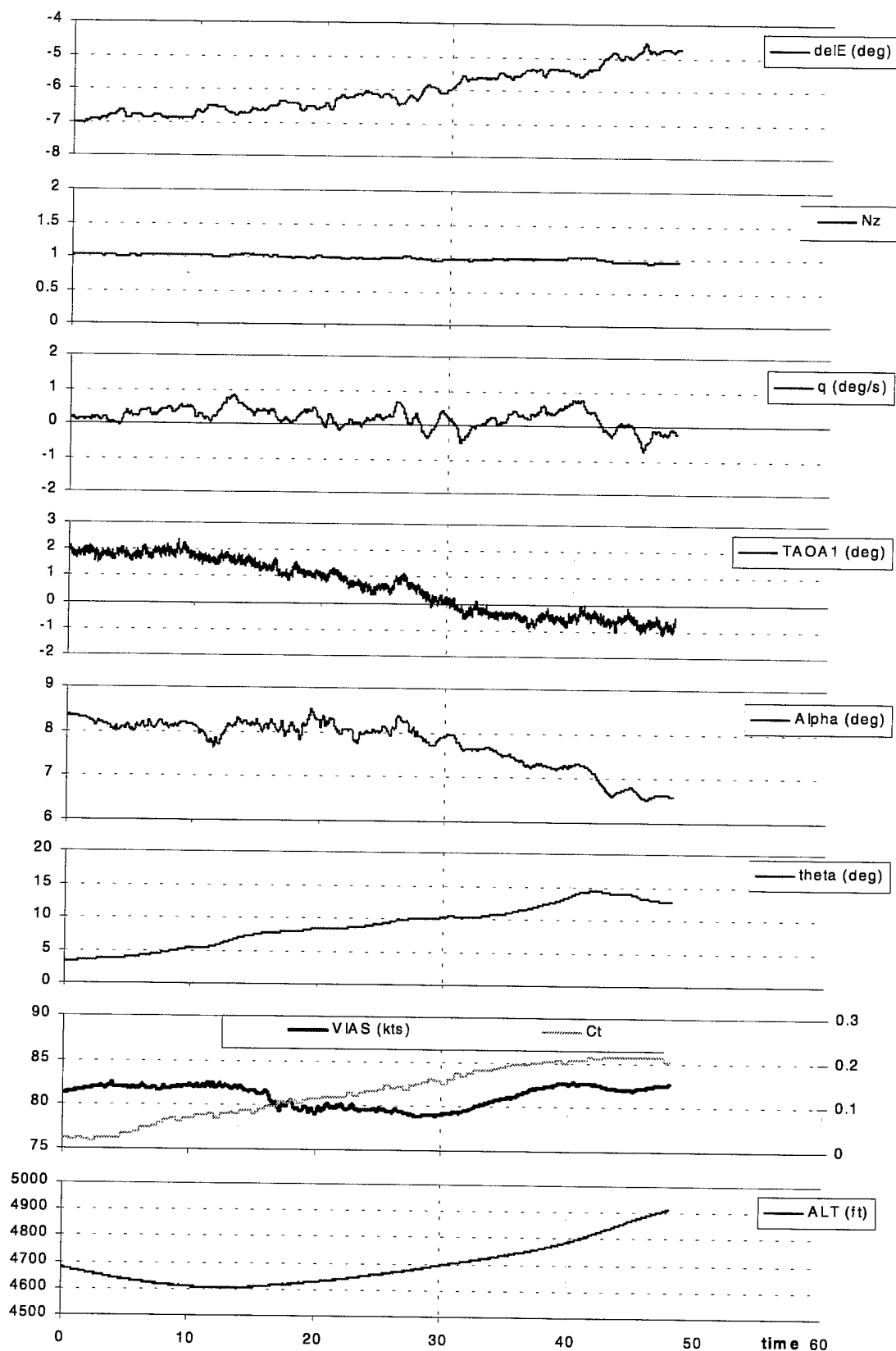


Figure C-17a. Thrust transition, Baseline,  $\delta F = 0^\circ$ , VIAS =  $1.20V_s = 80\text{kts}$ .

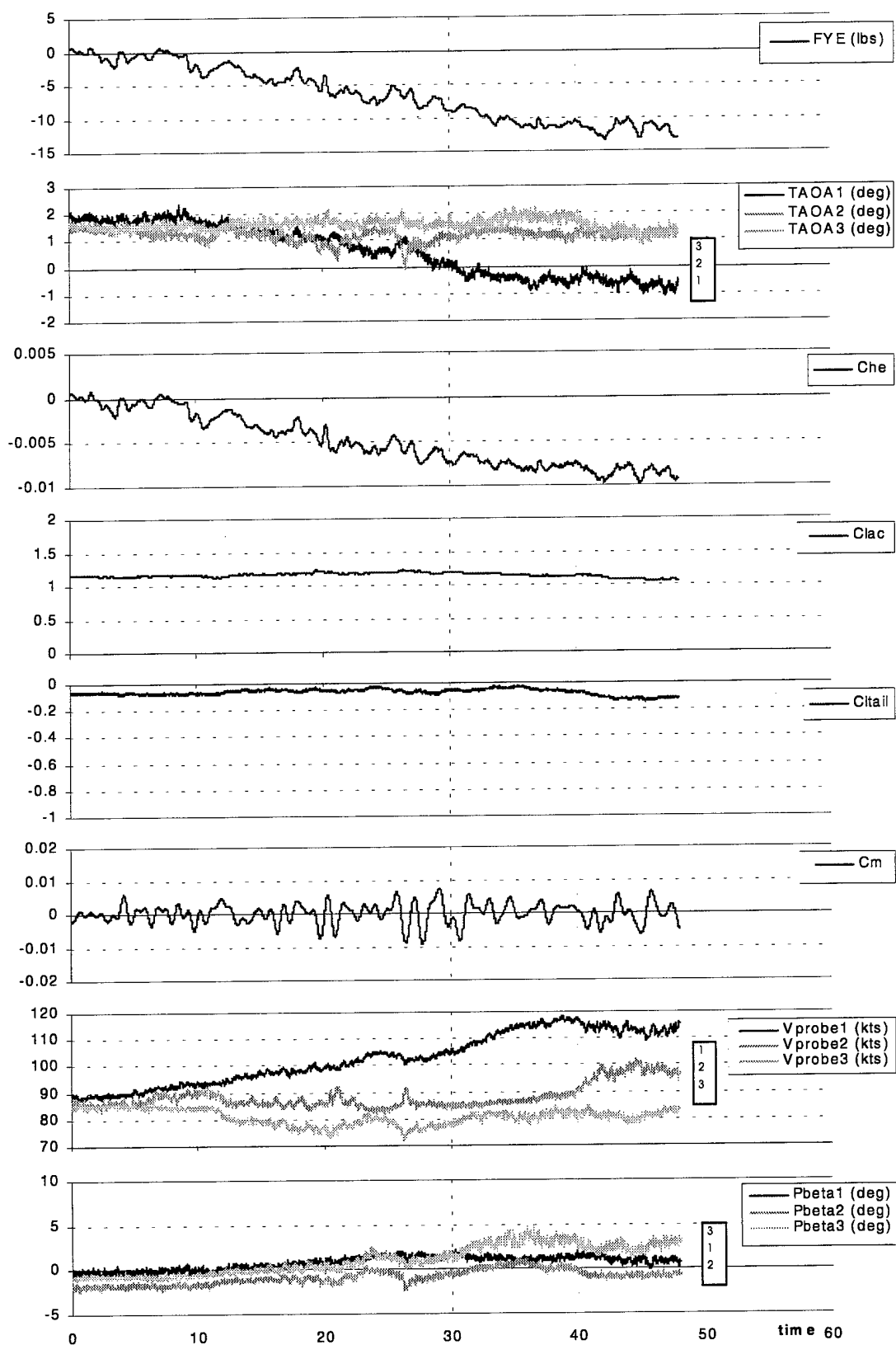


Figure C-17b. Thrust transition, Baseline,  $\delta F = 0^\circ$ , VIAS = 1.20Vs = 80kts.

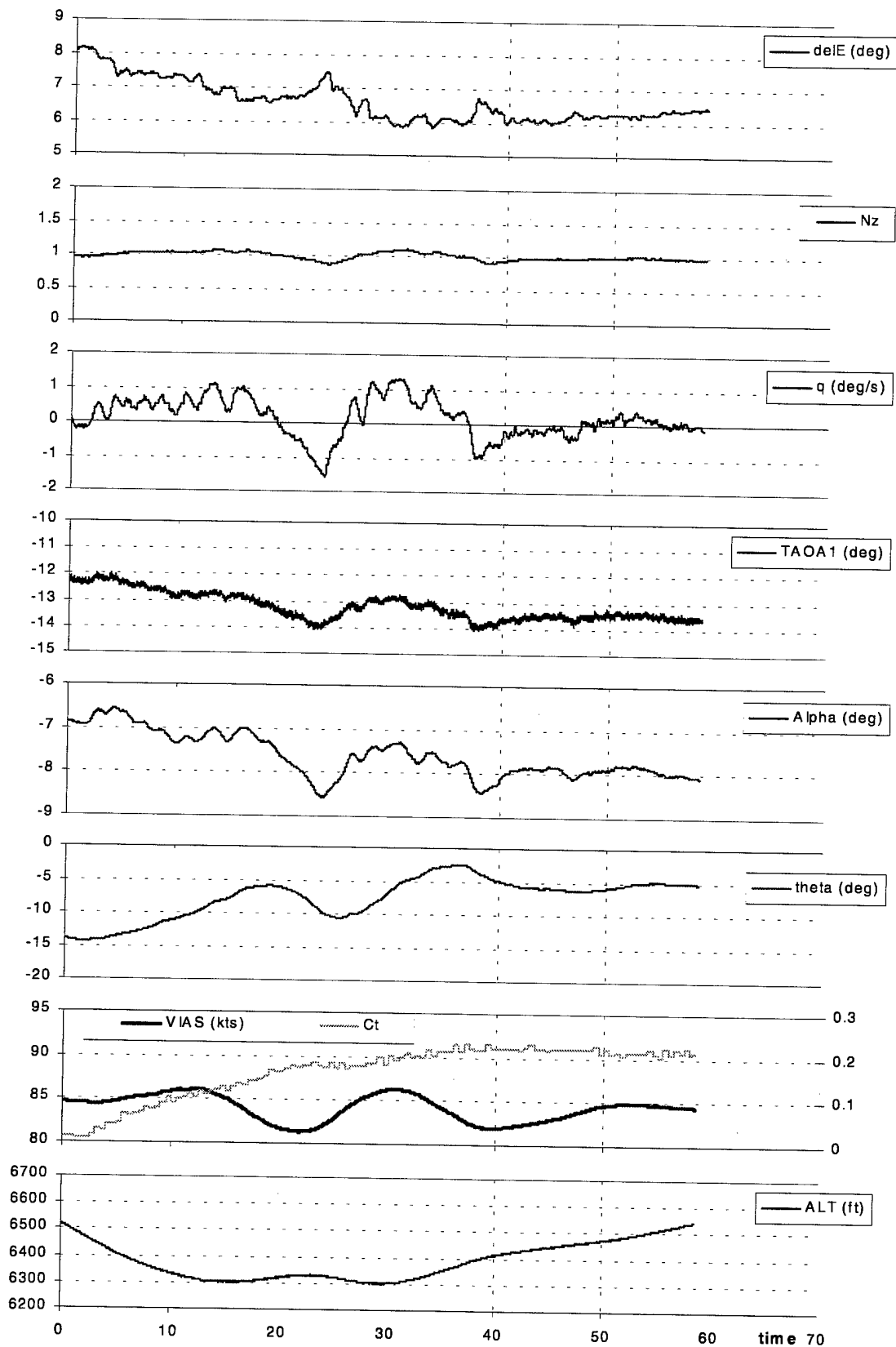


Figure C-18a. Thrust transition, Baseline,  $\delta F = 40^\circ$ , VIAS =  $1.63V_s = 85\text{kts}$ .



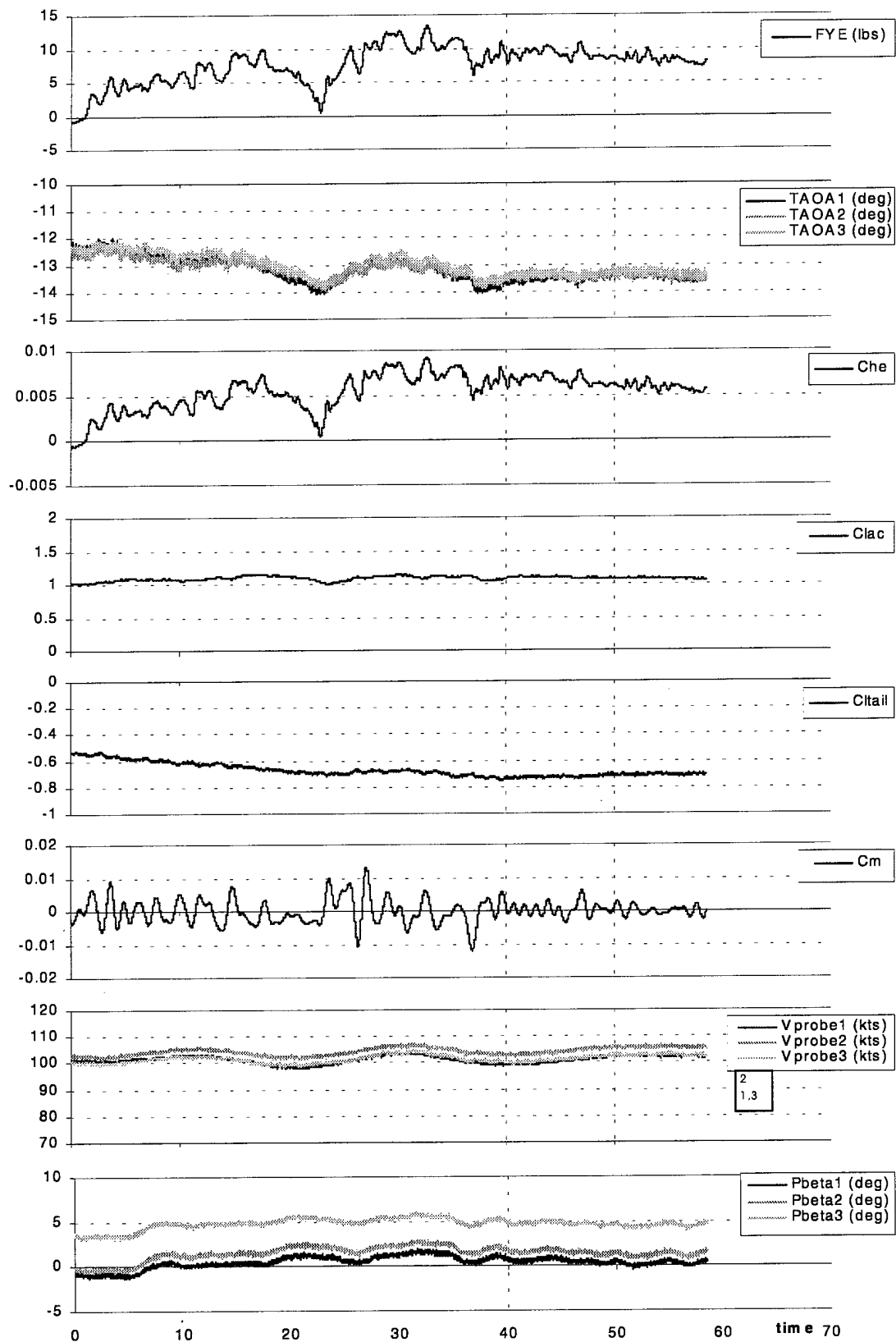


Figure C-18b. Thrust transition, Baseline,  $\delta F = 40^\circ$ , VIAS =  $1.63V_s = 85\text{kts}$ .

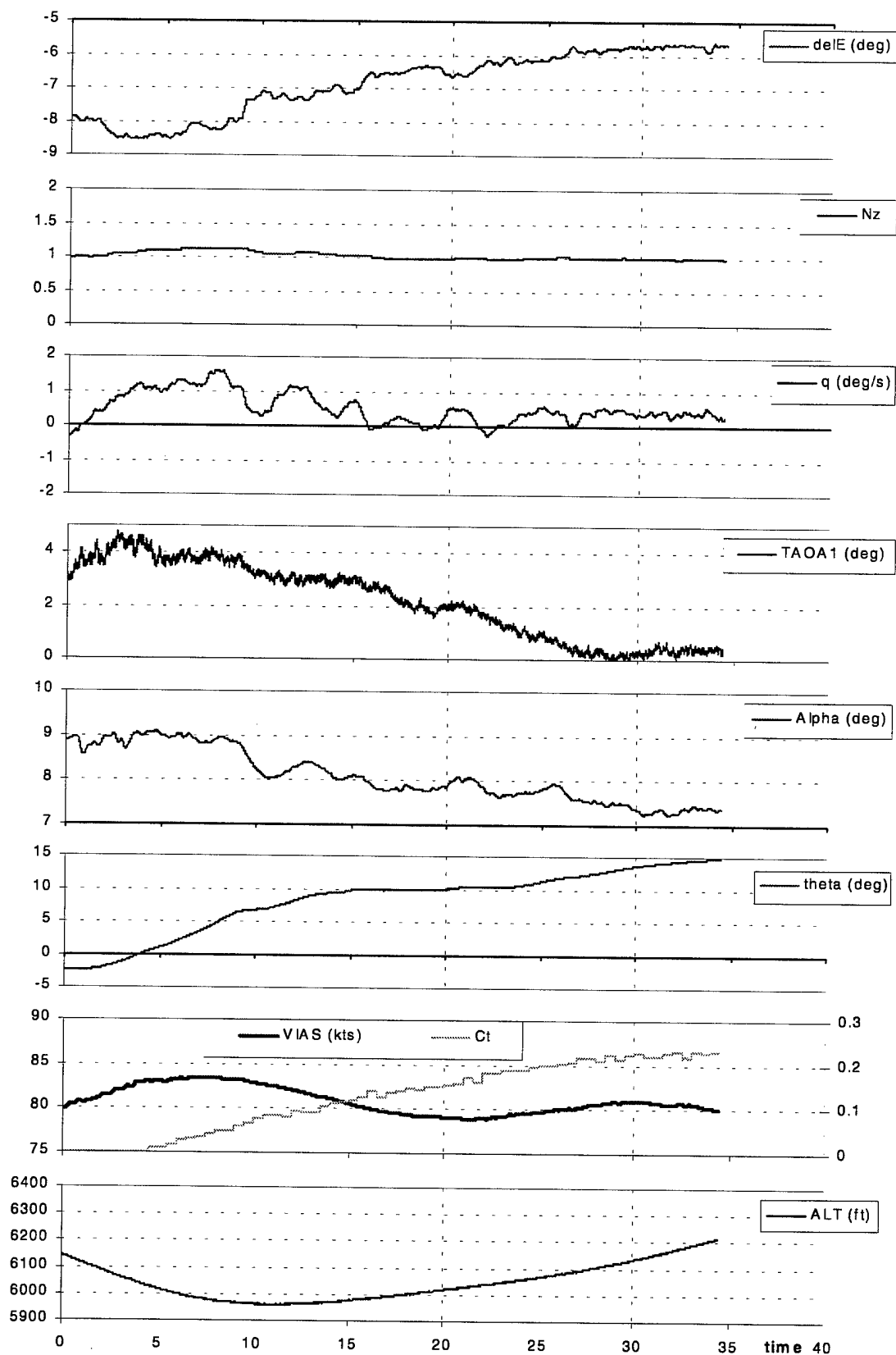


Figure C-19a. Thrust transition, Failed Boot,  $\delta F = 0^\circ$ , VIAS = 1.20Vs = 80kts.

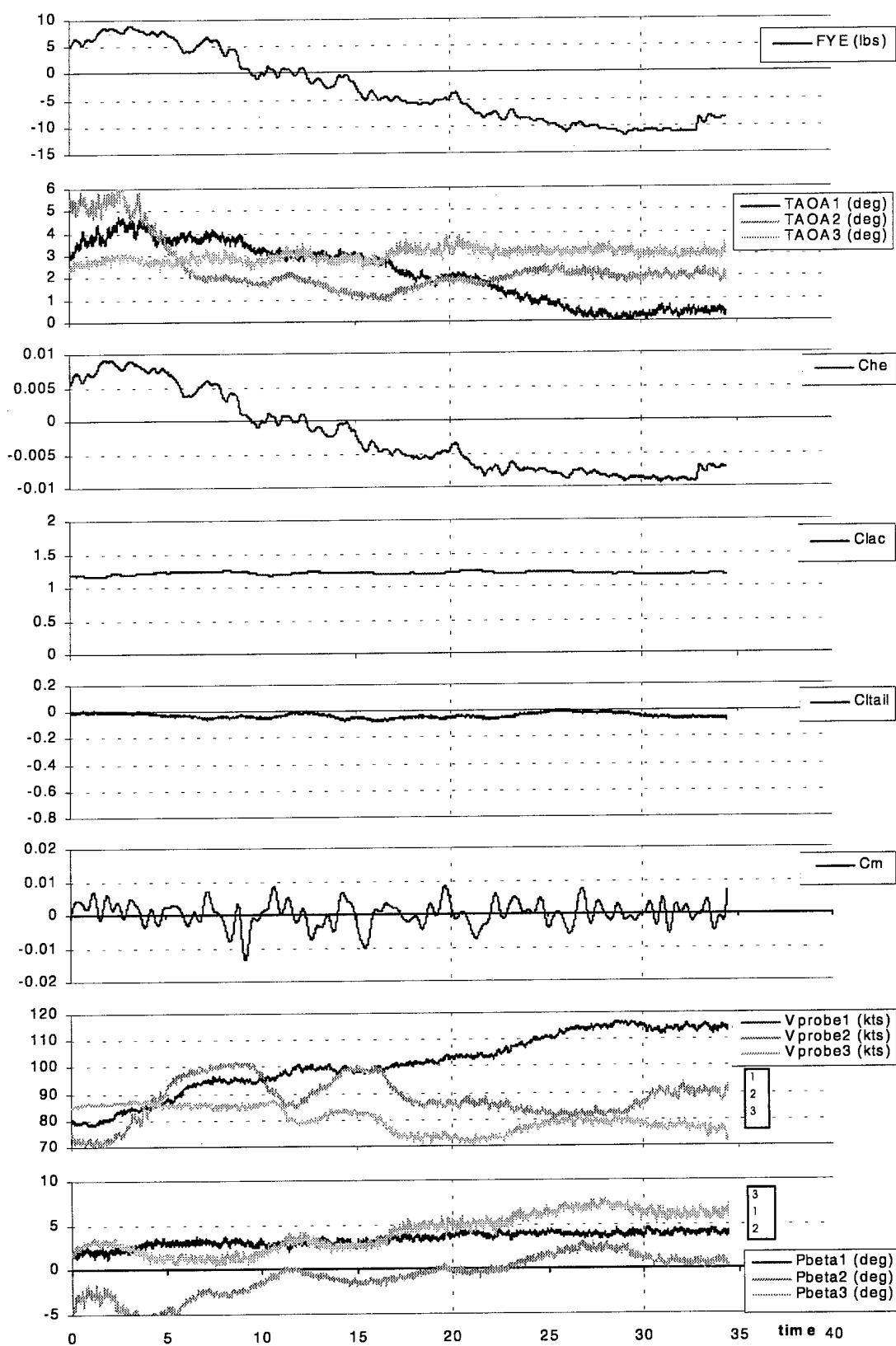


Figure C-19b. Thrust transition, Failed Boot,  $\delta F = 0^\circ$ , VIAS = 1.20Vs = 80kts.

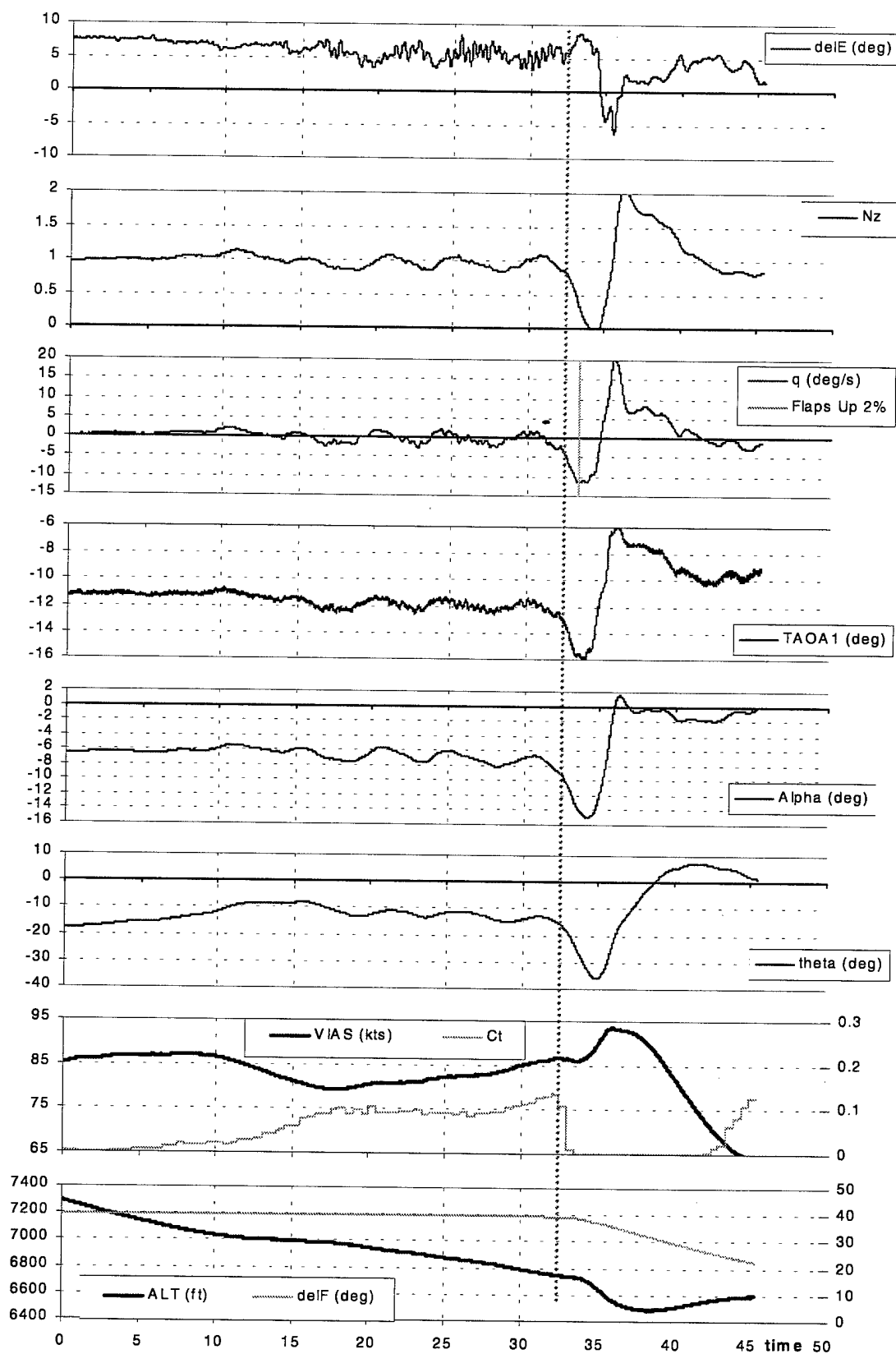


Figure C-20a. Thrust transition, Failed Boot,  $\delta F = 40^\circ$ , VIAS = 1.63Vs = 85kts.

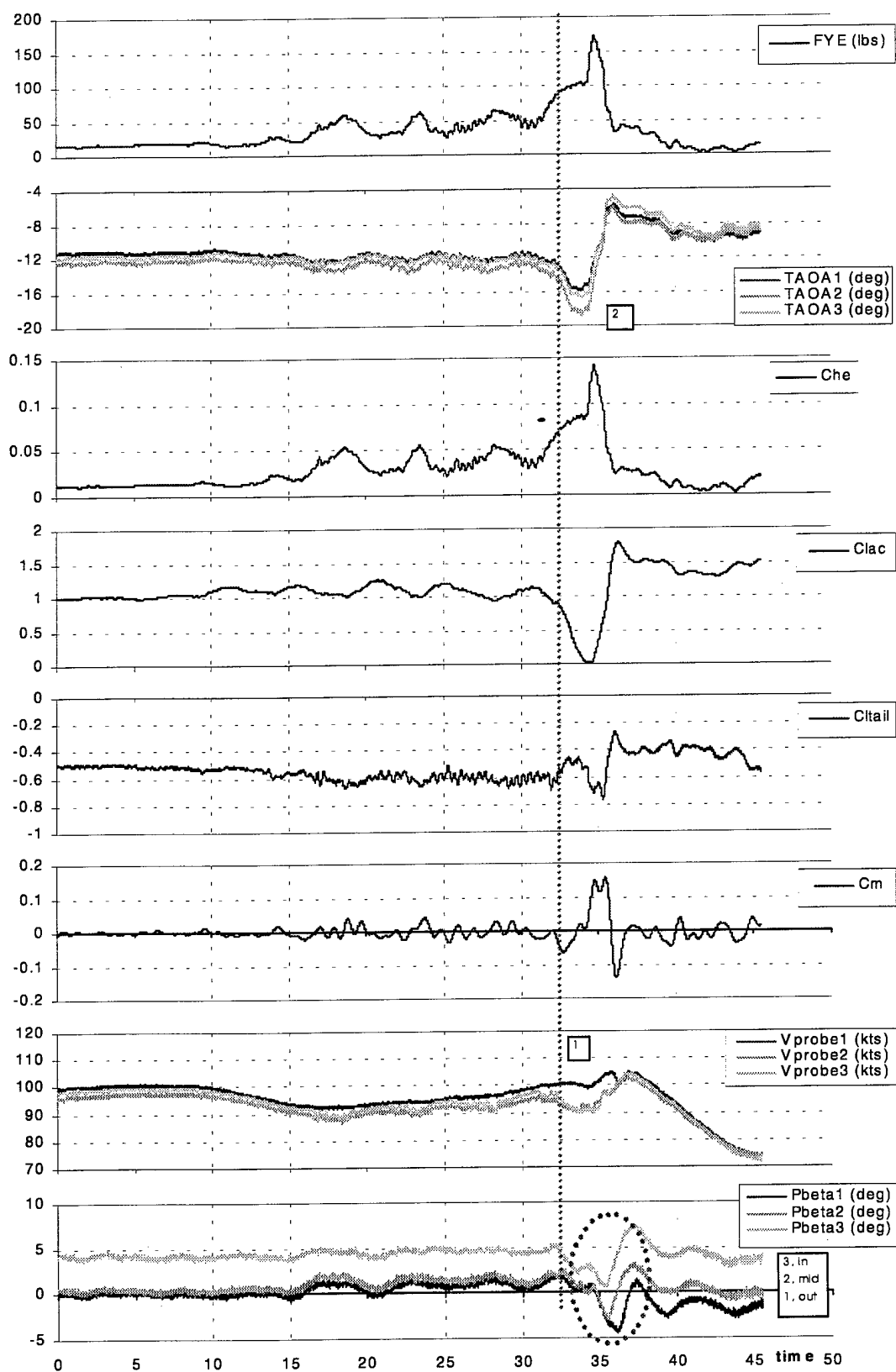


Figure C-20b. Thrust transition, Failed Boot,  $\delta F = 40^\circ$ , VIAS = 1.63Vs = 85kts.

## Appendix D. Pressure Coefficient Distributions of the Full Tail Stall

This appendix contains a detail of select time histories in Figure D1. The events before the stall to after the recovery are detailed. Indicated on the time histories are the times where the pressure distributions are presented. The stall point is also noted with the vertical line.

Figure D2 depicts the pressure tap locations. In Figure D3, the information presented around the  $C_p$  plots includes  $\alpha$ , time stamp,  $C_{l\_Tail}$  and  $\delta E$ . The suction surface pressures are denoted with the solid, blue line.

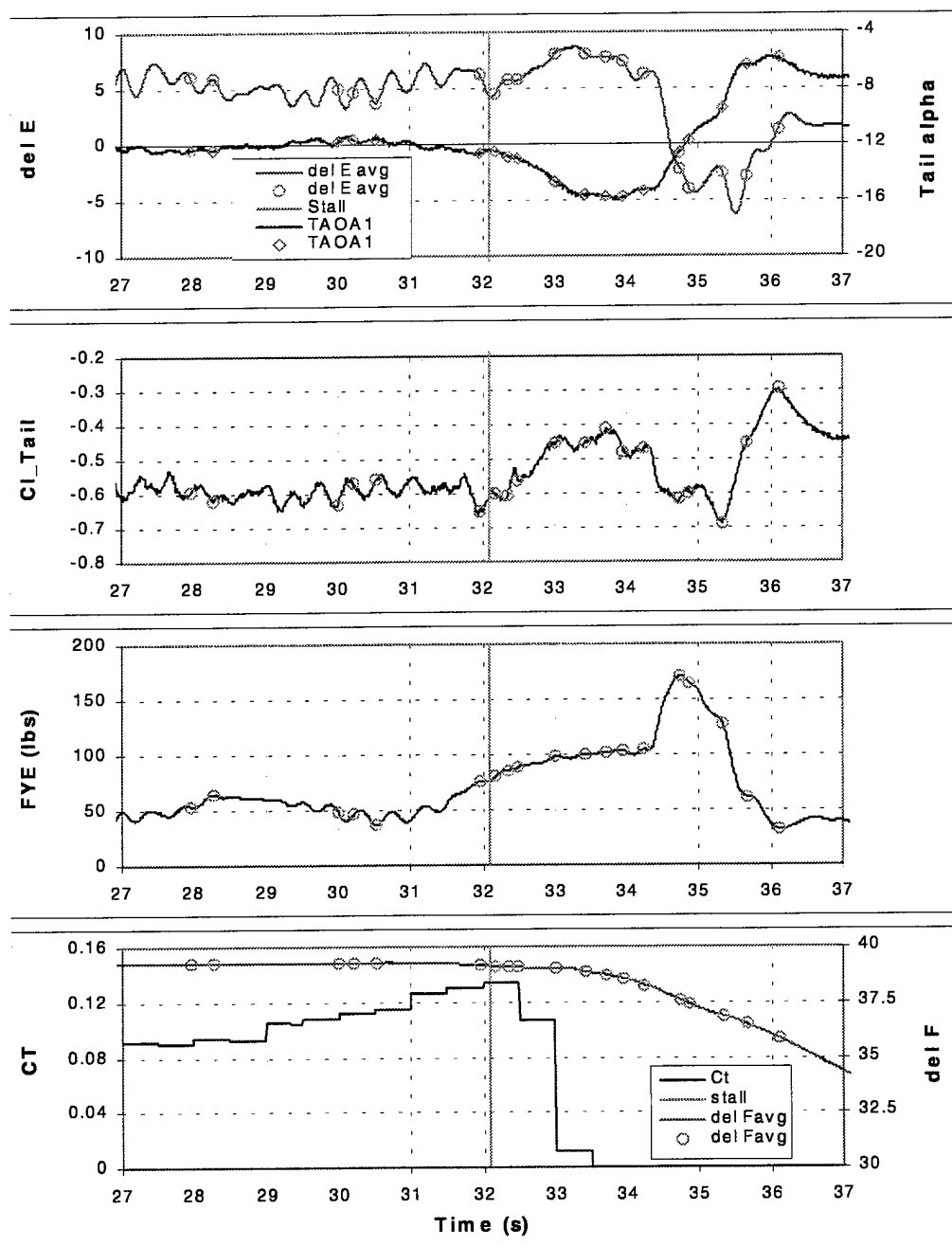
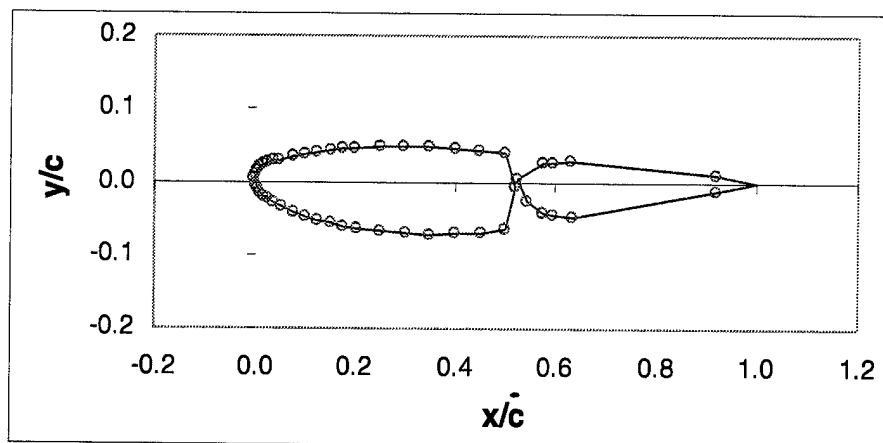


Figure D-1. Select time histories of the stall event. Circles indicate times presented in Figure D-3.



**Figure D-2. Location of pressure taps on clean airfoil.**

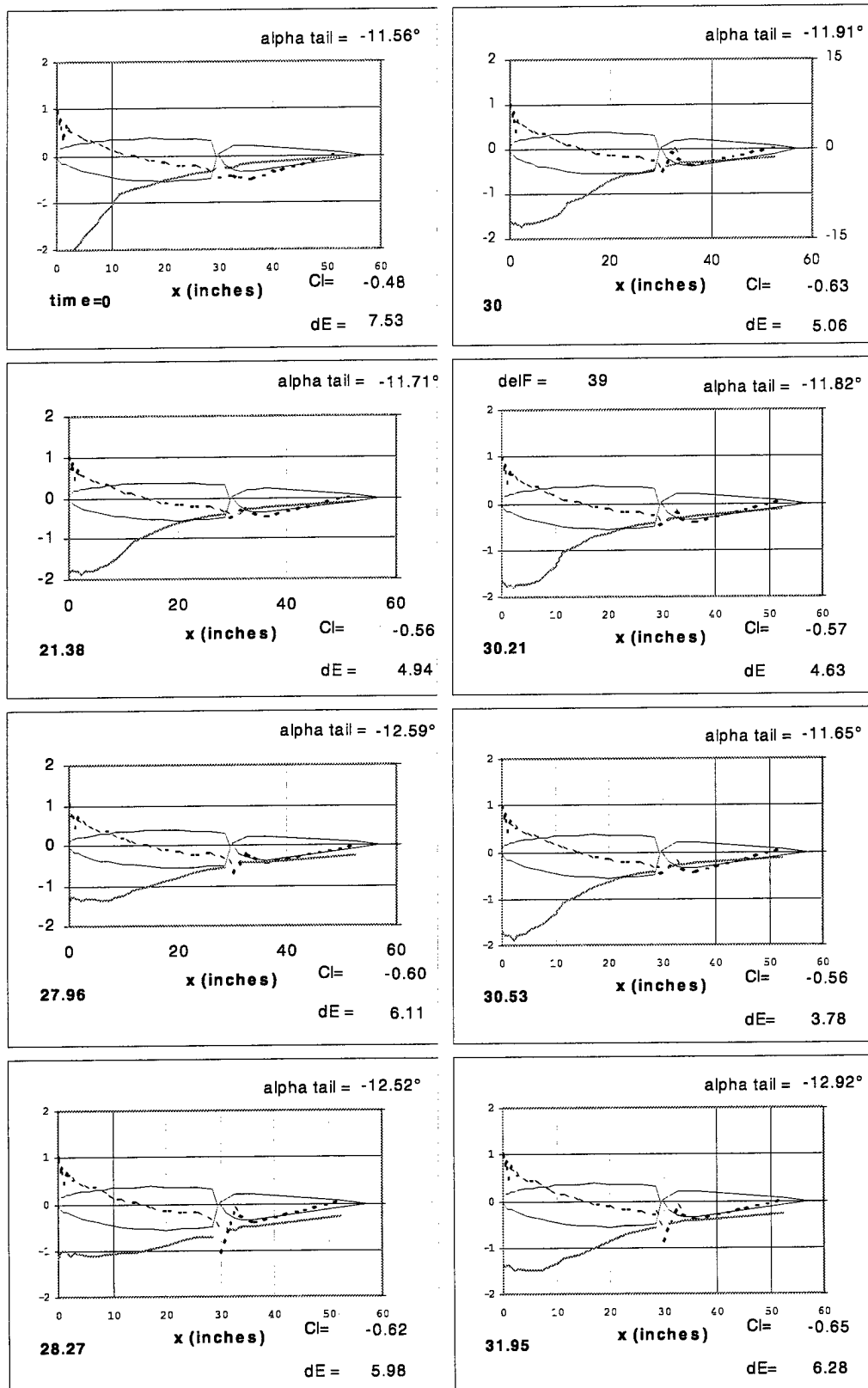


Figure D-3a. Plots of  $C_p$  for full tail stall event at various times. Solid, blue line for lower surface.



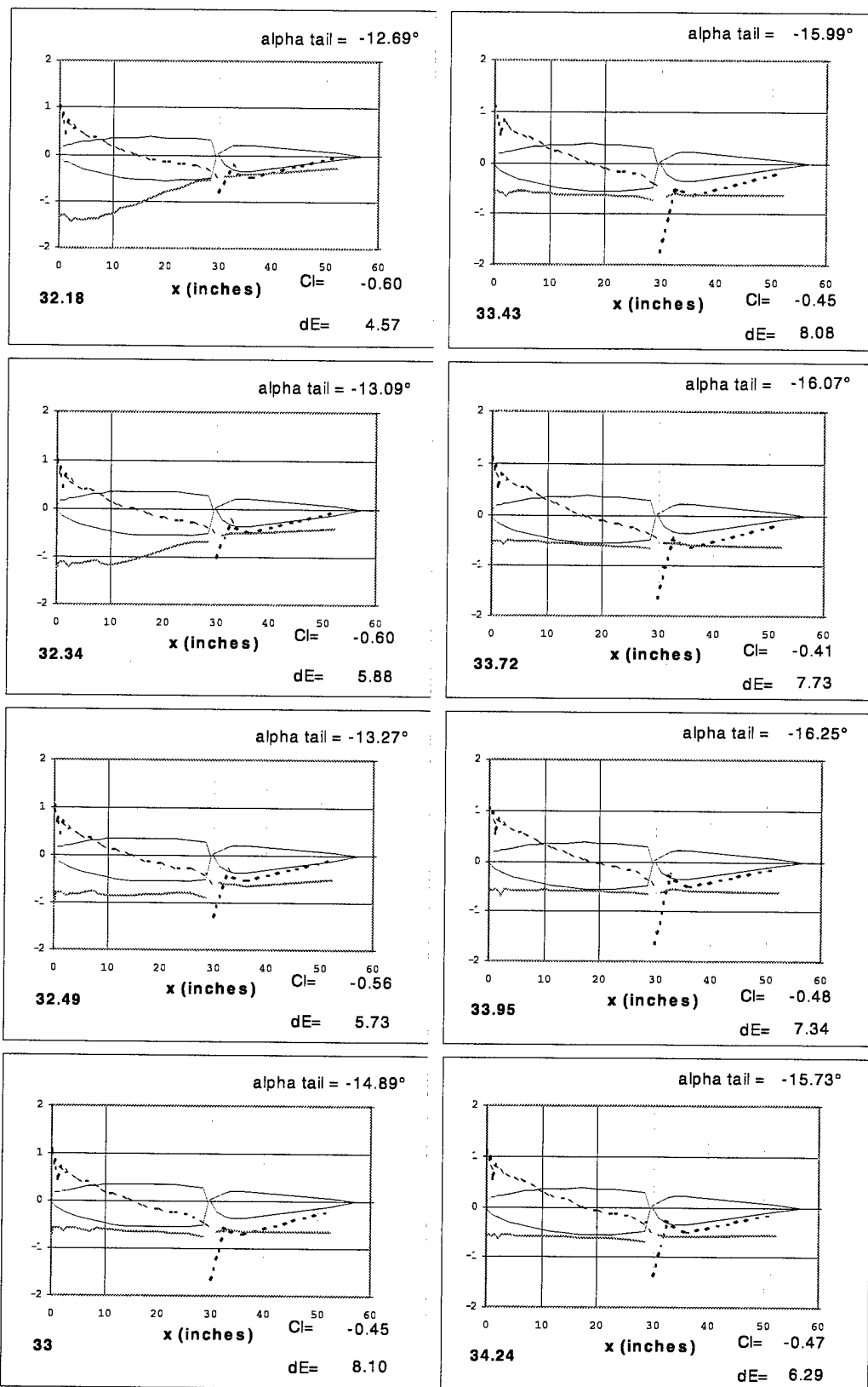


Figure D-3b. Plots of  $C_p$  for full tail stall event at various times. Solid, blue line for lower surface.

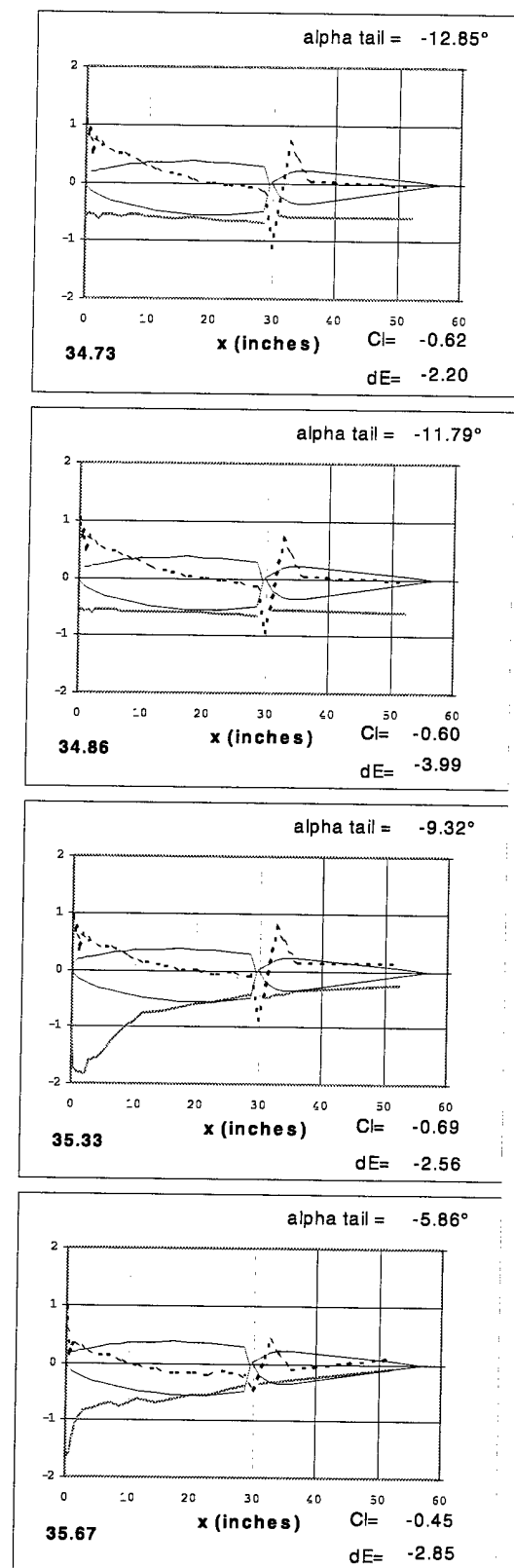


Figure D-3c. Plots of  $C_p$  for full tail stall event at various times. Solid, blue line for lower surface.

REPORT DOCUMENTATION PAGE			Form Approved OMB No. 0704-0188	
Public reporting burden for this collection of information is estimated to average 1 hour per response, including the time for reviewing instructions, searching existing data sources, gathering and maintaining the data needed, and completing and reviewing the collection of information. Send comments regarding this burden estimate or any other aspect of this collection of information, including suggestions for reducing this burden, to Washington Headquarters Services, Directorate for Information Operations and Reports, 1215 Jefferson Davis Highway, Suite 1204, Arlington, VA 22202-4302, and to the Office of Management and Budget, Paperwork Reduction Project (0704-0188), Washington, DC 20503.				
1. AGENCY USE ONLY (Leave blank)		2. REPORT DATE March 2000		3. REPORT TYPE AND DATES COVERED Technical Paper
4. TITLE AND SUBTITLE  NASA/FAA Tailplane Icing Program: Flight Test Program			5. FUNDING NUMBERS  WU-548-21-23-00 Interagency Agreement DTFA03-95-90001	
6. AUTHOR(S)  Thomas P. Ratvasky, Judith Foss Van Zante, and Alex Sim				
7. PERFORMING ORGANIZATION NAME(S) AND ADDRESS(ES)  National Aeronautics and Space Administration John H. Glenn Research Center at Lewis Field Cleveland, Ohio 44135-3191			8. PERFORMING ORGANIZATION REPORT NUMBER  E-12126	
9. SPONSORING/MONITORING AGENCY NAME(S) AND ADDRESS(ES)  National Aeronautics and Space Administration Washington, DC 20546-0001			10. SPONSORING/MONITORING AGENCY REPORT NUMBER  NASA TP-2000-209908 DOT FAA AR-99-85	
11. SUPPLEMENTARY NOTES  Thomas P. Ratvasky, NASA Glenn Research Center; Judith Foss Van Zante, Dynacs Engineering Company, Inc., 2001 Aerospace Parkway, Brook Park, Ohio 44142; and Alex Sim, NASA Dryden Flight Research Center, Edwards Air Force Base, California. Responsible person, Thomas P. Ratvasky, organization code 5840, (216) 433-3905.				
12a. DISTRIBUTION/AVAILABILITY STATEMENT  Unclassified - Unlimited Subject Categories: 08, 05, and 02  This publication is available from the NASA Center for AeroSpace Information, (301) 621-0390.			12b. DISTRIBUTION CODE  Distribution: Standard	
13. ABSTRACT (Maximum 200 words) This report presents results from research flights that explored the characteristics of an ice-contaminated tailplane using various simulated ice shapes attached to the leading edge of the horizontal tailplane. A clean leading edge provided the baseline case, then three ice shapes were flown in order of increasing severity. Flight tests included both steady state and dynamic maneuvers. The steady state points were 1G wings level and steady heading sideslips. The primary dynamic maneuvers were pushovers to various G-levels; elevator doublets; and thrust transitions. These maneuvers were conducted for a full range of flap positions and aircraft angle of attack where possible. The analysis of this data set has clearly demonstrated the detrimental effects of ice contamination on aircraft stability and controllability. Paths to tailplane stall were revealed through parameter isolation and transition studies. These paths are (1) increasing ice shape severity, (2) increasing flap deflection, (3) high or low speeds, depending on whether the aircraft is in a steady state (high speed) or pushover maneuver (low speed), and (4) increasing thrust. The flight research effort was very comprehensive, but did not examine effects of tailplane design and location, or other aircraft geometry configuration effects. However, this effort provided the role of some of the parameters in promoting tailplane stall. The lessons learned will provide guidance to regulatory agencies, aircraft manufacturers, and operators on ice-contaminated tailplane stall in the effort to increase aviation safety and reduce the fatal accident rate.				
14. SUBJECT TERMS  Aircraft icing; Tailplane icing; Stability and control; Aerodynamics; Aeroperformance			15. NUMBER OF PAGES 166	
			16. PRICE CODE A08	
17. SECURITY CLASSIFICATION OF REPORT Unclassified	18. SECURITY CLASSIFICATION OF THIS PAGE Unclassified	19. SECURITY CLASSIFICATION OF ABSTRACT Unclassified	20. LIMITATION OF ABSTRACT	

## Appendix E. Recommendations to the Pilot

Be aware that the tailplane is a more efficient collector of ice than a wing. If ice is detected on the windshield wiper or other objects with sharp leading edges, then it is probably also on the tailplane. The first recommendation is to activate the de-ice/anti-ice protection system. Another recommendation is to manually fly the plane. The cues for an impending horizontal tailplane stall are subtle and much more difficult to detect through the autopilot. Symptoms of contamination include changes in the trim point, difficulty in trimming, onset of PIO, and buffeting in the control yoke as the flow separates and reattaches aft of the hinge point. Also be aware that wing flap extension aggravates a tailplane stall situation. While the differences in tactile cues between a wing stall and a tailplane stall are subtle, the recovery procedure is diametric. When the tail stalls, recovery is achieved by reattaching the flow on the lower surface. This is opposite a wing stall, which requires that the flow reattach on the upper surface. To recover the aircraft, pull the nose back, raise flaps and be judicious with thrust. The reduction of thrust played a significant role in the recovery of the (modified) DHC-6. This is believed to be configuration specific; namely, for aircraft with thrust lines above the CG, adding thrust increases the nose-down pitching moment.

In other words:

IF ICE ACCUMULATION IS NOTED ON OBJECTS WITH SHARP LEADING EDGES (*i.e.*, WINDSHIELD WIPER) THEN

### Recommendations

- Activate Ice Protection
- Hand Fly Aircraft
- Extend Flaps with Extreme Caution

### Symptoms of Ice Accumulation on Horizontal Stabilizer (*Listed in order of increasing severity*)

If flaps have been fully or partially extended, look for:

- Change in Trim Setting from Non-icing Conditions
- Difficulty in Trimming
- Onset of PIO
- Buffet in Control Yoke (not airframe)

### Recovery Procedure

- Yoke Back
- Flaps Up
- Thrust Reduce (may be configuration specific)